The Voltammetric Applications and Frequency-Dependent Properties of Screen-Printed Electrodes and Carbon Nanomaterial Electrodes

Edward Peter Randviir

Manchester Metropolitan University

THE VOLTAMMETRIC APPLICATIONS AND FREQUENCY-DEPENDENT PROPERTIES OF SCREEN-PRINTED ELECTRODES AND CARBON NANOMATERIAL ELECTRODES

Edward Peter Randviir

Submitted in partial fulfilment of the requirements of Manchester Metropolitan University for the degree of Doctor of Philosophy

2014

School of Science and the Environment

Division of Chemistry and Environmental Science

Manchester Metropolitan University

This thesis reports the voltammetric applications and fundamental frequency-dependent properties of carbon-based electrode materials. A range of electrochemical systems hasve been investigated, and new materials have been electrochemically characterised, which will be of use to the field of electrochemistry.

In Chapter 3 of this thesis, different graphenes were utilised as electrode composite materials, and their electrochemical behaviour was de-convoluted. It was found that surfactant-free graphenes were useful for the detection of guanine in terms of a reduced activation potential, which is thought to be derived from a pi-pi adsorption mechanism. The oxygen reduction reaction was also focussed upon and it was found that the type of graphene utilised did not affect the electrochemical mechanism in the respective reactions, but the peroxide yields changed. This could have dramatic ramifications for users choosing carbon materials as catalyst supports.

Screen-printed electrodes were applied to novel systems including theophylline and creatinine, finding that their use as portable sensors was viable in two ways. For theophylline, a direct oxidation mechanism was useful for the detection of the medicine, while in the case of creatinine, an indirect detection method was found to be effective as creatinine is not electrochemically active. In Chapter 5, the first graphene screen-printed electrodes were developed and characterised. The result was two graphene screen-printed electrodes, with differing electrochemical properties, both of which could be used for different applications.

Finally, Chapter 6 focusses upon whether electrochemical impedance spectroscopy is useful for screen-printed electrodes and carbon modifications. The work in this thesis finds that a synergy could potentially be formed, and in particularly, has found that it would be wise to operate screen-printed electrodes around +0.2 V due to this being the point where there is no net charge at the electrode surface under standard conditions.

The primary focus of this thesis is to thoroughly investigate carbon-based electrode materials towards novel electrochemical systems, using existing electrochemical and frequency-dependent techniques, as well as understand the fundamental frequency-dependent properties of screen-printed electrodes. The objectives of these investigations are described in greater detail below.

Objectives

1. Contribute to the scientific understanding of electrochemical impedance spectroscopy and apply this into new electrochemical areas to allow the ability to readily derive mechanistic information.
2. Critically examine solid-liquid interfaces using existing electrochemical techniques, with a particular focus upon screen-printed electrodes.
3. Assess and evaluate the electron transfer at solid-liquid interfaces utilising graphene and related carbon allotropes and probe using electrochemical impedance spectroscopy and voltammetric techniques.
4. Develop electroanalytical sensors based upon electrochemical impedance spectroscopy and voltammetric techniques, and derive new novel detection methods for a range of key/model analytes.

It is not just through necessity that I firstly thank my unrelenting research supervisor, Professor Craig Banks, for giving me the opportunity to conduct the work which has gone into writing this thesis. His continual guidance and support, and rollockings, have turned me from an arrogant undergraduate to a more balanced and pragmatic postgraduate capable of writing such a document. I would also like to thank one of his companies, Kanichi Research Services, for their financial support throughout the duration of my PhD.

I regularly feel like I could not have completed this without the continual help from the Banks Research Group, who have been alongside me for the past three years. On a scientific level, I would like to thank Dr Dimitrios Kampouris, who has always been there to lend us intellectual insight into practically anything and everything scientific. His knowledge and expertise has provoked some of my best work, and I owe him a debt of gratitude for this. Then there are the many guys and girls who I have worked alongside during my time. I thank Dr Dale "AC/DC" Brownson for his in-lab entertainment, and his OCD approach to science; you made me a better experimental chemist. I thank Dr Jonathan Metters for his more levelled and consistent approach to his work – I have learned a lot from you and you will be sorely missed by the group. I would also like to send thanks to fellow lab rats, Chris, Jay, Thanos, Fang, Billie Jean, Luiz, and last but not least, Beth. You have all been there for me and put up with me for so long.

Finally, I would like to thanks my parents for their unconditional love and support throughout the umpteen years of education I have dragged myself through now. One message I can send to them is that it definitely won't be in vain. In fact this thesis marks the beginning of a new chapter for myself as an individual, and I want you to know that I couldn't have done it without you both, for one reason or another. To everyone mentioned, in addition to my girlfriend Helen, this thesis is dedicated to you.

35. Figure 3.4: Cyclic voltammetric responses arising from the electrochemical oxidation of 0.1 mM adenine, with respect to changes in pH, using a 10 ng surfactant-free graphene modified BPPG electrode. Inset, analysis of observed peak potential as a function of the solution pH which yields a linear response with a gradient corresponding to ~66 mV. Scan rate: 50 mV s^{-1}.
36. Figure 3.5: **A**: Cyclic voltammetric responses resulting from the electrochemical oxidation of 0.1 mM adenine in pH 7.2 PBS utilising: (blue line) bare BPPG; (red line) BPPG modified with 5 ng surfactant-free graphene; (grey line) BPPG modified with 10 ng surfactant-free graphene; and (green line) BPPG modified with 20 ng surfactant-free graphene. All scan rates are 50 mV s^{-1}.

    B: Observed voltammetric peak current as a function of the increasing amount of immobilised material for: (green line) graphite modified BPPG and (red line) graphene modified BPPG. The error bars quoted are the standard deviations calculated ($N = 5$).
37. Figure 3.6: **A**: Cyclic voltammetric response resulting from the electrochemical oxidation of 19 μM guanine in pH 7.2 PBS utilising: bare BPPG (green line); BPPG modified with 5 ng surfactant-free graphene (red line); and BPPG modified with 5 ng graphite (blue line).

    B: Observed voltammetric peak current (I_P) as a function of the increasing mass of immobilised material for: (green line) graphite modified BPPG; and (red line) graphene modified BPPG. The error bars quoted are the standard deviations calculated ($N = 5$).
38. Figure 3.7: Chemical structure of SA.

93. Figure 6.2: Bode plots for EPPG (blue), BPPG (green), and platinum (red) electrodes. Parameters: +20 mV DC excitation potential; 10 mV AC amplitude; 10 frequencies recorded per decade. A 20 mV DC excitation potential was used because a slight excitation is required for the experiment, but Faradaic exchanges needed to be avoided; such a small offset satisfies these needs.
94. Figure 6.3: Bode plots for five SPEs: ESPE (blue); BSPE (green); SW-SPE (purple); GSPE (red); and LRI-SPE (grey). Parameters: +20 mV DC excitation potential; 10 mV AC amplitude; 10 frequencies recorded per decade.
95. Figure 6.4: Bode plot for 1 mM $K_3[IrCl_6]$ in pH 7.4 PBS with 0.1 M KCl electrolyte. Parameters: +20 mV DC excitation potential; 10 mV AC amplitude; 10 frequencies recorded per decade; LRI-SPE utilised.
96. Figure 6.5: Bode plot for 1 mM $K_3[IrCl_6]$ in pH 7.4 PBS with 0.1 M KCl electrolyte. Parameters: +550 mV DC excitation potential; 10 mV AC amplitude; 10 frequencies recorded per decade.
97. Figure 6.6: Nyquist plots for 1 mM $K_3[IrCl_6]$ in pH 7.4 PBS for the non-Fardaic (blue) and Faradaic (green) cases. Parameters: variable DC excitation potential; 10 mV AC amplitude; 10 frequencies recorded per decade; +0.02 V DC potential (non-Faradaic case); +0.52 V DC potential (Faradaic case); frequency range: 10000000 – 0.2 Hz.
98. Figure 6.7: RC circuit used to model capacitance values from PZC experiments, utilising EIS.
99. Figure 6.8: Quantum capacitance for single layer graphene. Reprinted from Reference 466.

*	Bulk solution
A	Surface area
AC	Alternating Current
ATR	Attenuated Total Reflectance
BDD	Boron-Doped Diamond
BPPG	Basal-Plane Pyrolytic Graphite
BSPE	Basal-plane Screen-Printed Electrode
C	Concentration
C_{DL}	Double layer capacitance
CNT	Carbon NanoTube
CV	Cyclic Voltammetry
CVD	Chemical Vapour Deposition
D	Diffusion coefficient
DC	Direct Current
DPV	Differential Pulse Voltammetry
EIS	Electrochemical Impedance Spectroscopy

E^0	Standard potential
E	Cell potential
E_P	Peak potential
EMF	ElectroMotive Force
EPPG	Edge-Plane Pyrolytic Graphite
ESPE	Edge-plane Screen-Printed Electrode
F	Faraday constant
GC	Glassy Carbon
GO	Graphene Oxide
GSPE	Graphene Screen-Printed Electrode
HOPG	Highly Ordered Pyrolytic Graphite
HPLC	High Performance Liquid Chromatography
IR	Infra-Red
I_P	Peak current
j	Flux
k	Boltzman constant
k^0	Electron transfer rate constant
LoD	Limit of Detection

LRI-SPE	Low Resistance Ink Screen-Printed Electrode
LSV	Linear Sweep Voltammetry
MWCNT	Multi-Walled Carbon NanoTube
n	Number of electrons transferred
n'	Number of electrons transferred in the rate-determining step
R	Molar gas constant
R_{CT}	Charge transfer resistance
R_S	Solution resistance
RSD	Relative Standard Deviation
SCE	Saturated Calomel Electrode
SEM	Scanning Electron Microscopy
SPE	Screen-Printed Electrode
SWCNT	Single-Walled Carbon NanoTube
SW-SPE	Single-Walled carbon nanotube Screen-Printed Electrode
SWV	Square Wave Voltammetry
t	Time
T	Temperature
TEM	Transmission Electron Microscope

UV/Vis	UltraViolet/Visible light spectrophotometry
XPS	X-Ray Photoelectron Spectroscopy
XRD	X-Ray Diffraction
Z	Impedance
Z'	Real complex plane impedance
Z''	Imaginary complex plane impedance
Z_W	Warburg impedance
ω	Frequency (angular)
υ	Scan rate
ϕ	Interfacial potential
α	Kinetic parameter - anode
β	Kinetic parameter - cathode
θ	Phase angle
η	Overpotential
ψ	Nicholson parameter

CHAPTER 1
ELECTROCHEMISTRY

INTRODUCTION TO ELECTROCHEMISTRY

Throughout this thesis, a number of physical and chemical parameters have to be taken into consideration, because the origin of electrochemical responses is not from any one particular process; rather the electrochemical responses obtained in each experiment is a summation of various phenomena encountered. Therefore in this Chapter, the fundamentals of electrochemistry are briefly explained in sufficient detail to satisfy the work conducted, starting with an introduction into electrochemistry, the theory of which is utilised throughout the entirety of this thesis. Many areas are covered, from setting up an electrochemical experiment, to interpretation of data, to factors which need consideration when selecting electrode materials.

1.1 ELECTROCHEMISTRY

The field of electrochemistry concerns the study of electron transfer reactions between an electrode and a reactant contained within solution.[1] Electron transfer reactions are vitally important, in both the technological and natural world. For instance, a standard voltaic cell requires an electron transfer reaction in order for the chemical energy stored within the cell to be converted into electrical energy for use outside of the cell.[2] Conversely in nature, electron transfer reactions are required for important biological processes such as photosynthesis for the production of sugars from carbon dioxide and water in plants,[3] and in respiratory processes (e.g. Kreb's cycle, electron transport chain[4]) taking place in plants, animals, and bacteria alike. All these processes have at least these two things in common: the passage of electrical current, and the production of electrical energy from chemical potential energy.[5] In fact, all electrochemical (Faradaic) processes meet these two requirements, and a

vast array of techniques, phenomena, devices, and technologies revolve around these processes. It is the job of electrochemists to study such electron transfer reactions in order to understand, improve, and consolidate such reactions for applications within the technological world.

Electrochemical reactions differ from chemical reactions insofar as electrons are transferred between a reactant and an electrode (at the electrode|solution interface), as opposed to chemical reactions where electrons are transferred between molecules and take place in a bulk solution (or at surfaces in a heterogeneous reaction, but no electrons are transferred between the surface and the molecule). Scientists have the capability to monitor such electrode|solution interactions by use of a (or a combination of) electrochemical technique(s), which are divided generally into two categories: potentiometric; and potentiostatic measurements. There are many similarities between these techniques, such as the requirement for two conducting electrodes in contact with an ionic electrolyte containing an electroactive target (collectively called an electrochemical cell). The conducting electrodes are a working electrode for electrochemical reactions to take place as well as a high-impedance (zero-current) reference electrode, which is required for the monitoring of working electrode potential and/or current fluctuations. Without the reference electrode, the measurement of a potential drop at one interface is not feasible,[1] thus the fixed-potential reference electrode is introduced; all electrochemical activity is then directly ascribable to the working electrode|solution interface. The differences between the two subsets of electrochemical methods are that potentiostatic techniques *control* the potential, whereas potentiometric methods *measure* the potential in an electrochemical system.

Mentioned in the previous paragraph was the notion that two conductors separated by an electrolyte are termed an electrochemical cell, or simply just “cell” for short. The cell is the key component in any electronic circuit without an external power supply. Cells which

power a device through spontaneous conversion of chemical energy into electrical energy at an electrode surface are termed as *galvanic* cells.[5] Galvanic cells are obviously hugely important in modern day society as they power a host of different of electrical devices ranging from laptops and gaming devices through to mobile phones and electronic razors, through either a primary cell (non-rechargeable) or a secondary cell (rechargeable). Fuel cells are a further type of galvanic cell, which provide a much higher power density than a primary or secondary galvanic cell; such cells are hoped to power electric cars on a global scale one day.[6-8]

Galvanic cells are of little importance to this work, however, as the majority of this thesis focusses upon *electrolytic* cells. Electrolytic cells are subjected to an external electric field, which catalyses electrochemical reactions from a source of target molecules in the cell. The external voltage must be higher than the open-circuit potential of the cell to be termed an electrolytic cell, otherwise it would be simply a galvanic cell with the open circuit potential as the cell's potential output. Using electrolytic cells, one can perform desired electrochemical reactions at electrode surfaces (oxidation of ascorbic acid for example[9]), whilst controlling the potentials of the system by altering the properties of the electrode|solution interface. An example of an electrolytic cell is provided in Figure 1.1.

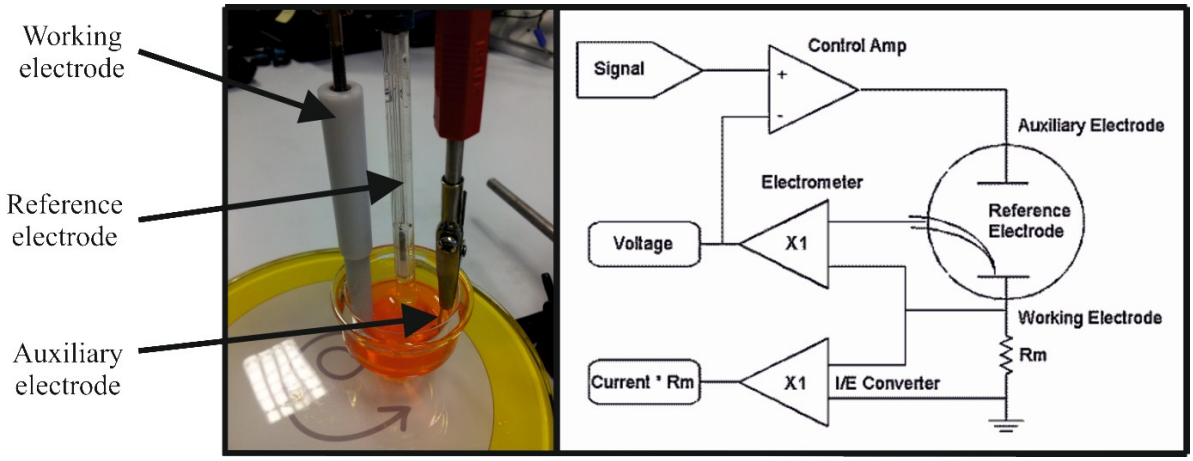

Figure 1.1: Left: typical three electrode cell setup consisting of (from left to right) a working electrode, a reference electrode, and an auxiliary electrode. Right: simple potentiostatic circuit, reprinted from Gamry.[10]

1.2 FARADAIC PROCESSES

Electrochemists, like everyone else, face many problems when interpreting data; one such problem is deducing the origin of an observed passage of current. This is important as two types of processes occur at electrodes, which contribute to the observed currents: Faradaic; and non-Faradaic processes. The latter phenomenon describes a process where a current (or transient current) is observed due to anything other than a charge transfer process, such as adsorption, desorption (or voltammetric stripping), solution composition changes, biorecognition events, diffusion through porous electrodes, or changes in electrode surface area. Clearly, the list is long and distinguished, so controls have to be set in place to minimise such non-Faradaic effects, or at the very least keep them under strict control. If such processes remain controlled, any observed changes in potential or current are attributed to the Faradaic, or charge transfer, processes occurring at the electrode|solution interface. Generically, a reversible charge transfer process is denoted as in equation 1.1, where a redox-active species is oxidised and reduced at an electrode surface (*n* denotes the number of electrons, *e*, involved in the reaction):

$$Ox + ne \leftrightarrow \mathrm{Re}d\,. \tag{1.1}$$

It is this transfer of electrons which the field of electrochemistry is concerned with. This is because the current response obtained from interfacial charge transfer is directly proportional to the concentration of the electroactive species in the bulk solution. However, in electrolytic cells, these processes do not just spontaneously occur, as alluded to in the opening section. Rather, such a process must be instigated by an external electric field or potential. This potential provides energy for the Faradaic process to be thermodynamically favourable. The thermodynamics of electrode systems are detailed, yet are simplified by the Nernst equation (equation 1.2), which describes the relationship between electrochemical potential and the relative activity of chemical species, where E is the potential of the process under scrutiny, E^0 is the standard cell potential, R is the molar gas constant, 8.314 J K^{-1} mol^{-1}, T is the absolute temperature, n is the number of electrons transferred, F is the Faraday constant, 96485.33 C mol^{-1}, and a is the relative activity of the chemical species present.

$$E = E^0 + \frac{RT}{nF}\ln\left(\frac{aOx}{a\,\mathrm{Re}d}\right) = E^0 + \frac{2.303RT}{nF}\log\left(\frac{aOx}{a\,\mathrm{Re}d}\right) \tag{1.2}$$

Normally, electrochemistry operates with relatively low analyte concentrations, thus one can assume that the molecule activity is equal to the concentration (an approximation which can be made due to low intermolecular activity at low analyte concentrations), provided it is kept in mind that the concentration relates specifically to the concentration at the electrode surface.[5] Thus, the Nernst equation assumes the following form (under standard conditions) in most textbooks, where [Ox] and [Red] represents the concentration of the relevant electroactive species:[1, 11]

$$E = E^0 + \frac{0.059}{n}\log\left(\frac{[Ox]}{[\mathrm{Re}d]}\right) \tag{1.3}$$

The theoretical potential deduced from the Nernst equation is the potential required for the system in question to undergo an electrochemical reaction, and hence instigate charge transfer reactions, creating a current, which can be measured by the working electrode. If this potential is negative, the reaction is thermodynamically favourable, and thus the species *Ox* in equation 1.1 will be reduced, losing *n* electrons in the process and forming the reduced species *Red*. The current produced from the reduction of species *Ox* to *Red* exists due to a change in oxidation state, and is termed a Faradaic current because it obeys Faraday's law; that is, one mole of a reactant species will ideally produce *n* times 96485.33 Coulombs, under standard conditions. The electrochemical current measured at the working electrode surface, in a voltammetric experiment, is plotted as a function of the applied potential (termed a voltammogram), and represents graphically a complete current-potential plot where much information is available for user interpretation. It is noteworthy that all voltammograms adopt different curves dependent upon several phenomena which are Faradaic and non-Faradaic in nature; it is for the electrochemist to pontificate and de-convolute such data.

However, the vast majority of 'simple' electrochemical measurements unfortunately can quickly turn into a headache for any electrochemist. Electrochemical responses can be indicative of a reactant, or a product, or a reactant reacted with a product, and so on. Simply put, there are a number of reaction routes in which the reactions may proceed. Independent of the reaction route, the measured current is related to the mass transport in the solution phase. Mass transport in solution is a determining factor in electrochemical measurements as it is responsible for transporting molecules to and from the surface of electrodes, and in some cases may limit the observable current which is a problem in cases,[12] yet can be exploited in other cases.[13] Not all systems are equal, as while some systems exhibit currents that are affected profoundly by mass transport effects, others do not. Thus, mass transport has to be considered when assessing the overall rate of reaction and ascribing the rate-determining step

as an effect of electron transfer or mass transport. Intuitively, a series of experiments must be completed in order to ascertain such data. Many permutations must be explored, such as electrode material, size, rate of potential sweeping, (and so on) to elucidate the exact origins of an electrochemical reaction. The potential range of the reaction must also be considered as it may have an effect upon the rate-determining step of an electrochemical reaction. Some reactions are mass-transport limited, meaning that the observed currents are limited by the rate at which the electroactive species is transferred to the surface of an electrode; these cases are thermodynamic in nature because the kinetics of electron transfer are not being compromised, and thus obey Nernstian relationships and are termed 'reversible'.

1.3 MASS TRANSPORT AND FICK'S LAWS

A good deal of emphasis was placed upon mass transport in the previous section because the transport of electroactive species to and from an electrode affects the overall rate of an electrochemical reaction. It should be stressed that the term 'mass transport' is a general phrase for a collection of three phenomena: diffusion, convection, and migration. It is imperative for these three modes of mass transport not to be confused. *Diffusion* is the net movement of molecules due to a physical response to an imbalance of concentration; diffusion proceeds from a high to a low net concentration. *Migration* is the movement of charged species through an electric field. *Convection* is the physical movement of a liquid phase, which can be categorized into forced or natural convection. An example of forced convection would be stirring of a solution, whereas natural convection is a physical response to a molecule's surroundings; natural convection poses a limitation to some electrochemical techniques and will be discussed later. The three modes of mass transport are described in Figure 1.2.

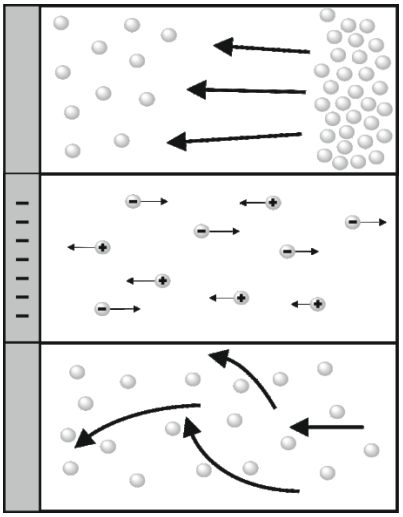

Figure 1.2: Three modes of mass transport in solution: diffusion (top); migration (middle); convection (bottom). The grey section on the left hand side represents the electrode surface.

But how does one ascertain which mode of mass transport is prevalent in a voltammetric experiment, for example? Obviously all three modes exist in unison; nevertheless it so happens that in the majority of cases, diffusion is the major contributor to mass transport effects. This is because under normal conditions, an electrochemist will introduce a large quantity of background electrolyte (such as KCl; concentrations in excess of 0.1 M[11]) to nullify the effects of migration and limit the effects of potential drop to short, nano-scale distances from the electrode surface.[11] Natural convection is considered a negligible mass transport effect too, provided the scan rate of an experiment is sufficiently high (100 mV s^{-1} for a voltammetric experiment would be more than suitable to negate effects of natural convection). This leaves diffusion as the major contributing mass transport factor, and is described mathematically by Fick's laws, originally pioneered by Adolf Fick in 1855.[14]

Diffusion is a process which will always take place from a high to a low concentration, and thus molecules will diffuse *down* the concentration gradient, hence the

negative term in equation 1.4. Mathematically, at any point, x, there will be a diffusive flux, which is quantified by Fick's first law:

$$j = -D\frac{\partial c}{\partial x} \tag{1.4}$$

where j is the diffusive flux, D is the diffusion coefficient of the electroactive species, and c is the concentration of the electroactive species. From Fick's first law we notice a new term, the diffusion coefficient, which is a fundamental concept in any system where diffusion occurs, including electrochemical theory. The diffusion coefficient of an electroactive species represents the distance in which the electroactive species will diffuse in two dimensions in a given time, t, as described in the following equation:

$$\sqrt{\langle x^2 \rangle} = \sqrt{2Dt}\,, \tag{1.5}$$

or in three dimensions, the equation becomes:

$$\sqrt{\langle x^2 \rangle} = \sqrt{6Dt}\,. \tag{1.6}$$

The Stokes-Einstein equation is used to describe the diffusion coefficient, and relates it to the temperature, the viscosity of the liquid (η), and the hydrodynamic radius (R) of the diffusive species:

$$D = \frac{kT}{6\pi\eta R}\,, \tag{1.7}$$

where k is the Boltzmann constant. Such diffusion coefficients are normally only valid under the condition of excess background electrolyte, due to the negation of charge migration. Typically, a diffusion coefficient for a given electroactive species in solution will have a value of the order of 10^{-5} – 10^{-6} cm^2 s^{-1}, though there are exceptions in the case of some ionic

liquids and organic solvents.[11, 15] Diffusive flux is also related to Faradaic current density through equation 1.8:

$$I = nFAj \tag{1.8}$$

where A is the surface area of the electrode. Thus, substituting diffusive flux from Fick's first law into the above equation leaves:

$$I = -nFAD\frac{\partial c}{\partial x}, \tag{1.9}$$

which is a general expression for the current response with respect to concentration. At any given time and at a specified point, current is *directly* proportional to the concentration gradient of the electroactive species. However, Fick's first law of diffusion doesn't consider diffusion from one point to another, it only considers diffusion at some point near the electrode. This limits the use of Fick's first law as diffusion is not usually steady-state; that is to say, diffusion is time-dependent. Therefore a second law accounts for diffusion from one point to another, assuming that the diffusion of the species towards a *planar* electrode is linear (*i.e.* in one direction, as in the case of macroelectrodes) in the region under scrutiny, and takes time and position into account.

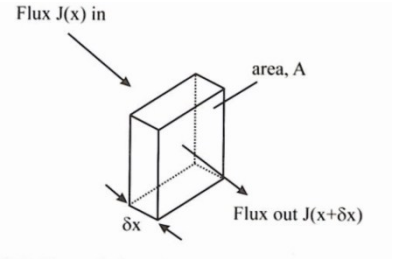

Figure 1.3: Fick's second law is considered in terms of a cross sectional cubic region of known area. The flux in, J(x), and out, J(x+δx), of the cubic region is considered as a function of the distance between two opposing faces of the cubic region, x. Reprinted from Reference 11.

Figure 1.3 depicts a scenario in which the diffusion of an electroactive species is considered in terms of position and time. There are two points in Figure 1.3 where the flux will have different values due to their relative distance from the concentrated bulk solution, which are separated by a distance, x. Fick's second law, presented in equation 1.10, considers the rate of change of concentration with respect to the concentration of the bulk solution and the separation between these two points.

$$\frac{\partial c}{\partial t} = D\frac{\partial^2 c}{\partial x^2} \tag{1.10}$$

Fick's second law breaks down when the diffusion profile at the electrode becomes non-linear; *i.e.* the electrode is spherical, or in the case of microelectrodes. The overall diffusive flux is described as a combination of these components, which forms the Nernst-Planck equation for a single dimension, given in equation 1.11, where $\partial c/\partial x(x, t)$ is the concentration gradient (at distance x and time t), $\partial\phi(x, t)/\partial x$ is the potential gradient, z and $c(x, t)$ are the charge and concentration respectively of the electroactive species, and $V(x, t)$ is the hydrodynamic velocity (in the x direction) in aqueous media.

$$j(x,t) = -D\frac{\partial c(x,t)}{\partial x} - \frac{zFDc(x,t)}{RT}\frac{\partial\phi(x,t)}{\partial} + c(x,t)V(x,t) \tag{1.11}$$

In electrochemical experiments the physical processes occur at distances in the region of 10-20 Å from the electrode surface. It is in this region in which concentration profiles change (reactants tend to decrease in concentration while products increase), and thus movement of molecules down concentration gradients occurs mainly within this small region. This region is termed as the Nernst diffusion layer, depicted in Figure 1.4, for the case of a simple electron process.

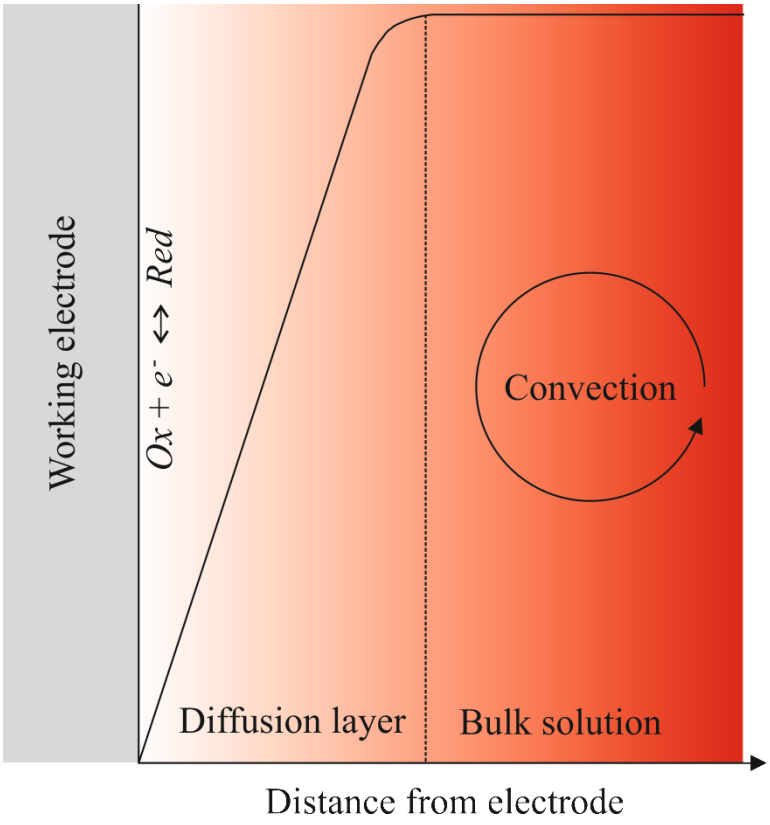

Figure 1.4: Illustration of the Nernst diffusion layer.

The Nernst diffusion layer model is used by electrochemists to deduce the mass transport coefficient, m_T, by considering the flux in this region. If c^* is considered to be the concentration of electroactive species in the bulk solution, then

$$j = D\frac{\partial c}{\partial x} = \frac{Dc^*}{\delta}, \tag{1.12}$$

where δ is the diffusion layer thickness. Combining equation 1.12 with equation 1.8 gives

$$I = nFA\frac{Dc^*}{\delta}, \tag{1.13}$$

and

$$m_T = \frac{D}{\delta}, \tag{1.14}$$

so equation 1.15,

$$I = nFAc^{*}m_{T}, \tag{1.15}$$

is a useful equation which links current to the mass transport coefficient, m_T; an important mathematical connotation when considering electrode kinetics.

1.4 ELECTRODE KINETICS

In a situation where the mass transport is sufficiently high, the electrochemical reaction is said to be controlled by the rate of electron transfer between the electrode and the electroactive species. This too needs to be rigorously considered by the electrochemist. This is because the current-potential relationships expressed in a kinetically controlled experiment differ greatly from that of a diffusionally controlled experiment. In the simple reaction

$$Ox + ne \underset{k_b}{\overset{k_f}{\longleftrightarrow}} \mathrm{Re}\,d\,, \tag{1.16}$$

the rate of the forward reaction is given by

$$k_f = k^0 \exp\left(\frac{-\alpha F}{RT}[E - E_f^0]\right), \tag{1.17}$$

while the rate of the backwards reaction is given by

$$k_b = k^0 \exp\left(\frac{-(1-\alpha)F}{RT}[E - E_b^0]\right), \tag{1.18}$$

where E is the cell potential, k_f and k_b are the rates of the forward and backward reaction, respectively, E^0_f and E^0_b are the standard potentials of the forward and backward reactions, respectively, k^0 is the overall electron transfer rate constant, α is the dimensionless transfer coefficient of the anodic process, R is the molar gas constant, and T is the temperature**.** In a potentiostatic experiment using a three electrode cell, and under the assumption that the diffusion coefficients for the reactants and the products are equal, one can express the

forward and backwards rate constants in terms of the applied electrode potentials (in a Nernstian manner) through use of the equation 1.17 and 1.18.

A combination of mass transport coefficients and electron transfer rate constants can be mathematically expressed in terms of the overall flux in an electrochemical experiment. This overall expression is given in equation 1.19 (where j_O and j_R are the respective fluxes of the two hypothetical species, *Ox* and *Red*), however it is noteworthy that this equation is difficult to solve unless some extreme cases are met, as described below.

$$j = \frac{k_f j_{O,\lim} - k_b j_{R,\lim}}{m_T + k_f + k_b} \tag{1.19}$$

In a case where the rate of the forward reaction is far greater than the product of the mass transport coefficient and the rate of the backwards reaction,

$$k_f >> k_b m_T , \tag{1.20}$$

then the rate of the forward reaction is limited by the diffusive flux component, so it follows that

$$j = j_{O,\lim}; \tag{1.21}$$

therefore:

$$j_{O,\lim} = \frac{D[Ox]^*}{\delta} . \tag{1.22}$$

The limiting flux of species *Ox* will be observed in cases where a large oxidative overpotential is applied to the cell. The exact opposite is true for the case of

$$k_b >> k_f m_T . \tag{1.23}$$

However in the case of

$$m_T >> k_f k_b , \tag{1.24}$$

the system is under the control of electrode kinetics, and the current is sensitive to the potential applied to the system. This leads to three types of voltammetric systems electrochemists typically encounter:

- An electrochemically *reversible* system, which is one where the electron transfer constant is sufficiently high, so that the current response is limited by the mass transport ($k^0 >> m_T$). In such a case, two waves, an oxidation and a reduction wave, will be seen in a current-potential plot, which are collected around the formal potential of the redox couple.
- An electrochemically *irreversible* system, which is one where the mass transport is sufficiently high so that the current response is limited only by the rate of electron transfer ($m_T >> k^0$). In such circumstances, little current flows around the formal potential for the redox couple, therefore large *overpotentials* must be applied at the anode and cathode to drive the electrochemical reaction.
- An electrochemically *quasi-reversible* system represents the intermediate case ($k^0 \sim m_T$).

1.5 VOLTAMMETRIC EXPERIMENTS

Perhaps the most commonly used electrochemical procedures today are sweep-based experiments, such as Cyclic Voltammetry (CV), Differential Pulse Voltammetry (DPV), or Square Wave Voltammetry (SWV). Any voltammetric experiment employs at least a three electrode electrolytic cell which is subjected to a known potential, which is ramped up or down as a function of time. An example of such a procedure is depicted graphically in Figure 1.5; this is a typical example of a CV experiment in which the voltage ramp is reversed. The current is measured by the working electrode during said potential ramping, and is plotted as

a function of the applied potential at the same point in time. An example of such a plot, termed a voltammogram, is presented in Figure 1.6. An important parameter in any voltammetric experiment is the scan rate, which is the speed of the potential ramp (measured in V s^{-1}).

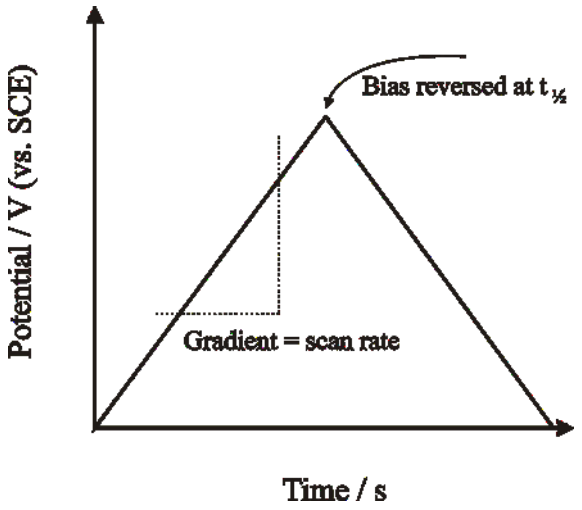

Figure 1.5: Cyclic voltammetry applied potential waveform, depicted as a function of time.

Cyclic voltammetry is a very useful technique for electrochemists, and the shape of a voltammogram is often used as evidence for a particular reaction mechanism, or for proof of a typical electrochemical reaction. The magnitude of the current responses are useful for the electrochemist because they can be used to determine unknown concentrations of an analyte (electroanalysis), and can also give information regarding the mass transport, and qualitative parameters such as diffusion coefficients can be calculated. Furthermore, the shape of the wave can be used to show reaction mechanisms (E, EC, CE, ECE *etc*. where E = electrochemical and C = chemical), qualitative proof of adsorptive properties of a particular material, and even the surface morphology of an electrode; in particular where carbon-oxygen species are concerned.[16-18]

However, a voltammogram is not simply rationalised to the layman. Figure 1.6 details four regions of interest which are key to understanding why such a current-potential curve

adopts such a unique shape. The voltage ramping starts at t_0, where the current is stable because no electrochemical process is taking place. However, as the potential is ramped towards the standard potential of the cell half reaction, the Faradaic processes start to activate, which happens in region A. Prior to this region, the concentration of reactants at the electrode surface is assumed to be equal to the bulk solution concentration and the concentration of products is assumed to be nil. Once the electrode process initiates in region A, the concentration of products increases at the electrode surface. The observed current increases because of electrons being transferred between the electrode and the reactants, until the concentration of reactants decreases sufficiently. In region B, the concentration of reactants in the diffusion layer has decreased below the concentration of the products, which causes the current response to deplete. The size and shape of the overall wave is dictated by the rate of the electron transfer, the scan rate, and the contribution of mass transport effects. In the region after the wave (as the ramping approaches $t_{1/2}$) the background current observed is due to small Faradaic contributions and capacitative effects from the Helmholtz plane (see later). After $t_{1/2}$, the bias is reversed and the opposite phenomenon is observed in the case of a reversible reaction. Before region C, the concentration of products is at a maximum and the concentration of reactants is assumed to be nil. During region C, the reverse reaction has been initiated and thus the concentration of reactants increases at the electrode surface until region D, where the current becomes limited due to the products becoming unavailable for the reaction; which is the reverse to region B. Prior to t_1, the concentration of the reactants is again assumed to be equal to the bulk solution and the concentration of the products is assumed to be nil. The difference between the peak potentials (ΔE_P) observed in region B and D give an indication of the reversibility of the redox couple (see Section 1.2); a separation of 59 mV indicates electrochemical reversibility for a one electron process, assuming standard conditions.

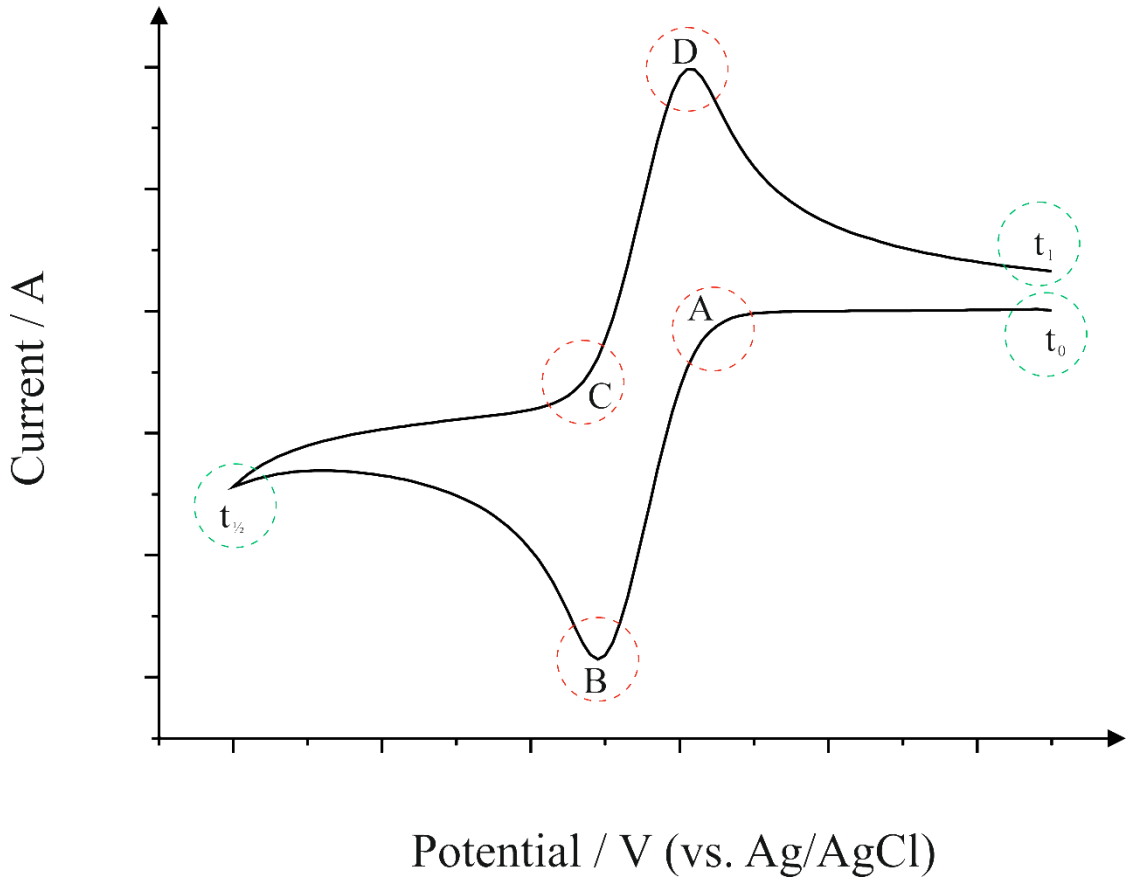

Figure 1.6: Voltammogram typical of the outer-sphere redox probe hexaamine-ruthenium (III) chloride. The green zones illustrate changes in potential bias, and the red zones indicate changes in the current due to a combination of Faradaic and non-Faradaic processes.

There are also many variations of voltammetric experiments which are used for different purposes. Linear Sweep Voltammetry (LSV) uses the same ramp process as CV, apart from the potential is not reversed. This technique is used if one only wishes to observe one half reaction of the cell. SWV and DPV are used by electroanalytical chemists as they apply different voltage waveforms to the cell and carry the advantage of being able to detect target molecules at very small concentrations. Staircase voltammetry is used for users who prefer to limit the amount of capacitative charging. Finally, anodic stripping voltammetry is very common for trace metal analysis, and as the name suggests, the observed currents are

typical of a molecule being stripped from an electrode surface instead of a conventional Fardaic process.

1.6 INTERPRETING VOLTAMMETRIC DATA

Voltammetry, as discussed previously, offers much in the way of qualitative information for the user. However it is also a vital tool for quantitative analysis of a given system. Quantitative analysis of a voltammogram starts with the analysis of the peak height (current, *I*) and the peak position (potential, *E*) as depicted in Figure 1.7.

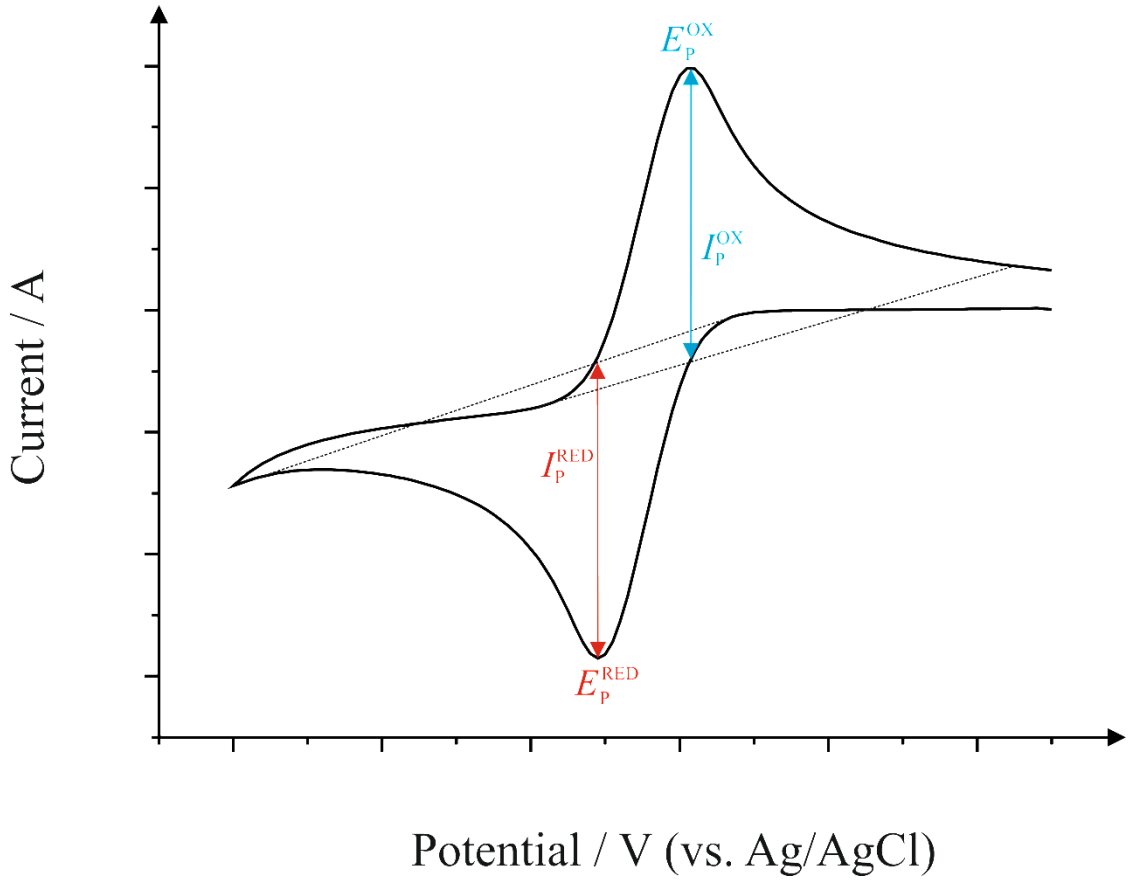

Figure 1.7: Typical voltammogram for the outer-sphere redox probe hexamine-ruthenium (III) chloride with relevant analytical parameters labelled.

The peak current for a given reversible (defined previously) redox couple is given by the Randles-Ševćik equation, given in equation 1.25, where I_P is the voltammetric peak

current, F is the Faraday constant, A is the electrode area (in cm^2), D is the diffusion coefficient of the analyte (in $cm^2\ s^{-1}$), υ is the scan rate (in $V\ s^{-1}$), C is the concentration of the analyte (in $mol\ cm^{-3}$), and n is the number of electrons transferred in the electrochemical process.

$$I_P = \pm 0.4463 nFAC\left(\frac{nF\upsilon D}{RT}\right)^{\frac{1}{2}} \tag{1.25}$$

It follows that the current is proportional to the square root of the scan rate; the gradient of such a plot is useful for estimating electron transfer rate constants (see later). In a completely reversible process one would ideally observe a forward and reverse electrochemical process equal in magnitude, however this is rarely the case due to side reactions occurring. Furthermore, it is very rare that a current will return to zero once a Faradaic process is complete (due to double layer charging and side reactions). Thus, analysis of peak currents normally uses baseline correction.

The second parameter denoted in Figure 1.7 is the peak potentials, which are related to the standard electrode potential of the redox process. The peak potentials can be used to obtain the formal potential (E^0) of the cell *via* the following equation:

$$E^0 = \frac{E_P{}^A + E_P{}^C}{2}, \tag{1.26}$$

where A and C represent the anodic and cathodic peak potentials (E_P). But the most common peak potential analysis an electrochemist will perform is the peak-to-peak separation (ΔE_P), which is theoretically 59 mV for a one electron process, according to equation 1.2/1.3, assuming the concentration of the oxidation and reduction species are equal. The theoretical value of 59 mV (see equation 1.2/1.3) for a one electron process is rarely met, however. This can be due to a number of factors, including electrode homogeneity and 'age' of the sample.

Additionally there are many scenarios where more than one redox couple is observed, hence more than one formal potential and more than one ΔE_P. In such a case it can be tricky to analyse the voltammetry as one has to deduce whether there are two processes overlapping if the user is unlucky enough to be working with an analyte with two formal potentials sufficiently close to one another. And yet, even if there is actually only one process present, the user may observe increasing ΔE_P as the scan rate of the experiment is increased as a result of the electron transfer contribution equalling the mass transport contribution to the observed voltammetry. The Randles-Ševćik relationship for a reversible case is still valid and is used habitually by electrochemists to analyse datasets. There is a point in which the predicted peak currents deviate from normality and as such a modified equation is utilised (see later). The Randles-Ševćik equation becomes extremely useful for the modern day electrochemist when combined with the Nicholson equation (equation 1.27) because the effective electron transfer rate constant of the electroactive species can be accurately estimated as a function of the ΔE_P, provided the user has already deduced the diffusion coefficient (for example using the Cottrell equation with amperometry). The original paper by Nicholson relates the kinetic parameter, ψ, to the ΔE_P.[19] Originally, the user would calculate the ΔE_P using CV, then deduce ψ from a table kindly provided in the paper, or calculate the kinetic parameter from a working curve. However a more practical method to estimate the electron transfer rate constant was devised in 2004,[20] which instead produces a linear correlation between the scan rate and the kinetic parameter, calculated *via* the relationship described in equation 1.28 where $X = \Delta E_P$ in mV (when $n = 1$); the gradient of the graph is equal to k^0. This makes the estimation of k^0 very simple experimentally, as one only needs to perform a scan rate study to extract such useful information.

$$\psi = k^0 \left[\pi D n \upsilon F / RT \right]^{-\frac{1}{2}} \qquad (1.27)$$

$$\psi = \left(-0.6288 + 0.021X\right) / \left(1 - 0.017X\right) \tag{1.28}$$

The revised Nicholson method is only applicable in the case of a quasi-reversible system as the ΔE_P should not increase as a function of scan rate in a totally reversible reaction. Similarly, in the case where the mass transport contribution to the CV far exceeds the rate of the electron transfer, the irreversible case, the Nicholson equation cannot be used. This doesn't mean that irreversible electrochemical systems are not useful, however. In fact some of the most intriguing electrochemical systems, such as uric acid, ascorbic acid, norepinephrine, and picric acid, are irreversible systems.

It follows that there should be a relationship between peak current and scan rate for the case of an irreversible system. A typical irreversible system will see either two peaks separating out very quickly because the rate of electron transfer is much slower than the mass transport contribution of the voltammetry. In such a case, a potential far in excess of the formal potential of the cell is required to drive the process (equation 1.29, where α is the transfer coefficient and *n'* is the number of electrons involved up to the charge transfer step); such a potential increases as the applied scan rate increases. The Randles-Ševćik equation is thus modified further to account for such phenomena, and is expressed in equation 1.30, where *n* is the overall number of electrons in the electrochemical reaction.[21]

$$E_P = E^0 - \frac{RT}{\alpha n' F}\left[0.78 - \ln\left(\frac{k^0}{D^{\frac{1}{2}}}\right) + \ln\left(\frac{\alpha n' F \upsilon}{RT}\right)^{\frac{1}{2}}\right] \tag{1.29}$$

$$I_P = \pm 2.99x10^5 n(\alpha n')^{\frac{1}{2}} ACD^{\frac{1}{2}}\upsilon^{\frac{1}{2}} \tag{1.30}$$

For a simple one electron process, the reversible, quasi-reversible, and irreversible wave shapes adopt unique and distinguishable voltammetric profiles. These three types of profiles are depicted in Figure 1.8. The voltammetric wave shape for a reversible system

(blue line), shows a redox couple with a ΔE_P of 59 mV; the quasi-reversible system (green line) shows an increased peak separation and a perturbation in the peak current. The irreversible case (red line) exhibits a very large ΔE_P and peak current perturbation.

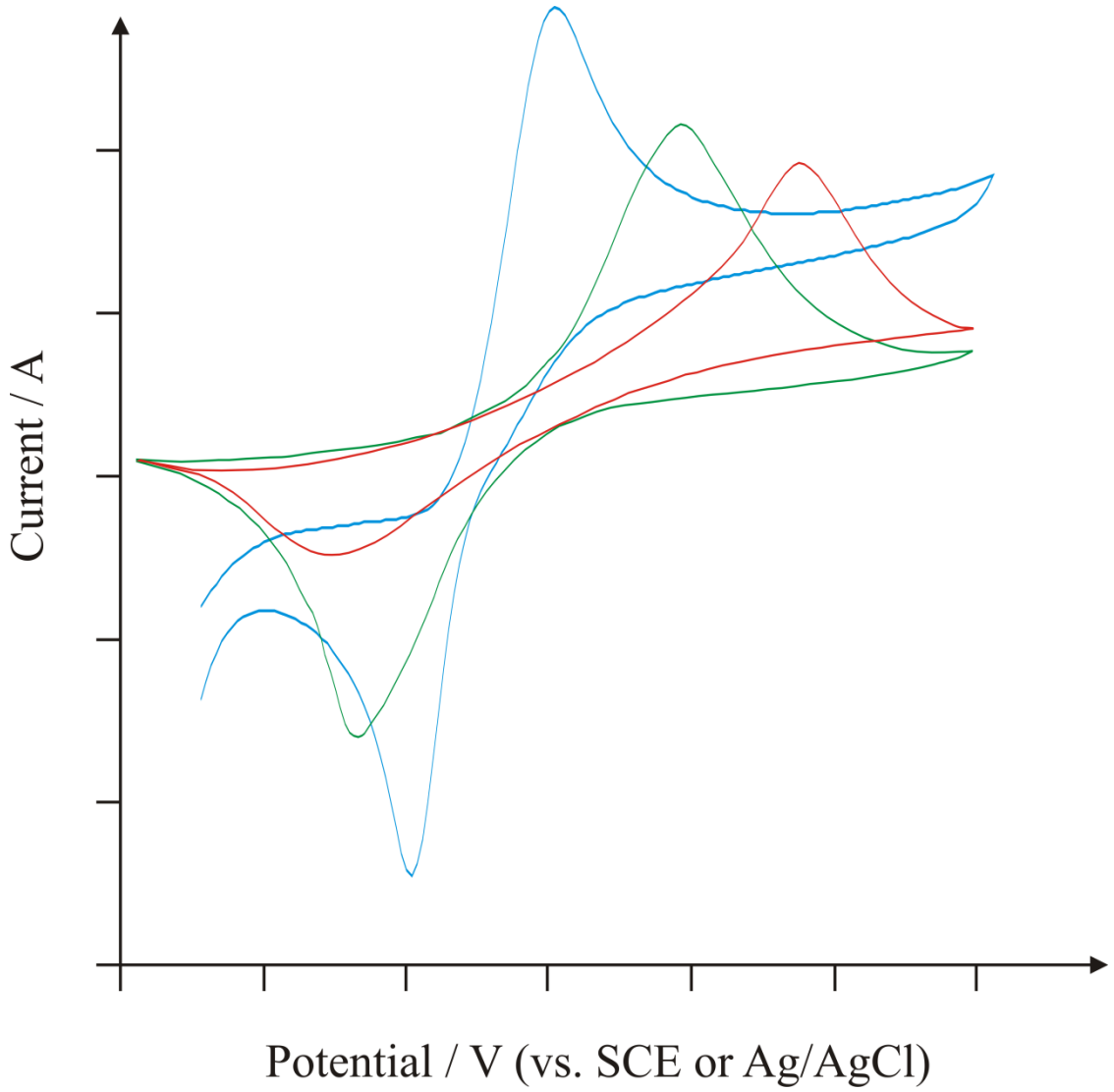

Figure 1.8: Voltammograms for an electrochemically reversible (blue line), quasi-reversible (green line), and irreversible (red line) electron transfer process.

The peak current observed in electrochemical experiments is not only dependent upon concentration, as in the Randles-Ševćik equation. The peak current is also dependent upon the equilibrium potential of the system, or the activation overpotential required to trigger an

electrochemical process. The dependence of current upon such an activation potential is described in detail by the Butler-Volmer equation, which is presented in equation 1.31:

$$I = Aj_0 \left(\exp\left[\frac{\alpha_a nF}{RT} \left\{ E - E_{eq} \right\} \right] - \exp\left[\frac{-\alpha_c nF}{RT} \left\{ E - E_{eq} \right\} \right] \right), \quad (1.31)$$

where I is the current, A is the electrode surface area, j_0 is the current density, α_a and α_c are the transfer coefficients of the respective anodic and cathodic processes, n is the number of electrons transferred, F is the Faraday constant, R is the gas constant, (E-E_{eq}) is the activation potential of the electrochemical reaction. The equation accounts for a scenario where both an anodic and cathodic process are in operation (reversible and quasi-reversible) by the introduction of the transfer coefficients. Equation 1.31 essentially states that the activation overpotential for a given process is an exponential function of the observed current, a phenomenon which can be exploited using Tafel analysis, for example.

A further type of voltammetric data analysis is the interpretation of oxidation and reduction peaks using Tafel analysis. Tafel analysis can be performed when the user believes the system to be a pure charge transfer mechanism. Tafel analysis is generally useful for comparing the electrocatalytic ability of electrode substrates, because it delivers a quantitative measure of the amount of charge passed between the solution and electrode as a function of the change in applied potential, ΔV, or in some texts, overpotential, denoted as η.[22] Equation 1.32 is one of the many modern day expressions of the original Tafel equation reported in 1905 by Julius Tafel:[23]

$$\ln i = \ln i_0 - \frac{\alpha nF\eta}{RT}, \quad (1.32)$$

where i_0 is the exchange current density. Tafel plots (ln$i$ *versus* η) , such as the one depicted in Figure 1.9, are particularly useful for corrosion analysis.

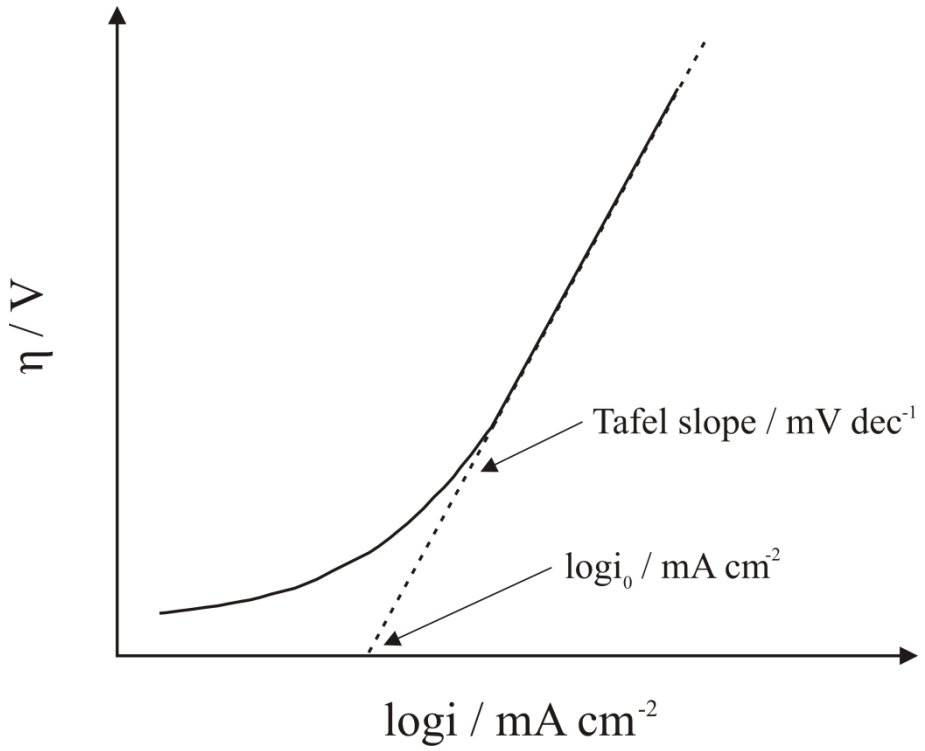

Figure 1.9: Typical Tafel plot for analysis of a pure charge transfer mechanism. Redrawn from Reference 24.[4]

1.7 LIMITATIONS OF CYCLIC VOLTAMMETRY

It would be normal to question the applicability of the Randles-Ševćik equations to electrochemical systems, considering the number of permutations involved. There are many cases where the most reversible of systems appear to be quasi-reversible at sufficiently high scan rates. In most literature, users select scan rates between 1 – 1000 mV s^{-1} as these speeds fall well within the limitations of CV.

The lower limitation of CV is natural convection. The total signal observed in a voltammogram according to Marcus theory is a combination of electron transfer and mass transport effects. However, at sufficiently slow scan speeds, the natural Brownian motion of the electroactive species in solution becomes faster than the rate of mass transport and becomes responsible for the overall current response. Effectively the current becomes limited

by the natural convection in the cell and thus scan rates below 1 mV s^{-1} are rarely, if ever, used. Conversely, the upper limitation of CV is the double layer charging effects upon the electrode surface. A sufficiently high scan rate induces a larger Nernst diffusion layer due to the high electric field created by the high scan speed; this phenomenon attracts more charged species to the electrode surface. The charged species also attract oppositely charged species with them, hence upon an electrode surface resides a charged double layer, known as the Helmholtz plane (Figure 1.10). At normal scan rates, this can usually be ignored, unless one is looking at a particularly bulky or highly charged analyte. However it is a phenomenon which is unavoidable at high scan rates, so users wishing to conduct high scan rate experiments must look further towards ohmic drop compensation to obtain accurate results due to the double layer charging which essentially 'masks' voltammetric signals.

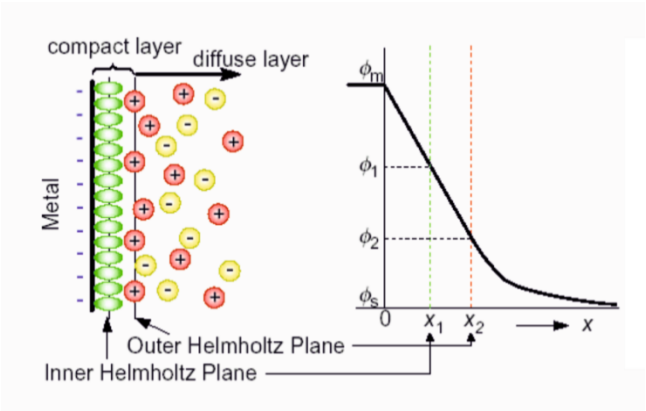

Figure 1.10: Schematic diagram of the electrical double layer, denoting the so-called Inner and Outer Helmholtz Plane (IHP, OHP). Image courtesy of New Mexico State University.[25]

1.8 AMPEROMETRIC EXPERIMENTS

Perhaps the second most common type of electrochemical experiments are amperometric experiments, and in particular chronoamperometry. In chronoamperometry, a fixed non-Fardaic potential is applied to an electrochemical cell for a known period of time, before jumping to a Faradaic potential and during this time the current is measured and plotted as a function of time. After the potential step, the Faradaic current observed decays in a non-linear fashion as described by the Cottrell equation (not quoted). The mass transport in the case of chronoamperometry is governed completely by diffusion and thus the current-time relationship observed is indicative of the change in concentration gradient at the electrode surface. Amperometry is useful for calculating diffusion coefficients and is also used electroanalytically, where currents are generated upon specific interactions with electrode composite materials. Amperometry is not used within this thesis so shall not be introduced in detail.

1.9 POTENTIOMETRIC EXPERIMENTS

Voltammetric and amperometric techniques are dynamic electrochemical techniques because an input variable is changed to stimulate a desired response. Potentiometric experiments differ in that they are stagnant, and very little changes within the solution under scrutiny. Potentiometric experiments use a two electrode system consisting of a working electrode and a reference electrode (often housed within the same unit); the overall potential of the experiment is the potential difference between the reference and the working electrodes. The observed potential difference is logarithmically related to the analyte concentration *via* equation 1.2. Hence, plotting the potential, or ElectroMotive Force (EMF), against the logarithm of the concentration should give a linear response with a slope close to 59 mV. Potentiometric experiments are useful for detecting specific target analytes by using

polymer membrane technologies that cannot be used voltammetrically because of the insulating nature of the polymer. Many literature examples are presented where potentiometry is preferred to a dynamic technique; noteworthy contributions determine concentrations of many cations including cobalt,[26] lead,[27] and bismuth,[28] hydrazine,[29] and the widely used glass pH electrode.

1.10 ELECTROCHEMICAL IMPEDANCE SPECTROSCOPY EXPERIMENTS

The frequency-dependent properties of electrodes can be studied using Electrochemical Impedance Spectroscopy (EIS). This technique is increasing in popularity because the user has the ability to ascertain even more phenomena than for the case of CV. In a typical EIS experiment, a small amplitude sinusoidal voltage is applied to cell over a range of frequencies, alongside a fixed DC excitation potential. The excitation results in changes in the environment at the electrode surface, manifesting as a change in output current. The magnitude and phase angle (relative to the AC voltage) of the current are measured by the potentiostat, and are transformed into an impedance contribution *via* Ohm's law (equation 1.33). Impedance is, however, a complex quantity, and can be very difficult for the user to interpret data without sufficient experience. The impedance and phase angle difference are plotted as a function of frequency (in the case of a Bode plot – Figure 1.11A), or the real and imaginary impedances are plotted against one another (in the case of a Nyquist plot – Figure 1.11B). Nyquist plots are common in electroanalysis where users are investigating the effect of concentration upon the impedance of a system.

$$V = IR \tag{1.33}$$

The application of EIS is unfortunately limited at the present time, for many reasons. One reason is because common potentiostats are unable to reliably scan at frequencies below 0.1

Hz and above 1 MHz. Another reason is that EIS is generally misunderstood by the field of electroanalysis due to the complex nature of the topic. A third reason is that many users have to use equivalent circuit models to improve data resolution and to allow the researcher to gather an understanding of the very specific frequency-dependent electronic processes happening (charge transfer, capacitance, inductance, diffusion, solution resistance); however one can input any combination of these impedance elements and make a good impedance fit without actually thinking about the processes taking place prior to equivalent circuit modelling. Therefore electrochemists normally prefer to tackle a system which has the minimum number of contributing factors possible, i.e. little adsorption and polymerisation of the reactants to the electrode surface. Regardless of the above, EIS is extremely useful and will be the focus of the final Chapter of this thesis. A more descriptive introduction of EIS is provided in Chapter 2.

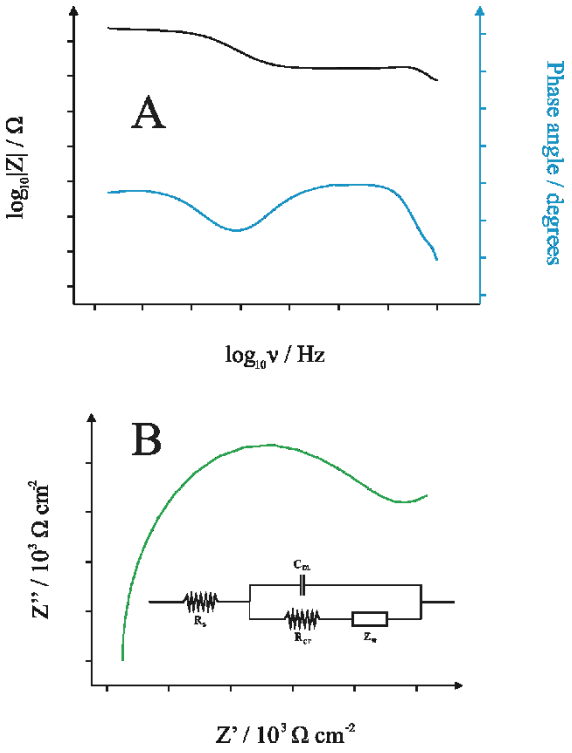

Figure 1.11: Two types of data presentation for EIS: Bode plot (A); and Nyquist plot (B). Inset in B is the equivalent Randles circuit used to model the data for 1 mM $K_3[IrCl_6]$ in pH 7.4 PBS using a BPPG electrode.

1.11 ELECTROANALYSIS

Electroanalysis is the analytical branch of electrochemistry which concerns using electrochemical techniques to elucidate concentrations of specific target analytes within a given medium. Just like any other technique such as chromatography or UV/Vis photospectrometry, electrochemical methods, within their limitations, carry respective advantages and disadvantages for the analysis of target analytes. For example, a potentiostatic setup combined with electrodes is a small-scale piece of equipment which can be purchased at an extremely low cost compared to a typical chromatography setup, for example. Furthermore electrochemical methods, in general, are quick, reliable, and portable; the latter of which is a common stumbling-block for many technologies which are too large to be used in the field. Hence, probably the biggest selling point for electrochemical methods is the

ability to transfer the lab to the field, which in theory would reduce analysis time, prevent sample contamination, and from a more commercial point of view, be cheaper than existing methods.

The drawback to using electrochemical methods as analytical techniques is that without specific tailoring of an electrode surface, the methods are generally far from specific. Take for example the case of dopamine, ascorbic acid, and uric acid; three very common analytes studied by electrochemists. These analytes on carbon electrodes exhibit peak oxidation potentials within a very small range, yet in a biological sample such as interstitial fluid, urine, or blood, one may require to study only one of these molecules. Therefore an electrode must be designed to specifically generate a current response which is indicative of the molecule in question. There are reams of examples of specific analyte detection within the literature, all of which explore the electroanalytical capabilities of such electrodes.

According to any form of the Randles-Ševćik equation, the peak current should increase linearly as a function of the square root of the scan rate. The peak current should also increase linearly as a function of the bulk concentration of the electroactive species. That is to say, under ideal electrochemical conditions (no side reactions; purely homogeneous surface *etc*.) doubling the concentration of the target analyte should double the current. In practise this isn't always observed (ionic strength, electrode passivation, polymerisation, ohmic drop), but normally at sufficiently low concentrations, this phenomenon is readily observed. Electrochemists thus endeavour to test the limitations of the Randles-Ševćik relationship by optimisation of fundamental parameters such as the scan rate, with the view to produce working calibration curves which are useful to detect unknown concentrations of target analytes. The implications of transferring this sort of technology into the field is potentially huge, given the scale of economics. There are many examples that are praiseworthy, the most exciting, in the opinion of the author, concerns using electrochemistry forensically[30, 31] (for

detection of poisons and drugs) and medicinally[32] (for detection of sugars and even diagnosis of ailments). There will be a particular focus upon electroanalysis within this thesis.

1.12 POTENTIAL OF ZERO CHARGE

In physical chemistry, a fundamental concept exists, called the point of zero charge. The point of zero charge describes the point at which the electrical charge upon a surface equals zero. This concept is usually investigated in colloidal science, and is frequently described in terms of pH.[463] In terms of pH, the point of zero charge would be the pH at which the surface of a colloidal particle would exhibit zero charge. This would normally cover a pH range and is described as the isoelectronic point. The isoelectronic point is a useful piece of qualitative information which chemical engineers would consider when selecting and/or tailoring a surface which is to come into contact with a solution of a set pH. Methods to deduce the point of zero charge include zeta potential measurements and potentiometric titrations.[464] The same logic can also be applied to electrode surfaces, in a slightly different way. The Potential of Zero Charge (PZC) is the potential applied across an electrode in which the net charge in the ion cloud surrounding the electrode is zero. Therefore, instead of a chemical factor balancing the charge between the surface and the solution, an applied potential provides the balance. This is dependent upon the type of electrode surface and the electrolyte (or more specifically, the mass/charge ratio of the anions and cations in the electrolyte). The PZC is a useful measurement for electrochemists because it gives an indication as to the safest operating conditions of a surface which may reduce the chance of ions reacting with the electrode and prevent fouling and passivation.

1.13 ELECTRODE MATERIALS

As introduced previously, a typical three electrode system consists of a working, an auxiliary, and a reference electrode. The auxiliary electrode tends to be made from an inert metal, such as nickel or platinum and should be as large as possible so that it doesn't limit the flow of current. The reference electrode is usually (but not limited to) either a Saturated Calomel Electrode (SCE) or an Ag/AgCl electrode because the formal potential of these two systems is extremely watertight and differs negligibly under different environments. The working electrode is the electrode of interest in almost every electrochemical experiment that will ever be conducted by scientists. The characteristics of a working electrode differ depending upon the requirements of that electrode. The working electrode *always* needs to be highly inert to the solvent and background electrolyte; corrosive electrolytes such as HCl or H_2SO_4 require chemically inert electrodes such as platinum (not gold for H_2SO_4!). Less abrasive aqueous conditions such as phosphate buffer can be easily operated using carbon electrodes. However one must also consider the activation potential of the electroactive species when selecting an electrode and must strike a balance between chemical reactivity and electrochemical activity. A selection of working electrodes will be discussed in terms of pros and cons.

1.14 GOLD AND PLATINUM ELECTRODES

Two very common types of metal working electrode are gold and platinum electrodes, pictured in Figure 1.12. They are wise choices in some circumstances because they are generally chemically inert. Both electrodes are useful over a wide analytical range where they exhibit very fast electron transfer rate kinetics, particularly in the cathodic region. Unfortunately, the hydrogen evolution reaction proceeds at low potentials in the anodic region for both platinum and gold, so their use is limited in aqueous conditions particularly.

Surface oxides can also form upon the surface of metal electrodes; this may have to be taken into account in the case of old electrodes. The major advantage of metal electrodes is their use in organic media. Many non-metallic electrodes cannot be used in organic media due to electrode passivation and even dissolution, yet this is not the case with gold or platinum.

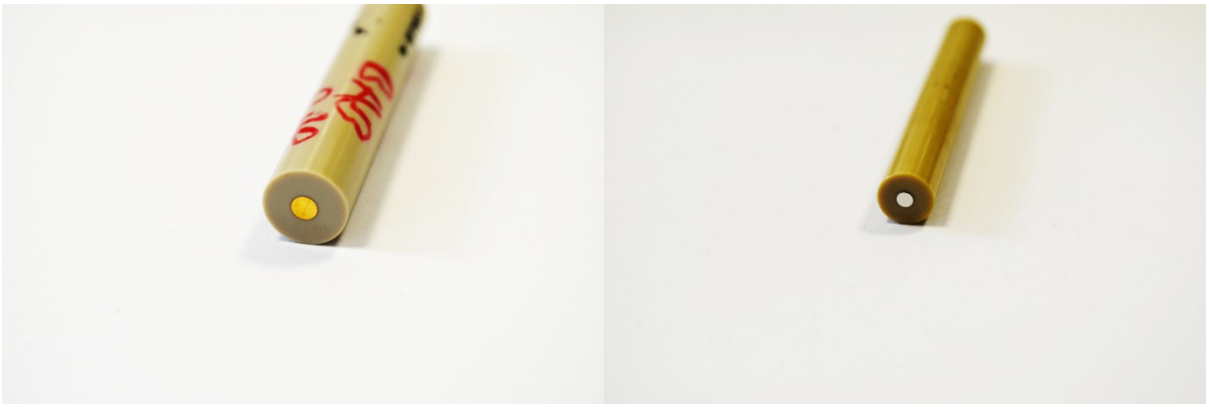

Figure 1.12: Gold (left) and platinum (right) working electrodes.

A metal electrode must be properly prepared before use. A key thing to note in all electrochemical methods is the surface homogeneity issue. Electrochemistry is fundamentally a surface-based science and is very sensitive to surface species (oxides, carboxylic acids, ketones) and surface morphology; the latter of which can also contain electronically anisotropic effects (see Section 1.18). So in order to keep an electrode homogeneous in nature, the user has to polish the electrode surface meticulously prior to use. In the case of metal electrodes, agglomerated alumina slurry is the chemical of choice for polishing, using consecutive slurries of decreasing particle sizes (ranging from 1.00 – 0.05 microns). The electrodes are cleaned intensively with high resistivity deionised water before use.

1.15 CARBON ELECTRODES

The choice of electrode material is not limited to metallic electrodes. Many non-metallic materials can be used as working electrodes, including many forms of carbon, which

prove to be quite popular in the literature. The evident popularity of carbon electrodes is due to lower cost and the ability to scan further in the anodic range. This is especially true in the case of unreactive carbons such as glassy carbon; however it will be seen that not all carbon electrodes react the same and all have their individual uses depending upon the system employed.

1.16 GLASSY CARBON

A glassy carbon electrode (Figure 1.13) is an amorphous carbon electrode consisting of both sp^2 and sp^3 hybridized carbon conformations, yet with no apparent lattice or crystalline structure as depicted in Figure 1.14. This non-porous structure gives the surface a mirror-like glassy finish, hence the name glassy carbon. Glassy carbon electrodes are very useful because they can be used in a range of media including aqueous and organic solvents, and in ionic liquids without dissolution or chemical penetration of the electrode surface. Glassy carbon electrodes are also much cheaper than noble metal electrodes, hence the combination of cost and versatility makes glassy carbon a very popular electrode of choice, notwithstanding the slower electron transfer rate kinetics compared to platinum or gold electrodes. Glassy carbon also carries the benefit of a lack of chemical reactivity, thus there are generally less surface oxide species to affect electron transfer.

Figure 1.13: Glassy carbon working electrode.

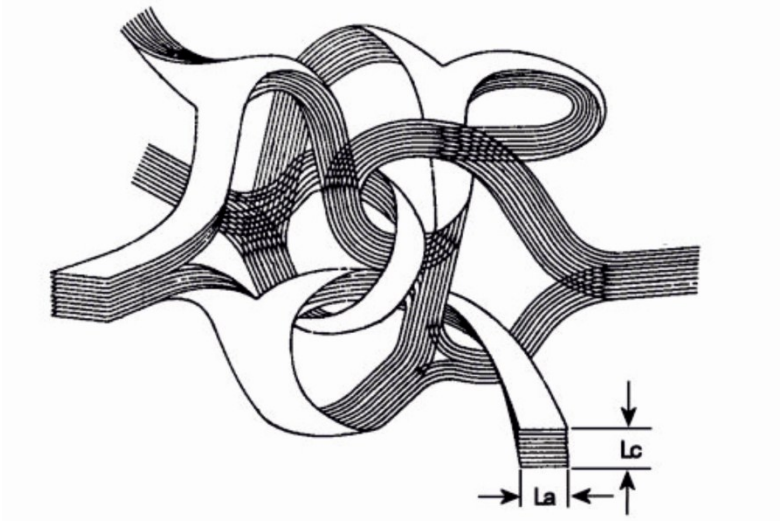

Figure 1.14: Schematic of the glassy carbon structure, depicting its random, intertwined, amorphous nature. The parameters L_a and L_c represent the intraplanar and interplanar microcrystalline size, respectively. Image courtesy of Nature.[33]

Glassy carbon electrodes are generally prepared in the same way as noble metal electrodes. The surface can be polished utilising alumina slurry or diamond spray (decreasing particle size as with alumina).

1.17 BORON-DOPED DIAMOND

Boron-Doped Diamond (BDD), depicted in Figure 1.15, is another type of carbon electrode which is less commonly utilised, yet has its own benefits. The structure of BDD is highly crystalline sp^3 hybridised carbon (*viz* diamond), doped with atomic boron, which introduces holes, or Schottky defects, into the lattice. The solid state structure of BDD is illustrated in Figure 1.16. The holes are areas in which electrons can be accepted – boron is well known to have pi acceptor orbitals for such an electronic transition. Essentially this introduction of holes makes the diamond structure conducting, and therefore the level of doping dictates the effective rate constant when using the electrode. Authoritative work by Ferreira and co-workers investigated the doping level of BDD films using a CVD technique and found that a film prepared using a B/C ratio of 5000 ppm in the fabrication process gave the fastest electrochemical rate constant for ferricyanide and hydroquinone. BDD is not as conducting as other carbon electrodes such as glassy carbon, but has the advantage of possessing an extremely large aqueous potential window with respect to the normal hydrogen electrode. This means that the electrode can be implemented with electrochemical systems requiring large anodic potentials for electron transfer, which is useful, even with the compromised peak currents due to lack of surface activity. Additionally the lack of surface activity is a benefit because the surface is not fouled very easily. BDD electrodes do not contain any surface pi character unlike other electrodes, thus the possibility of organic molecules adsorbing upon the surface *via* pi-pi stacking is almost nil, which is considered an advantage. However, BDD generally produces smaller currents and exhibits larger activation potentials as a consequence of the relatively labile surface; this can be seen as a disadvantage of BDD and therefore these factors must be considered before one selects BDD as an electrode of choice.

Figure 1.15: Boron-doped diamond working electrode.

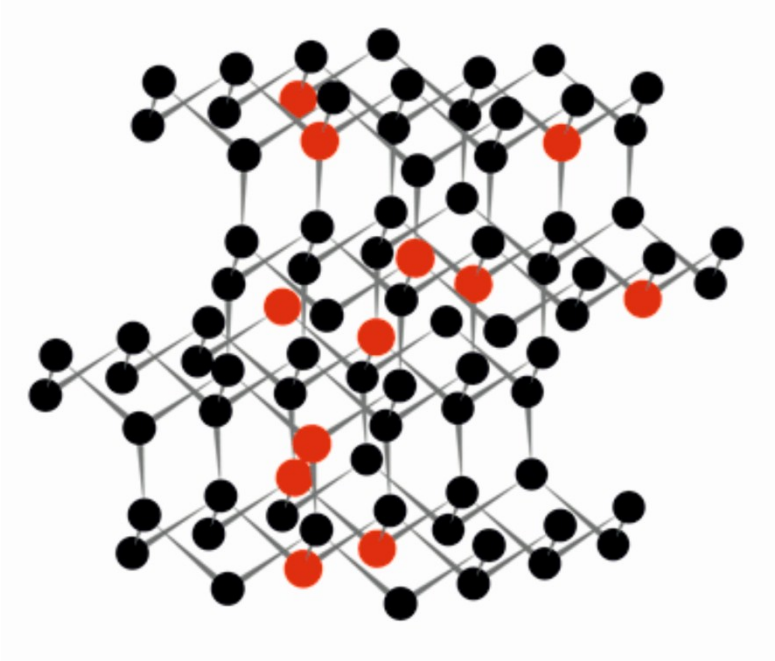

Figure 1.16: Suggested solid state structural lattice for BDD. The black dots represent sp^3 hybridised carbon atoms and the red dots represent the atomic boron dopant, which introduces holes for electron movement. Image courtesy of ESRF.[34]

1.18 ANISOTROPIC CARBON MATERIALS

Carbon is a very interesting electrode material due to its electronic anisotropy. That is to say, certain types of carbon exhibit different electronic properties in different geometric

planes. This is especially true for sp^2 hybridized graphitic structures and consequently electrodes are commonly fabricated from graphitic materials.

Graphite is a planar, layered hexagonal structure of sp^2 hybridized atomic carbon (Figure 1.17). The hybridization of the s and p orbitals allows the hexagonal conformation to be adopted whilst being stabilized by the remaining pi bonding and anti-bonding orbitals above and below the hexagonal plane. This orbital structure exhibits a resonant electron structure throughout the entire plane where electrons are free to 'hop' between the pi bonding orbitals very quickly without a change in the structure. However, electrons cannot transfer between the layers with such ease because the orbitals do not overlap; instead the layers are held together by Van der Waals interactions. The structure thus gives rise to fast electron transfer in one plane, yet slow electron transfer in another plane. Graphite is consequently an electronically anisotropic material as it exhibits different electronic properties in different planes. The edges of the individual graphite sheets shown in Figure 1.17 (graphene), where there are higher electron densities, are the reactive sites where electron transfer between graphite and a redox probe is readily observed. The top and bottom of a graphene sheet are termed the basal plane, and is the region where little or no electron transfer is observed without defects.

Looking at graphene from a quantum mechanical point of view, the edges can be thought of as having a high Density of States (DoS). This is because the structure of graphene permits electrons to flow in one direction, but inhibits electron flow in another direction. Graphite electrodes with a high DoS are likely to permit electron movement, and thus are normally orientated in an edge-plane-like manner. Conversely a low DoS suppresses electron transfer between the electrode and the target analyte, as is the case with basal-plane-like graphite structures. In many cases, electrochemical responses at graphite electrodes are considered in terms of the DoS associated with the number of graphene layers.

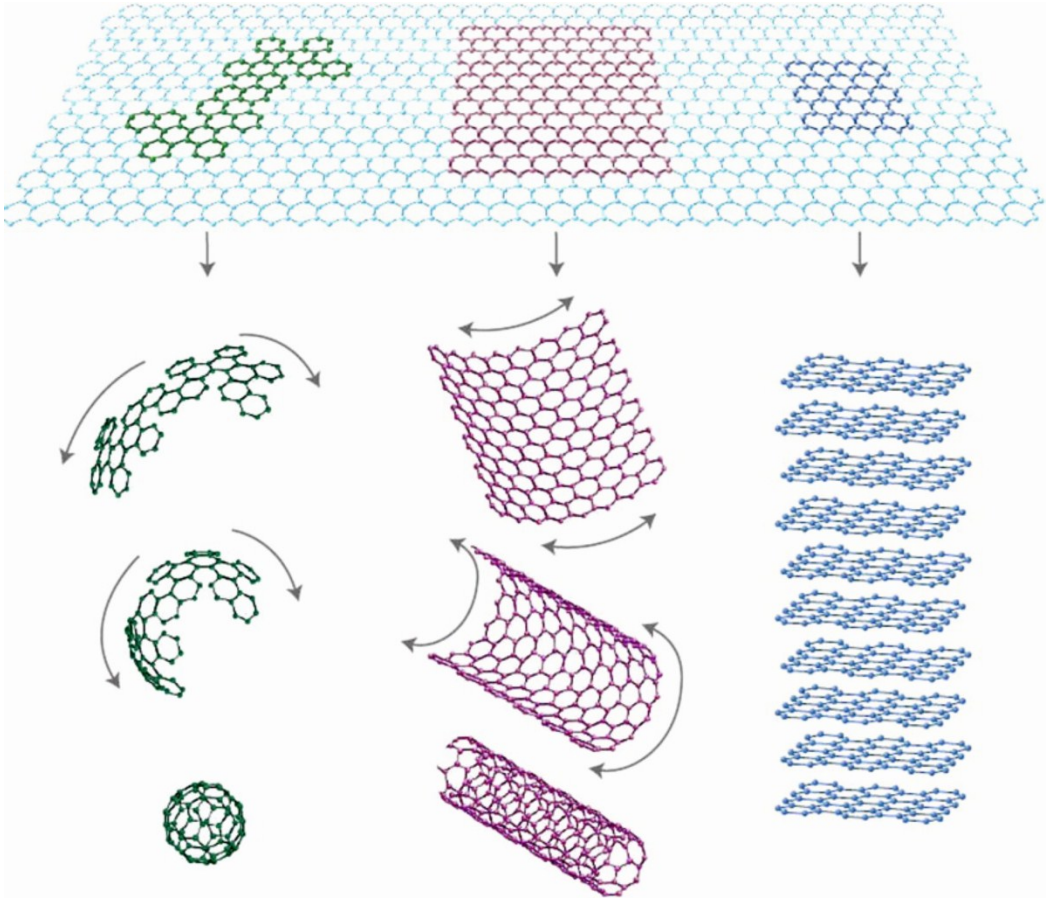

Figure 1.17: Schematic diagram depicting the types of allotropic carbon. Top: graphene - described by some as the mother of all carbon materials. Bottom left: Buckminster fullerene - essentially a graphene sheet in a ball, though these structures exhibit pentagons and hexagons for perfect structural stability. Bottom middle: carbon nanotube - a rolled up graphene sheet. Bottom right: graphite - stacked graphene sheets. Image courtesy of Nature.[35]

Graphite itself is observed in different forms, depending upon the number of defects apparent within the graphite structure, and the type of stacking between the singular hexagonal sheets. The stacking of the sheets is held together by van der Waals interactions between the basal planes. This electronic interaction is possible because although electron transitions between the sheets are unfavourable, an electromagnetic attractive force still exists between the graphene sheets due to the existence of pi bonds. The stacking of graphene sheets differs between graphite samples, too, which affects the quality of the graphene and

hence, the conductivity. The two modes of sheet stacking are termed hexagonal and rhombohedral stacking, due to the geometry of the resultant unit cell (Figure 1.18). The more thermodynamically favourable hexagonal structure comprises an "ABAB…."-type sheet structure. In this structure, L_c is approximately 0.25 nm, and L_a is approximately 0.67 nm, while in the rhombohedral configuration, L_a increases to approximately 1.01 nm.[36] The rhombohedral conformation is not normally observed on its own, rather it exists as a blend of both rhombohedral and hexagonal stacking modes. Rhombohedral graphite will reorganise to hexagonal graphite above temperatures of 1300 ºC.

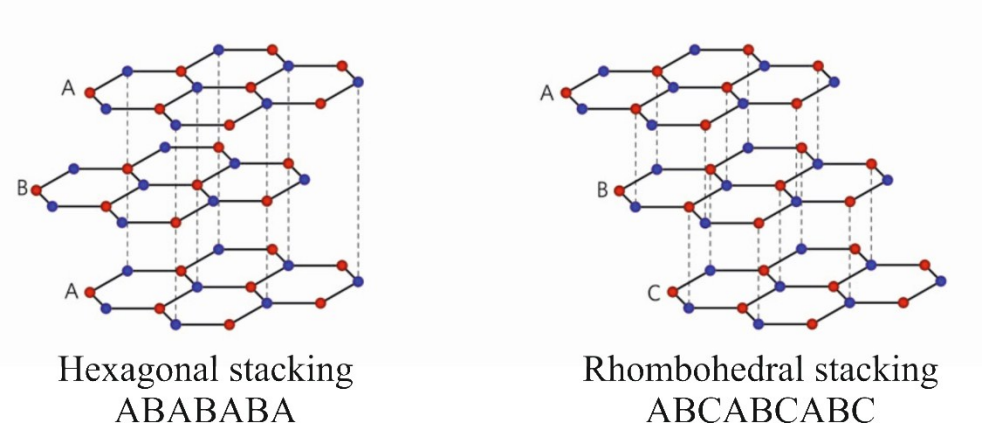

Figure 1.18: Two types of graphite stacking modes. Image adapted from Nature.[37]

A specific type of graphite, Highly Ordered Pyrolytic Graphite (HOPG) is commonly utilised for graphite electrodes. HOPG is not found naturally; it is produced synthetically by heating hydrocarbons to high temperatures and annealing under very high pressures. The resultant HOPG structure is slightly different to a standard graphite structure; the stacked graphene sheet remains, but the sheets held together by sections of defective sp^3 hybridised carbon in addition to the Van der Waals forces. This structure gives HOPG the strength and lack of permeability of glassy carbon, while maintaining the electronically anisotropic properties of graphite. Pyrolytic graphite will often be quoted to contain a mosaic spread of less than 1º; HOPG has a mosaic spread of less than 0.1º. This mosaic spread is a measure of

interplanar deviation, *ergo* defects. HOPG is considered the least defective of any type of graphite.

HOPG, like all other forms of graphite, is electronically anisotropic, and it is this form of graphite which is used for two types of graphitic electrodes: Edge Plane Pyrolytic Graphite (EPPG); and Basal Plane Pyrolytic Graphite (BPPG). EPPG electrodes are machined in such a way that the edge planes of the graphite form the surface of the electrode, thus the electronically dense region of the graphite is exposed to the solution and thus electrochemical reactions proceed at fast rates. The surface of an EPPG electrode is shiny (Figure 1.19), much like a glassy carbon electrode, and due to the orientation of the sheets, is more or less impenetrable by most chemicals. EPPG can therefore be utilised in both aqueous and organic media as well as ionic liquids. BPPG electrodes on the other hand are machined in such a way that the basal plane of the graphite form the surface of the electrode, thus the electrochemical reactions proceed at much slower rates than that of an EPPG electrode. The appearance of BPPG is a grey, pencil-like finish as depicted in Figure 1.19. The BPPG electrode is useful for fundamental carbon electrochemistry but has more limitations than its sister electrode EPPG. BPPG cannot be utilised in organic media because organic solvents generally strip the BPPG surface. Both electrodes have their respective uses, particularly for the fundamental understanding of carbon-based electrochemistry. EPPG and BPPG electrodes are prepared in the same way, by polishing the surface on a polishing pad using diamond spray of decreasing particle sizes (1.00 micron; 0.25 micron). The electrodes are doused in deionised water to remove any adsorbed material prior to electrochemical experimentation.

Figure 1.19: Edge (left) and basal (right) plane pyrolytic graphite working electrodes.

1.19 COMPOSITE ELECTRODES

A composite electrode is an electrode which has been fabricated from several materials, so the resulting surface exposed to the electroactive species is different from the original starting electrode material. Several materials and methods are utilised for composite electrodes; Table 1.1 details a handful of such electrode composites. Electrode composites are extremely useful because they are normally easy to fabricate in the lab, contain properties which are selective to a particular target analyte, can separate out voltammetric signals and increase the peak resolution, and so on. A typical method for the fabrication of an electrode composite is to drop-coat an aliquot of a solution-based electrode composite material upon an electrode surface and leave under nitrogen to evaporate the solvent; this process is pictured in Figure 1.20. The composite material will thus be on the surface of the electrode and will be responsible for electron transfer. Another method is to leave an electrode within a solution and allow the composite to self-assemble upon the electrode surface. This method will only work for certain molecules, such as sulphur-containing compounds upon a gold electrode, or molecules with strong pi-pi interactions.

Table 1.1: Electrode composite materials and their uses.

Electrode Composite	Detected species	Ref.
Nafion/graphene film	Lead, cadmium	[38]
CNT/glucose oxidase (sol gel)	Glucose	[39]
Graphite/polyurethane	Indole-3-acetic acid	[40]
Cuprous oxide modified carbon sol gel	Carbohydrates	[41]
12-tungstosilicic acid film	Nitrite	[42]
MWCNT/Nafion/bismuth	Lead, cadmium	[43]
Cobalt phthalocyanine in paraffin film	Epinephrine	[44]

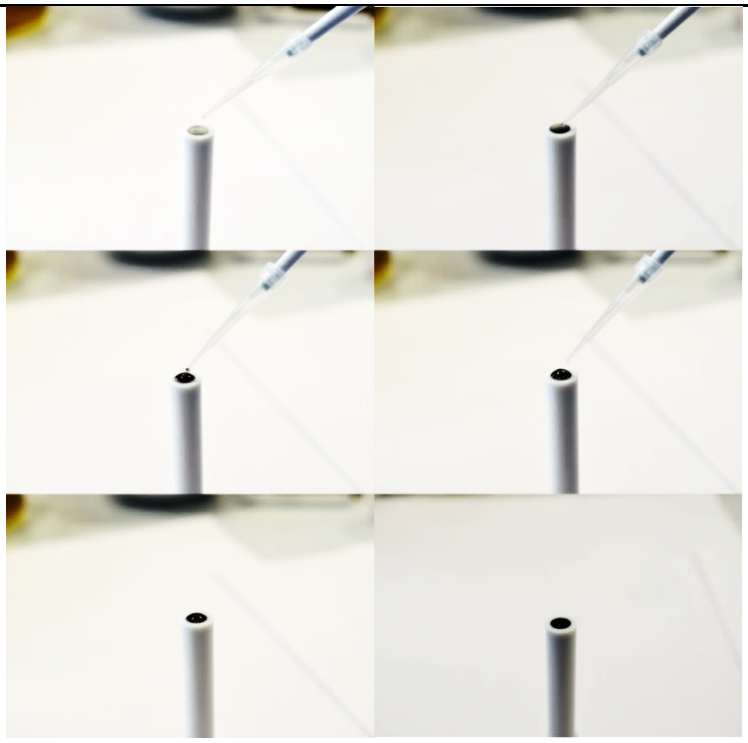

Figure 1.20: Step by step demonstration of the drop-coating procedure for the fabrication of a composite electrode.

There are also many carbon-based electrode composites, specifically graphene and Carbon NanoTubes (CNTs), the structures of which are depicted in Figure 1.17. The general conductivity and thermal stability of CNTs and graphenes makes them extremely attractive electrode composite materials. Indeed, CNTs have been investigated by electrochemists for a very long time and form a conductive electrode foundation for many electrode composites. Similarly with graphene, the attractiveness appears to lie within the conductivity of graphene but also its ability to adsorb and bind to other composites and wire composite materials to electrodes in a more efficient manner. The electrochemical reactivity of graphenes are, however, a very contentious issue. There are many types of CNTs such as Single- and Multi-Walled CNTs (SWCNT/MWCNT) which adopt structures such as Russian Doll, Swiss Roll, or bamboo structures (or usually a combination). CNTs can also be rolled in different planes to give zig-zag or armchair style nanotubes which changes the properties of the CNTs. The fabrication method of the CNTs is also a factor in dictating the relative electrochemical activity of a particular CNT. Flash Vacuum Pyrolysis (FVP) and Chemical Vapour Deposition (CVD) are two methods of creating CNTs, but any fabrication method involving chemicals has to be strictly monitored because electrochemical responses are often indicative of metallic impurities encapsulated within the CNTs and not of the carbon structure itself. Similarly with graphenes, the production method is important as exfoliation chemicals such as sodium cholate hydrate (surfactants) are often responsible for observed electrocatalytic behaviour of solution-based graphene structures, and even graphenes which are not chemically exfoliated can exhibit defective areas which change the electrochemical application of that particular type of graphene. Given the variety in graphene performances, it would be a large task to report every type of graphene ever produced and give a qualitative estimate of the apparent electrochemical performance of said graphene when used as an electrode material. Instead, a considerable section of this thesis will focus upon characterising

certain graphenes, which will be used as a reference point for future work with these types of graphenes.

1.20 SCREEN-PRINTED ELECTRODES

Electrochemical methods are generally small scale experiments, which are low cost and simple to conduct. The drawback to electrochemical methods in the lab is the rigorous electrode preparation techniques which are required to create a near perfect electrode surface, with no grain boundaries, reactive sites, or adsorbed material. Such electrodes (gold, platinum, BPPG, EPPG) tend to be expensive, too. This collection of issues effectively means that electrochemistry could not be transferred into the field, as field experiments generally require disposable platforms with no pre-treatment or recourse. Thus, a method to create disposable, mass-producible electrodes without the need for recourse was required.

Screen-Printed Electrodes (SPEs) gave researchers a solution to these problems. SPEs are mass producible, lightweight, low-cost, and require no pre-treatment or recourse, and they operate in the same way as conventional electrodes.[45] Screen-printed carbon electrodes are fabricated using a thixotropic fluid such as a carbon ink. A carbon ink is usually a specifically tailored mixture of graphite, carbon black, solvents, and polymeric binders.[45] Carbon inks are very viscous, meaning that the fabrication of electrodes from them is by no means a simple process. A base substrate is selected to print the carbon ink upon; this material is usually ceramic, but thin flexible materials such as polyester are also suitable. Certain factors must be considered when choosing a base substrate: flexibility; longevity; hydrophobicity; and durability are factors that need to be considered. The inks are pressed through a mesh screen of a specific design by a squeegee blade. This process prints even carbon layers upon the substrate. The screen design defines the working, counter, and reference electrodes (in terms of both the position and the size of the electrodes). The electrodes are then cured in an oven

for the ink to dry, for roughly 30 minutes at 60 ºC. The counter electrode is normally just the carbon ink, so no further printing or modification is needed for the counter electrode. However in most cases, the working and reference electrodes have to be printed on top of the first carbon layer. There are some scenarios where the carbon ink is used as the working electrode, so no further working electrode printing is required too. The reference electrode, however, is required to be a redox system of a fixed, known potential. An Ag/AgCl paste is a common reference material utilised for SPEs. The paste is printed on top of the reference section of the electrode using a different screen where only the reference electrode is defined. The electrodes require further curing at 60 ºC for another 30 minutes. The working electrode, if required, is printed next and cured once more. Finally, a dielectric paste is printed over the top of the layers to define the electrodes and protect the connections.[45] Figure 1.21 depicts a schematic of the printing process and Figure 1.22 depicts the end product of the screen-printing process.

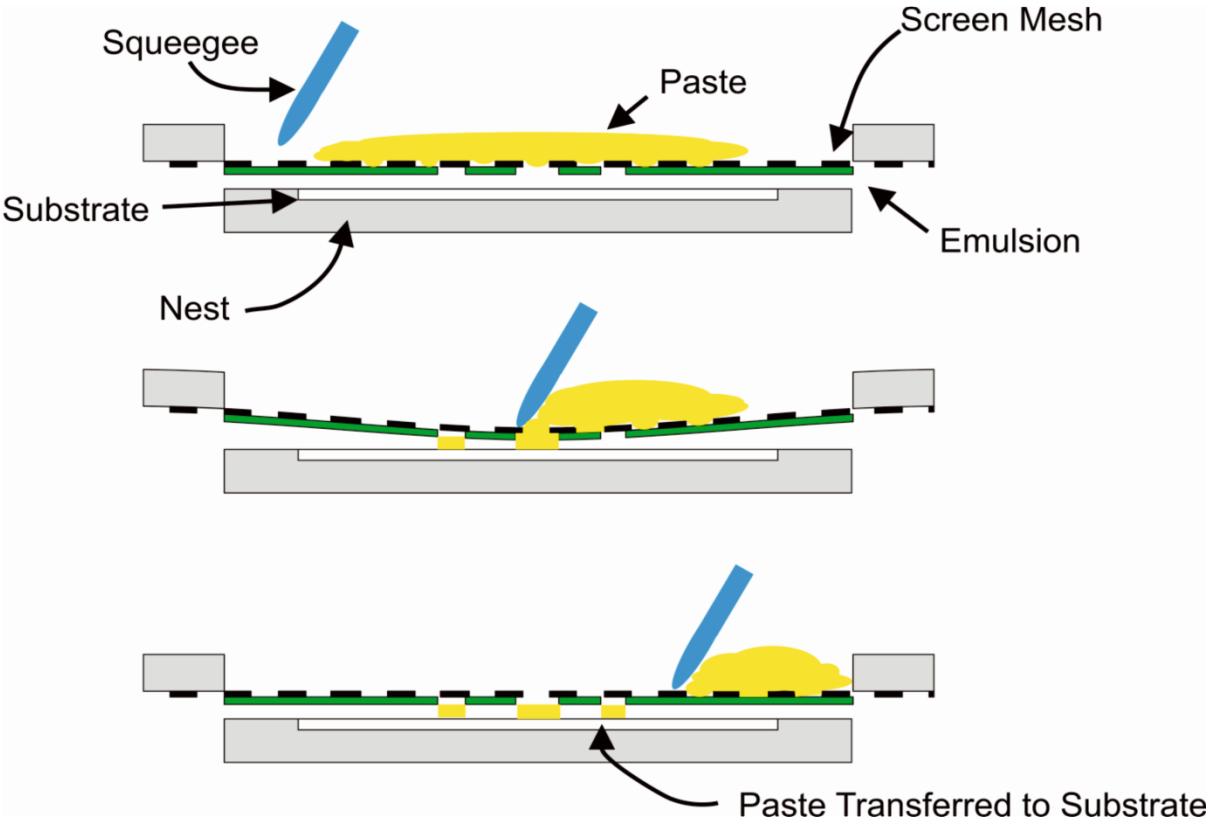

Figure 1.21: Schematic diagram of the screen-printing process. Reprinted from Reference 45.

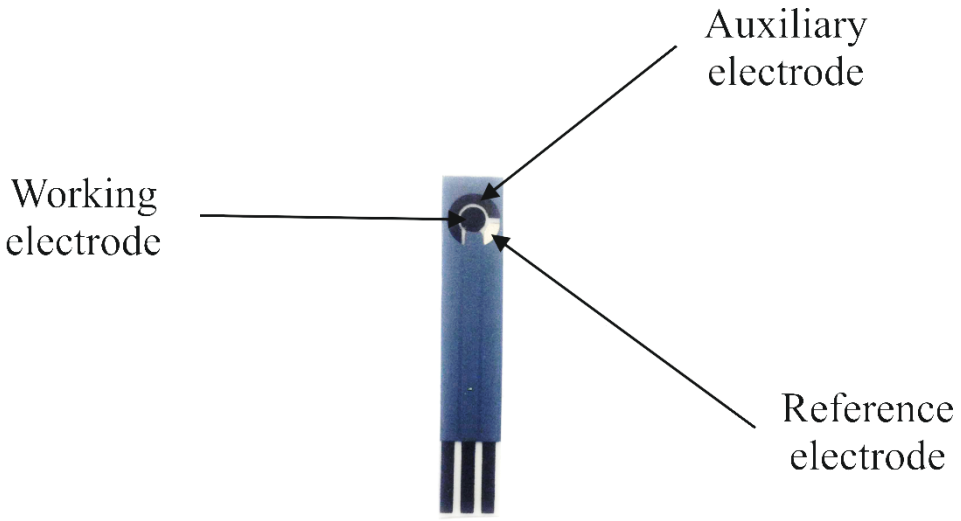

Figure 1.22: Typical screen-printed electrode. Typical dimensions are as follows: 12 mm width; 41 mm length; 2.54 mm pitch; 3 mm working electrode diameter.

SPEs have been applied to the medicinal sector for some time already; the point-of-care glucose sensor utilised in hospitals using screen-printed technology which requires a small sample of blood for analysis of blood glucose is one example. In fact, the glucose sensor is a billion dollar per annum market. Researchers are constantly trying to find new directions for SPEs by looking at different electrochemical techniques, chemical systems, and applications in forensic or environmental science. Table 1.2 disseminates some of the applications of SPEs. The work conducted in this thesis will investigate the application of SPEs using different techniques (CV, EIS) as well as investigate some new and some existing chemical systems.

Table 1.2: List of pertinent SPE methods and their applications.

SPE	Chemical System	Application	Ref.
Molecularly Imprinted Polymer	2,4 dichlorophenoxyacetic acid	Environmental monitoring	[46]
Bismuth film	Lead	Blood screening (poisons); environmental monitoring	[47]
Rhodium/graphite; cytochrome C	Cholesterol	Health monitoring	[48]
Prussian blue	Hydrogen peroxide	Health monitoring	[49]

In the next Chapter, the application of electrochemical impedance spectroscopy is reviewed. The review will explore a brief history of the technique, before discussing some of the fundamental principles surrounding electrochemical impedance spectroscopy. The review addresses the technique in a non-biological context and a biological context; in particular focussing upon corrosion, battery performance, and antigen/antibody binding. The review will close by investigating the current applications of electrochemical impedance spectroscopy to graphenes and SPEs, and it will be found that there are currently very few applications, particularly in the latter case. This observation will formulate the basis of the latter part of this thesis.

CHAPTER 2
ELECTROCHEMICAL IMPEDANCE SPECTROSCOPY: FUNDAMENTAL CONCEPTS THROUGH TO BIOLOGICAL APPLICATIONS

Electrochemical techniques such as CV, DPV, and SWV are consistently used electroanalytically by the electrochemical field, to determine concentrations of a range of target analytes across several media including blood, serum, and urine. Voltammetric methods have been so successful that commercial sensors are available, for instance the case of the glucose sensor. Voltammetric methods struggle when faced with extremely low concentrations, however, except perhaps in the case of heavy metal detection where stripping methods give highly accurate and sensitive results. The field has consequently turned towards impedance as a tool for electroanalysis, in the hope that the highly sensitive nature of the technique can lead to lower detection limits, higher reproducibility, and higher electrode versatility, for example. In order to achieve this in a point-of-care approach, the frequency-dependent properties of SPEs must be rigorously and carefully considered, in addition to the frequency-dependent nature of a whole range of different carbons. This thesis consequently takes the direction of applying electrochemical impedance spectroscopy to SPEs. In order for the reader to understand the technique and its capabilities, Chapter 2 provides a detailed review of the fundamentals of electrochemical impedance spectroscopy and reviews some pertinent biological applications of the technique.

Electrochemical Impedance Spectroscopy (EIS) is a technique which has been utilised by many institutions for over a century[50, 51] for purposes such as corrosion analysis,[52, 53] adsorption properties of molecules (interfacial behaviour)[54, 55] and also to monitor the performance of batteries and fuel cells[56, 57] amongst many other applications. The technique is based upon complex mathematical transforms first described in the late 19th century by Oliver Heaviside to yield real values of impedance in temporal space. Heaviside is also credited with the invention of terminologies such as impedance,[58] admittance and conductance.[59] Critically, he defined the 'operational impedance' as the ''complex ratio of the voltage and current in an AC circuit'',[60, 61] which is denoted as:

$$Z(\omega) = \frac{V(\omega)}{I(\omega)} \tag{2.1}$$

where Z is the total impedance, V is the voltage, I is the current, j is the imaginary component and ω is the frequency. The subsequent development of impedance in relation to diffusional electrochemical systems (discussed later) was first reported by Warburg in 1899[50] and the principles have been implemented increasingly to the present day to the point where EIS has now branched away from universities and into industry for quality control purposes (paints, emulsions, corrosion).[60] In fact, almost any process which changes the conductivity of a system can be recognised by EIS, hence a multitude of properties can be elucidated using the technique.

A common approach in electrochemistry is the application of layers of chemicals, polymers, or coatings to electrodes (known as composite electrodes) which provide useful enhancements in terms of electron transfer and sensitivity. The effects of these different layers and coatings can be identified using EIS,[62, 63] including electrochemical contributions

from polar, ionic and dielectric relaxation processes[60] in the electrolyte system as well as within the electrode, at the electrode surface and within the double-layer region. Exchange-current densities, charge transfer resistances, double-layer capacitances,[64] and other key parameters of an electrochemical system under investigation can also be measured. EIS can also be used to estimate physical parameters such as surface roughness and the porosity of an electrode.[65]

The use of EIS in biological applications has also been reported since as early as 1925.[60] One of the first reported uses of EIS in these applications estimated the overall impedance of biological cells,[66] and has more recently been utilised to study the activity of enzymes combining with target molecules.[67] The technique is now widely reported in bioanalytical applications as a result of the many years of work in developing the technique; in fact, biological applications cover a large portion of EIS research today. It is clear that there is a large volume of information available to the researcher and hence explains why the use of EIS is increasing rapidly as more is learnt about the technique.

2.2 FUNDAMENTAL PRINCIPLES OF ELECTROCHEMICAL IMPEDANCE SPECTROSCOPY

In principle, impedance is simply the opposition force to electrical current in a circuit and is measured in the same units as resistance, Ω.[68] However, resistance differs from impedance because resistance obeys Ohm's law, and is observed in DC circuits where the resistance is technically the impedance with zero phase angle, since the current is not alternating. The concept of resistance can only be applied in an AC circuit if certain criteria are met: i) the AC voltage and current must be in phase with each other; ii) the resistance is frequency-independent; and iii) the resistance can be applied to all currents and voltages.

Unfortunately in the vast majority of cases the phase angle is not equal to zero, as capacitative and/or inductive effects are observed at almost all frequencies (*vide infra*), hence a more general principle must be used to account for frequency-dependence; the concept of impedance essentially allows a quantitative representation of the opposition force to electrical current in these cases (as in AC circuits).

EIS experiments can be setup in a number of ways, but are generally grouped into galvanostatic and potentiostatic impedance experiments. The former is not covered in the experimental work, thus will not be discussed in detail, however the main principle of galvanostatic EIS is to apply a fixed sinusoidal current in conjunction with a fixed DC potential across a three electrode cell. This combination induces an AC voltage sinusoid, created from the Faradaic or non-Faradaic processes taking place at the working electrode surface. Equation 2.2 is then computed to calculate the impedance from the applied fixed AC sinusoidal current input, and the variable sinusoidal voltage being produced. This mode is useful for galvanostatic cells. In most electroanalytical EIS experiments (as in AC polarography[60]), a fixed sinusoidal voltage is applied by a potentiostat across a three electrode cell, in addition to a fixed DC voltage. The resultant electrochemical reaction at the working electrode surface creates an AC current, which is measured by the potentiostat and then equation 2.2 is applied in this case to calculate the total impedance of the system. Potentiostatic mode is useful for electrolytic cells. Equation 2.2 is the fundamental expression which calculates impedance as a function of potential, current, time (t), and the phase angle (ϕ), the latter of which changes depending upon the type of component under study (capacitor, inductor). It is the task of the user to de-convolute this impedance value by attributing certain features of an EIS trace to a specific process.

$$Z = \frac{V_t}{I_t} = \frac{E_0 \sin(\omega t)}{I_0 \sin(\omega t + \phi)} = Z_0 \frac{\sin(\omega t)}{\sin(\omega t + \phi)} \qquad (2.2)$$

The amplitude of the fixed sinusoidal voltage should be dependent upon the type of molecular system under investigation;[69] biological molecules tend to be subject to smaller voltages than non-biological ones as the structures of the biological molecules are easily denatured this way. Another method of assembling an EIS experiment (and in particular for use within biological applications) is to construct a composite upon the electrode surface which will attract target analytes and thus affect the conductivity of the system through either a blocking or a 'molecularly wired' admittance mechanism. In most cases where this strategy is applied, impedance measurements are performed in a blank buffer solution or a known redox probe (such as potassium ferricyanide (II)[70] or hexamine-ruthenium (III) chloride[71]) after the composite and target analyte have been assembled upon the electrode surface. Subsequently when the load is applied at a set frequency, a current will flow through the electrochemical cell which is recorded by the potentiostat and converted by the software *via* equation 2.2 into an impedance value with a real and imaginary component. This process is repeated across a frequency range where different values are deduced for the real and imaginary components of the overall impedance value.

EIS, as discussed previously, requires manipulation of complex numbers to deduce true values for the impedance. This is achieved by the software in which the user selects to obtain impedance spectra; Solartron Analytical[72] and Ivium[73] are examples of such companies offering EIS equipment and the relevant software. The data can be presented in a variety of ways, for instance real and imaginary impedance components are plotted against one another in Nyquist plots (Figure 2.1), which have to be interpreted properly to deduce solution resistances, charge transfer resistances and Warburg impedance as well as time

constants, whereas in Bode plots, the impedance and phase angle is plotted against frequency, which can be helpful to find capacitative or inductive effects of electrochemical systems. Nyquist plots will be referred to in this section more extensively than other forms of graphical EIS representation as they are most useful for electroanalytical purposes. For further information on Bode plots, see Scully and Silverman.[74]

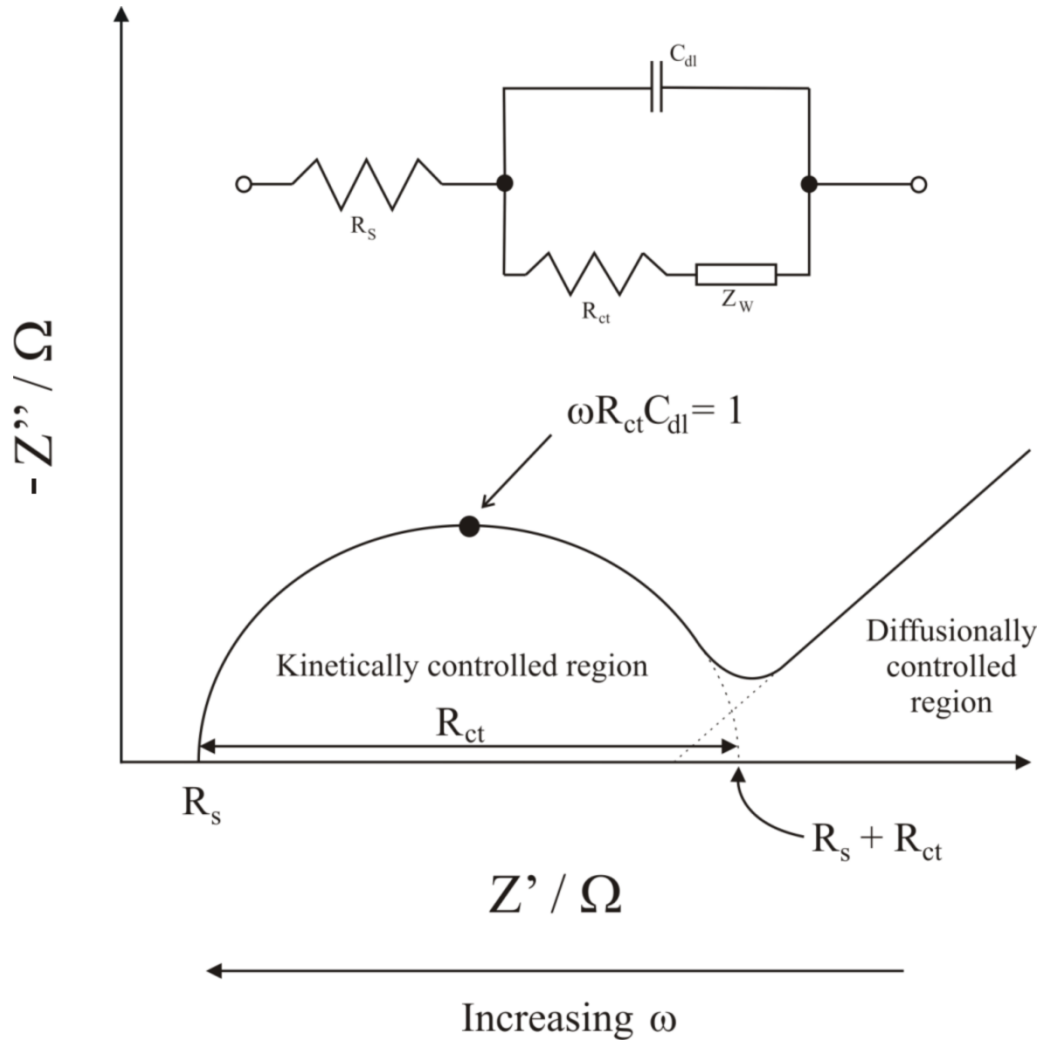

Figure 2.1: Simple Randles equivalent circuit and appropriate Nyquist trace for an "ideal" electrochemical cell.

Two fundamental equations (equations 2.3 and 2.4) describe the real and imaginary impedances of the Nyquist plot, depicted in Figure 2.1:

$$Z' = R_S + \frac{R_{CT}}{1 + \omega^2 {R_{CT}}^2 {C_{DL}}^2} \tag{2.3}$$

and

$$Z'' = \frac{{R_{CT}}^2 C_{DL} \omega}{1 + \omega^2 {R_{CT}}^2 {C_{DL}}^2} \tag{2.4}$$

where *Z'* and *Z''* are the observed impedances due to the real and imaginary parts, respectively, R_S is the solution resistance, R_{CT} is the charge transfer resistance, ω is the angular frequency and C_{DL} is the double layer capacitance. Further, values of capacitance and inductance are related to current and voltage *via* equations 2.5 and 2.6:

$$I = CV \tag{2.5}$$

$$I = V / L \tag{2.6}$$

where *C* is the capacitance, and *L* is the inductance. Hence, by substituting the Ohm's law-like relationship in equation 2.2 into equations 2.5 and 2.6, the impedance can be written in terms of capacitance or inductance *via* equations 2.7 and 2.8:[60]

$$Z = \frac{1}{C} \tag{2.7}$$

$$Z = L. \tag{2.8}$$

A further Ohm's Law-like relationship can be used to calculate the total impedance of a circuit with numerous components, by simply taking the sum of the impedances of each component (provided the impedance components are in series):[60]

$$Z_{total} = Z_1 + Z_2 + Z_3 + ...Z_x \quad (2.9)$$

2.3 DATA INTERPRETATION

The data interpretation part of EIS is perhaps the most important aspect of the whole procedure. In a typical experiment, the user will design a circuit diagram, usually available in an EIS fitting program, which acts as an "equivalent circuit" for a computer simulation. This equivalent circuit is essentially used to de-convolute the observed EIS traces, within a reasonable error margin. Returning to Figure 2.1, this is a typical electroanalytical scenario attributed to a simple electron process, where there is a high frequency capacitative component, coupled with a charge transfer resistance in series with a low-frequency diffusional component named the Warburg impedance (Z_W). The combination of these elements is known as a Randles circuit;[75] such circuits are habitually used to simulate EIS experiments in simple, ideal, heterogeneous, non-adsorptive electrochemical mechanisms. Naturally, most cases are far more complex than this. For instance, factors like adsorption changes impedance, so this must be accounted for, as well as enzyme binding (*i.e.* biorecognition). Each component that the user inputs into the equivalent circuit fitting program is contributing in the simulation to the total observed impedance. A number of combinations of circuit models account for coatings, membranes, adsorption, and induction.[76-80]

The Warburg component accounts for the diffusion of the ions in solution in an electrochemical reaction. For instance at high frequencies, Warburg impedance is not observed as diffusion occurs over much longer time periods than the operational frequency and thus the relatively slow movement of molecules in solution renders impedance contributions to be obsolete. Hence, Warburg contributions are generally seen in the low frequency region; the right hand side of Figure 2.1 illustrates the diffusional controlled region of a Nyquist plot obtained using EIS. The solution resistance is independent of the frequency and is observed in Figure 2.1 at the highest frequency where the real axis is intersected (R_S). The charge transfer resistance (R_{CT}) is the opposition experienced to electron movement and is a real quantity. R_{CT} is observed in Figure 2.1 at the second extrapolated intersection with the real axis in the mid- to low-frequency region; this region is marked as the kinetically controlled region of the Nyquist plot in Figure 2.1, and is related to the heterogeneous electron transfer rate constant, k^0, by following equation 2.10, which is derived from Butler-Volmer kinetics.[81, 82] If:

$$I_{EIS} = I_{Ox} + I_{\mathrm{Re}d} \tag{2.10}$$

and Butler-Volmer kinetics states that:

$$I_{EIS} = \left[AFC_{\mathrm{Re}d} k^0 \exp \frac{(1-\alpha)nF}{RT} \right] - \left[AFC_{Ox} k^0 \exp \frac{-\alpha nF}{RT} \right]. \tag{2.11}$$

Also,

$$R_{CT} = \frac{\Delta E}{\Delta I} \tag{2.12}$$

and

$$\frac{1}{R_{CT}} = \frac{dI_{EIS}}{dE} \quad . \tag{2.13}$$

Consequently, by factorisation of equation 2.11 and combining with equation 2.13, equation 2.14 is left:

$$R_{CT} = \frac{RT}{n^2F^2Ak^0C_{\mathrm{Red}}{}^{(1-\alpha)}C_{Ox}{}^{\alpha}} \quad . \tag{2.14}$$

Operating at the half-wave potential assumes that the concentration of the oxidation and reduction species are equal, therefore equation 2.14 can be simplified to:

$$R_{CT} = \frac{RT}{n^2F^2k^0AC} \quad . \tag{2.15}$$

Where E is the electrode potential, I is the current in the EIS experiment, α is the electron transfer coefficient, R is the molar gas constant, T is the temperature, n is the number of electrons transferred in the electrochemical reaction, F is the Faraday constant, A is the electrode area, C is the concentration of the electroactive species, and i_0 is the exchange current density. This equation was first reported by Randles in 1947,[82] and forms an extremely important aspect of this thesis, from a fundamental and electroanalytical point of view.

The double layer capacitance (C_{DL}) can be roughly estimated from Figure 2.1 by the Z''_{max} of the semicircle. However recent authoritative work by Wang and Pilon has explained that the capacitances measured using EIS at low frequency are unreliable at best, with the paper quoting some literature reporting EIS capacitances exhibiting a 20% discrepancy.[83, 84] Furthermore, the value of the habitually quoted RC circuits by electrochemists is questioned in work by Rubinson and Kayinamura who state (on the modelling of RC circuits) ‘’*the overall impedance expressions corresponding to most models give little or no direct*

information about the physical meaning of the elements for such models''.[85] The capacitative element of an electrochemical cell is often represented by a constant phase element (CPE) which, simply put, accounts for factors which affect the capacitance of a system like surface inhomogeneities resulting in differing reaction rates upon the surface which introduces multiple time constants.[86] CPEs are discussed in a recent review by Dominguez-Benetton *et al.*[87]

The previous paragraph notwithstanding, in modern day analysis, graphical estimations of EIS parameters are simply not accurate enough. Therefore, equivalent circuit modelling is commonly utilised nonetheless. Figure 2.1 depicts a Randles circuit for modelling of a simple electrochemical process. Any software package will fit a simulation to observed EIS experimental data and produce estimations for R_S, R_{CT}, C_{DL}, and Z_W. It is very important to be able to use digital software for accurate results. This does, however, perhaps limit EIS to the lab (at least until automatic fitting can be achieved in a scaled-down potentiostat).

In an applicatory sense, Sluyters and Oomen (1960)[60, 88] estimated the electron transfer rate constant of the $Zn(Hg)/Zn^{2+}$ couple in a 1M $NaClO_4$ and 1mM $HClO_4$ electrolyte at a hanging mercury drop electrode. They scanned from 20 kHz – 20 Hz, due to this being the region where frequency-dependent behaviour of Faradaic processes can be observed, and because the quality of electronics will likely have limited the frequency range. In this frequency range they observed a single semicircle on a Nyquist plot, characteristic of near-ideal charge transfer resistance (see Figure 2.2).[89]

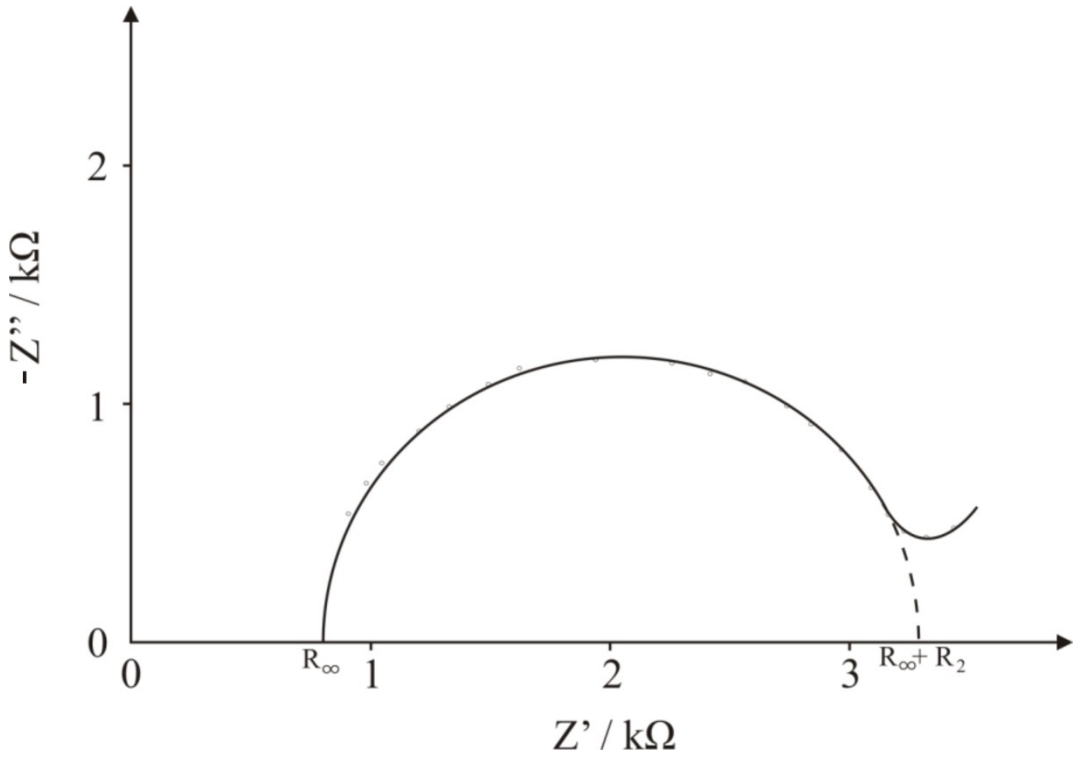

Figure 2.2: Nyquist plot illustrating the frequency-dependent impedance characteristics of a Zn(Hg)/Zn^{2+} couple. The circles are approximate experimental data values; the line is a best-fit line to illustrate the required parameters for investigation. Redrawn from Reference 89.

Interpretation of Figure 2.2 reveals the solution resistance, (depicted as R_∞), to be approximately 800 Ω and is easily attainable simply by observing the first intersection of the semicircle with the real axis. The semicircle is extrapolated in the mid- to low- frequency region to the real axis to reveal $R_2 + R_\infty$, which is an estimate of the sum of the charge transfer resistance and the solution resistance. Note in this thesis, R_2 is referred to as R_{CT}. The R_{CT} is estimated to be *ca.* 2500 Ω. This method of estimating the R_{CT} is scarcely used today; electrochemists will more often estimate parameters using equivalent circuits. From the R_{CT}, estimated from the Nyquist plots from a range of concentrations of Zn^{2+} ions, the authors estimated the electron transfer rate constant, k^0, of the Zn(Hg)/Zn^{2+} couple to be 3.26 x 10^{-3} cm s^{-1} (± 3.6 %) *via* equation 2.14:[60, 90]

It is clear from this section that the wealth of information that can be gained from EIS could be extremely useful for scientists. The fundamentals of EIS cannot be summarised in a few pages of a thesis, but this section has covered much of the basics required to apply EIS to electroanalytical systems. To further the understanding of EIS, some different applications of EIS are now explored.

2.4 NON-BIOLOGICAL APPLICATIONS

As mentioned previously, EIS is a technique commonly utilised for observing corrosion of metals and monitoring the degradation of paints and emulsions, for monitoring the performance of lithium-ion cells, and development of specific materials which may have useful medicinal impacts but do not contain enzymes or proteins. This section very briefly highlights the non-biological applications of EIS and recent developments

A very common employment of EIS is the monitoring of corrosion upon metallic surfaces. It is well known that the level of corrosion upon a metal surface is related to the current which can flow through the metal in the absence of an external electric field, and the phenomenon is aptly named the 'corrosion current'[91] and this phenomenon was initially exploited in the early 1970s to measure the extent of corrosion at a metal|water/air interface. In fact, the circuitry in Reference 91 was meticulously designed to measure the ionic conductor resistance across a pair of electrodes which were to be subjected to a DC voltage. Such a design revolutionised the way corrosion is measured. There is a whole field devoted to corrosion science in the present day, and EIS is a very popular technique for this purpose.[92-98]

An elegant review by Epelboin *et al.* published in 1972[99] summarises the known methods for the detection of corrosion at surfaces (such as the plotting of current-potential curves and the measurement of double-layer capacities) before suggesting impedance as a

tool for the measurement of corrosion. Their review describes how the most useful entity for the measurement of corrosion rate is in fact the so-called 'transfer resistance', which the review defines as the extent of Faradaic impedance at infinite frequency. The suggestion that transfer resistance is the most adequate method of measuring corrosion is rationalised by the fact that the transfer resistance is a purely resistive quantity and therefore less variables affect transfer resistance (given that it is frequency-independent). For a mathematical evaluation of corrosion rates, see Epelboin *et al.* The use of EIS was later implemented for the detection of corrosion on metals coated with polymer coatings as early as 1973 by Menges and Schneider[100] who plotted the impedance modulus against the applied frequency as a function of exposure time to nitric acid on polymer coatings applied to steel.

Presently, EIS is being used to study corrosion for use in a plethora of applications. First, the application to dental treatments is considered. The use of EIS in dental alloy studies has been known for over a decade; a well cited paper on this area of research is by Pan *et al*., who conducted work on titanium alloys in biological environments.[101] More recently, Mareci *et al.*[102] have utilised EIS to study the corrosion resistances of dental alloys in an artificial saliva,[103] which is reportedly approximately pH 5.6. Their EIS experiments utilising an alloy named VeraBondB (which comprises of 12.7 % Cr, 9 % Mo, 1.95 % Be, 2 % Al and the rest Ni) showed that at short immersion times in biological environments, the impedance is far lower than that of long immersion times, showing that the alloy in question exhibits a high level of inactivity after exposure for 1 week to artificial saliva. Furthermore, their studies showed that a higher Cr percentage made the alloy more noble and hence more favourable to be used as an alloy for use in dental treatment.

Other recent corrosion work has been reported by Xue *et al.*, who have used EIS to investigate corrosion rates of magnesium alloys for use as biodegradable implants for medicinal purposes.[104] Their paper describes how the main obstacle which prevents

magnesium-based implants is the fast degradation rates associated with current magnesium implants as described by Song *et al.*[104, 105] Xue *et al.* effectively increase the corrosion resistance of the magnesium alloy magnesium-yttrium (Mg – 4Y) by applying a coating comprising of 1,2-bis-triethoxysilyl ethane (BTSE) silane (dispersed in water containing epoxy resin) upon the Mg-4Y working electrode and use EIS to measure the corrosion resistance. Figure 2.3 illustrates the Nyquist plots obtained from their EIS experiments conducted in subcutaneous tissue on mice, and it is clear to see that the resistance of the bare Mg-4Y material in Figure 2.3A has increased upon the addition of the epoxy BTSE silane in Figure 2.3B. This increase of resistance eludes to the Mg-4Y biological implant design exhibiting a longer lifetime due to a higher resistance to corrosion. Furthermore, their studies also found that the implants exhibited *higher* corrosion resistances *in vivo* rather than *in vitro* (conducted in simulated bodily fluid) and hence the work holds potential for development of implants which degrade slowly and are not harmful to the human body.

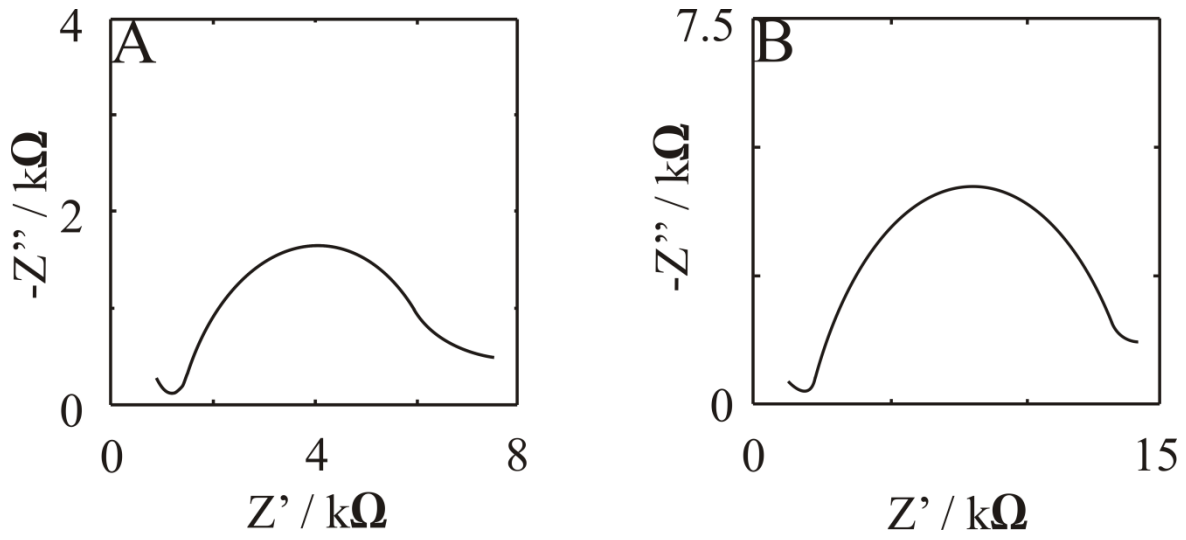

*Figure 2.3: Nyquist plots of **A)** Mg-4Y working electrode and **B)** working electrode coated with epoxy BTSE silane conducted in the subcutaneous tissue of mice. Adapted from experimental data taken from Reference 104.*

Another interesting non-biological application of EIS focusses upon the monitoring of lithium-ion and fuel cells. The monitoring of interior cell degradation is very important for electrochemical devices, mainly for safety purposes *i.e.* prevention of leakage and exposing toxic substances to the atmosphere or human beings. With lithium-based batteries being recalled from shop shelves in 1991,[106] researchers had to redirect their work towards the design of safer batteries for the general public. Lithium-ion batteries provided a solution and researchers continue to pursue them today. In particular, lithium metal phosphates attract a considerable amount of attention from researchers due to the compounds being apparently highly safe.[107]

In the case of lithium-ion cells, many institutions focus upon modifying the lithium electrode to enhance the electrode transfer kinetics and use EIS to monitor this.[108-110] For instance, Liu *et al.* created a fast-ion conductor, $Li_{2.8}(V_{0.9}Ge_{0.1})_2(PO_4)_3$, using a solid state reaction, applied upon a steel conducting plate of which the electron transfer kinetics were studied using EIS with a lithium-based electrolyte. Their work shows high frequency impedance contributions ascribed to ion migration through the applied lithium-based surface films as well as diffusion and charge transfer.

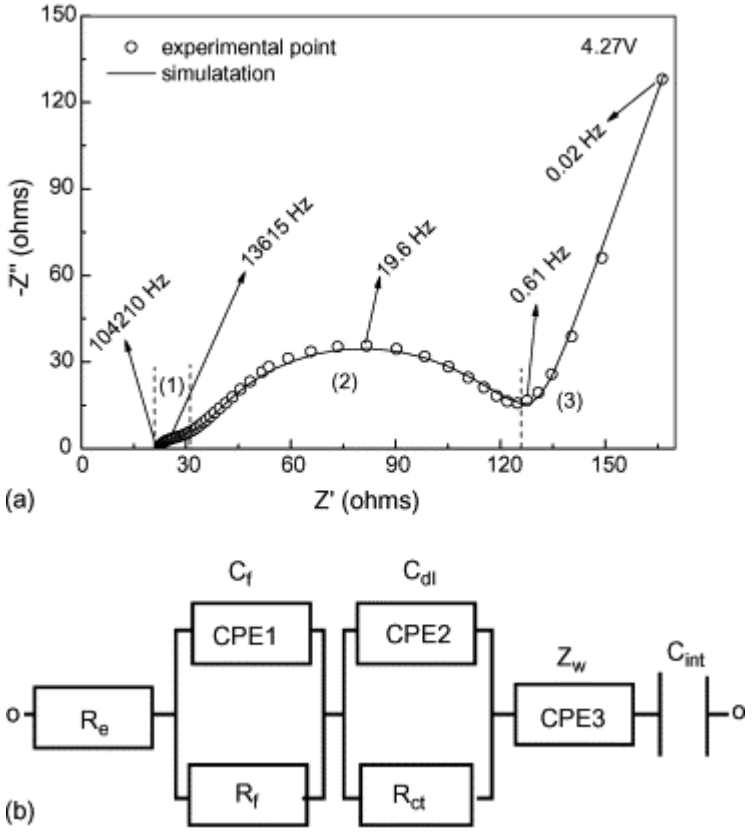

*Figure 2.4: (**a**) The impedance response of $Li_{2.8}(V_{0.9}Ge_{0.1})_2(PO_4)_3$ at +4.27 V during the first charge cycle, and its fitting with the equivalent circuit. (**b**) Equivalent circuit used to fit the experimental data. Reproduced from Reference 108.*

Depicted in Figure 2.4 is a Nyquist plot of the $Li_{2.8}(V_{0.9}Ge_{0.1})_2(PO_4)_3$ from their work, which has been held at a potential of +4.27 V. The circles are experimental data and the line is the simulated data using the proposed equivalent circuit in Figure 2.4 (b). The high frequency domain (1) shows a small perturbed semicircle that the authors attribute to ion migration through the $Li_{2.8}(V_{0.9}Ge_{0.1})_2(PO_4)_3$ surface film. The ion migration contribution is modelled differently to a Randles circuit; instead the authors proposed two regions of kinetically-controlled impedance behaviour. The first higher frequency region is the ion-migration region and is modelled as a double-layer capacitor (CPE) and a resistor in parallel (C_f and R_f, respectively). The second region on the Nyquist plot is the charge transfer region, which is modelled as a second CPE and resistor in parallel (C_{DL} and R_{CT}, respectively). The

CPE in this case accounts for the surface composite, which introduces error into the data due to a more porous surface. The diffusional component is replaced too by a CPE, placed in series with the circuit. Such an element accounts for non-uniform diffusional patterns. The remaining part of the circuit is a capacitor which is termed the "accumulate capacitor", though the authors fail to offer an explanation for this component. The authors estimate the diffusion coefficient of the Li^+ ions in the electrochemical system to be $D_{Li^+} = 10^{-8} – 10^{-7}$ cm^2 s^{-1} (dependent upon holding potential) by calculating the Warburg factor, σ_W:[108, 111]

$$Z_W = \sigma_W \omega^{-\frac{1}{2}} \tag{2.16}$$

and substituting σ_W into equation 2.20, which relates D_{Li^+} to the applied potential, E, the concentration of Li^+, x, and the molar volume, $V_{m,}$.[108, 111]

$$D_{Li^+} = \frac{1}{2}\left[\left(\frac{V_m}{FA\sigma_W}\right)\left(-\frac{dE}{dx}\right)\right]^2 \tag{2.17}$$

Noteworthy, the gradient of a plot of Z' and Z'' vs. $1/\omega^2$ is equal to σ_W, which can then be substituted into equation 2.20 as all the other terms are known. The values deduced for the diffusion coefficient, by comparison to the author's previous work, show ''*excellent diffusion performance*''[108] on the basis that previous diffusion coefficients for other materials were estimated to be one order of magnitude slower.[112] This example highlights how diffusion coefficients (and subsequently electron transfer coefficients) can be estimated by use of EIS. Further, it is known that the underlying electrode affects electrochemical measurements when surface coatings are applied, and as in this case, the underlying material is steel, which can corrode, potentially introducing more factors as the age of the device increases.

Other work by Yan *et al.* has used a lithium metal phosphate film in an attempt to improve the performance of lithium-ion batteries.[107] Unlike Liu *et al.*, who experimented with different cation ratios for lithium-ion performance,[108] Yan *et al.* alternate the anion ratio in the sol-gel synthesized $Li_3V_2(PO_4)_{3-x}Cl_x/C$.[107] The working electrodes were fabricated in-house, in conjunction with polytetrafluoroethylene (PTFE), as opposed to the film technique discussed previously. EIS of the electrodes in a lithium-based electrolyte ($LiPF_6$) was conducted to estimate the diffusion coefficients of several variations of anion content by varying the value of the anion stoichiometry, *x*. Their work displays a reduced charge transfer resistance as the level of anion doping increases. The authors report that the increase in anion doping stimulates electrochemical activity of the lithium in the $Li_3V_2(PO_4)_{3-x}Cl_x/C$ complex which increases conductivity and subsequently decreases R_{CT}. The diffusion coefficient is estimated to be 5.78 x 10^{-10} cm^2 s^{-1} ($x = 0.12$) through the use of equation 2.21:

$$D = \frac{R^2T^2}{2A^2n^4F^4C^2\sigma^2} \quad (2.18)$$

This equation is derived from equation 2.22[113]

$$\sigma = \frac{RT}{n^2F^2A\sqrt{2}}\left(\frac{1}{D_O^{\frac{1}{2}}C_O^*} + \frac{1}{D_R^{\frac{1}{2}}C_R^*}\right), \quad (2.19)$$

so equation 2.22 assumes that $D_R = D_O$. In comparison to the previous example, the diffusion rate is 3 orders of magnitude slower with the anionic doping method in these given examples.[107, 108, 114]

Another parameter which is extremely useful and can be elucidated *via* EIS is the exchange current density of an electrochemical cell, which is essentially the net current of an electrochemical cell in the absence of an external electrical field. This parameter is a key part

of a lithium-ion EIS study conducted by Wang *et al.*[63] In their work, they calculate the exchange current density, i_0, *via* the charge transfer resistance taken from a Nyquist plot. Wang *et al.* utilise equation 2.23 to estimate the exchange current densities of various lithium-containing compounds.[63]

$$i_0 = \frac{RT}{nFR_{CT}} \tag{2.20}$$

Further, they introduce the concept of surface film resistance in a quantitative fashion, observed as double semicircles in their EIS spectra. That is, the diameter of the semicircle of the proposed surface film contribution on the Nyquist diagram corresponds to the surface film resistance.[63] This component is modelled in the same way as the example in Figure 2.4, apart from the "accumulate capacitance" has been removed. Therefore, it seems that a generic impedance model for an electrode with a porous barrier is presented in Figure 2.4. Such a model is potentially useful for SPEs, if of course the carbon layers offer any porosity. This will be covered later in this thesis.

This section has touched briefly upon how EIS can be utilised to monitor corrosion resistance and to estimate diffusion coefficients within lithium ion cells to gain insights into their performance. Further uses for non-biological applications include proton exchange membrane fuel cells (PEMFCs). Given that today's PEMFCs do not operate efficiently under extreme conditions (low humidity, high temperatures etc.), research has been ongoing for many years to improve the efficiency of PEMFCs under these conditions.[56] EIS is a technique which is used to monitor newly designed substrates for PEMFCs, and has been rigorously reviewed by many people, including Zhang and co-workers in 2007[115] and 2008[116], by He and Mansfield in 2009,[57] and more recently, Borole *et al.*[117] Also, this section has

propitiously found a second circuit model in this section which will be discussed in further detail later in the thesis. The remainder of this section focusses largely upon the biological applications of EIS which are more specifically directed towards the sensing applications of EIS. The next section shall discuss these highly relevant biological applications of EIS including biosensing and DNA detection.

2.5 BIOLOGICAL APPLICATIONS

This section has so far covered fundamental principles associated with EIS, and has also explored some pertinent non-biological applications of EIS including corrosion detection, electrochemical activity of lithium ion cells and monitoring fuel cell performance. This section will assess the plethora of biological applications utilising EIS and overview the range of information which can be extrapolated from EIS in biological applications. It is worthy of note that work by Samanta and Sarkar[118] reviews literature regarding the immobilisation of biomacromolecules upon substrates and discusses the relative merits of the different methodologies applied; such techniques are commonplace from this point forward.

Firstly, EIS has been used in the development of DNA biosensors. An example of the use of EIS in the detection of DNA damage is a paper by Hlavata *et al.*[119] In their work, Screen-Printed carbon Electrodes (SPE) are utilised, which is rarely seen in the literature for the case of EIS. A composite is applied to the surface of the SPE, consisting of SWCNTs, which are known to be beneficial for the detection of DNA,[120] chitosan (CHIT) obtained from shrimp shells (normally used as a blood clotting agent), and the DNA which has a known base sequence. A Nyquist plot comparing different electrode modifications in 1 mM $[Fe(CN)_6]^{3-/4-}$ is shown in Figure 2.5, where it can be seen that the addition of the SWCNTs

and CHIT on the electrode surface increases the charge transfer resistance which appears as a larger semicircle in the plot.

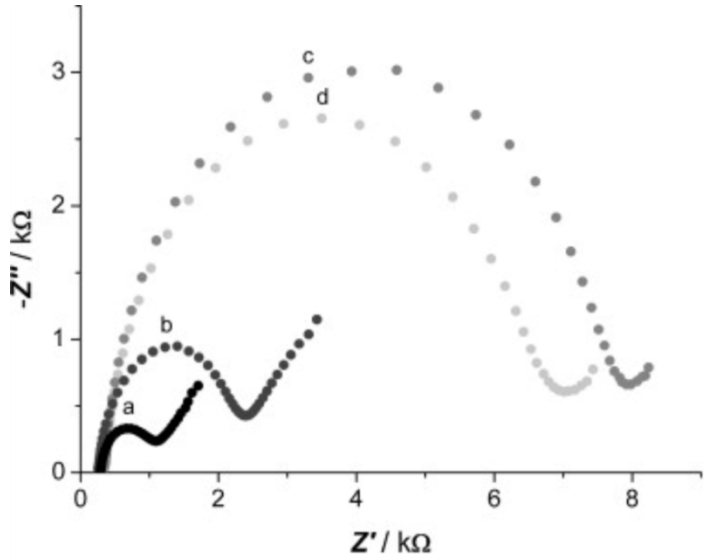

*Figure 2.5: Nyquist plots in the presence of 1 × 10^{-3} mol L^{-1} $[Fe(CN)_6]^{3-/4-}$ in 0.1 mol L^{-1} PBS at pH 7.0. DC potential: +0.1 V vs. Ag-SPE/AgCl; frequency range: 0.1–5000 Hz; AC amplitude: 10 mV. (**a**) no thioridazine present in the solution, measured at the SWCNT–CHIT/SPCE; (**b**) 10^{-7} mol L^{-1} thioridazine present in the solution, measured at the SWCNT–CHIT/SPCE; (**c**) no thioridazine present in the solution, measured at the DNA/SWCNT–CHIT/SPCE; (**d**) 1 × 10^{-7} mol L^{-1} thioridazine present in the solution, measured at the DNA/SWCNT–CHIT/SPCE. Reproduced from Reference 119.*

Comparing (c) to (d), where the difference is only that the electrolytic solution in (c) contains no DNA binding agent (thioridazine) and (d) contains the binding agent, there is a small change in the charge transfer resistance. This is ascribed to the binding agent combining with the DNA on the electrode. They offer an explanation for this improvement in conductivity, by suggesting that the structural change observed during the binding exposes guanine moieties (which are presumably electrochemically altered in some way). This change in the structure allows the redox probe to access the electrode surface more feely, and thus reduce the

"transfer resistance", though it is clear that this is not simply a Faradaic effect, but a combination of Faradaic and non-Faradaic effects.[119] Such work is merely qualitative, which is unfortunate because it would have been beneficial for readers to observe the change in impedance with respect to DNA percentages. Furthermore, there is no equivalent circuit proposed for this work, which probably means that simulations were not performed.

A recent development of the use of biological substrates in tandem with EIS concerns label-free biosensors,[121] which have been studied for over a decade in conjunction with EIS.[122, 123] Siddiqui *et al.*,[121] reported their interpretation of the antibody-antigen binding mechanism using UltraNanoCrystalline Diamond (UNCD) microelectrode arrays. Their work firstly shows that the attachment of antibodies to an electrode surface introduces an observed charge transfer resistance to the system, whereas the bare UNCD electrodes, rather than exhibiting charge transfer, show only diffusional components in their corresponding impedance spectra. Further, upon the introduction of *E. Coli* to the electrode *via* a specific binding mechanism to the corresponding antibody cast upon the electrode surface, the overall impedance increases further. Through these observations and simulations, the authors have designed a theoretical equivalent circuit for the observed phenomenon and this is shown in Figure 2.6.

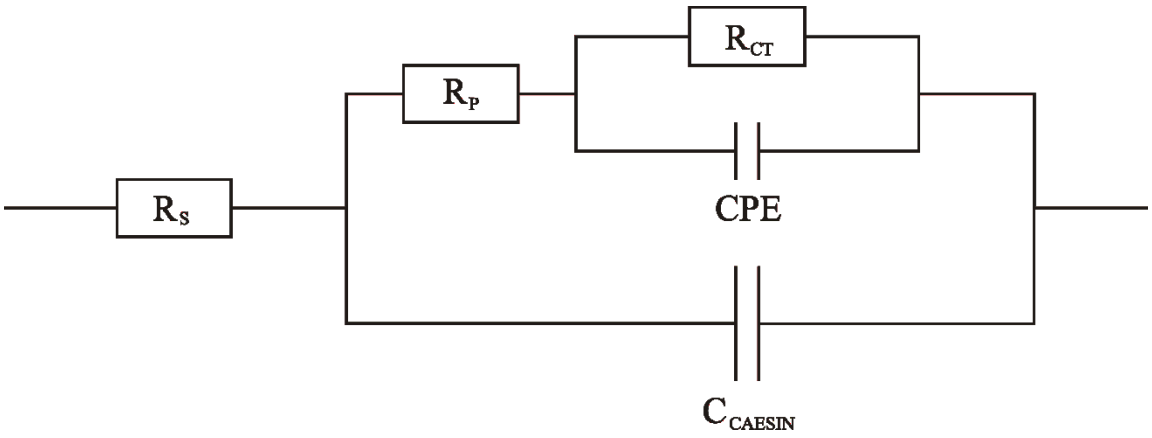

Figure 2.6: Redrawn equivalent circuit model used in reference 121 to model the effect of surface porosity and capacitance observed with respect to the caesin composite electrode.

The equivalent circuit above rationalises the impedance contributions exhibited from both the deposited surface antibody matrix, casein, and the pores associated with UNCD microelectrodes. R_S appears in the equivalent circuit model as is the case with all solution-based circuit modelling. R_{CT} and the capacitance are modelled in parallel to account for the typical RC circuit, however the diffusional component has been removed as there is no diffusional behaviour associated with this system when UNCD is modified. Instead, a large capacitance was observed, which is modelled as C_{CAESIN}, in parallel with the RC circuit. The remaining component is R_P, which is the resistance attributed to the pores, which is a likely phenomenon as solution particles become trapped in tight spaces. Returning to their work, it is observed that after the bacteria is bound to the antibody, the semicircle in the Nyquist plot has increased massively compared to the case of the antibody only, which shows an increase in the charge transfer resistance. According to the authors,[121] this happens due to the bacteria being a large molecule which blocks the electrode surface even more so than the antibody which has been deposited upon the surface.

Similar work concerning antibody/antigen recognition has been conducted by Mathebula *et al.*[124] who have used EIS for the detection of TuBerculosis (TB). In their article, they report a novel method to self-assemble an antigen layer upon a gold electrode. First, a layer of a long-chain organic compound (N-(2-mercaptoethyl)octadecanamide, MEODA) is assembled upon the electrode surface by immersing the electrode in cysteamine before adding stearic acid. The electrode is then incubated in a solution of dry DiMethylFormamide (DMF) containing Mycolic Acids (MA) for 48 hours. The MAs are the antigens in this case, as they act as the recognition molecules for the TB. The electrodes were then immersed in SAPonin (SAP) which is a blocking agent, utilised in this case to block all non-specific adsorption/binding sites and hence the impedance measurements taken after the TB binding

step can be assumed to be a result of the bound TB. These electrodes were then used in EIS experiments on human sera which were HIV and TB positive (HIV^+TB^+) and negative (HIV^-TB^-) as their study is focused upon combating TB in HIV/TB co-infected individuals as TB is the biggest killer for HIV infected individuals.[125] Their work demonstrates a highly selective electrode for HIV^+TB^+, with the ability to recognise a specified DNA sequence attributable to a sexually transmitted disease; such an important technique is not available *via* electrochemical methods such as cyclic voltammetry because DNA molecules do not exhibit electrical conductivity and are not electroactive. Instead, the mechanism in this work is a blocking mechanism. Basically, the apparent charge transfer resistance observed is simply a measure of the DNA hybridisation taking place at the electrode surface. The level of hybridisation is also related to the concentration according to their work, so the method is semi-quantitative as well as qualitative.

Further work involving the use of antibodies has been described by Liu *et al.*[126] who have devised a method to implement EIS electroanalytically for the detection of HbA1c, a type of haemoglobin which is used to elucidate the concentration of glucose in blood plasma. Their method is based on a concept named ‘’competitive inhibition assay’’ where in this case the HbA1c and the antibody are suspended together in a series of sera in which the HbA1c concentrations are varied. The competitive inhibition derives from the fact that the percentage of antibody adsorbed to the electrode composite is dependent on the amount of antibody complexing with the HbA1c; in other words the higher the concentration of the HbA1c, the less antibody available for adsorption to the electrode composite, and thus the charge transfer resistance will decrease compared to lower concentrations of HbA1c as, intuitively, there is less material blocking the flow of electrons through the electrochemical cell. The resultant experiments show a negative correlation between HbA1c concentration and charge transfer resistance. The method describes a useful glucose determination method, and though there

are already many glucose detection technologies available, the pursuit of more accurate results is always desired by scientists; EIS could provide that solution.

Other recent work in biological applications includes: the impedimetric detection of myoglobin by Wang *et al.*[127], though their use of a +205 mV holding potential for biological applications should be questioned as there is a possibility of denaturation; electrochemical detection of morphine and diclophenac in pharmaceutical samples by Mokhtari *et al.*;[128] and work by Santos *et al.*[129] which focusses upon the electron transfer mechanisms of HorseRadish Peroxidase (HRP) immobilised upon a glassy carbon electrode with nafion and polymyxin in a diffusionless system, with a view to understanding the electron transfer mechanisms of this particular enzyme. Interestingly, the latter example loosely links charge transfer resistance to electron hopping between the iron centre of the HRP and target molecules such as O_2 and H_2O_2. The evidence to support this is cycling their composite electrode 500 times in O_2 saturated media and measuring the impedance which is compared to the impedance of a bare glassy carbon electrode. It is found that the charge transfer resistance decreases with cycling in this particular electrochemical system, which they believe is due to a slow electron transfer rate between the enzyme and the O_2 which has been suggested previously by Venarusso *et al.*[130] EIS has also recently been utilised by Prats-Alfonso *et al*. for the use of detection and quantitative measurement of p53-antibodies,[131] which are used in medicinal technologies as prognostic indicators for ovarian cancer and biomarkers for other types of cancer. In a quantitative context, the authors use EIS to detect said antibodies to a *picomolar* concentration, which demonstrates that the technique of EIS can be, in some cases, extremely sensitive. Further examples regarding electrochemical aptamer-based biosensors (pre 2011) are reported in a review by Ferapontova and Gothelf.[132]

There is a massive scope for EIS in conjunction with biological systems. This is highlighted by the many different methodologies presented in this section. It is clear that EIS

in biological systems requires extremely meticulous engineering of electrode composites and very strict methods and controls in order for an analytical procedure to be of any value. In this sense, one could argue that any EIS-related methodology could take potentially years or decades to get to market. Irrespective of such an opinion, the possibilities are there to see for everyone. The next section will focus upon graphene composite electrodes utilised for sensing applications.

2.6 GRAPHENE COMPOSITE ELECTRODES

The use of graphene-based derivatives in electroanalysis has accelerated over the past few years; especially since the Nobel Prize for physics was awarded to Geim and Novoselov in 2010 for the fabrication and characterisation of single layer graphene.[133,64] Graphene has, unfortunately, rarely seen success in terms of beneficial electrochemical responses which could be utilised for sensing applications in its pristine form (defined in Chapter 1).[135] More often than not it has been shown to perturb the electrochemical response of known electroactive biologically relevant analytes such as ascorbic acid and NADH.[136] Graphene composites are applied to electrodes in a number of ways which were discussed in Chapter 1. More information about electrode modifications are provided by Bard (1983)[137] and for specific information about self-assembled monolayers, Bain,[138] Nuzzo[139] or Porter.[140]

Given the use of graphene-based derivatives in modern electrochemistry, this section focusses mainly upon graphene utilised in conjunction with EIS for biological applications. This section will also report other carbon-based electrode composites,[141-143] as they are widely reported by researchers attempting to find more solutions for everyday problems and applications in electroanalysis. The current volume of literature regarding graphene and EIS is comparably low to the other topics covered within this work; thus this thesis will

investigate EIS with many types of carbon materials. There are some reviews in graphene available[144] that provide some useful literature reports focussing upon DNA analysis, bio-sensing and immunoassays - a review by Bonanni *et al.* offers an excellent schematic representation of a generic graphene/biomolecule impedance setup.

One of the first examples of graphene-based impedimetric sensing is reported by Bonanni and Pumera who apply so-called ‘’hairpin’’ DNA oligomers (with a complimentary base sequence to that of Alzheimer’s disease) to graphene-coated electrodes.[145] They report that upon immersion into a solution containing DNA oligomers with the complimentary base sequence, the R_{CT} of the redox probe potassium ferrocyanide decreases compared to a non-immersed electrode. Intuitively, this shows that when the electrode is immersed in the complimentary solution, a spontaneous DNA hybridisation takes place. The authors continue to attribute the decrease in observed R_{CT} to the hybridized DNA strands desorbing from the electrode surface, a claim which is unsubstantiated within their work, *i.e.* there is no electrode surface characterization pre- and post-experiment. Nevertheless the work represents a new sensing platform for such diseases. Graphene-based apta- and immuno-sensors have also been developed by the same group.[146, 147]

Graphene has been proposed as a novel material to coat metallic surfaces with a view to reducing corrosion and the experiments conducted by Raman *et al.* utilise EIS as a means to study this effect.[148] Copper sheets were engineered and washed with deionised water and acetone prior to experiments. The EIS experiments were conducted in 0.1 M NaCl using a frequency range of 1 MHz – 10 mHz. Figure 2.7 illustrates Bode plots obtained for uncoated and graphene coated copper in 0.1 M NaCl and it is clear from Figure 2.7a that the impedance at high frequencies is far higher for the graphene coated copper than it is for the uncoated copper. In fact, the impedance is almost 2 orders of magnitude larger for the graphene coated copper compared to the uncoated copper. This work is somewhat novel,

considering previous efforts to coat metals with graphene have yielded improved corrosion resistances, but only twice that of the uncoated metal,[149] albeit in a different electrolyte.

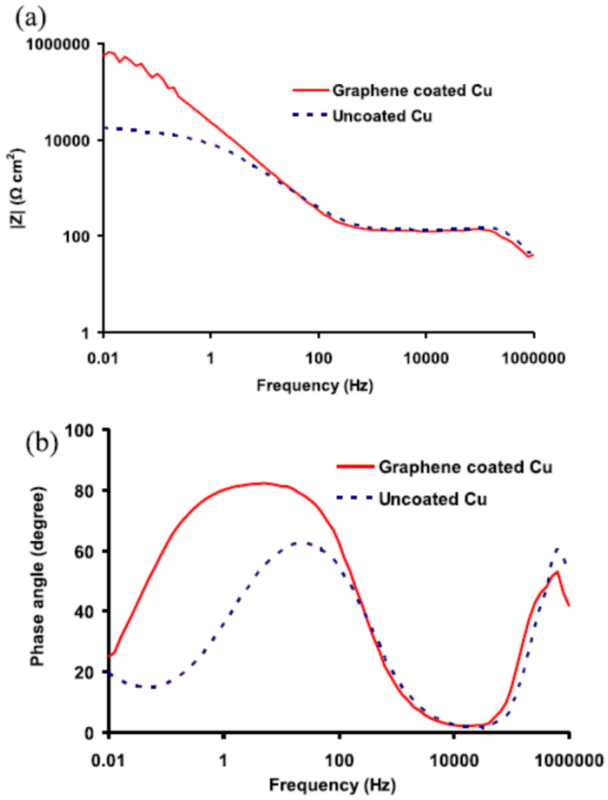

*Figure 2.7: Bode plots of the uncoated and graphene coated copper: (**a**) impedance modulus and; (**b**) phase angle. Reprinted from Reference 149.*

Graphene has also been formed *in situ* for use as anodic coatings in microbial fuel cells. Previous studies have utilised carbon nanotube networks in biofilms for the same purpose, yielding positive results in terms of decreased fuel cell resistance,[150] yet graphene may prove to be a completely different scenario. A graphene network was formed in the biofilm on the fuel cell's anode by mixing graphene oxide with acetate and injecting the solution into a well-used Microbial Fuel Cell (MFC) whose voltage output was less than 50 mV. The solution was later replaced by acetate. A graphene network was subsequently formed by microbial reduction of graphene oxide in the biofilm and characterised by SEM

imaging which showed the networks formed upon the anodes were that indeed of graphene.[151] According to the authors, EIS measurements of the anodes revealed charge transfer resistances to decrease by approximately half upon the addition of the graphene scaffold to the biofilm, thus suggesting the graphene scaffold increases the conductivity of the system.[151] An improvement in conductivity is useful for fuel cells to improve efficiency.

Turning attention back to graphene uses in biological applications, work by Hu *et al.* describes a ''label-free electrochemical DNA hybridization assay using functionalized graphene as a platform.''[152] Modern technologies for the sensing of DNA require label-free, fast, and non-destructive techniques for analysis and have been studied by many groups.[153] EIS and voltammetric techniques currently lead the way in label-free DNA sensing, however EIS offers a wealth of information regarding changes at the surface of the electrode composites as well as possible DNA strand conformation changes. Hu *et al.* construct a composite comprising of graphene and 3,4,9,10-Perylene TetraCarboxylic Acid (PTCA), which is used as a platform to immobilise single stranded DNA (ssDNA), shown in Figure 2.8. The advantage in this case of immobilising ssDNA with a known base sequence is that a target ssDNA strand with the complementary base sequence can selectively bind to the ssDNA upon the surface which clearly will have an effect upon the observed spectra obtained *via* EIS. In the case of Hu *et al*., the complimentary target molecule is the pol gene of the *Human Immunodeficiency Virus-1* (HIV-1). A pol gene is simple to use as it is a retrovirus that encodes its reverse transcriptase enzyme. Figure 2.8a shows the effect of the increase in concentration of the pol gene on the *Z'* and *Z''* components of EIS, and it is apparent that the charge transfer resistance increases as the concentration of pol gene increases. Furthermore, control experiments were conducted utilising mismatched DNA strands of differing base sequences, all of which exhibited lower transfer resistances than the pol gene and thus less binding to the ssDNA at the surface. Unfortunately, the paper doesn't conclude their

impedimetric bioassay by plotting R_{CT} *versus* concentration which would have been useful to assess whether the technique could be incorporated into electroanalysis.[152] However, inspection of Figure 2.8b would suggest at least a gradual, if not linear, increase in R_{CT} as the concentration of pol gene present increases. It should be kept in mind that this mechanism is different to the desorption method report in reference [152], thus the addition of more material to the electrode increases the observed R_{CT}.

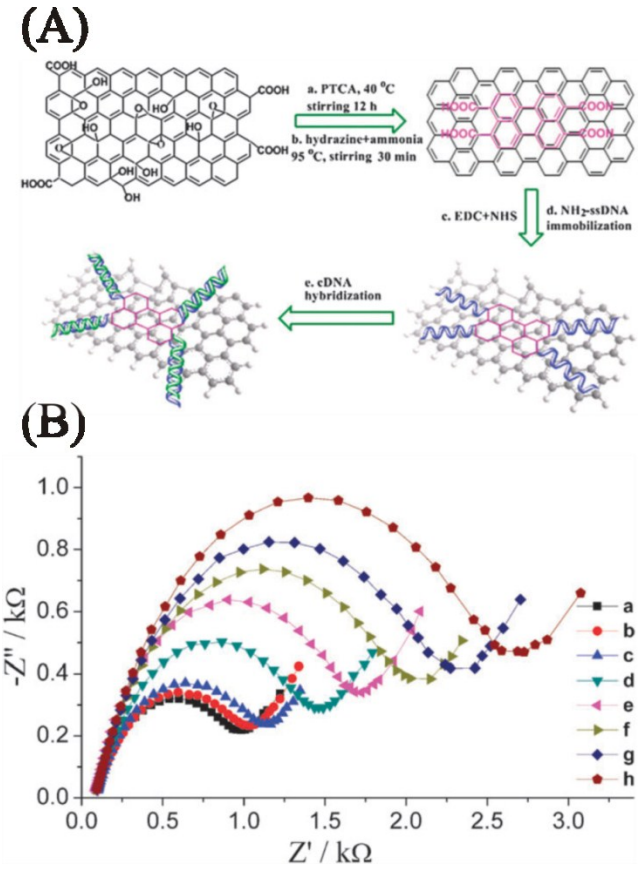

*Figure 2.8: Schematic diagram (**A**) of the formation of the graphene/PTCA network and the ssDNA binding step; and EIS data for the graphene/PTCA/ssDNA composite (**B**) in solution of differing concentrations of pol gene: without hybridization (**a**) and after hybridization with its complementary HIV-1 pol gene sequences of different concentrations: 1.0 x 10^{-12}, 1.0 x 10^{-11}, 1.0 x 10^{-10}, 1.0 x 10^{-9}, 1.0 x 10^{-8}, 1.0 x 10^{-7} and 1.0 x 10^{-6} M (**b**–**h**). Adapted from Reference 152.*

Further recent advances in graphene technology carry on with the theme of sexually transmitted diseases, and concern the electrochemical detection of the *Neisseria Gonorrhoea* bacterium which is responsible for the sexually transmitted disease gonorrhoea.[154] A chemically prepared polyaniline and iron oxide nanocomposite is deposited upon an indium tin oxide electrode in the work by Singh *et al.* which, upon addition of an amino labelled DNA probe, selectively exhibited an increased charge transfer resistance when immersed in a solution of complimentary DNA taken from gonorrhoea bacteria. Comparably, the total impedance was found to be larger than when the electrode was immersed in *K. Pneumoniae, S. Aureus, E. Coli* or *N. Sicca*. This work suggests that graphene related composites could be utilised to create miniaturised sensing platforms to selectively detect different strains of bacteria and (hopefully) their concentration levels. It is an exciting prospect to think that disease could be diagnosed on-the-spot instead of taking extended periods of time by sending samples to labs and using time consuming techniques such as PCR and ELISA.

Finally, using similar EIS methods to those described previously in this section, Wang *et al.* devise a method incorporating graphene oxide for the impedimetric detection of the infamous Methicillin-Resistant *Staphylococcus Aureus* (MRSA) DNA.[155] Similar to previous graphene examples, they specifically design their electrodes in a manner which connects the graphene to the surface *via* chemical linkage; they used 3-AminoPropylTriEthoxySilane (APTES) as a molecule to link the graphene oxide to the glassy carbon surface as described in their previous work.[156] To prepare the DNA containing electrode, they simply employ the drop-casting method by which they pipette 50 μL of the relevant ssDNA upon the surface and dry under closed humid conditions for 6 hours. Next, varying concentrations of the complimentary DNA were applied to the electrode surface for 30 minutes. The electrodes were subsequently washed with PBS to remove any loosely bound material. Control experiments were conducted using non-complimentary DNA. EIS experiments took place in

0.01 PBS (pH 7.4) with 0.1 M KCl. The EIS data obtained concluded that the concentration of the MRSA complimentary DNA largely affected the charge transfer resistance. Their work is a clear indication that the MRSA binds to the electrode as the charge transfer resistances are far larger than the random DNA fragments used in the control experiments. Hence, the method has potential use for the label-free detection of the deadly bacteria[155] and has the advantage of being quick and relatively cheap.

This section has discussed a few applications of carbon materials to EIS. As a general observation, the graphenes are generally used as base materials for electrode composites, and are wired to the underlying electrode using chemical binders. The graphene's high surface area and surface defects are likely responsible for the adsorption properties of the graphene. Graphene therefore appears to be a good material to use for non-Faradaic EIS protocols, yet Faradaic methods may not be entirely appropriate due to the slow electron transfer rate kinetics of graphene.

2.7 SCREEN-PRINTED ELECTRODES

Screen-Printed Electrodes (SPEs) are disposable electrodes which can be specifically tailored for the detection of target analytes;[157] they have been introduced in Chapter 1. SPEs are particularly useful because of disposability, the lack of need of surface pre-treatment before and during measurements, reduced sample size required for analysis (~ < 20 μL) and their scale of economics due to the ability to be mass produced. SPEs also exhibit excellent reproducibility (< 5%, depending on the system) within and between batches, highlighted by incorporation into sensors for diabetics to measure their blood glucose on-the-spot. However, currently the use of SPEs is practically limited to voltammetric techniques and the direction of research focusses upon tailoring analyte specific SPEs,[158] and the use of novel electrode

geometries such as microelectrode SPEs,[159] and screen-printed microelectrode arrays[160] for the voltammetric determination of target analytes. This section shall subsequently briefly explore the current literature regarding SPEs for use with EIS which surprisingly are almost incongruous with one another in research today.

The earliest notable contribution is in 2006 by Lu and Chen.[161] In their work, they created SPEs for the sensing of glucose *via* drop-coating a mixture of Fe_3O_4 nanoparticles and ferricyanide onto a carbon SPE, after which glucose oxidase was drop-coated onto the electrode. Unfortunately EIS was only used in their study to characterise their electrodes, which intriguingly were found to exhibit a larger R_{CT} upon the addition of glucose oxidase. An interesting approach would be to use the generic methodologies seen in this review to study the effect upon R_{CT} of the glucose oxidase and the effect of glucose concentration.

The following year, gold SPEs were fabricated by Balkenhohl and Lisdat as impedimetric immunosensors.[162] The electrodes are coated with a layer of sodium-4-styrensulfonic acid, which acts as an anchor for transglutaminase, a molecule associated with the autoimmune disorder, celiac disease. After application of the enzyme, bovine serum albumin was applied to the electrode to block non-specific binding sites. The SPE could then be used for the impedimetric detection of anti-transglutaminase antibodies. Different types of antibodies were studied, and it was observed that the immunosensor without anti-transglutaminase exhibits a smaller R_{CT} than the one with the transglutaminase. In fact, according to their experimental data, the R_{CT} is over double for the immunosensor incubated with the antibody (39.7 kΩ compared to 97.6 kΩ). In addition to this, concentration studies were performed but unfortunately did not yield a linear calibration plot which would have allowed its use as an analytical sensor.

More recently, Rohrbach and co-workers have developed a screen-printed sensor for the detection of lysozyme,[163] an enzyme most notably found in tears and egg white and is

reported to exhibit cell destruction properties.[164] Carbon nanotube SPEs have been modified with an amino-modified DNA aptamer which recognises lysozyme. The results of concentration studies are presented in Figure 2.9 as a Nyquist plot and a plot of concentration *versus* R_{CT}. Figure 2.9A shows that the R_{CT} decreases upon lysozyme incubation. The authors state that the R_{CT} levels off above lysozyme concentrations of 400 µg L^{-1}, represented in Figure 2.9B. This is not entirely correct as the R_{CT} value gradually increases again; nevertheless % RSD measurements would benefit the work.

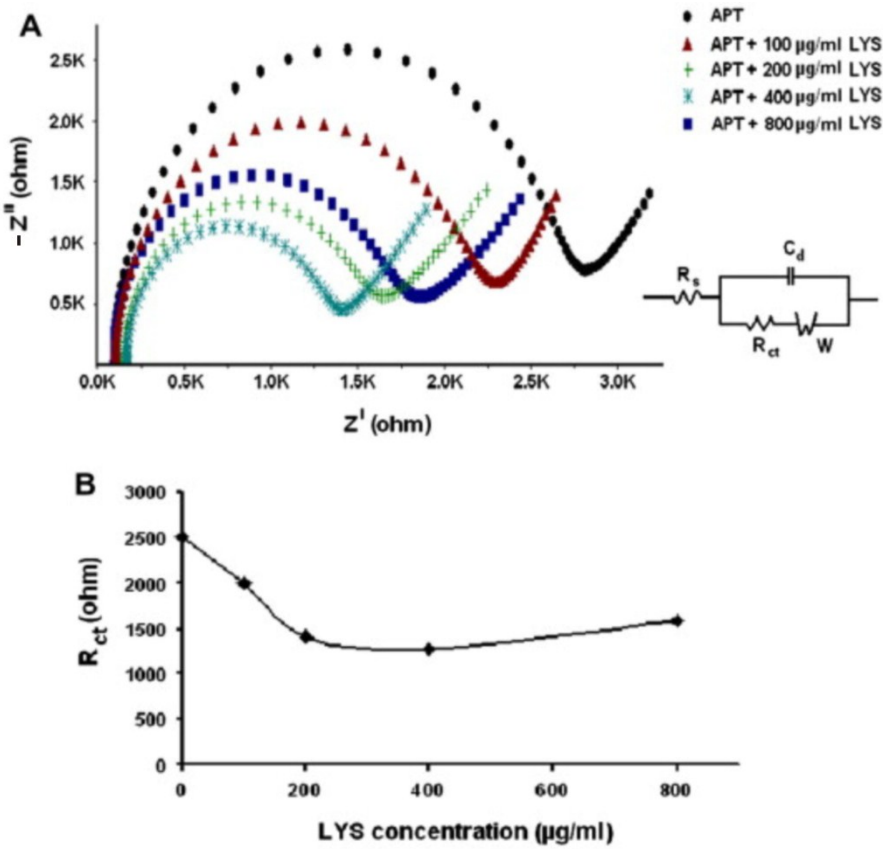

Figure 2.9: Nyquist diagrams recorded with supporting electrolyte solution 2.5 mM $K_3[Fe(CN)_6]/K_4[Fe(CN)_6]$ (1:1) containing 0.1 M KCl by using MWCNT–SPEs with 200 µg mL^{-1} immobilized aptamer for different lysozyme concentrations such as 0, 100, 200, 400, and 800 µg mL^{-1}. Reproduced from Reference 163.

There have been further studies utilising SPEs, for instance for the detection of lead using bismuth-modified SPEs,[165] short DNA strand HIV detection utilising carbon SPEs modified with chitosan and Fe_3O_4 nanoparticles,[166] and the detection of *E. Coli* using gold SPEs.[167] There is evidently a scope of interest within the electrochemical field to apply SPEs and EIS to analytically useful measurements as highlighted in the above examples. It is perfectly reasonable to suggest an interesting line of inquiry would be to apply the techniques towards the sensing of the diseases as highlighted in the previous section with the benefit of SPEs for the potential use for an on-the-spot, quick and disposable sensing method, avoiding the need for sending samples away for laboratory testing. There are many more exciting examples of EIS for sensing purposes. Table 2.1 provides an overview of some of these exciting examples.

Table 2.1: An overview of pertinent EIS applications to biological systems.

No.	Electrode	Sensing Element	Detection Limit	Notes	Ref
1	GCE/Pty/Au/Pt_{NP}[a]	PEP DNA[b]	3.6 x 10^{-13} M	Au/Pt nanoparticles formed on film surface *via* electrodeposition	[168]
2	CNT/CHIT/PGE[c]	Hepatitis B	13.25 µg mL^{-1}	Electrode characterization only	[169]
3	GCE/CNT/PEI/Do[d]	NADH	3 x 10^{-6} M	Surface oxides formed from dopamine act as a redox mediator for NADH	[170]

4	Ab2-HRP/Ag/Ab1/GR-MWCNT/GCE[e]	Human IgG[f]	0.2 ng mL^{-1}	Method based on immunoassay. Labour intensive	171
5	Au/Cx5s/MCE[g]	Cocaine	0.1 µM	Near linear increase in impedance with the logarithm of cocaine concentration, (R^2 = 0.98)	172
6	Hg^{2+} specific DNA films on Au	Hg^{2+}, Pb^{2+}	1 pM, 0.1 pM	Increased admittance exhibited as the ions improve conductivity[h]	173
7	GCE	Acetaminophen	-	Linear regression of concentration *vs.* R_{ct} with R^2 = 0.9889. Claims that GCE is a good bare electrode for sensing purposes	174
8	Au-SAM[i]	*E. Coli*	-	Label-free method for the detection of *E. Coli* with appropriate control experiments	175
9	Au microelectrode arrays[j]	Cortisol	1 pM	Potential for wireless health monitoring, non-invasive and monitoring can take	176

				place when the subject is asleep	
10	Glucose oxidase on gold	Glucose	39 mg dL^{-1}	Potentially increase the sensitivity of glucose sensing for diabetes applications	[177]
11	Gold SPEs modified with a thiolated antibody	Wound infection biomarkers[k]	1.1 nM	Conducted in 'mock wound fluid'	[178]
12	InvA-gene based electrode composite	Salmonella	0.5 pM	Complex electrode fabrication involving polymerase chain reaction (PCR)	[179]
13	DNA modified gold electrode	Breast cancer gene, BRCA1	0.05 nM	Exonuclease used to cleave double stranded DNA upon the electrode surface, the leftover ssDNA used to bind to the target DNA	[180]
14	Gold electrode modified with relevant aptamer	B-estradiol (sex hormone)	2 pM	Concentration studies found a linear increase in charge transfer resistance with increasing concentration	[181]
15	ITO composite electrode[l]	Trace water in	0.65 ppm	Termed a 'microgap	[182]

		organic solvents		impedance sensor'	
16	ssDNA and gold nanoparticles on a gold electrode	Chronic lymphocytic leukemia	1 pM	Highly selective, sensitive, and fast detection towards the sequence-specific DNA for leukemia	[183]
17	Interdigiated microelectrodes coated with indium tin oxide	Salmonella	$10^2 – 10^4$ cfu mL^{-1}	Salmonella detection in milk samples	[184, 185]
18	Functionalised gold electrode[m]	Rhodopsin	10 ng mL^{-1}	Work is aimed at developing a biosensor for detection of retinal proteins	[186]
19	Conducting polymer film[n] on GC	Vitellogenin	0.42 µg L^{-1}	Authors claim their sensor can be considered as an alternative to the laborious ELISA technique	[187]
20	Gold nanoparticles and aryl diazonium salts on gold electrodes	Anti-biotin IgG	5 ng mL^{-1}	Apparent sensitive and selective platform for detection of large molecules	[188]
21	Stainless steel	Food pathogens	10^5 cfu mL^{-1}	2 electrode system utilised. Long data	[189]

				collection times	
22	Self-assembled monolayers on gold[o]	Human IgG	2 – 10 μg mL^{-1}	Impedance signal amplified by a protein – streptavidin network on the electrode surface which made the detection limits lower	[190]
23	Modified graphite electrode[p]	Amylase in saliva	-	Potential for label-free biochips according to the authors	[191]
24	Nanostructured polycarbonate substrate[q]	Der p2[r]	0.1 pg mL^{-1}	Extremely low detection limit reported	[192]
25	Pt[s]	Xanthine	0.1 mu M	The electrode was used for determination of xanthine in fish meat when in storage	[193]
26	Pt/yttria stabilized zirconia	Oxygen (partial pressures)	-	τ is inversely proportional to the pressure	[194]
27	Gold composite electrodes[t]	Cobalt ions	10^{-9} M	Highly sensitive polymeric cobalt sensors	[195]

28	Molecularly imprinted polymers	Urea/Creatine	10 ng mL^{-1} / 40 ng mL^{-1}	Good selectivity	[196]
29	$Au/SiO_2/Si$ in a PVC membrane	Zinc ions	10^{-8} M	Highly sensitive	[197]
30	Gold interdigiated electrodes upon a glass substrate	Organo-phosphorous compounds	1 pM	A potential application for the detection of these toxic class of compounds which are found in pesticides	[198]
31	Anti-C-reactive protein upon nanocrystalline diamond	C-reactive protein[u]	10 nm	Highly sensitive label-free immunosensor	[199]
32	DNA monolayers on gold.	Simeltaneous detection of lead, silver and mercury ions	10 pM, 10 nm, and 0.1 nm, respectively.	Claims to be a cost effective sensor that has been tested in lake water and calf serum	[200]
33	Propargyl-funtionalised ferrocene upon gold	Ascorbic acid	2.6 pmol L^{-1}	Sensor successfully applied to detect ascorbic acid in urine samples	[201]
34	Gold interdigitated electrodes on a glass substrate	Monoclonal mouse IgG, sarcosine, lead sulfide	pM range	Combines EIS with microfluidics	[202, 203]

35	Nanocrystalline diamond	Human IgE[v]	0.03 µg mL^{-1}	Linear relationship between capacitance and IgE concentration	204
36	Graphene oxide modified GCE	Rabbit IgG antibody	0.67 nM	Functionalisation of hydroxide groups on graphene oxide utilised to tailor electrode to specific needs	205
37	Screen-printed carbon electrodes	Gold nanoparticles	-	A method is devised to characterize the diameters of the gold nanoparticles	206
38	Gold microelectrodes functionalized with an amino thiol and carbon nanotubes	D-dimer[w]	0.1 pg mL^{-1}	Development of rapid point-of-care analysis for deep vein thrombosis	207
39	Modified gold electrode[x]	Food borne mycotoxin	0.08 ng dL^{-1}	Sensor has 30 second response time	208
40	RNA composite upon gold	Hepatitis C	~800000 IU mL^{-1}[y]	Amplification required for better detection limits	209

[a]Pty – polytyramine; Au-Pt_{NP} – gold/platinum nanoparticles. [b]Phosphoenolpyruvate carboxylase. [c]Single-walled carbon nanotube-chitosan modified pencil graphite electrode. [d]Multiwalled carbon nanotubes modified with dopamine functionalized polyethylenimine upon a glassy carbon electrode. [e]Horseradish peroxidase conjugated goat anti-human IgG (Ab2-HRP), goat anti-human IgG (Ab1), chemically reduced graphene (GR), multi walled carbon nanotube (MWCNT). [f]Human immunoglobulin. [g]Gold electrode modified with specific aptasensor for cocaine binding (Cx5s), which has been chemically thiolated to self-assemble onto the gold electrode, and subsequently treated with

mercaptoethanol (MCE). [h]An impedance sensing model seldom seen. [i]α-Mannoside self-assembled upon a gold electrode with a thiolated spacer to reduce steric hindrance. [j]Arrays modified with dithiobis (succinimidyl propionate) self-assembled monolayer. [k]Namely TREM-1 (Triggering Receptor-1 Expressed on Myeloid cells), MMP-9 (Matrix MetalloPeptidase 9), and HSL (N-3-oxo-dodecanoyl-L-HomoSerineLactone).[l]Composite consists of PDMDAAC (poly(dimethyldiallylammonium chloride)) and ferro/ferricyanide. [m]Gold electrodes are functionalized with goat IgG and an anti-rhodopsin antibody. [n]Conducting polymer film made by cycling the electrode between 0V and +1.6V in a 0.1 M solution of tetrabutylammonium perchlorate/dichloromethane with 1 mM 5,2':5'2''terthiophene-3'-carboxylic acid dissolved in. [o]Thioctic acid assembled on gold before addition of the antibody. [p]Graphite electrode is held at a fixed potential of -0.2 V in an acetate buffer containing 3-hydroxyphenylacetic acid for 60 seconds, before being held at the same potential for 60 seconds in acetate buffer containing anti- human saliva alpha-amylase (anti-HSAf) which acts as the binder for the amylase.[q]Polycarbonate mold was created using a nickel template, which was then 'sputtered' with gold to create a thin gold film upon the substrate before electrodeposition of gold nanoparticles to create a monodisperse layer. [r]Der p2 = dust mite antigen.[s] Zinc oxide nanoparticles/chitosan/MWCNT/polyanilineand xanthine oxidase upon platinum.[t]Polyvinylchloride and polymethylhydrosiloxane were the polymers used for the film, which incorporated a macro-cyclic molecule, calix-6-arene, into the structure. [u]C-reactive protein is produced in the liver and is highly prevalent when inflammation of a part of the body occurs.[210v]Human immunoglobulin E.[w]D-dimer is a molecule associated with deep vein thrombosis.[x]Gold electrode modified with 11-amino-1-undecanethiol which harbours anti-ochratoxin-A antibodies.[y]By the article's own admission, the reported units for their instrumentation are generally unknown and no conversion factors are reported. IU = international unit.

2.8 SUMMARY

Throughout the history of EIS, there have been many trials and tribulations which have prevented the technique from becoming one that can be used in industrial environments, for instance in the early 1960's the lack of advancement of electronics meant that only single frequencies could be measured in one experiment and as such experiments were cumbersome, if not vastly time consuming.[60] However, the technique has advanced to a point where it is better understood by an increasing number of scientists and further the technique has been used industrially, for example, in the case of corrosion measurements. As observed, EIS is being extensively researched for use with biological platforms and is a technique of choice for many institutions and the technique also being modified now for specific uses such as molecular binding using plasmonic-based EIS.[211] Unfortunately the technique is still not

fully understood, specifically by electrochemists (typified by the use of EIS as more of a means of supporting voltammetric evidence for electrochemical work rather than a primary technique). However, due to the wealth of information available from the use of EIS, there is no doubt that the research community will continue to use and improve their knowledge of the technique and in future it shows a great amount of potential for applications in electroanalysis (particularly as a medicinal technology) as it potentially offers a quicker and cheaper route for detection of target analytes. In particular, if impedimetric technology was applied more to SPEs, utilising the benefits of disposable sensors could be utilised to detect the diseases of, for example, HIV, gonorrhoea and MRSA, providing de-centralised clinical testing and also negating lengthy immunoassay/ELISA techniques. Critically, it is shown in Table 2.1 that EIS is a highly sensitive technique with detection limits as low as the *picomolar* range; the future use of EIS in biological applications looks highly promising.

2.9 THE NATURE OF THE WORK COVERED IN THIS THESIS

This thesis takes inspiration from the hard work conducted and presented in Chapter 2. It is apparent from the literature that EIS is more used as a qualitative method for confirmation of DNA attachment/detachment, or for investigation of an electrode composite in terms of whether the coating is conducting or insulating. Instead, this thesis contains more of a thrust towards electroanalytical applications of EIS, particularly with common carbon substrates. A problem with the research in the field is that the electrode materials are extremely complex, and this thesis will eventually go back to the basics and investigate properly the electroanalytical properties of simple screen-printed carbon electrodes, due to their inherent advantages which were discussed in Chapter 1.19.

Additionally there will be an emphasis towards carbon materials for electrochemical applications, because though the field is understanding carbons more each day, there are still areas which need focussing upon, such as the applied electrochemistry of pristine graphene and oxygenated graphenes such as Q-Graphene^{TM} and graphene oxide. This thesis therefore explores the application of pristine graphenes and oxygenated graphenes towards common electroactive analytes, and explores the impedimetric responses of such carbon modifications cast upon carbon macroelectrodes.

The penultimate Chapter is dedicated to exploring the medicinal benefits of SPEs, the inspiration of which was taken from the economic and portability benefits of SPEs, which can be exploited for point-of-care technologies. Such electrochemical protocols for these applied circumstances will be qualified using robust lab-based techniques such as UV/Vis spectrophotometry and High Performance Liquid Chromatography (HPLC).

The final chapter will focus upon characterising the equipment and electrodes utilising EIS. This Chapter represents an entirely fundamental perspective and builds upon previous knowledge regarding SPEs and carbon nanomaterials; thus satisfying the thesis title "The Frequency-Dependent Properties of Screen-Printed Electrodes and Carbon Nanomaterial Electrodes".

This thesis focusses upon three major topics: the use of carbon materials as electrode composites; the use of Screen-Printed Electrodes (SPEs) for electroanalytical applications; and finally the application of Electrochemical Impedance Spectroscopy (EIS) to SPEs, with an extra focus upon the electroanalytical benefits of EIS. Many techniques are benchmarked against analytical techniques such as High Performance Liquid Chromatography (HPLC), and UV/Vis spectrophotometry. In this Chapter, which contains published work,[17, 18, 212] the use of carbon materials as electrode composites is explored, by observing electron transfer reactions typical of DNA bases, oxygen, and redox probes such as potassium ferrocyanide (II) and hexamine-ruthenium (III) chloride.

EXPERIMENTAL

All chemicals used, unless otherwise stated, were of analytical grade and were used as received without any further purification and were obtained from Sigma-Aldrich. All solutions were prepared with deionised water of resistivity not less than 18.2 MΩ cm and were rigorously degassed with high purity, oxygen-free nitrogen prior to electrochemical measurements.

Voltammetric measurements were carried out using a Palmsens (Palm Instruments BV, The Netherlands) potentiostat. All measurements were conducted using a three electrode system. The EPPG working electrode (Le Carbone, Ltd. Sussex, UK) was machined into a 4.9 mm diameter, with the disc face parallel with the edge plane as required from a slab of HOPG (highest grade available: SPI-1, equivalent to Union Carbide's ZYA grade); alternatively, the BPPG working electrode (Le Carbone, Ltd. Sussex, UK) was machined as above, but with the disc face parallel to the basal plane as required. A platinum wire and a

Saturated Calomel Electrode (SCE) were used as the auxiliary and reference electrodes, respectively.

The pristine graphene was commercially obtained from 'Graphene Supermarket' (Reading, MA, USA), and is known as 'Pristine Graphene Monolayer Flakes', comprising entirely of pristine graphene platelets dispersed in ethanol (solution was 1 μg mL^{-1}) that have not been oxidised, reduced, or chemically modified in any way and are free from surfactants. The graphene was synthesized *via* the substrate-free gas phase method, as previously reported,[213-215] and are sonicated in ethanol to form a homogeneous suspension before being dispatched.[215] The graphene has been previously characterised independently; the TEM images depicted in Figure 3.1 show the graphene to be a hexagonal lattice and very highly ordered, with an average flake thickness of 0.35 nm (1 monolayer) with an average particle (lateral) size of 550 nm (150-3000 nm).

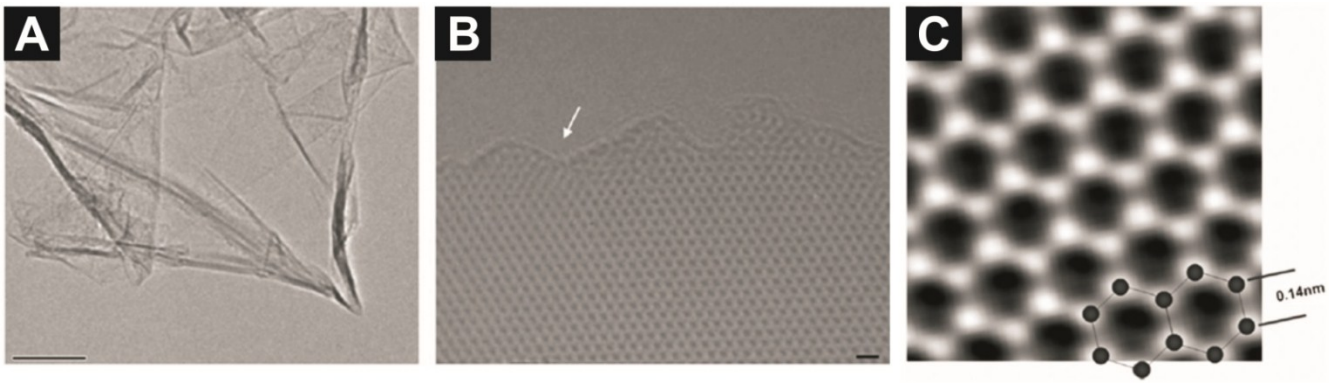

*Figure 3.1: **A**: a low magnification TEM image of the graphene sheets; the scale bar is 100 nm. **B**: a high-resolution TEM image, where the white arrow indicates the edge of the graphene sheet; the scale bar is 4 Å. **C**: an atomic resolution image of a clean and structurally perfect synthesised graphene sheet. Individual carbon atoms appear white in the image. The image was obtained through the reconstruction of the electron exit wave function from 15 lattice images using MacTempas software. Images courtesy of Reference 216.*

XPS chemical analyses for pristine graphene were performed with a VG-Microtech Multilab electron spectrometer and revealed the material to comprise of 95.04 % atomic carbon and 4.96 % atomic oxygen; the low O/C ratio indicates near true graphene. The graphite utilised was 99.99 % synthetic graphite powder obtained from Sigma Aldrich, with a particle diameter of < 150 μm. The graphite particles were suspended in a solution of 50:50 water and ethanol; to a concentration of 1 μg mL^{-1} - the same concentration as the commercially received graphene solution. The electrodes were modified with graphene/graphite by pipetting aliquots of the relevant amount of solution on the surface of the electrode, followed by drying in an oven at a temperature of 50 ºC for 5 minutes. The electrodes were cooled to room temperature before experiments were run.

Q-Graphene powder was commercially obtained from Graphene Supermarket (Reading, MA, USA) and was suspended in a mixture of water:ethanol (50:50) at 1 μg mL^{-1} prior to the modification electrode surfaces. Q-Graphene is synthesised, as reported by the suppliers, *via* a Chemical Vapour Deposition (CVD) method in the presence of a catalyst; the exact details are proprietary information. The company's description of the material is provided: *"This nanomaterial (which exhibits a large surface area of ca. 55 m^2 g^{-1}) consists of hollow, porous, multi-wall carbon nanospheres or polyhedral structures with a narrow size distribution, an average particle size of approximately 80 nm, and an average aspect ratio close to 7:5. Such structures are also referred to as carbon Q-dots or nano-onions, which are close relatives of fullerenes."*

XPS (K-Alpha, Thermo Scientific) was used to analyse the filter surface. The XPS procedure and Raman analysis for Q-Graphene were outsourced to the University of Alicante, who also provided the following experimental details: "*All spectra were collected using Al-K radiation (1486.6 eV), monochromatised by a twin crystal monochromator, yielding a focused X-ray spot with a diameter of 400 μm, at 3 mA × 12 kV. The alpha*

hemispherical analyser was operated in the constant energy mode with survey scan pass energies of 200 eV to measure the whole energy band and 50 eV in a narrow scan to selectively measure the particular elements. Thus, XPS was used to provide the chemical bonding state as well as the elemental composition of the filter surface. Charge compensation was achieved with the system flood gun that provides low energy electrons and low energy argon ions from a single source. SEM images and elemental analysis were obtained with a JEOL JSM-840 model and the TEM images were obtained with a JEOL JEM-2010 equipped with an X-ray detector for the EDS microanalysis from OXFORD, INCA Energy TEM 100. For XPS analysis the Q-Graphene was used as-received from the supplier and for the Raman spectroscopy the Q-Graphene samples were deposited on SiO_2/Si. A few 'flakes' of Q-graphene were transferred onto the quartz slide Si/SiO_2 substrate with a thickness of 300 nm SiO_2 on Si. Raman spectra were recorded using Jasco confocal microscope (X100 objective) spectrometer with a 532 nm excitation wavelength, at a very low laser power level (1.25 mW) to avoid any heating effects."

Electrodes were modified using the drop-casting technique (see Section 1.18). Appropriate control experiments were performed in terms of ethanol modified electrodes for the purpose of ensuring that the electrochemical responses obtained were not a result of the solvents utilised; such control experiments revealed that ethanol has no effect upon the responses observed.

The adenine and guanine solutions were prepared according to previous literature reports.[218, 219] A 0.5 mM stock solution of adenine was prepared in pH 7.2 PBS (50 mM KH_2PO_4, 50 mM K_2HPO_4 and 0.1 M KCl) and kept below 5 ºC in the dark. The guanine solution was prepared by saturating pH 7.2 PBS (50 mM KH_2PO_4, 50 mM K_2HPO_4 and 0.1 M KCl) with guanine and subjecting to vigorous stirring using a vortex for 2 minutes. The solution was cooled below 5ºC then filtered to remove excess guanine. UV/Vis

spectrophotometry confirmed the guanine concentration to be ~19 μM (using data from UV/Vis Atlas.[220]). The salicylic acid was made up in pH 5 PBS and to a concentration of 0.5 mM. Redox probes (potassium ferrocyanide, hexamine-ruthenium (III) chloride, potassium hexachloroiridate) were made up in pH 7.4 PBS with 0.1 M KCl background electrolyte. Biologically relevant analytes were made up to a concentration of 1 mM with 0.1 M KCl background electrolyte. The sulphuric acid solution utilised was of the highest possible grade available from Sigma-Aldrich (99.999 %, double distilled for trace metal analysis) and was used at a concentration of 0.1 M. To oxygenate the solution, the solution was subject to rigorous bubbling of 100 % medicinal grade oxygen through a small volume of the solution for 45 minutes, assuming this to be a completely saturated solution at room temperature as described by Gara and Compton.[221] The electrochemical cell was closed with Parafilm™ during testing to reduce exposure to air, preventing loss of oxygen from the sample. Furthermore, the cell was continuously bubbled with oxygen between voltammetric measurements.

3.1 ELECTROCHEMICAL OXIDATION OF DNA BASES USING GRAPHENE-MODIFIED ELECTRODES

3.1.1 INTRODUCTION

Following the reported unique electronic properties of graphene in 2004,[222] many beneficial reports emerged describing its unique electrochemical properties which could hold potential applications in a myriad of areas, including supercapacitors,[223] batteries,[224] fuel cells[225] and biosensors for molecules such as ascorbic acid,[226, 227] uric acid,[226, 228] dopamine,[226, 229] acetaminophen,[230] and DNA bases.[231, 232] Yet independent literature reports from Pumera[233] and Brownson[234] suggest that graphene may not be such a beneficial electrode material as first thought. Pumera *et al.* reported that single-, few- and multi-layer graphene offer no significant advantage over graphite for the detection of uric acid in terms of sensitivity,[233] whilst the work of Brownson[234] proves that graphene exhibits slow electron transfer kinetics due to its low proportion of edge plane sites.

DNA bases are interesting electroactive target molecules which require fast and non-invasive detection methods. One commonly employed strategy is the label-free electro-oxidation of target bases following hybridization, using methods such as Cyclic Voltammetry (CV), Differential Pulse Voltammetry (DPV) or Square Wave Voltammetry (SWV). In this pursuit, a variety of electrode substrates have been explored such as mercury[235], metallic[218, 236] and a variety of carbon electrodes including carbon SPEs[237] and carbon nanotube modified electrodes.[238, 239] Tomschik *et al.*[235] report adenine and cytosine exhibiting reduction waves at a mercury hanging drop electrode. This work also reports adsorptive components of the waves, as does Compton *et al.*[218, 219] whose papers focus upon various types of graphitic

electrodes. SPEs have also been utilised in the sensing of DNA bases by Hart *et al.*[237] who report that SPEs can be utilised effectively for the electrochemical sensing of both adenine and guanine dissolved in aqueous alkaline solutions.[237] In addition to the above examples, carbon nanotube modified graphitic electrodes have been shown to increase the peak currents towards guanine[238, 239] compared to the bare underlying electrode, which is consistent with the nanotubes having a greater density of edge plane sites, coupled with the basal-like walls of the carbon nanotubes, which according to Compton *et al.* combine to give an improved electrochemical response towards guanine.[219]

The possibility that graphene may improve DNA base detection methods followed. Dong *et al.*[231] utilised graphene modified Glassy Carbon (GC) electrodes to detect short oligomers with known base sequences quickly and effectively without the need for chemical labelling or hybridization. Their paper[231] elegantly demonstrates that a chemically reduced graphene oxide film immobilized upon a GC electrode exhibits larger and sharper peak currents compared to both bare GC and graphite modified GC electrodes using DPV. Another paper by Dubuisson *et al.* [240] reports that epitaxially grown graphene on silica enhances the peak currents compared to that of Highly Ordered Pyrolytic Graphite (HOPG). Pumera *et al.*[241] also explored the electrochemical detection of DNA bases utilising graphene, reporting that graphene modified electrodes exhibit an improved electrochemical response over electrodes such as GC, Edge Plane Pyrolytic Graphite (EPPG), multi-walled carbon nanotubes and graphite modified GC electrodes. It has been reported that for adenine, the density of edge plane sites are critical with an EPPG electrode exhibiting the highest peak current.[218] Conversely for guanine, there are two dominating and controlling factors: the density of edge plane sites required for electrochemical oxidation; and the density of basal plane sites at which guanine may adsorb.[219] Husale *et al*. independently investigated graphene

adsorptive properties, reporting that ssDNA selectively adsorbs onto the basal sites of graphene *via* a π-π stacking mechanism.[242]

The origin of the apparent electrocatalysis observed using graphene-related electrode composites was the subject of much scrutiny by the scientific field prior to this work. There were numerous reports claiming graphene-based composites were catalysing electrochemical reactions due to its high level of conductivity. However it is now known that this was not the case, and electrocatalytic observations were linked to other chemicals, such as metal ions or surfactants intercalated within graphene sheets.[243] Intuitively, graphene should not catalyse electrochemical reactions because the majority of the structure is essentially a graphite basal plane, leaving a small amount of edge planes for electron transfer.[234, 244] However, the basal plane of graphene has shown to exhibit adsorptive properties, in the shape of π-π interactions.[245-247] As a consequence of the structure of graphene, one can intuitively expect the electrochemical oxidation of guanine to display some unusual characteristics, given the high proportion of basal sites available for adsorption of the DNA base. This section explores the electrochemical oxidation of adenine and guanine using commercially available graphene which is free from surfactants and was not previously been explored towards these highly important target analytes as of 2011.

3.1.2 RESULTS AND DISCUSSION

ELECTROCHEMICAL OXIDATION OF ADENINE

This section focusses upon the electrochemical oxidation of adenine and guanine, the structures of which are given in Figure 3.2.

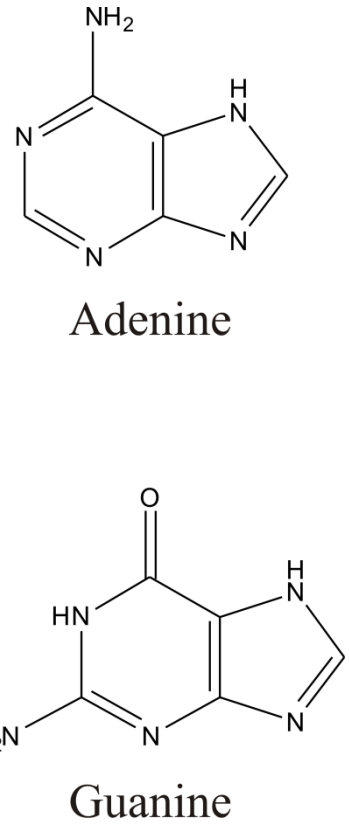

Figure 3.2: Chemical structures of adenine and guanine.

The electrochemical oxidation of 0.1 mM adenine in pH 7.2 PBS using EPPG and BPPG electrodes is first considered. Figure 3.3 displays typical voltammetric profiles where a

large sharp peak is observed at +0.95 V (*vs*. SCE) at the EPPG electrode, while at the BPPG electrode the voltammetric peak occurs at +1.03 V (*vs*. SCE). Both electrochemical responses are in excellent agreement with independent literature reports[218, 248] where it has been reported that the density of edge plane sites upon the electrode surface greatly influence the electrochemical response of adenine.[218]

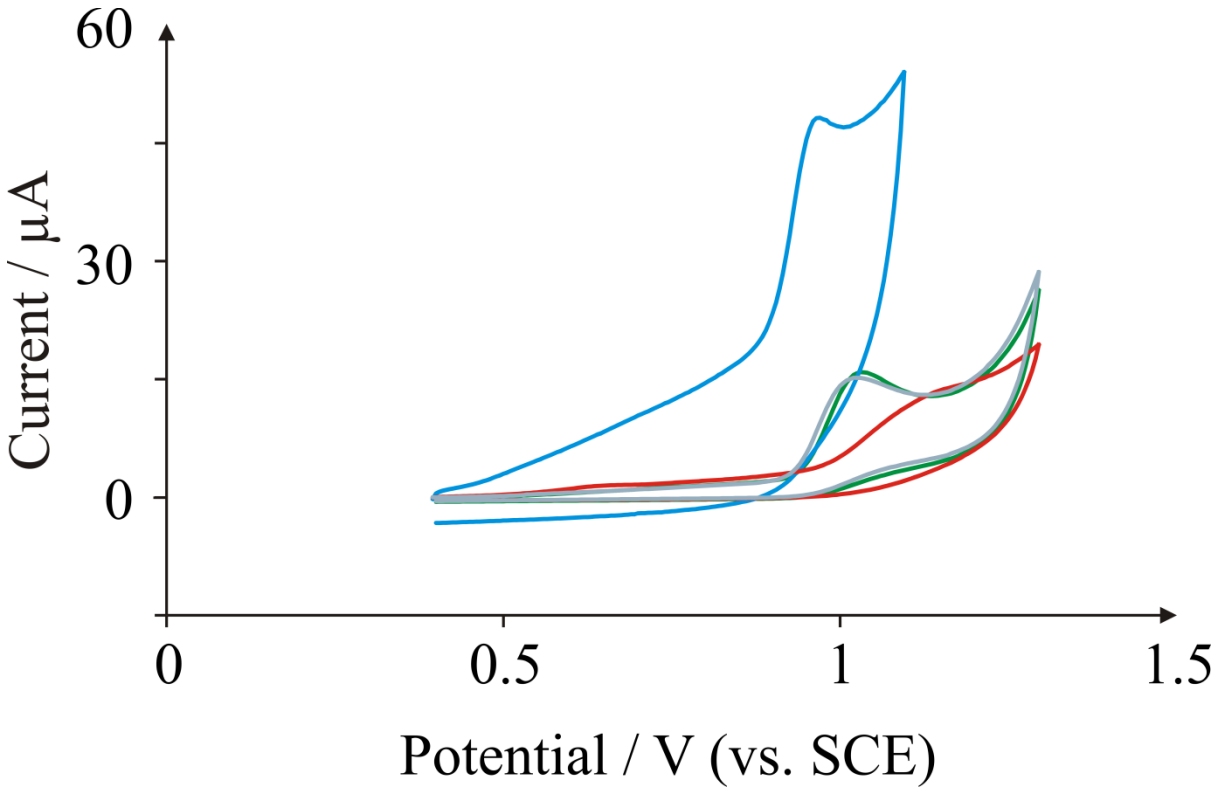

Figure 3.3: Cyclic voltammetric response arising from the electrochemical oxidation of 0.1 mM adenine in pH 7.2 PBS at various electrode substrates: EPPG (blue line); BPPG (green line); 10 ng surfactant-free graphene modified BPPG (red line); and 10 ng graphite modified BPPG (grey line). Scan rate: 50 mV s^{-1}.

Attention was turned to exploring the electrochemical response of adenine utilising the commercially received graphene, and for comparative purposes, graphite. Figure 3.3 depicts a typical voltammetric profile from the immobilisation of graphene upon a BPPG electrode, where in comparison to the supporting underlying BPPG electrode, a shift to

higher oxidation potentials is observed for the case of graphene to *ca.* +1.20 V (*vs*. SCE), and also a vast broadening of the peak is observed. For comparative purposes, the response of a graphite modified BPPG electrode towards the electrochemical oxidation of adenine was explored, where as shown in Figure 3.3, a small reduction in the oxidation potential from introducing graphite is evident compared to graphene and BPPG. It is known that the electrochemical oxidation of adenine is highly dependent on the density of edge-plane-like sites/defects,[218] and thus the underlying BPPG electrode has a low edge plane site density and therefore a response at higher oxidation potentials is observed compared to EPPG. It therefore comes as no surprise that the oxidation potentials are reduced upon the introduction of graphite to the BPPG electrode surface, since the former has a high density of edge plane sites.

The effect of pH on the electrochemical oxidation of adenine was next explored. Using 10 ng graphene immobilised upon a BPPG electrode, the effect of changing the solution pH upon the voltammetric response was investigated. Figure 3.4 depicts the observed cyclic voltammetric response with analysis of the peak potential arising from the electrochemical oxidation of adenine as a function of solution pH displayed inset in Figure 3.4.

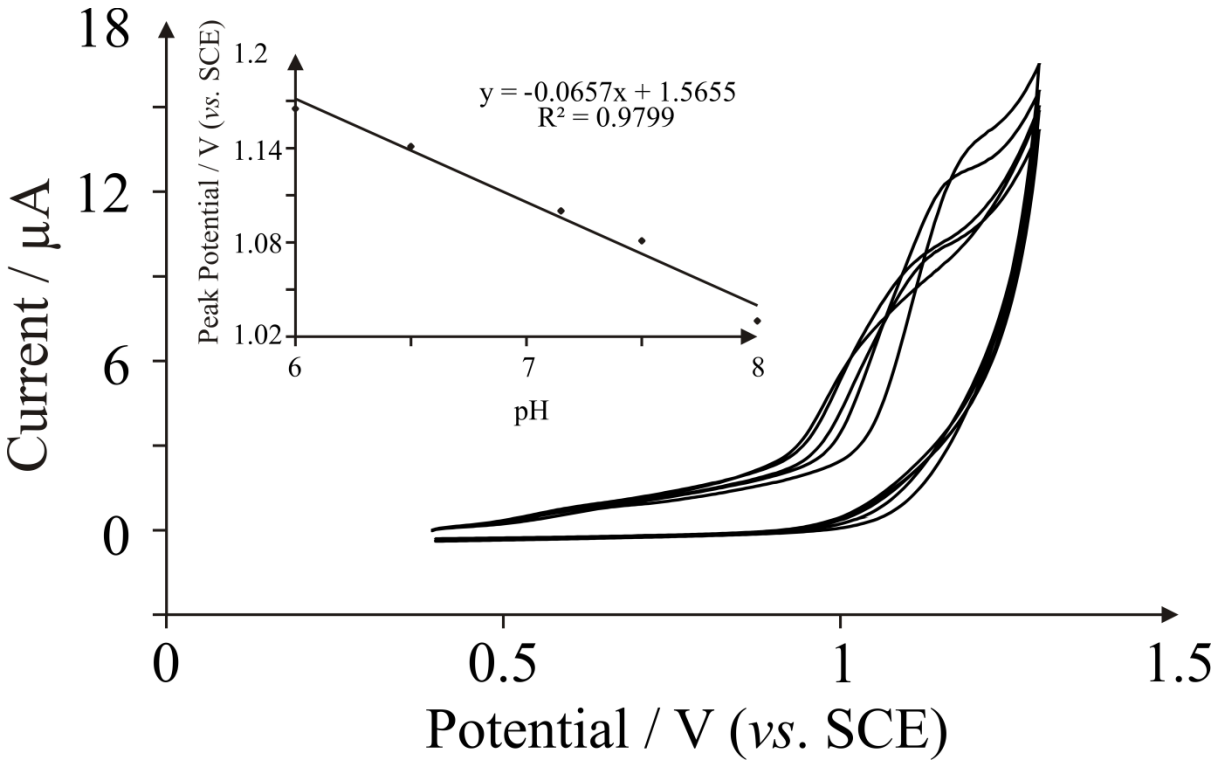

Figure 3.4: Cyclic voltammetric responses arising from the electrochemical oxidation of 0.1 mM adenine, with respect to changes in pH, using a 10 ng surfactant-free graphene modified BPPG electrode. Inset, analysis of observed peak potential as a function of the solution pH which yields a linear response with a gradient corresponding to ~66 mV. Scan rate: 50 mV s^{-1}.

A linear shift in the peak potential with respect to increasing pH is found to exhibit a gradient of 66 mV, indicating an overall equal proton and electron transfer. This is in strong agreement with independent literature reports conducted utilising bare EPPG electrodes which yielded a gradient of 58 mV;[218] the slight discrepancy attributed to problems with reproducibility of the graphene electrodes. The electrochemical oxidation of adenine at graphitic electrode substrates is reported to be an overall process involving 6 protons and 6 electrodes with irreversible chemical steps.[218] The observed shift in peak potential as a function of pH at the graphene modified electrode suggests that for the oxidation of adenine, the number of protons and electrons transferred prior to the chemically irreversible step is equal, which is identical to that observed on EPPG electrodes,[218] suggesting no difference in the electrochemical mechanism is observed when using graphene.

Figure 3.5 depicts the effect of graphene coverage supported upon a BPPG electrode and for comparative purposes, the effect of increasing amounts of graphite. As depicted in Figure 3.5A, additions of graphene result in the voltammetric oxidation peak shifting to higher potentials, where, upon the modification of 20 ng graphene, the oxidation peak is observed at +1.20 V (*vs*. SCE) as opposed to +1.03 V (*vs*. SCE) observed at bare BPPG in Figure 3.3. Analysis of the voltammetric peak current, as shown in Figure 3.5B, changes upon the addition of graphene and graphite on the electrode surface. The peak current decreases from *ca.* 9 μA at a bare BPPG electrode to *ca.* 1 μA at a BPPG electrode modified with 20 ng graphene. The % RSD (N = 5) observed at the bare BPPG was found to be 22 %, inferring that the detection of adenine even with a non-graphene modified BPPG electrode is analytically unacceptable. The % RSD (N = 5) for the modifications with graphene are as follows: 7.5 % for 5 ng modification; 19 % for 10 ng modification; and 32 % for 20 ng modification. Interestingly, the addition of graphite upon a BPPG surface enhances the observed average peak currents, which is consistent with the increase in edge plane density at the electrode surface. The peaks are sharper and less broad for the graphite modified electrodes, which is attributed to the larger amount of edge plane sites at the electrode surface which graphite offers compared to bare BPPG. Graphite modified electrodes yield very good analytical reproducibility, as shown in Figure 3B, and surprisingly the % RSD measurements (N = 5) taken for graphite are far lower than bare BPPG: 22 % for bare BPPG; 4.5 % for 5 ng; 6 % for 10 ng; and 3.5 % for 20 ng. In summary, the graphite modified BPPG electrode was found to be the most useful electrode for the effective electrochemical detection of adenine.

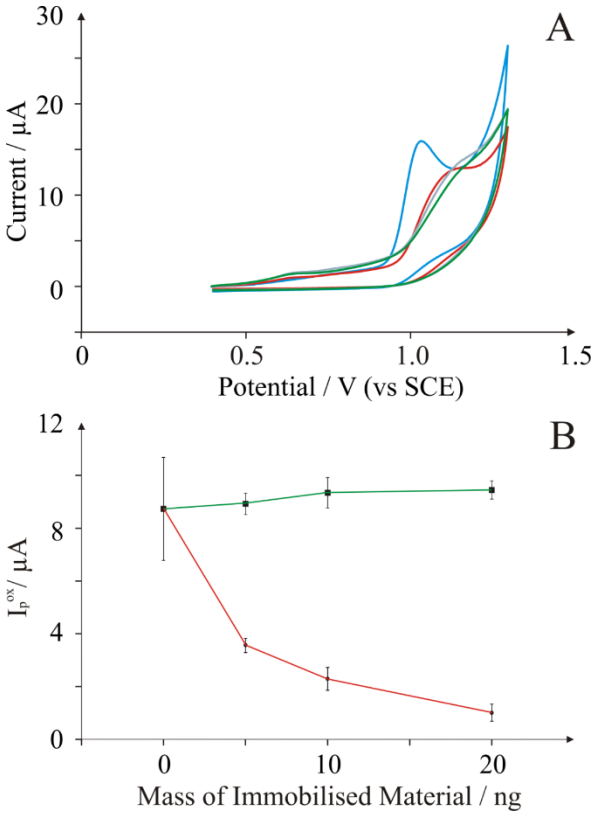

*Figure 3.5: **A**: Cyclic voltammetric responses resulting from the electrochemical oxidation of 0.1 mM adenine in pH 7.2 PBS utilising: (blue line) bare BPPG; (red line) BPPG modified with 5 ng surfactant-free graphene; (grey line) BPPG modified with 10 ng surfactant-free graphene; and (green line) BPPG modified with 20 ng surfactant-free graphene. All scan rates are 50 mV s^{-1}.*

***B**: Observed voltammetric peak current as a function of the increasing amount of immobilised material for: (green line) graphite modified BPPG and (red line) graphene modified BPPG. The error bars quoted are the standard deviations calculated (N = 5).*

It is known that graphene is anisotropic with respect to electron transfer such that basal sites exhibit slow electron transfer, while its edge plane sites exhibit fast electron transfer,[234, 244] and it has been proposed that graphene stacks upon a BPPG surface in a non-covalent π-π fashion.[234] Additionally it has been reported that adenine is significantly influenced by the density of edge plane sites,[218] that is, solely its electronic structure rather than contribution from oxygenated species. Thus it is likely that the immobilised graphene orientates parallel to the underlying electrode surface in a manner in which the basal planes

of the graphene are exposed, rather than the edge planes. Consequently the overall percentage of edge plane sites on the modified electrode surface are low,[234] which accounts for the poor voltammetry (increased overpotentials; broadening of peaks) observed in the case of graphene modified electrodes. Interestingly this response is quite different to that observed by Goh and Pumera[249] who report that graphene modified electrodes exhibit an improved response compared to the underlying graphitic electrode substrate. The graphene used in that study is fabricated using surfactants where the latter might contribute to the observed response, rather than the graphene itself as reported in other cases.[250]

ELECTROCHEMICAL OXIDATION OF GUANINE

The electrochemical oxidation of 19 μM guanine in pH 7.2 PBS was next considered using EPPG and BPPG electrodes which were immersed in guanine solution for one minute prior to measurement, as recommended in previous studies.[219] Typical voltammetric responses obtained for the electrochemical oxidation of guanine at various electrode substrates are displayed in Figure 4A; where the resultant potential due to the oxidation of guanine is +0.73 V (*vs*. SCE) for bare BPPG. The observed potential at a bare BPPG electrode is in strong agreement with Compton *et al.*[219] Upon increasing the accumulation time to 30 minutes, the peak potential with a BPPG electrode remained the same, while the peak potential resulting from the electrochemical oxidation of guanine with a graphene modified BPPG decreased by 15 mV. However, the peak current resulting from the electrochemical oxidation of guanine increased with bare BPPG, while with a graphene modified BPPG electrode, the peak current decreased.

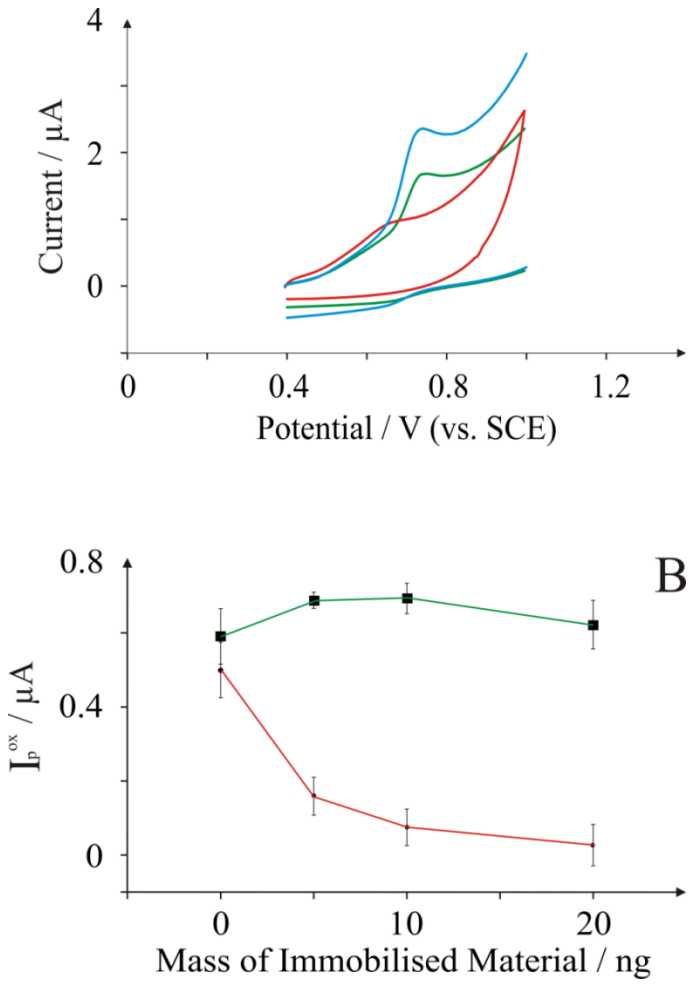

Figure 3.6: ***A:*** *Cyclic voltammetric response resulting from the electrochemical oxidation of 19 µM guanine in pH 7.2 PBS utilising: bare BPPG (green line); BPPG modified with 5 ng surfactant-free graphene (red line); and BPPG modified with 5 ng graphite (blue line).*

B: *Observed voltammetric peak current (I_P) as a function of the increasing mass of immobilised material for: (green line) graphite modified BPPG; and (red line) graphene modified BPPG. The error bars quoted are the standard deviations calculated (N = 5).*

Attention was then turned to exploring the electrochemical response of guanine at graphene modified electrodes. Figure 3.6A also compares a graphene modified electrode with a bare BPPG electrode and careful inspection reveals a reduction in the oxidation potential from +0.73 V (*vs*. SCE) observed at a BPPG electrode to +0.64 V (*vs*. SCE) following the modification with 5 ng surfactant-free graphene; note however that the voltammetric peak is

greatly reduced. Figure 3.6B shows the effect of increasing the amounts of graphene where a reduction in the voltammetric peak height is evident, yet the voltammetric potential was not observed to change. Authoritative work by Compton[219] has demonstrated that there are two dominating and controlling factors present contributing to the electrochemical response of guanine upon graphitic surfaces: one being the proportion of basal sites for guanine adsorption; and the second being the edge plane sites available for electrochemical oxidation.[219] It is reasonable to assume that this is the case for graphene on the electrode surface, such that the large proportion of basal sites promotes adsorption of guanine but unfortunately the proportion of edge plane sites required for electron transfer is low, due to graphene's unique structure, giving the voltammetry observed in Figure 3.6.

The effect of pH on the electrochemical oxidation of guanine was next explored. Using 10 ng graphene immobilized upon a BPPG electrode, the effect of changing the solution pH upon the voltammetric potential corresponding to the electrochemical oxidation of guanine was investigated. Analysis of peak potential *versus* solution pH displayed a linear shift in peak potential with respect to increasing pH, exhibiting a gradient of 55 mV. This observation suggests an equal proton and electron transfer, similar to the case for adenine. This value is in excellent agreement with independent reports by Hart *et al.*[237] and Compton *et al.*[219] The effect of scan rate was also explored using the graphene modified electrode where a plot of peak current as a function of the square root of scan rate was constructed, where a vaguely linear response was observed at slow scan rates with deviation at higher scan rates. In this case, the reproducibility exhibited by graphene is a key issue that likely inhibits reliable mechanistic information to be derived in the case of adenine and guanine.

In addition to the reduction in peak potentials using graphene modified electrodes, the peak currents decrease about tenfold from *ca.* 0.5 μA at a bare BPPG electrode to *ca.* 0.05 μA at a 20 ng surfactant-free graphene modified BPPG electrode, and are presented in Figure

3.6B. Noticeably for graphite, the opposite trend is observed. As shown in Figure 3.6B, the observed error bars are larger than for adenine, and the % RSD values (bare BPPG 13 %; 5 ng modification 16 %; 10 ng modification 34 %; 20 ng modification 38 %) are far larger than what would be analytically acceptable (typically less than 5 %). As is also seen for adenine, the peak current observed increases with increasing amount of graphite immobilised on the electrode surface. The % RSD measurements yield largely unacceptable reproducibility: 13 % for bare BPPG; 3 % for 5 ng graphite; 6 % for 10 ng graphite; and 10.5 % for 20 ng graphite. Previous literature utilising graphene containing surfactants fails to report the reproducibility of the electrode modification towards adenine and guanine,[249] thus comparisons of sensitivity utilising surfactant containing graphene cannot be made.

3.1.3 SUMMARY

This section has investigated the use of commercially available surfactant-free graphene towards the electrochemical detection of the DNA bases adenine and guanine. It has been shown that in the case of adenine, the introduction of graphene on a BPPG electrode surface increases the peak potential observed in the electrochemical oxidation compared to the peak observed at a bare BPPG electrode, and additionally reduces the magnitude of the voltammetric peak current compared to the bare underlying BPPG electrode. Also for adenine, it is demonstrated that the electron transfer mechanism for the electrochemical oxidation of adenine remains unchanged upon the introduction of graphene to a bare BPPG surface.

In stark contrast to the findings for adenine, it is found that the introduction of graphene on a BPPG surface *reduces* the observed peak potential resulting from the electrochemical oxidation of guanine, compared to that observed at a bare BPPG electrode.

This is attributed to the large amount of basal sites that graphene offers for the effective adsorption of guanine towards the electrode surface. Conversely, the peak currents are found to decrease upon the addition of graphene at a BPPG electrode surface, which leads to the conclusion that graphene offers very little in the way of edge plane sites which are reported to be required for the efficient electron transfer at graphitic electrode surfaces. In comparison to a recent literature report[241] using double, few and multi- layer graphene modified electrodes towards the sensing of adenine and guanine, it was observed that, for guanine, the analytical sensitivity (slope of a current response *versus* concentration plot) was found to occur in the order: few layer > double layer > mutli-layer. It can be surmised that in that study, the adsorption of guanine upon the basal plane sites of graphene also occurs, where the amount of edge plane sites giving rise to the observed (analytical) order such that double layer graphene exhibits a response which is improved by the few layer graphene, where there is a greater proportion of edge plane sites available over the former giving rise to an improved analytical response.

In the case of the surfactant free commerically available graphene, critically, a poor level of reproducibilty is observed when using graphene modified electrodes towards the electrochemical sensing of adenine and guanine, but interestingly an acceptable level of reproducibility is observed when using graphite modified electrodes. The use of this particular type of graphene is questionable as an electrode material for the sensing of DNA bases; such observations will benefit those constructing sensors for the electrochemical detection of DNA damage.

3.2 DO KNOWN ADSORPTIVE AROMATIC COMPOUNDS OFFER REDUCED OXIDATION POTENTIALS?

Probably the most intriguing point from the previous section is the notion that the adsorptive properties of graphene have a unique effect upon the direct electrochemistry of guanine. Therefore, one must consider whether other electroactive aromatic compounds are influenced in a similar way. This section briefly explores salicylic acid, to determine whether this is the case. If graphene does indeed display reduction in oxidation potentials, it could open up an avenue for uniquely tailored electrochemical sensors.

3.2.1 INTRODUCTION

If *any* aromatic ring adsorbs to the basal plane of graphene sheets, then one can simply find an electroactive substance with preferably one aromatic ring and test to see whether the peak potential changes after application of graphene to the electrode surface. Therefore Salicylic Acid (SA) was chosen as a model analyte for this purpose, because it is a relatively simple electroactive aromatic phenolic acid which is widely used in organic synthesis and is analogous to the active ingredient in aspirin, acetylsalicylic acid. It is a plant hormone which is also used as anti-acne treatments. It is produced synthetically *via* oxidation of phenol using carbon dioxide and sodium hydroxide, the intermediate of which is ‘’worked up’’ with sulphuric acid to produce the product. SA has many known medicinal benefits, including anti-inflammatory properties, relief of aches and pains, and as a treatment for ulcers. However as with most medicines it can also cause death if consumed in high dosage. The structure of SA is given in Figure 3.7.

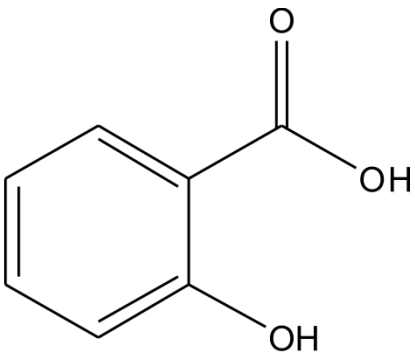

Salicylic acid

Figure 3.7: Chemical structure of SA.

Current methods of detection of SA include chemiluminescence[251-253] and HPLC,[254-256] both of which are time consuming methods which require sample extraction and transport to a lab. Determination utilising electrochemical methods could provide a quick and cheap method of analysis in hospitals for instance, and therefore this section utilises the known adsorption properties of SA[257-259] to determine the electrochemical oxidation potentials when utilising graphene modified electrodes compared to EPPG and BPPG carbon electrodes.

3.2.2 RESULTS AND DISCUSSION

First considered is the electrochemical oxidation of SA utilising bare EPPG and BPPG electrodes. Figure 3.8 depicts the electrochemical oxidation of SA in pH 5 PBS, utilising bare EPPG and BPPG electrodes. The striking observation from Figure 3.8 is that the oxidation potential for both the EPPG and the BPPG electrode is similar; +1.05 V for the former and +1.03 V (*vs*. SCE) for the latter. This would suggest that, in the case of SA, the density of states is not a governing factor in the electron transfer.

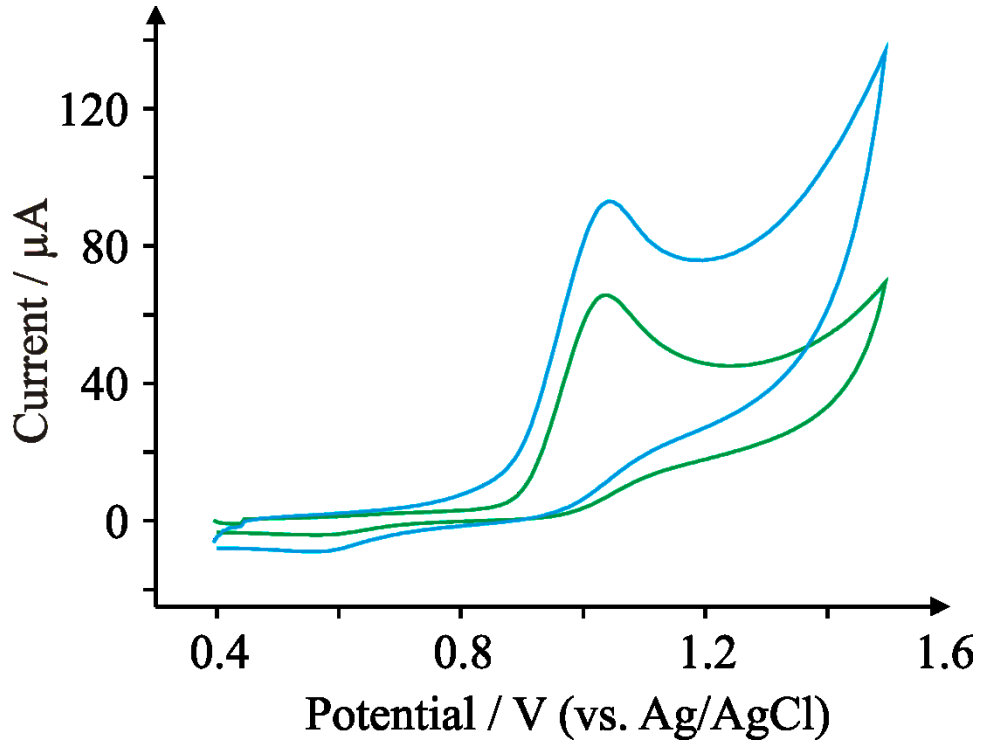

Figure 3.8: Cyclic voltammetric profiles typical of 1 mM SA in pH 7.4 PBS using a bare EPPG electrode (blue line) and a BPPG electrode (green line). Scan rate: 50 mV s^{-1}.

From Figure 3.8 it would appear that the density of basal planes available for adsorption has little effect upon the oxidation potential as the oxidation potentials for both EPPG and BPPG are the same. Similarly, the number of edge planes available for electron transfer has little effect upon the oxidation potential. It is likely that in the case of SA, the number of edge planes required for efficient electron transfer is significantly low, to a point where a BPPG electrode surface has enough point defects and grain boundaries to give a response typical of an EPPG electrode. Previous studies utilising glassy carbon electrodes have independently shown the electrochemical oxidation of SA to occur at +1.14 V (*vs*. Ag/AgCl) by Torriero *et al*. in pH 2.38 Britton-Robinson buffer solution,[260] and +0.845 V (*vs*. SCE) at a graphite electrode by Suatoni *et al*.[261] Furthermore, the peak currents observed at both BPPG and EPPG profoundly surpass what is observed at a GC electrode at the same scan rate; 200 mV s^{-1}.

Attention was next turned to the electrochemical oxidation of SA utilising graphene modified electrodes. As SA has been shown in previous literature to adsorb onto basal planes, an introduction of graphene onto the electrode surface will theoretically provide an increased amount of basal sites available for the adsorption of SA. Figure 3.9 compares the electrochemical response of SA on both graphene modified EPPG and BPPG electrodes.

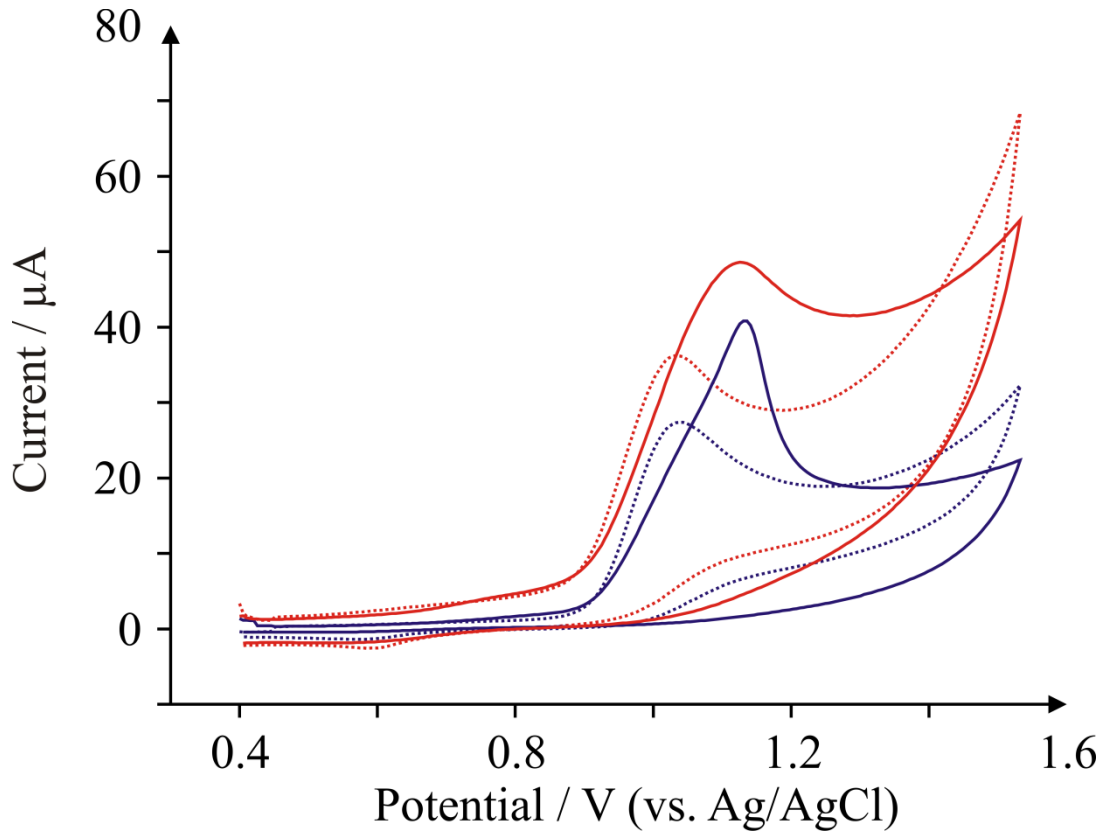

Figure 3.9: Cyclic voltammetric profiles typical of 1 mM SA in pH 7.4 PBS using a 20 ng pristine graphene covered EPPG (red line) and BPPG (purple line) electrode. The dotted lines represent the bare electrode responses. Scan rate: 50 mV s^{-1}.

A small increase in the peak potential is observed for the case of a graphene modified EPPG electrode, where the potential increases from +1.03 V to +1.08 V (*vs*. SCE). Such an increase in peak potential is unfortunately too small to consider further. The wave observed for the case of BPPG is sharper and looks more like a stripping mechanism, potentially suggesting

that SA is not oxidised *per se* by the graphene, but the high potential forces any adsorbed material to be stripped from the surface, producing the sharp drop in current as seen in Figure 3.9. The peak potential itself doesn't change significantly and thus the case is not the same as observed for guanine. In terms of the mechanism, SA oxidises upon the electrode *via* a 1 proton 1 electron mechanism,[262] which in this case is aided by adsorption.

However, the exciting part of this work is that the graphene appears to induce adsorption of the SA; something which is known in the literature. The ''texture'' of the surface is thought to be paramount to the relative adsorption of SA and therefore one might expect increased adsorption with increased graphene coverage given that there would be an increase in surface defects providing the so-called ''texture''.[263] Thus, the next thing considered was the coverage of graphene upon the observed electrochemical response. Figure 3.10 depicts the observed change in peak oxidation current with respect to the global coverage of graphene upon a BPPG electrode surface.

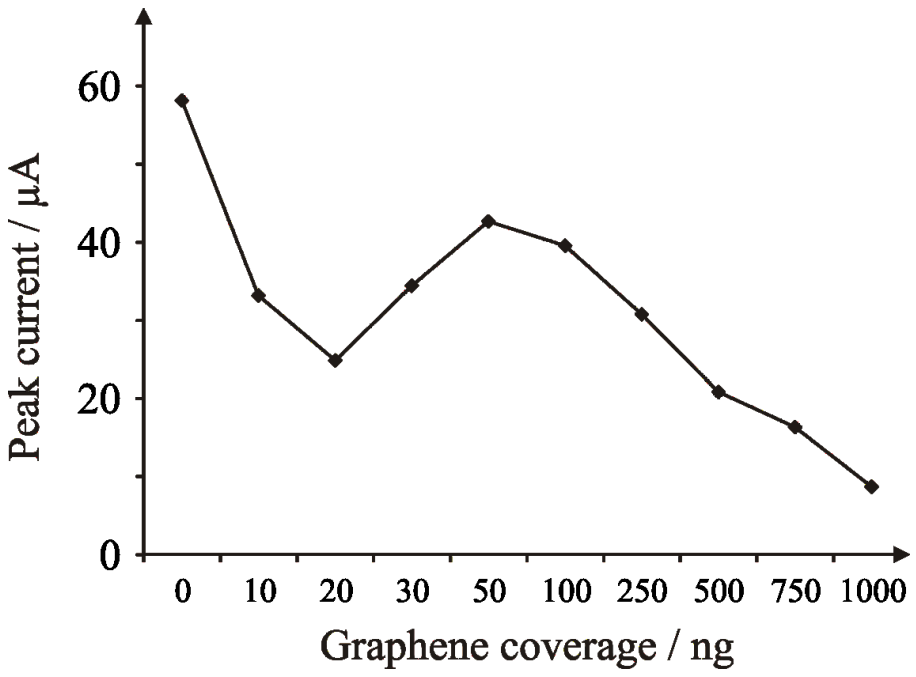

Figure 3.10: The effect of graphene coverage, cast upon a BPPG electrode, on the peak current of SA. The % RSD in each case was no more than 15%.

The first conclusion from Figure 3.10 is that graphene exhibits no benefit in terms of the peak currents observed. However it is noted that the current fluctuates as the global coverage increases. There is an initial decrease in peak current which can be attributed to the increased basal plane nature of the electrode surface. Yet upon further addition of graphene, the peak current increases, suggesting that the graphene either stacks to form graphite or it orientates itself in a fashion in which more edge plane sites become available for electron transfer. The former case is probably more likely as π-π stacking of graphene is a common occurrence. Such stacking creates graphite which contains more edge-plane-like sites exposed to the electroactive substance. The result is an increase in the flow of electrons in the electrochemical reaction. Further additions result in a further decrease in current. Unfortunately there is no other literature to compare to in terms of electrochemical oxidation of SA utilising graphene. This effect is replicated in the case of EPPG, yielding almost identical results. Furthermore, potential *versus* coverage studies found a similar pattern.

Next considered is the effect of the scan rate upon the electrochemical oxidation of SA. Changing the scan rate allows more insights into whether the electrochemical process is diffusional or not. Figure 3.11 depicts the effect of scan rate upon the electrochemical oxidation of SA utilising a 50 ng graphene modified BPPG electrode.

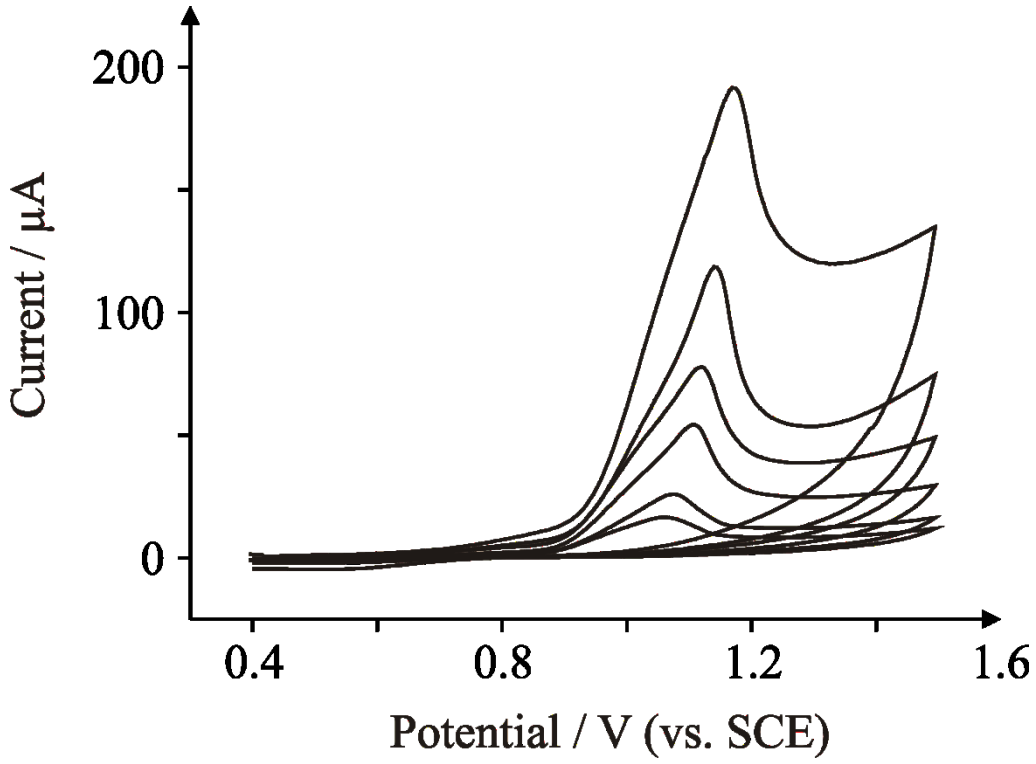

Figure 3.11: Scan rate study (10 – 400 mV s^{-1}) of 1 mM SA in pH 7.4 PBS utilising a 50 ng graphene modified BPPG electrode.

In Figure 3.11, it can be observed that the sharp peak remains consistent throughout the entire scan range. Secondly, the oxidation potential doesn't change dramatically like in some cases, which is perhaps an indication that SA is indeed adsorbing to the surface and is undergoing an adsorptive electrochemical mechanism. In a process where diffusion is limiting the electrochemical process, the oxidation potential would not change, assuming that the electrodes are completely homogeneous in nature. Yet in a process where the electron transfer is limiting the electrochemical process, the oxidation potential would change a lot. In this case, the oxidation potential is changing slightly, suggesting that the mass transport contribution is about equal to the electron transfer process. However, this could also be an effect of diffusionless voltammetry; unfortunately further analysis cannot be considered here because there is no reduction wave. Nevertheless one can mathematically estimate whether

the process is diffusional or thin layer (thin layer behaviour is observed when an electrode composite holds the electroactive material close to the electrode surface so diffusional elements of the voltammetry are negated) by plotting $\log_{10} I_P$ *versus* $\log_{10} \upsilon$. This plot is depicted in Figure 3.12. The gradient of such a plot gives an estimation of the level of diffusion one can ascribe to the system. It should be noted however that this is not an exact science, but it is still useful. A value of 0.4 would suggest diffusional behaviour, whilst a value closer to 0.8 suggests thin-layer behaviour. The gradient in Figure 3.11 is 0.63, which is midway between these two extreme behaviours. This suggests that there is both a diffusional and an adsorptive component in the voltammetry. This behaviour was found to be independent of the global coverage of graphene.

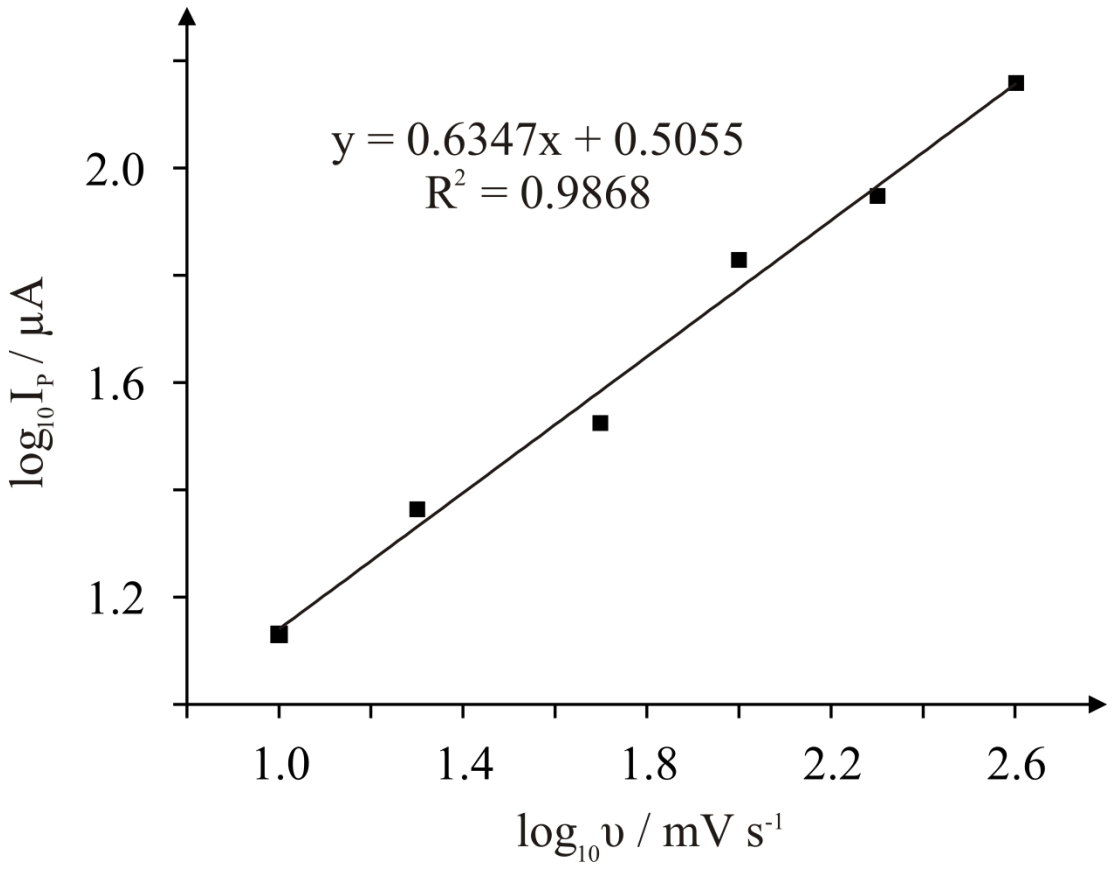

Figure 3.12: $\log_{10}$ current/scan rate plot, plotted to ascertain diffusional or thin-layer voltammetric effects.

3.2.3 SUMMARY

The electrochemical oxidation of SA was considered in order to determine whether the adsorption of an electroactive species reduces the oxidation potential when graphene is used as an electrode material. However upon comparison of a bare electrode to a graphene-covered electrode, no significant difference in oxidation potential was noted, unlike in the case of guanine. Yet there were some surprising observations stemming from this section of work. The graphene coverage played a significant role in the peak current and exhibited "Zone I" and "Zone II" behaviour as reported in authoritative work by Brownson *et al*.[264] The oxidation of SA is thought to exhibit a combination of diffusional and adsorptive effects, determined by changing the scan rate of the voltammetric experiments. In conclusion, it is believed that there are adsorptive interactions between the graphene and SA, which could be beneficial in some way, but the observed oxidation potentials are unchanged as a result of the adsorption and thus it cannot be said that any electroactive aromatic molecule will display beneficial oxidation potentials when graphene is introduced as an electrode material.

3.3 ELECTROCHEMISTRY OF OXYGENATED CARBON MATERIALS

The previous work on DNA bases adds to the ever growing amount of literature reporting the not-so-beneficial properties of graphene as an electrocatalytic electrode material;[264-266] though did shed some light upon a potential benefit with respect to the adsorptive properties of graphene. This next section will follow on from that and focus more upon characterising some carbonaceous materials which exhibit high levels of oxygen content.

3.3.1 INTRODUCTION

The modification of electrode substrates with graphitic materials has been a prevalent area of research for a considerable number of years.[267-272] Such an approach is utilised with the aim of improving the electrochemical performance obtained at the modified electrode in comparison to that of the underlying electrode substrate.[267-272] Commonly used graphitic materials are graphite,[234, 268] CNTs,[219, 268] carbon onions,[271, 273, 274] and more recently graphene,[226, 227, 231, 272, 275] with each material displaying differing electrochemical characteristics. These differing electrochemical properties are due to the graphitic materials exhibiting their own respective level of electronic anisotropy, or Density of States (DoS), yet the electrochemical properties are also influenced by the presence of impurities such as oxygen functionalities,[268, 272] which may alter the electrochemical properties of carbon materials quite dramatically.

Graphite is comprised from stacked sheets of graphene, which is a hexagonal array of sp^2 hybridised, one atom thick atomic carbon.[268, 272] Of all forms of graphite, Highly Ordered Pyrolytic Graphite (HOPG) is the graphite of choice for electrochemists due to its high purity and highly anisotropic electrochemical properties. However all types of carbon materials,

including graphitic species, contain different ratios of edge to basal plane content and thus this ratio dictates the electrochemical response observed.[120, 268, 272, 276-278] We already know from Chapter 1 that graphene and graphite exhibit some radically divergent properties; this section will investigate another carbon composite termed "Q-Graphene", which is a highly oxygenated type of carbon material; this serves to add to the high depth of electrochemical knowledge surrounding CNTs, graphene, and carbon onions.[271, 273, 279-282]

Given that edge plane sites give rise to fast electron transfer rates, many electrochemists are pursuing the isolation of a carbon allotrope with the maximum/optimal edge plane density possible in order to achieve increasingly reversible electron transfer kinetics, which can potentially be utilised with the reported beneficial properties of graphene to produce the next generation of enhanced electronic devices. Resultantly, the search for a new and improved carbon-based electrode material is continued herein. In this section, a recently synthesized and commercially available type of graphene-related material, Q-Graphene, is electrochemically and physically characterised. A range of well-known inner- and outer- sphere redox probes in addition to key biologically relevant molecules are used to de-convolute the electrochemical responses typical of Q-Graphene. Such responses are critically contrasted to that of EPPG, BPPG, graphite and pristine graphene modified electrodes, which reveals further insights into the electrochemistry of these fascinating materials.

3.3.2 RESULTS AND DISCUSSION

PHYSICOCHEMICAL CHARACTERISATION OF Q-GRAPHENE

First considered is the structural characterisation of Q-Graphene *via* SEM and TEM. Figure 3.13 reveals the Q-Graphene material to comprise of hollow carbon nanospheres of

multi-layer graphene. Single layer graphene is also observed, which appears to exhibit an intraplanar microcrystalline size, L_a, of 100 nm and an interplanar microcrystalline size, L_c, of 0.35 nm, comparing well with pristine graphene which has an L_a of 550 nm and an L_c of 0.35 nm, respectively.[234]

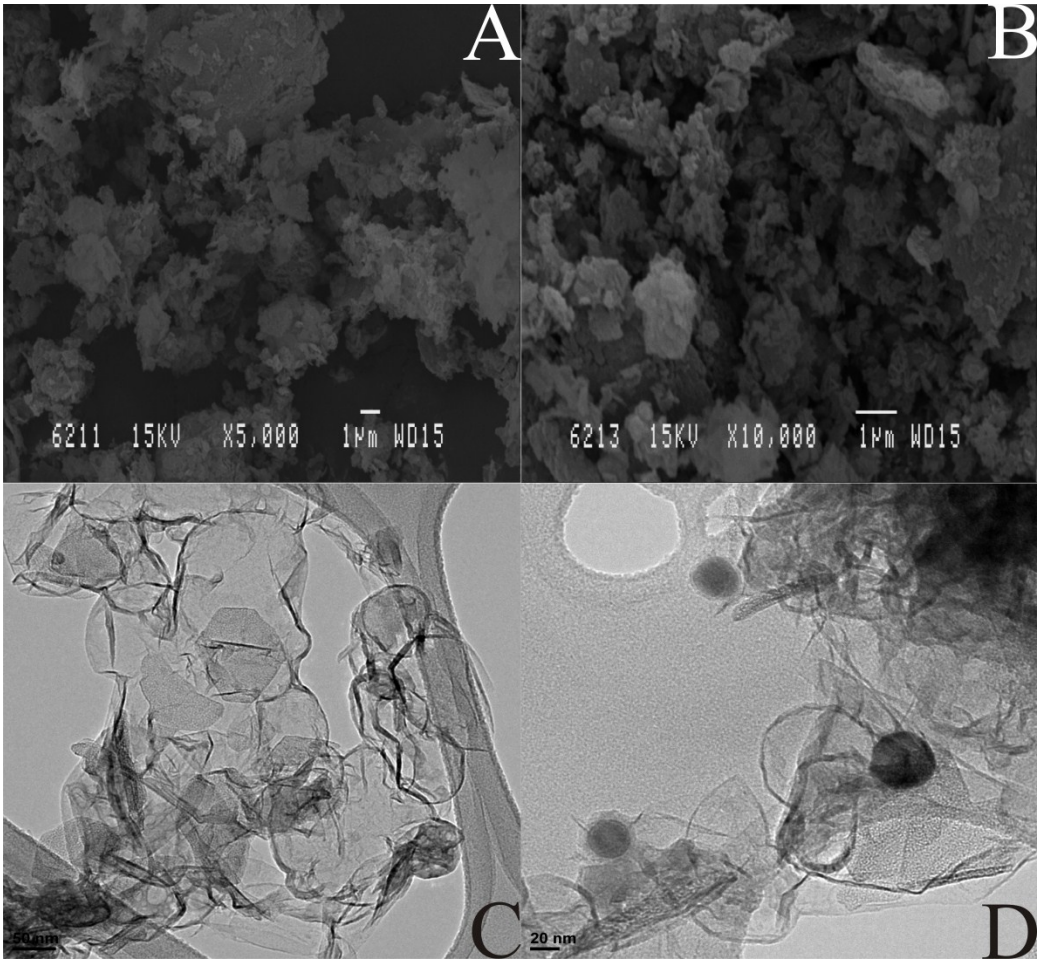

*Figure 3.13: SEM (**A**, **B**) and TEM (**C**, **D**) images obtained for Q-Graphene. Obtained with gratitude from the University of Alicante.*

XPS was conducted on Q-Graphene, revealing 44.3 % atomic carbon and 36.0 % atomic oxygen along with 16.2 % atomic magnesium, 1.3 % atomic sodium, 1.0 % atomic chlorine and 1.2 % atomic sulphur. From inspection of Figure 3.13D, the magnesium impurities are clearly present among the sample (shown as black dots), and are typically less than 50 nm in diameter. The presence of metallic impurities housed within carbon allotropes

is not unfamiliar, most notably for the case of CNTs.[281, 282] In these instances their presence contributes either detrimentally or beneficially to the electrochemical activity. In the case of Q-Graphene, the large amount of magnesium impurities likely arise from the fabrication approach, which requires magnesium oxide catalysts (no further information was disseminated from the manufacturer). Magnesium oxide is unlikely to be directly electrochemically active in the aqueous solutions and voltammetric potential windows employed in this study, but of course should still be kept in mind when Q-Graphene is utilised in the future by researchers.

Returning to the XPS characterisation, analysis of the carbon content (44.3 %) reveals this to comprise of 35.5 atomic % at 284.3 eV, which is characteristic of graphitic groups, and 8.9 atomic % at 285.8 eV, which corresponds to C-O and C=O bonds. The overall XPS spectra and the de-convoluted C1s and O1s regions are depicted in Figure 3.14. It is clear that the O/C ratio for Q-Graphene is found to correspond to 0.81, which interestingly is higher than literature values for graphene oxide, which has been reported to have varying O/C ratios ranging from 0.20[283] to 0.49[284] and far higher than that of pristine graphene which has been reported to have an O/C ratio of 0.052.[234]

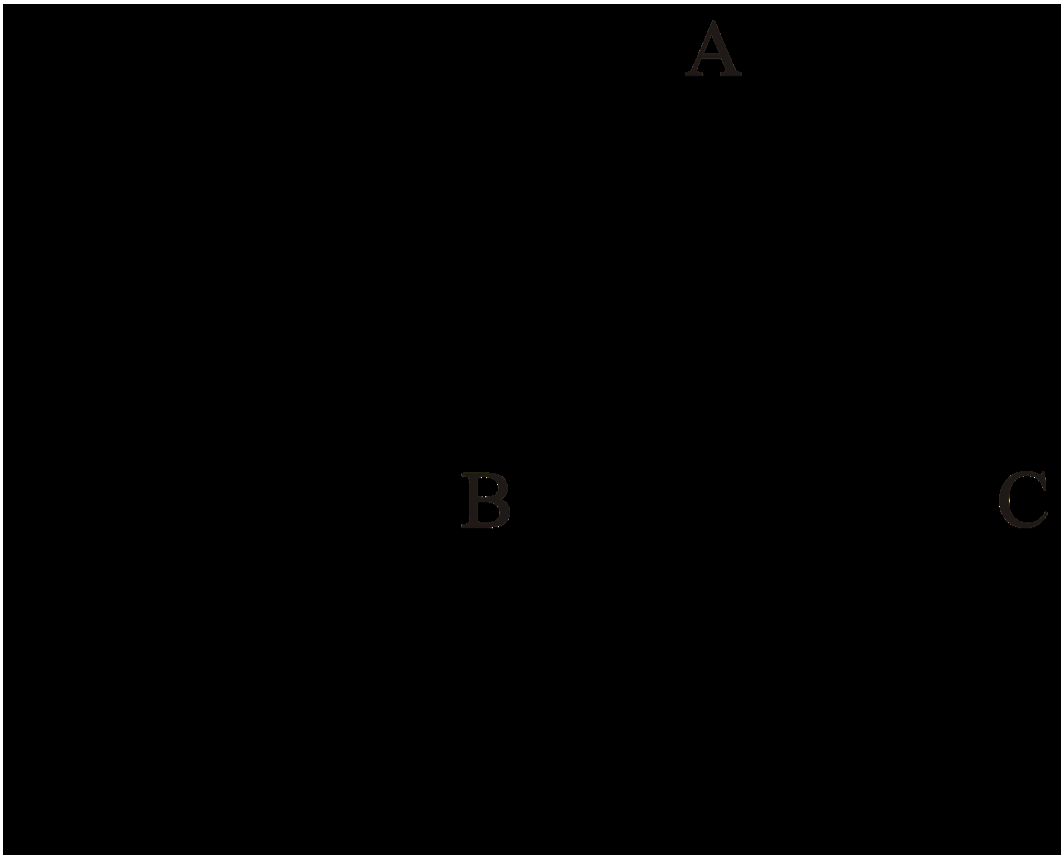

*Figure 3.14: XPS spectra of the commercially available Q-Graphene. **A**: Overall spectra, **B**: C1s and **C**: O1s regions. Obtained with gratitude from the University of Alicante.*

Attention is now turned to Raman spectroscopy. Figure 3.15 shows the Raman spectrum of Q-Graphene, exhibiting D (1341 cm^{-1}), G (1587 cm^{-1}) and 2D (denoted as G´, 2688 cm^{-1}) modes. It is well established in the literature that a single layer of graphene consists of two dominant Raman-allowed spectral features associated to the G band occurring around 1580 cm^{-1}, and 2D band, the wavenumber of which depends upon the laser energy.[285] In this case, the laser energy corresponded to 2.33 eV, providing a wavenumber close to 2700 cm^{-1}. The 2D band is broader and weaker than the G band, signifying multi-layer graphene.[286] Surprisingly, the D band, which is the band associated with graphitic disorder, is still present in the Raman spectrum occurring at 1341 cm^{-1}. This contribution is ascribed to graphene edges, stacking disorder between two layers and atomic defects within the layer.[285] A

combination of the D and G peaks gives rise to a 3S peak at 2910 cm^{-1} as a result of lattice disorders, as shown for graphene oxides. There is normally no D peak (*ca.* 1340 cm^{-1}) in the case of pristine graphene and the presence of a D peak in Raman spectroscopy indicates the presence of defects upon the surface of graphene sheets.[287, 288] Contrasting Raman spectra were obtained, and indicate that the Q-Graphene is inhomogeneous in nature. Thus, depending on the location that is probed, single layer graphene may be observed, while in other areas, few- and multi-layered graphene is observed, as in Figure 3.15.

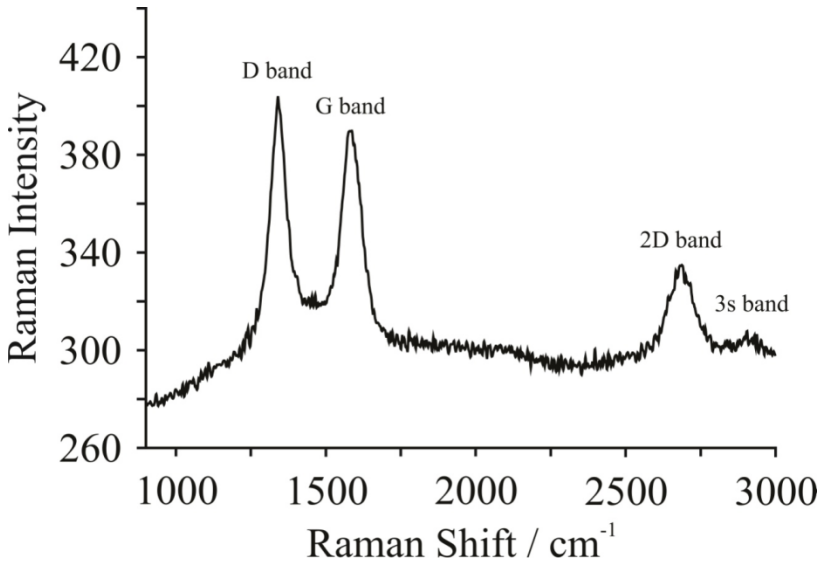

Figure 3.15: Raman spectrum for Q-Graphene. Laser intensity: 1.25 mW. Obtained with gratitude from the University of Alicante.

In summary, Q-Graphene is clearly a material that is inhomogeneous in nature. It has a large O/C content, which is much higher than previously reported for other graphenes and yet consists of hollow carbon nanospheres (TEM/SEM) and a mixture of single and few-layer graphene (Raman) making it an interesting electrode material to study. The next section will characterise the material electrochemically.

Next considered is the electrochemical behaviour of Q-Graphene modified electrodes towards well known and widely characterised inner- and outer- sphere electrochemical redox probes. The CV characterisation of the inner-sphere probe potassium ferrocyanide (II)[289] is first explored utilising unmodified BPPG and EPPG electrodes in addition to BPPG and EPPG electrodes following modification with 20 ng of a carbon-based modification. As is depicted in Figure 3.16A the ΔE_P for both BPPG and EPPG decreased somewhat dramatically with the introduction of Q-Graphene onto the electrode surface (indicating improvements in the electrochemical response), with the former decreasing from +0.43 to +0.14 V (*vs.* SCE) and the latter decreasing from +0.09 to +0.07 V (*vs.* SCE).

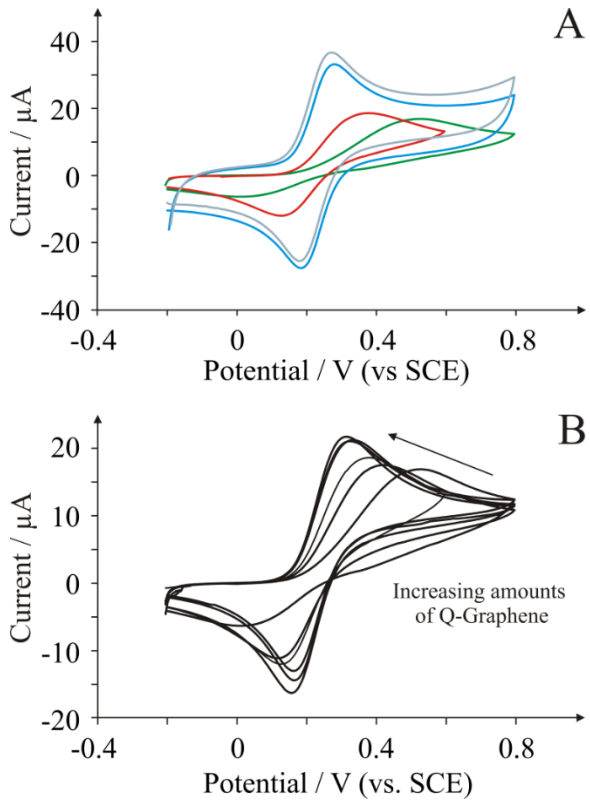

*Figure 3.16: CV response observed for potassium ferrocyanide (II). Scan rate: 50 mV s^{-1}. **A**: at an unmodified BPPG (green line) and a 20 ng Q-Graphene modified BPPG (red line) electrode; at an unmodified EPPG (blue line) and a 20 ng Q-Graphene modified EPPG (grey line) electrode. **B**: utilising increasing amounts of Q-Graphene upon a BPPG electrode.*

To ensure that the voltammetric response is diffusional in nature and not due to thin-layer type behaviour, the peak current, I_P, was monitored as a function of the applied voltammetric scan rate, υ. A plot of $\log_{10}I_P$ *versus* $\log_{10}\upsilon$ revealed a linear response with a gradient corresponding to an average of 0.4 across the varying masses of Q-Graphene studied, which is close to the ideal value of 0.5 and indicates a diffusional electrochemical process rather than a thin-layer effect. Thin layer effects have been previously observed in the case of CNT modified electrodes and give a false impression of 'electrocatalysis', when in reality there is a change in mass transport.[290] The heterogeneous electrochemical rate constant, k^0, deduced for the Q-Graphene modified BPPG electrode was estimated using the well-known Nicholson method as described by equation 1.27 in Section 1.6.[291] The k^0 of the Q-Graphene modified EPPG electrode was estimated to correspond to 1.86 x 10^{-2} cm s^{-1} utilising a literature diffusion coefficient of 6.30 x 10^{-6} cm^2 s^{-1};[292] this value suggests faster electrode kinetics at Q-Graphene than that observed at the unmodified EPPG, which was found to exhibit a k^0 of 4.66 x 10^{-3} cm s^{-1}. On an anisotropic level this would mean that Q-Graphene contains a greater proportion of reactive edge-plane-like sites, however given that EPPG is well-known to possess almost 100% edge planes (and therefore electronically similar to Q-Graphene), the effect is more likely due to some other constituent of the Q-Graphene structure, namely the oxygenated functionalities or indeed the impurities housed within the structures.[278]

Next considered is the effect of coverage of the immobilised Q-Graphene on the voltammetric response of potassium ferrocyanide (II), which is summarised in Figure 3.16B. The E_P corresponding to the oxidation of potassium ferrocyanide (II) is observed to shift to less electropositive values and the peak current increases as the amount of Q-Graphene is increased upon the BPPG surface. The smallest ΔE_P that can be achieved corresponds to

+0.14 V (*vs.* SCE), achieved by casting 15 ng Q-Graphene on the electrode surface; subsequent additions are shown to have little or no effect upon the observed E_P and I_P.

Control experiments using graphite were also conducted. Table 3.1 highlights the observed ΔE_P values obtained using potassium ferrocyanide (II). It is clear that the ΔE_P decreases with the introduction of graphite compared to the bare underlying BPPG electrode, which is consistent with previous literature.[293] This is an effect of electronic anisotropy, as discussed numerous times already in this thesis. Recent work utilising pristine graphene has shown the inverse trend of that depicted in Figure 3.16B, where the addition of graphene resulted in an inhibited electrochemical performance, which was attributed to graphene's low proportion of edge plane sites.[234]

Table 3.1: Table detailing the ΔE_P obtained towards potassium ferrocyanide (II) at various modifications of BPPG and EPPG electrodes. Scan rate: 50 mV s^{-1} (vs. SCE).

Electrode Material	ΔE_P / V
BPPG	0.43
20 ng Q-Graphene – BPPG	0.14
20 ng Graphite – BPPG	0.38
EPPG	0.09
20 ng Q-Graphene – EPPG	0.068
20 ng Graphite – EPPG	0.09

Previous studies have shown that the electrochemistry of potassium ferrocyanide (II) is known to be highly surface sensitive, in addition to being highly dependent upon the DoS.[268] With this in mind, and contrasting the responses observed for graphite and Q-Graphene, it is likely that the impurities housed within the Q-Graphene structures and the oxygenated species contribute beneficially towards the observed voltammetry, in terms of a reduced ΔE_P. Of the two cases, the more likely scenario is that the oxygenated species are contributing beneficially, as the major impurities in magnesium are not electroactive within the potential window.

The reproducibility of the drop-casting method is next considered by assessing the % Relative Standard Deviations (% RSD) of the observed electrochemical responses. These studies ($N = 3$) revealed a value of 11 % for the unmodified BPPG electrode, and the following at modified BPPG electrodes: 2 % for 5 ng Q-Graphene; 10 % for 10 ng Q-Graphene; 19 % for 15 ng Q-Graphene; 5 % for 20 ng Q-Graphene; and 7 % for 25 ng Q-Graphene. Whilst there is some deviation observed, the % RSD values are generally acceptable and in line with other carbon based materials modified electrodes.[230, 294]

Attention was next turned to the electrochemical characterisation of Q-Graphene modified BPPG and EPPG electrodes utilising the outer-sphere redox probe,[289] hexaammine-ruthenium (III) chloride. The electrochemical reduction of hexaammine-ruthenium (III) chloride involves a simple one electron transfer process and the electrode kinetics are known to be relatively insensitive to surface oxides, with the observed electrochemical response depending mainly upon the DoS near the formal potential of the redox system. Figure 3.17A depicts typical CV profiles obtained using unmodified BPPG and EPPG electrodes and 20 ng Q-Graphene modified BPPG and EPPG electrodes. The response at the EPPG and BPPG electrodes are consistent with literature reports,[289, 295] where the ΔE_P inversely scales with the effective rate of electron transfer. For the case of EPPG and BPPG towards the

hexaammine-ruthenium (III) chloride, the ΔE_P values are usually similar, where only a low % global coverage of edge-plane-like sites is required to obtain fast reversible voltammetry.[295] However, this analyte is useful to evaluate graphene since Brownson *et al.* has shown there are extreme cases, as with pristine graphene, where a large ΔE_P is observed due to an exceptionally low % global coverage of edge planes.[234] The ΔE_P obtained at the unmodified BPPG electrode decreases from +0.075 to +0.060 V (*vs.* SCE) with the introduction of 20 ng Q-Graphene, while the ΔE_P for the unmodified EPPG electrode remains unchanged at +0.064 V (*vs.* SCE) following the modification with 20 ng Q-Graphene. The responses observed for the Q-Graphene modified EPPG is as expected given previous literature reports,[295] assuming that hexamine-ruthenium (III) chloride is insensitive to oxygenated species, because the Q-Graphene offers no benefit over EPPG in terms of reactive edge plane sites. Interestingly, Brownson *et al.* observed changes in the electrochemistry for hexamine-ruthenium (III) chloride in for the case of graphene oxide,[284] yet Q-Graphene displays no such difference despite the high O/C ratio. The inference upon comparison of these datasets is that the type of surface oxygenated species differs greatly between the two cases.

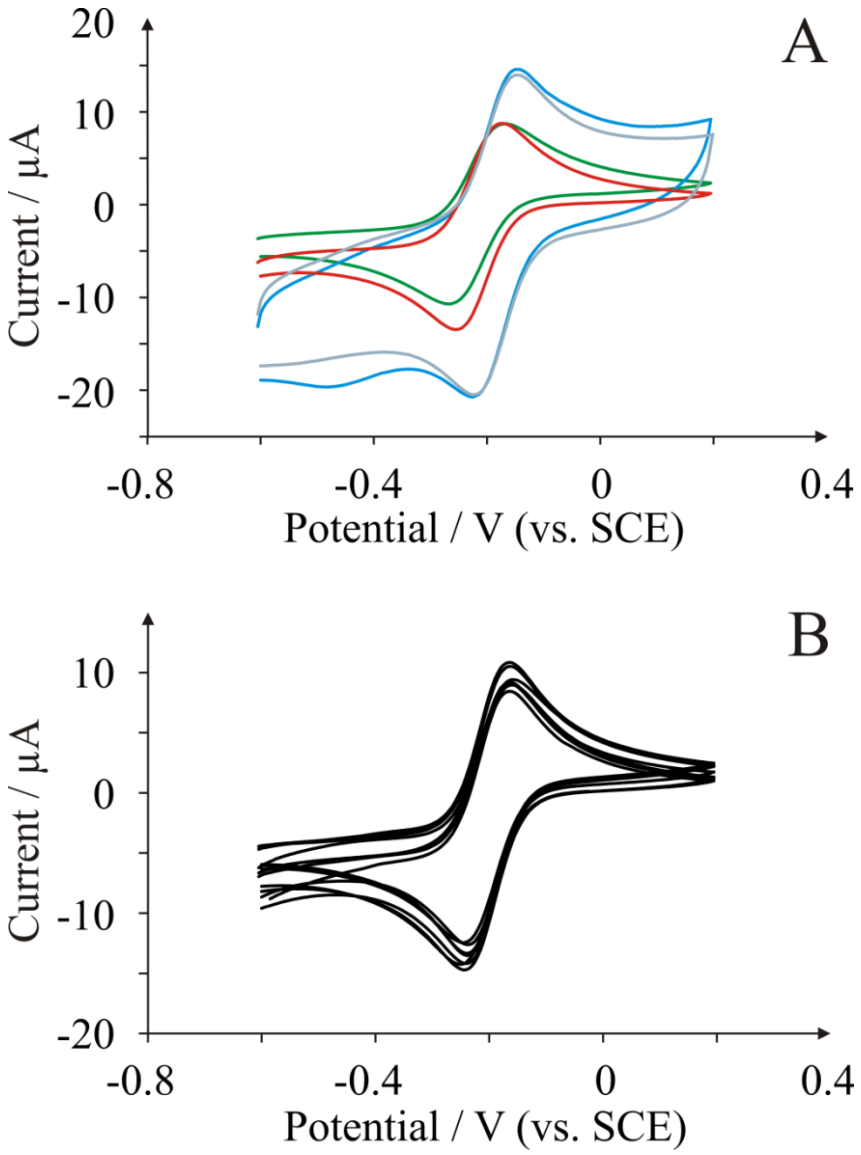

*Figure 3.17: CV response observed for hexaammine-ruthenium (III) chloride. Scan rate: 50 mV s^{-1}. **A**: at an unmodified BPPG (green line) and a 20 ng Q-Graphene modified BPPG (red line) electrode; and at an unmodified EPPG (blue line) and a 20 ng Q-Graphene modified EPPG (grey line) electrode. **B**: BPPG electrode with increasing amounts of Q-Graphene.*

The Nicholson method was used to estimate k^0 (utilising a literature diffusion coefficient value of 9.10 x 10^{-6} cm s^{-1}),[292] yielding a value of 5.60 x 10^{-3} cm s^{-1} at Q-Graphene, which is similar to that reported for EPPG.[296] Figure 3.17B depicts the CV profiles of hexaammine-ruthenium (III) chloride with regards to varying the coverage of Q-Graphene

cast upon the surface of a BPPG electrode. With increasing amounts of immobilised Q-Graphene, the voltammetry shows little to no change in both the E_P and I_P once one takes into account the % RSD. A summary of the ΔE_P values obtained for several modifications of EPPG and BPPG electrode is presented in Table 3.2. The table demonstrates the probe's dependence upon the DoS rather than the oxygenated species, because the BPPG electrode exhibits the largest ΔE_P and this decreases upon addition of Q-Graphene and graphite, whereas in the case of EPPG, the ΔE_P doesn't change because the DoS effectively remains unchanged.

Table 3.2: Table detailing the ΔE_P obtained towards hexaammine-ruthenium (III) chloride at various modifications of BPPG and EPPG electrodes. Scan rate: 50 mV s^{-1} (vs. SCE).

Electrode Material	ΔE_P / V
BPPG	0.075
20 ng Q-Graphene – BPPG	0.060
20 ng Graphite – BPPG	0.072
EPPG	0.064
20 ng Q-Graphene – EPPG	0.064
20 ng Graphite – EPPG	0.070

The % RSD measurements obtained towards the reduction of hexaammine-ruthenium (III) chloride at a fixed concentration of 0.5 mM were as follows (*N= 3*): 5 % for unmodified BPPG; 10 % for 5 ng Q-Graphene; 1 % for 10 ng Q-Graphene; 4 % for 15 ng Q-Graphene; 8

% for 20 ng Q-Graphene; and 5 % 25 ng Q-Graphene. The low standard deviation highlights a good level of reproducibility once again for such a probe. Table 3.3 lists ΔE_P values for another outer-sphere redox probe, potassium hexachloroiridate. Similar behaviour to hexamine-ruthenium (III) chloride is observed in this case and is not discussed in any further detail.

Table 3.3: Table detailing the ΔE_P obtained for hexachloroiridate (III) at various modifications of BPPG and EPPG electrodes. Scan rate: 50 mV s^{-1} (vs. SCE).

Electrode Material	ΔE_P / V
BPPG	0.11
20 ng Q-Graphene – BPPG	0.079
20 ng Graphite – BPPG	0.10
EPPG	0.070
20 ng Q-Graphene – EPPG	0.066
20 ng Graphite – EPPG	0.070

In summary, it is clear that the Q-Graphene possesses a high degree of edge-plane-like sites across its surface, such that the DoS is similar to that observed at EPPG. Such a DoS is beneficial in terms of fast electrode kinetics. It is not surprising that Q-Graphene exhibits a larger proportion of edge plane sites over that of pristine graphene, giving rise to favourable electron transfer kinetics and improved electrochemistry.[234] This section has deduced the electrochemical properties of Q-Graphene through the utilisation of both surface sensitive and insensitive redox probes. It has additionally shown that the oxygenated species

present on the Q-Graphene may contribute to the observed electrochemistry; something which is investigated further through the use of biologically relevant analytes.

ELECTROCHEMICAL RESPONSE OF BIOLOGICALLY RELEVANT ANALYTES

The investigation of Q-Graphene is furthered by exploring the electrochemical behaviour of biologically relevant analytes, which are of significant importance in a plethora of areas where electrochemistry is utilised. Norepinephrine, a catecholamine neurotransmitter that plays a pivotal role in the mammalian central- and sympathetic- nervous and cardiovascular systems, is investigated first. The concentration of this hormone within the blood is indicative of both physical and mental stress levels,[297] and is therefore required in clinical chemistry to be monitored. There is a wealth of literature regarding the electrochemical detection of norepinephrine utilising graphene modified electrodes,[275, 298] against which Q-Graphene can be benchmarked.

The CV of norepinephrine is first investigated at unmodified BPPG and EPPG electrodes and at 20 ng Q-Graphene modified BPPG and EPPG electrodes and is depicted in Figure 3.18A. The electrochemical oxidation of norepinephrine at the unmodified BPPG electrode occurs at +0.43 V (*vs.* SCE), which is consistent with previous literature reports.[295] Upon further inspection of Figure 3.18A, it is evident that the EPPG electrode exhibits the most electrochemically favourable response, in which the respective oxidation peak occurs at the lowest activation potential of +0.29 V. It is clear that the BPPG exhibits slower electrode kinetics when compared to that of the EPPG, which would indicate that the global coverage of edge plane sites significantly contributes towards the electrochemistry of norepinephrine. This is consistent with literature reports which state that the addition of CNTs upon a BPPG electrode results in an increased proportion of edge plane sites on the electrode surface and

consequently an improved electrochemical performance.[293] It is evident in Figure 3.18A that the immobilisation of 20 ng of Q-Graphene onto the BPPG electrode leads to an improvement in the electrochemical activity of the electrode. Interestingly, the immobilisation of Q-Graphene onto an EPPG electrode has the opposite effect. Therefore, in the absence of oxygenated species, the DoS significantly affects the electron transfer at the electrode|solution interface, yet oxygenated species play a more significant role when the edge plane content is sufficiently high. It is therefore necessary to investigate the mass of Q-Graphene further towards this particularly interesting target analyte.

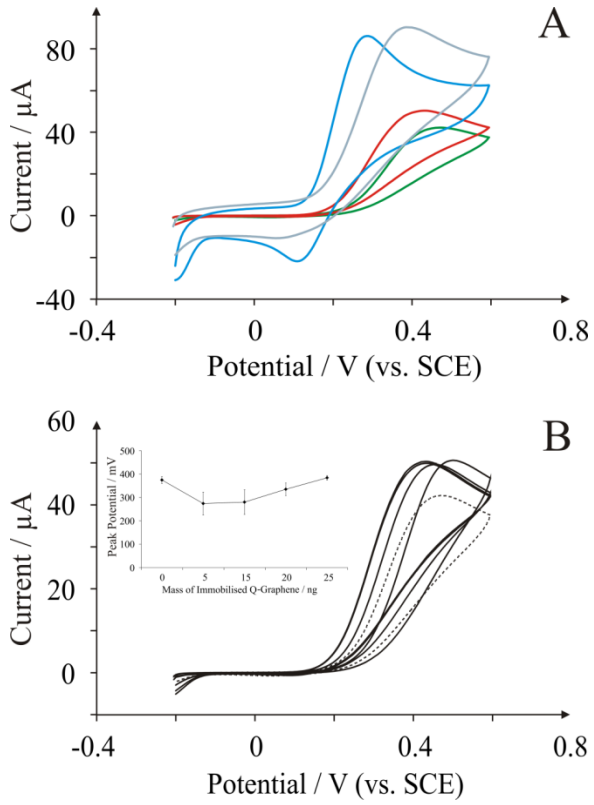

*Figure 3.18: CV response observed for norepinephrine. Scan rate: 50 mV s^{-1}. **A**: at an unmodified BPPG (green line) and a 20 ng Q-Graphene modified BPPG (red line) electrode; and at an unmodified EPPG (blue line) and a 20 ng Q-Graphene modified EPPG (grey line) electrode. **B**: a BPPG electrode with increasing amounts of Q-Graphene (dotted line is the bare BPPG electrode). Inset: E_P versus the mass of immobilised Q-Graphene upon the BPPG surface.*

The effect of varying the coverage of immobilised Q-Graphene on a BPPG electrode is next explored. Close inspection of Figure 3.18B reveals that the initial introduction of Q-Graphene results in an improved electrochemical response *via* a reduction in the E_P observed for the oxidation of norepinephrine. Additionally there is a reasonable improvement in the peak current, which is perhaps the more significant change observed between the bare electrode and the modified electrodes. Inset in Figure 3.18B is a graphic which demonstrates the change in E_P with respect to the mass of immobilised Q-Graphene. It is noted from this graphic that when the quantity of immobilised Q-Graphene is increased further, a detrimental response is observed *via* a shift in the E_P to more electropositive values, which eventually become greater than that obtained at the initial unmodified BPPG electrode. This response/trend indicates an interesting scenario where initially there is an improvement in the electrochemical response which is likely due to an increased density of edge plane sites as a result of introducing Q-Graphene onto an electrode substrate that exhibits a low degree of such electroactive sites. Yet upon further additions of Q-Graphene, the amount of oxygenated species present becomes too great, such that they dominate and give rise to a detrimental response. This observation is consistent with previous literature reports which have shown epinephrine to exhibit dramatic changes in voltammetry at electrochemically activated electrodes[226, 299] and through the introduction of oxygenated species.[226, 300] It is clear that the DoS has a large influence on the electrochemistry of norepinephrine. Furthermore the O/C ratio of the electrode material is also crucial, depending highly upon surface coverage. The % RSD measurements (N = 3) performed at a set concentration of 1 mM norepinephrine yielded values of: 4 % for unmodified BPPG; 13.5 % for 5 ng Q-Graphene; 15 % for 10 ng Q-Graphene; 5.5 % for 15 ng Q-Graphene; 2 % for 20 ng Q-Graphene; and 10 % for 25 ng Q-Graphene.

The next analyte investigated using this interesting carbon material is NADH, which is well understood and abundantly explored in electrochemistry[301] since it is an important coenzyme utilised in biosensor development.[302] The electrochemistry of NADH has been shown previously to be surface sensitive.[268] The response observed is highly dependent on the electronic structure of the electrode surface and the type of carbon oxygenated species that terminate the carbon material.[268]

CV was performed utilising unmodified BPPG and EPPG, and 20 ng Q-Graphene modified BPPG and EPPG electrodes; the voltammetric profiles are presented in Figure 3.19A. For the case of the unmodified EPPG and BPPG electrodes, an improved electrochemical response is evident at the EPPG over that of the BPPG, which can be attributed to the high global coverage of edge plane sites on the former over that of the latter. When immobilising 20 ng of Q-Graphene onto the surface of the BPPG electrode, the E_P representing the oxidation of NADH is observed to decrease from +0.76 to +0.70 V (*vs.* SCE) and additionally an increase in the I_P is evident. Overall, there is an improvement in the electrochemical response and thus a favourable interaction at Q-Graphene. Interestingly the opposite is observed upon modification of an EPPG electrode with 20 ng of Q-Graphene with the E_P of +0.55 V (*vs*. SCE) at the unmodified EPPG exhibiting little change, however, a significant increase in the I_P is observed with the introduction of Q-Graphene; again indicating favourable electrochemical interaction at the Q-Graphene modified electrode. Continually increasing the amount of Q-Graphene immobilised on the BPPG resulted in further decreases in the observed E_P. Furthermore, with respect to the % RSD in the I_P measured using a fixed concentration of 1 mM NADH, there was no deviation in the observed experimental error over 10 % at the BPPG electrode either pre- or post-modification with Q-Graphene.

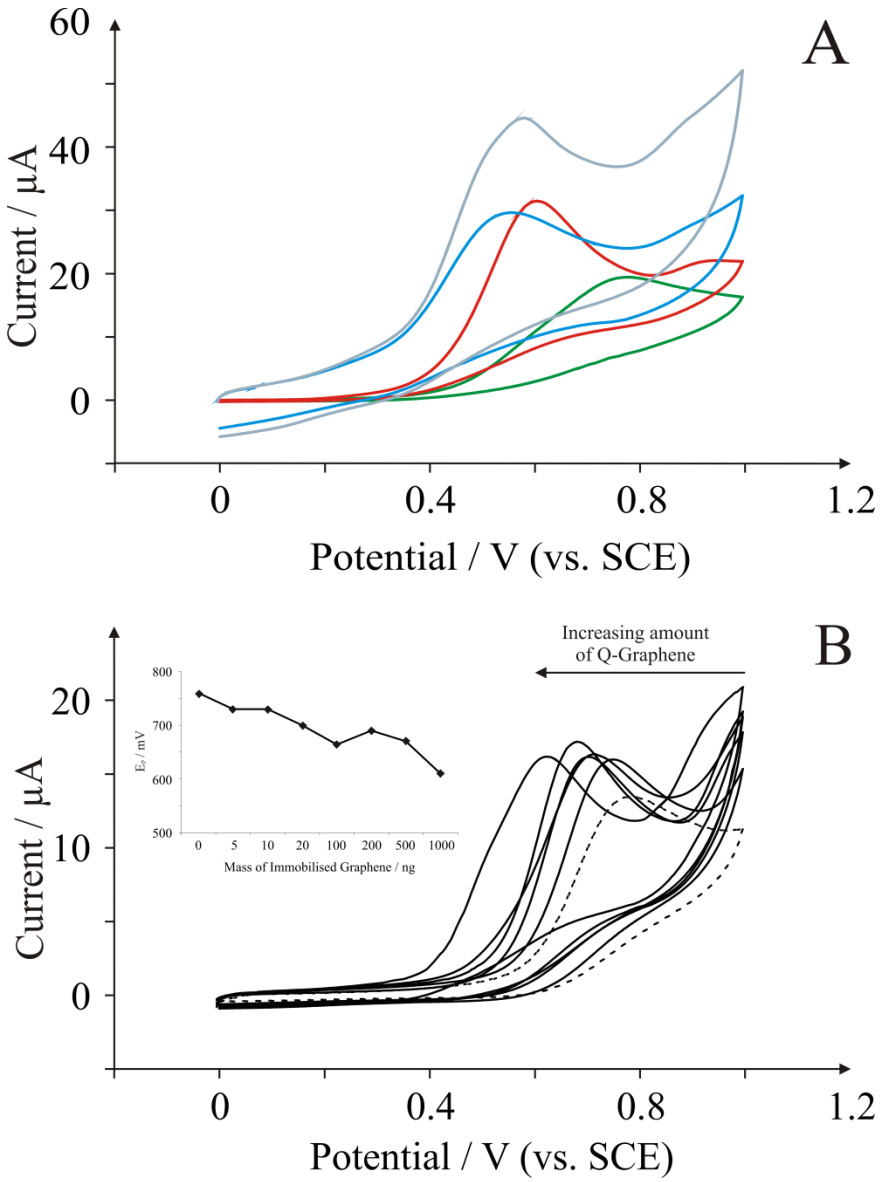

*Figure 3.19: CV response observed for NADH. Scan rate: 50 mV s^{-1}. **A**: at an unmodified BPPG (green line) and a 20 ng Q-Graphene modified BPPG (red line) electrode; and at an unmodified EPPG (blue line) and a 20 ng Q-Graphene modified EPPG (grey line) electrode. **B**: a BPPG electrode with increasing amounts of Q-Graphene (the dotted line is the unmodified BPPG). Inset: E_P as a function of mass of Q-Graphene.*

It is evident through inspection of Figure 3.19 that Q-Graphene exhibits a favourable electrochemical performance towards the oxidation of NADH, where improvements are observed over that of the unmodified supporting electrodes. Such observations indicate that

immobilising Q-Graphene upon a BPPG electrode results in improvements in both the E_P and I_P, which can be attributed to the Q-Graphene possessing a larger quantity of edge plane sites over that of the BPPG, and resultantly a material exhibiting slow electrode kinetics[278] is replaced with a material exhibiting a greater proportion of edge plane sites. In the case of the EPPG, immobilising Q-Graphene has little effect on the E_P as both materials clearly exhibit a similar electronic structure, however improvements in the I_P are observed, which is likely due to the specific oxygenated species present on the Q-Graphene resulting in a more favourable, presumably electrostatic, interaction with NADH such that electrocatalytic improvements are observed. Thus, such an electrode material could be useful for applications where the detection of NADH in a system is paramount.

This investigation is concluded by observing the electrochemistry of Q-Graphene towards the oxidation of *L*-ascorbic acid, which is a commonly utilised and well understood electroactive analyte that is often found to be present in biological samples.[303] Ascorbic acid is known to be sensitive to the electronic state of a carbon material, yet there are conflicting reports regarding its interaction with surface oxygenated species.[226, 276, 304]

Figure 3.20A depicts CV profiles for *L*-ascorbic acid at unmodified BPPG and EPPG electrodes, where the electrochemical response of the EPPG is, once again, favourable over that of the BPPG. Also shown in Figure 3.20A are the CV profiles at BPPG and EPPG electrodes following the immobilisation of 20 ng Q-Graphene, where it is evident that in both cases, the introduction of Q-Graphene results in an inhibited electrochemical performance. In the case of the BPPG electrode, the addition of 20 ng Q-Graphene causes the E_P to increase from +0.40 to +0.60 V (*vs.* SCE), and additionally a reduction in the I_P is evident. Interestingly, although a similar response is observed in the case of the EPPG being modified with 20 ng of Q-Graphene, this is to a lesser extent where the E_P is shifted from +0.20 to +0.25 V (*vs.* SCE) with little effect on the I_P. Also, increasing the amount of Q-Graphene

resulted in a further shift in the E_P to higher potentials, indicating a continued reduction in the electrochemical performance. There was no deviation in the observed experimental error over 10 % at the BPPG electrode either pre- or post- modification with Q-Graphene.

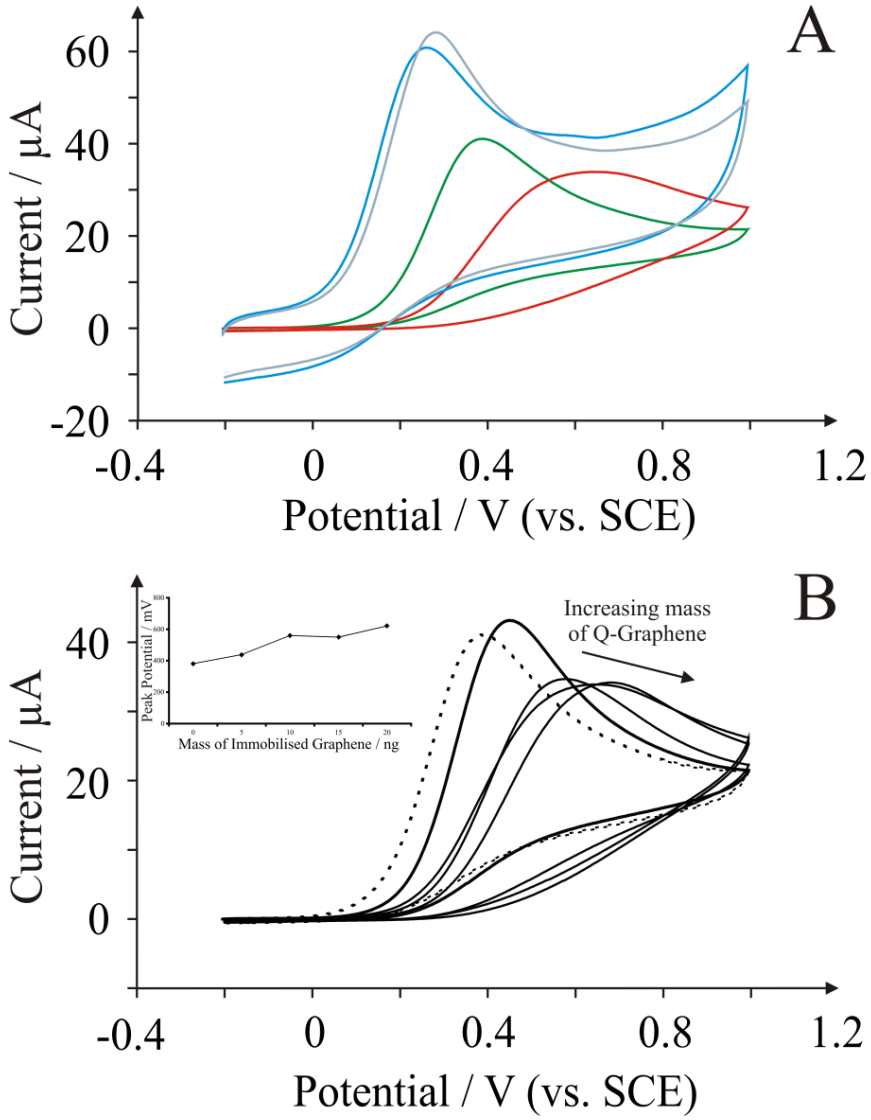

*Figure 3.20: CV response observed for L-ascorbic acid. Scan rate: 50 mV s^{-1}. **A**: at an unmodified BPPG (green line) and a 20 ng Q-Graphene modified BPPG (red line) electrode; and at an unmodified EPPG (blue line) and a 20 ng Q-Graphene modified EPPG (grey line) electrode. **B**: a BPPG electrode with increasing amounts of Q-Graphene, where the dotted line is the bare BPPG. Inset: E_P as a function of mass of Q-Graphene.*

It is clear from these observations that the oxidation of *L*-ascorbic acid is inhibited at Q-Graphene. This response is surprising and not as expected given that it is well-known that the electrochemistry of *L*-ascorbic acid is predominantly affected as a function of the density of available edge plane sites at graphitic electrodes, given earlier insights it is clear that Q-Graphene possesses a greater number of such sites over that of the BPPG and thus a beneficial response is expected. As this appears not to be the case here, it is therefore suggested that the large O/C content exhibited by Q-Graphene is detrimental in this specific instance. This results in a poor electron transfer process towards *L*-ascorbic acid at Q-Graphene which is contradictory to that usually reported in the literature. Hence in this unique case the presence of specific oxygenated species upon Q-Graphene are highly detrimental to its electrochemical performance. It can be concluded from this section that the type of oxygenated species must also be considered when assessing the relative merits of a carbonaceous electrode material.

3.3.3 SUMMARY

This section carefully explored the electrochemical responses observed at electrode surfaces modified with a new member of the graphene family, Q-Graphene, which is commercially available.[42] The selection of electrochemical analytes utilised ranged from simple analytes that are dependent upon electronic properties (DoS) through to ones which are dependent on surface oxygenated species, which allowed the electrochemical properties of the Q-Graphene to be fully de-convoluted. The ensuing investigations found that due to the unique structure of Q-Graphene, which has a large proportion of folded edges and edge-plane-like sites/defects across the sheet, it generally exhibits a response similar to EPPG. However, it has been shown that the high O/C ratio of Q-Graphene also significantly

contributes to the observed electrochemical response, which is strictly analyte dependant and as such can be either highly beneficial or detrimental in various cases. While a large amount of impurities (44.3 % atomic carbon and 36.0 % atomic oxygen along with 16.2 % atomic magnesium, 1.3 % atomic sodium, 1.0 % atomic chlorine and 1.2 % atomic sulphur) are present in the Q-Graphene arising from its fabrication process, in this study they are unlikely to contribute to the observed electrochemical activity. However, this still needs to be considered in future work where Q-Graphene is utilised in both electrochemical and non-electrochemical applications.

In summary, Q-Graphene, like other graphene types, has great potential as a new electrode material for future use in advanced electrochemical applications, particularly where a high level of edge-plane-like sites are required to tailor and optimise a specific response or through utilisation of its valuable oxygen content for beneficial implementation where the electrocatalytic or electro-inhibitory effects may be useful. Despite this rigorous work, careful control experimentation should always be exercised when approaching Q-Graphene as a sensory platform due to its mixed carbon allotropes and impurities. The next section will further the understanding of carbon materials by focussing upon the controversial oxygen reduction reaction.

3.4 THE OXYGEN REDUCTION REACTION UTILISING GRAPHENE MODIFIED ELECTRODES

To further the understanding of graphene composites, a thorough investigation into the Oxygen Reduction Reaction (ORR) is conducted. The ORR is a problem reaction in batteries and fuel cells because it has a tendency to foul electrode surfaces, either by formation of hydrogen peroxide, or formation of less reactive oxygenated groups upon the electrode surface. Therefore graphene could prove to be beneficial if it changes the reduction potential and, more importantly, eradicate some problem side reactions which are observed in batteries and fuel cells.

3.4.1 INTRODUCTION

The ORR has been studied extensively in order to obtain significant improvements of many inventions dependent upon electrochemical processes, including hydrogen-oxygen fuel cells,[305, 306] biosensors,[307, 308, 309] and metal-air batteries.[310-312] The ORR is, however, not an easily activated electrochemical reaction due to the strength of the dioxygen double bond (498 kJ mol^{-1}),[313] which leads to activation potentials for the electrochemical reduction of oxygen being relatively high, *ca* -0.5 to – 1.0 V on graphitic electrodes, for example.[221] Such reduction potentials on graphitic materials are dependent upon the type of graphitic surface (edge, basal etc.), the density of oxygenated species present, and the solution pH.[221, 314] The reaction pathway associated with the electrochemical reduction of oxygen proceeds *via* one of two pathways, depending upon the pH and the electrode material, and are highlighted by equations 3.1 – 3.4:[221, 315, 316]

The 2 Electron Pathway

Acidic

$$O_2 + 2H^+ + 2e^- \rightarrow H_2O_2 \quad E^0 = 0.670\ V \qquad (3.1)$$

Alkaline

$$O_2 + H_2O + 2e^- \rightarrow HO_2^- + OH^- \quad E^0 = -0.065\ V \qquad (3.2)$$

The Direct 4 Electron Pathway

Acidic

$$O_2 + 4H^+ + 4e^- \rightarrow 2H_2O \quad E^0 = 1.229\ V \qquad (3.3)$$

Alkaline

$$O_2 + 2H_2O + 4e^- \rightarrow 4OH^- \quad E^0 = 0.401\ V \qquad (3.4)$$

In acidic conditions, as studied in this section, the four electron pathway would be the preferred mechanism due to the lack of production of H_2O_2, which is a known interferent produced in electrochemical reactions. Research has shown that common catalysts such as

platinum nanoparticles (supported upon carbon substrates) primarily exhibit the non-peroxide forming direct four electron pathway,[221] however such electrodes are also widely known to be susceptible to fouling over a period of time; one of the reasons being the small, yet significant, presence of the two electron process. The two electron pathway described in equation 3.2 is an electrochemical route which creates the highly corrosive H_2O_2, forming radicals such as •OOH and •OH,[317] which require little activation energy to react with carboxylic terminating groups on Nafion (or similar) in Proton Exchange Membranes (PEM). Such processes effectively reduce fuel cell efficiency.[318] Consequently this section aims to investigate the ORR towards several graphene modifications and elucidate the electrochemical mechanism for each material (whether that be a two or four electron process); a direct four electron pathway would be highly favourable, producing water as a product (*viz.* equation 3.4) instead of hydrogen peroxide (*viz*. equation 3.2).

Graphenes, though electrochemically inert, have the potential to be used as catalyst supports in the ORR. Physical properties such as high surface area and mechanical strength make pristine graphene an ideal material to focus upon, and consequently may have potential to be utilised as a catalyst support which is free from any contaminants. As well as pristine graphene, the electrochemical reduction of oxygen using commercially available carbon modifications which exhibit high oxygen contents, such as Q-Graphene and Graphene Oxide (GO) are investigated. The aim of this section is to ascertain the electrochemical mechanism of each type of carbonaceous material and discuss in terms of edge planes and oxygenated species density.

3.4.2 RESULTS AND DISCUSSION

The ORR at graphitic electrodes is first investigated as a benchmark prior to further modifications with graphene/graphitic materials. Figure 3.21 depicts typical voltammetric profiles obtained for the electrochemical reduction of oxygen in 0.1 M H_2SO_4, utilising both EPPG and BPPG electrodes, which give rise to cathodic peaks at -0.58 V and -0.95 V (*vs*. SCE; 100 mV s^{-1}), respectively. Comparably, blank scans have been provided in Figure 3.21. A small reduction wave is evident at -0.48 V (*vs*. SCE; 100 mV s^{-1}) utilising an EPPG electrode in deoxygenated 0.1 M H_2SO_4, likely indicating the presence of trace amounts of oxygen dissolved in the solution after degassing. The responses observed at both electrode substrates are in excellent agreement with prior independent literature reports and the difference in voltammetric peak potentials highlight the dependence of edge-plane-like sites/defects on the electrochemical reduction of oxygen.[221] The EPPG electrode has a greater global surface coverage of edge-plane-like sites/defects over that of the BPPG electrode and hence the former gives rise to a voltammetric peak at a lower potential than the latter, indicating a higher activity towards the ORR.[221] Indeed it has been shown that in acidic media, as used here, the relative activity of carbon based electrodes varies greatly depending upon the type of carbon utilised (greatest to the lowest activity towards the reduction of oxygen): EPPG > GC > BPPG > BDD.[221] This indicates that the electronic strucutre (density of states) comprising the electrode surface is a key factor. The investigation is continued towards carbon-based electrode modifications with graphenes in order to see whether oxygenated species upon the surface further affects the ORR.

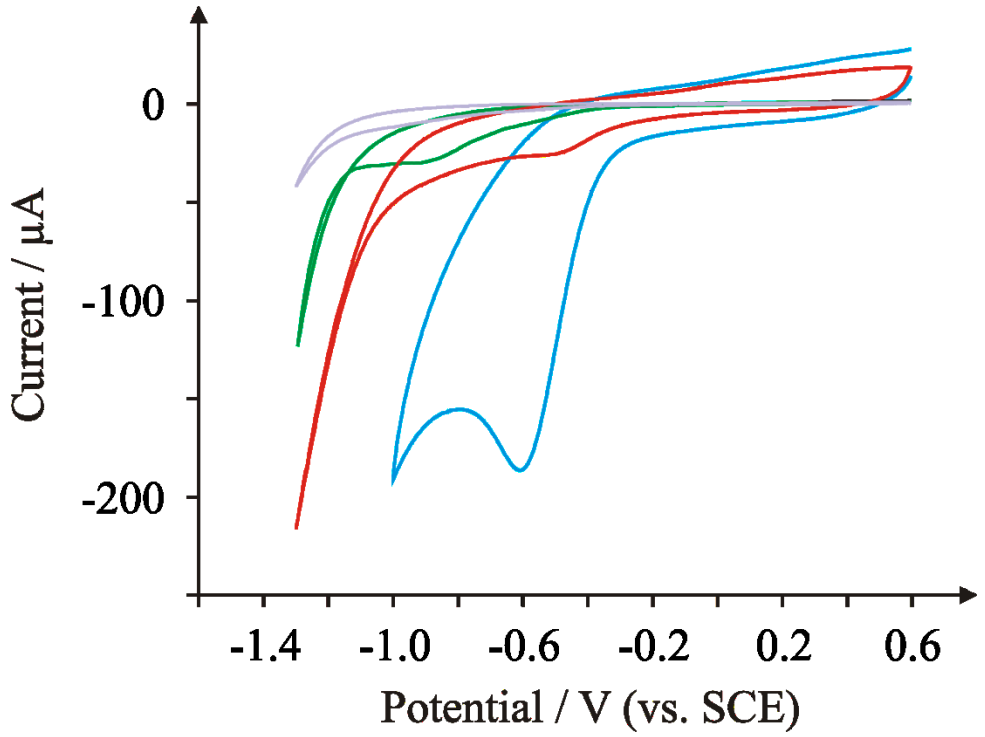

Figure 3.21: The ORR in 0.1M H_2SO_4 at an EPPG electrode (blue line) and a BPPG electrode (green line), and blank deoxygenated scans using an EPPG (red line) and BPPG (grey line) electrode. Scan rate: 100 mV s^{-1}.

ELECTROCHEMICAL REDUCTION OF OXYGEN UTILISING PRISTINE GRAPHENE

Attention was next turned to exploring the electrochemical reduction of oxygen at pristine graphene modified graphitic electrodes. Pristine graphene is utilised due to its commercial availability as well as its unique characteristics of non-chemically modified surfactant-free graphene, where the electrochemical responses observed are solely due to the graphene structure itself and not of the impurities or surfactants; these permutations are sometimes ignored in the literature.[319, 320] One may expect pristine graphene to exhibit electrode kinetics akin to that of BPPG according to previous literature reports,[320] and as shown in Figure 3.22, this rationale is confirmed.

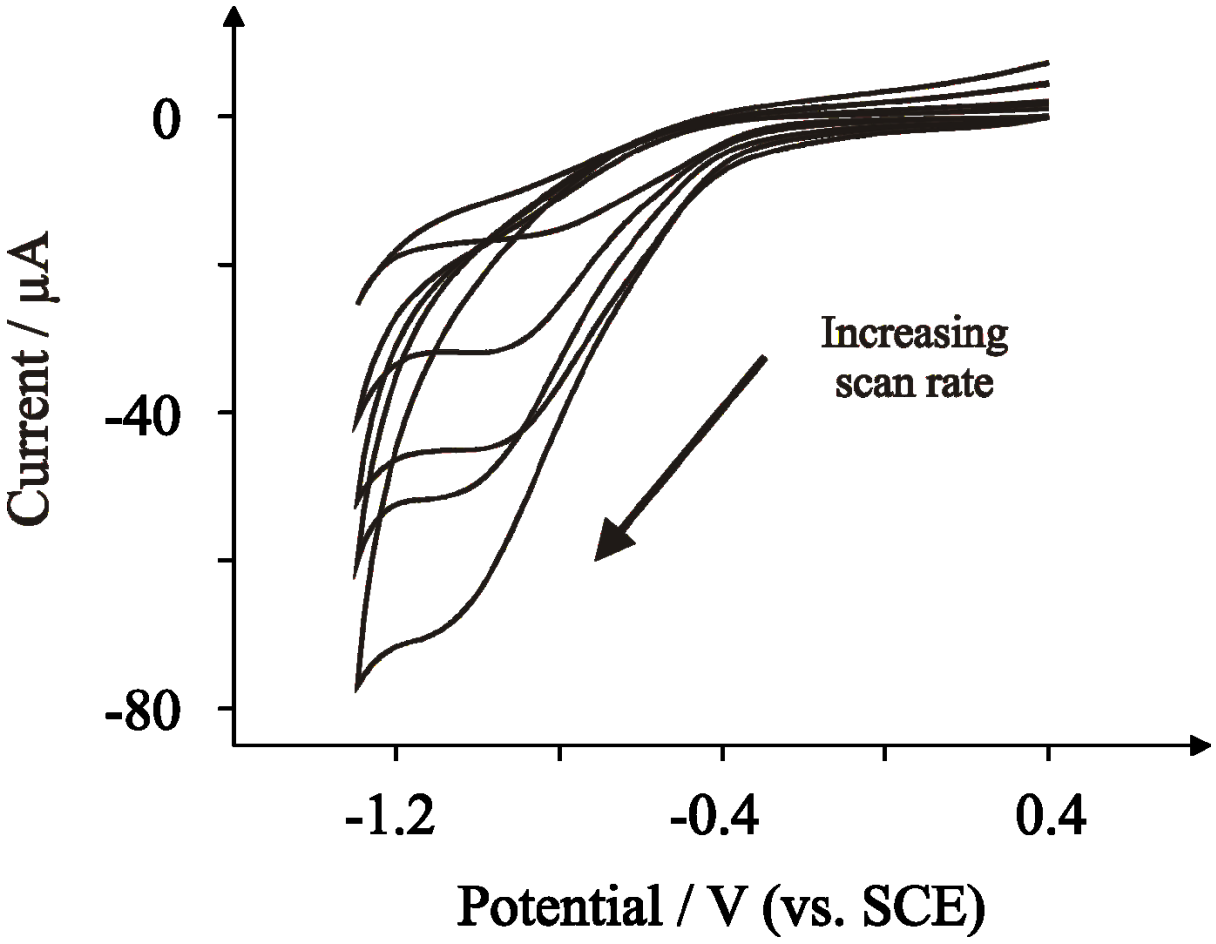

Figure 3.22: Scan rate study of the ORR utilising a 20 ng pristine graphene modified EPPG electrode. Scan rates: 10 mV s^{-1}; 50 mV s^{-1}; 100 mV s^{-1}; 200 mV s^{-1}; and 400 mV s^{-1}.

Inspection of Figure 3.22 shows typical voltammetric profiles with a reduction wave present at -1.02 V (*vs*. SCE; 100 mV s^{-1}) for an EPPG electrode modified with 20 ng pristine graphene. This corresponds to a potential much higher than the bare EPPG electrode (-0.58 V, see Figure 3.21). Additionally, in comparison to the EPPG electrode, the peak current decreases significantly and there is a broadening of the peak. Such voltammetric behaviour is typical of a system requiring a high overpotential to activate the electrochemical process. Upon comparison to the bare EPPG response observed previously in Figure 3.21, it is clear that the pristine graphene hinders the electron transfer processes. Similar observations are noted in the case of BPPG, where a peak potential of -0.95 V is observed at an unmodified

electrode which, upon addition of 20 ng pristine graphene, becomes more electronegative with a peak potential of -1.08 V (100 mV s^{-1}). The peak currents for both the graphene modified electrodes are noted to be similar. The peak potentials observed for the pristine graphene modified electrodes are far more negative than observed in the literature for multi-walled carbon nanotubes,[221] as one may expect due to the predominantly basal nature of the pristine graphene,[320] which exhibits slow electron transfer. Carbon nanotubes generally exhibit more edge-plane-like voltammetry,[321, 322] which reduces the observed voltammetric potential. If one requires an electrode material to activate oxygen reduction, pristine graphene is clearly not the correct material to choose because a higher overpotential (compared to edge plane graphite) is consistently required to activate the ORR.

Next considered is the effect of the scan rate upon the peak potential of the ORR. A scan rate study was performed for a 20 ng pristine graphene modified electrode, the results of which are depicted in Figure 3.22. Surprisingly, the increase in scan rate does not result in the reduction wave being lost out of the solvent potential window and only small increases in the potential are observed. Analysis of the voltammetric peak height as a function of the square-root of applied scan rate was found to be linear (I_P^{red} / μA = -0.2491 μA / (mV s^{-1})$^{0.5}$ - 6.2802 μA; $N = 8$; $R^2 = 0.83$) confirming a diffusionally limited process in operation.

The effect of pristine graphene coverage upon the observed voltammetric response was also investigated and is presented in Figure 3.23. Our experiments show that graphene initially causes the potential of the ORR to increase to higher (more negative) potentials and thus the rate of the electrochemical reaction becomes slower than that of a bare EPPG electrode. However, upon further addition of pristine graphene upon the EPPG surface (up to 100 ng), the peak potential decreases, indicating an increase in the rate of the electrochemical reaction. This is attributed to the graphene initially ordering itself upon the electrode surface in a stacked π-π fashion, which intuitively exposes more of the basal plane of the graphene

sheets.[320] However an increase in stacking of the graphene sheets exposes more edge-plane-like sites at the electrode surface which are known to exhibit faster electron transfer than the basal plane sites. These observations are not too dissimilar to work by Brownson *et al*. who proposed ‘’Zone I’’ and ‘’Zone II’’ type behaviour in the case of pristine graphene towards known redox probes such as potassium ferrocyanide,[320] where in this case, ‘’Zone I’’ would be the 0 - 10 ng region and ‘’Zone II’’ would be the region thereafter. Interestingly, Brownson *et al.* further proposed that ‘’Zone III’’ would be theoretically observed for a large graphene coverage, which would exhibit a ΔE_P of less than 59 mV under standard conditions (‘thin-layer’ type behaviour) for an ideal Nernstian system due to electroactive species being trapped at the electrode surface.[135] To speculate as to whether ‘’Zone III’’ type behaviour is being observed at 1000 ng, a plot of $\log_{10} I_P$ vs. $\log_{10} \upsilon$ was constructed yielding a linear gradient of 0.4 which corresponds to diffusional behaviour, whereas ‘’Zone III’’ type behaviour would exhibit a ‘thin-layer’ type gradient of 0.8.

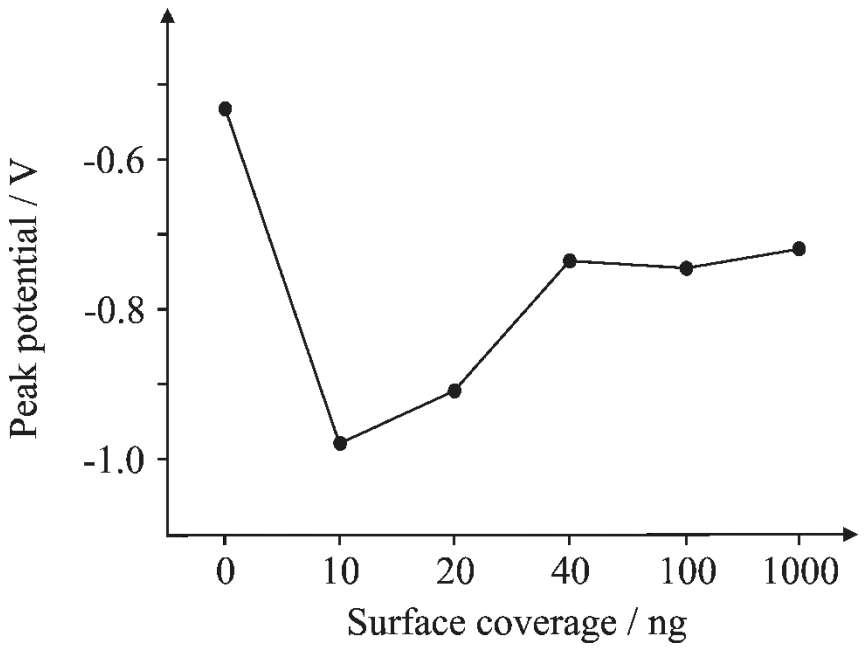

Figure 3.23: The effect of the E_P due to the mass of pristine graphene immobilised upon the surface of an EPPG electrode for the ORR. Scan rate: 100 mV s^{-1}.

Throughout this section, the observed electrochemical responses are considered in terms of both the density of states and also the density and composition of oxygenated species present. However due to the low oxygen content exhibited by pristine graphene, it is assumed that the role of oxygenated species (4.96% atomic oxygen, 531.64 eV, C=O and C-O groups) is less prevalent in the case of pristine graphene and therefore such analyses have not been considered for pristine graphene.

ELECTROCHEMICAL REDUCTION OF OXYGEN UTILISING Q-GRAPHENE

Attention is turned to graphitic species with several types of oxygenated groups present, as it has been shown in previous literature that differing oxygenated species can play a beneficial role in the reduction of the peak potential associated with the ORR.[323, 324] The first oxygenated graphene studied is Q-Graphene, a commercially available type of carbon powder, as it has been well characterised and shown in previous literature to contain large amount of oxygenated species with an O/C ratio of 0.81 (*via* XPS), mainly in the form of C=O terminating groups.[325]

Figure 3.24 depicts voltammetric profiles obtained from the electrochemical reduction of oxygen. At an EPPG electrode, the peak potential of -0.58 V observed at a bare EPPG electrode decreases slightly upon the addition of Q-Graphene, to -0.54 V (*vs*. SCE). The response on BPPG electrodes is different, where a small peak is observable at -0.91 V for a BPPG electrode modified with Q-Graphene, which is similar to a bare BPPG electrode which exhibits a peak potential of -0.95 V (*vs*. SCE). However there is also an additional voltammetric peak at -0.59 V (*vs*. SCE), which is similar to the edge-plane-like peak observed with a bare BPPG electrode.

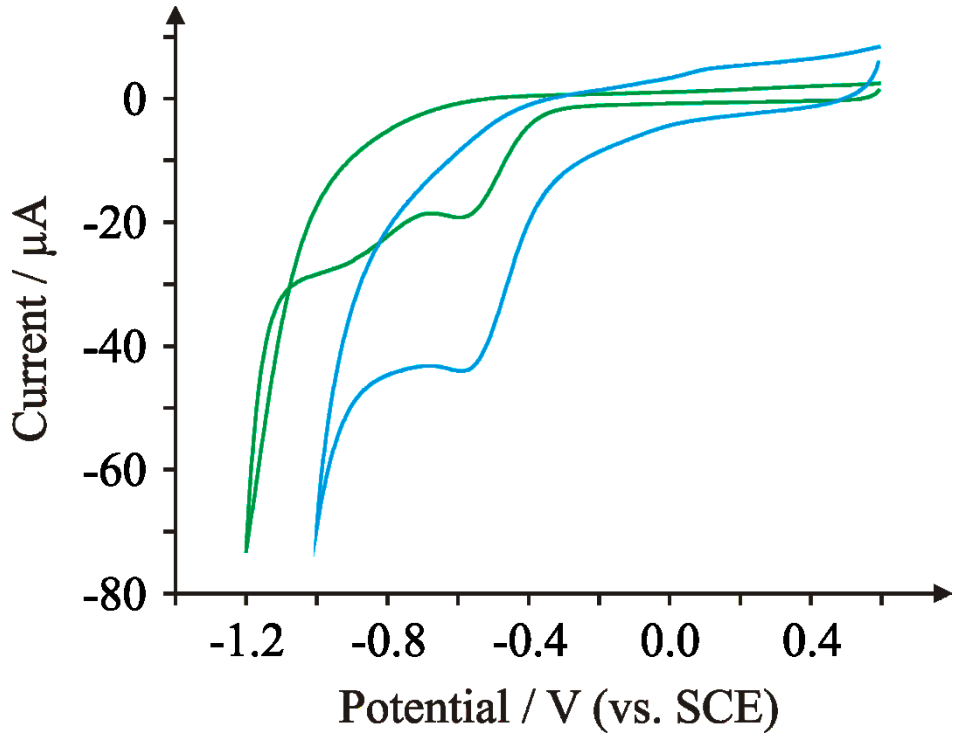

Figure 3.24: Cyclic voltammetric profiles depicting the electrochemical reduction of oxygen in 0.1 M H_2SO_4 utilising 20 ng Q-Graphene modified EPPG (blue line) and BPPG (green line) electrodes. Scan rate: 100 mV s^{-1}.

Q-Graphene has been shown in previous literature to exhibit varying properties, depending upon the target analyte, and more specifically the sensitivity of target analytes to oxygenated species.[325] Hence the density of oxygenated species associated with Q-Graphene appears to be dictating the electrochemical response. In the case of the ORR, the peak potential at a Q-Graphene modified EPPG electrode decreases. However, it has been shown previously that some oxygenated species can be beneficial for the ORR.[324] Specifically, Sarapuu *et al.* show in their work that electro-grafted anthraquinone groups can be beneficial for the reduction of oxygen, yet too many quinone species can be detrimental for the ORR.[324] In the case of Q-Graphene (44.3% carbon content with 8.9% surface oxygenated groups, C=O) the amount of carbonyl terminating groups are high and hence potentially inhibit

electron transfer. To test whether Q-Graphene is a case similar to this where there are too many oxygenated species present, a less oxygenated species must be tested (GO – see later).

The effect of coverage of Q-Graphene is also investigated, utilising masses ranging between 5 and 1000 ng, and shows that the peak potential is independent of the amount of Q-Graphene immobilised upon the surface of the electrode. The effect of the scan rate upon the observed peak potential of the ORR at Q-Graphene modified electrodes was explored and is depicted in Figure 3.25. A plot of peak current *versus* the square root of the applied scan rate was found to be linear (I_P^{red} / μA = -1.0334 μA / (mV s^{-1})$^{0.5}$ - 1.7055 μA; N = 6; R^2 = 0.95), pertaining to a diffusional process. Similar to pristine graphene, the reduction wave is still observed at scan rates as high as 400 mV s^{-1}.

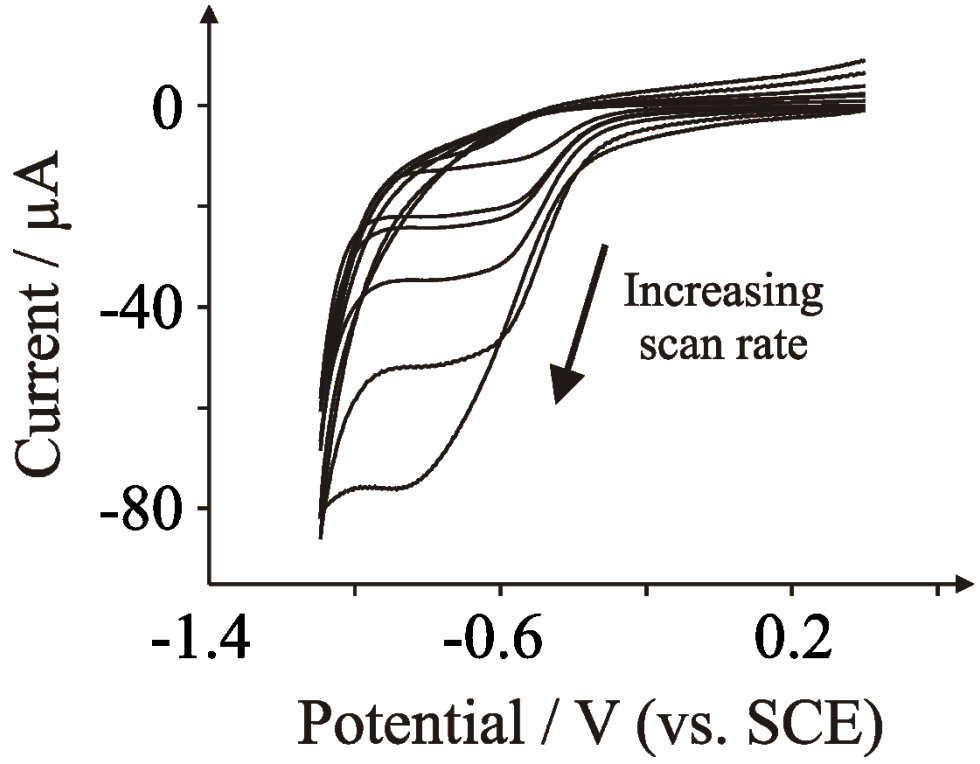

Figure 3.25: Scan rate study of the ORR in 0.1 M H_2SO_4 utilising a 20 ng Q-Graphene modified EPPG electrode.

Attention is turned to another oxygenated graphene species, GO. The GO utilised in this work was characterized in-house previously and exhibited an O/C ratio of 0.492 (*via* XPS),[284] indicating the graphene material to have more oxygen than pristine graphene, but less than that of Q-Graphene.[325] Figure 3.26 depicts voltammetric profiles obtained as a result of the electrochemical reduction of oxygen at GO modified electrodes. GO shows electrocatalytic properties compared to EPPG, where the peak potential reduces from -0.58 V (bare EPPG) to -0.51 V upon the addition of GO to an EPPG surface. Similarly, for the case of the BPPG electrode, the peak potential reduces from -0.95 V (bare BPPG) to -0.51 V. Therefore it can be assumed with reasonable confidence that the electrochemical response of GO is independent of the underlying electrode in this case. The electrochemical responses observed suggest that the oxygenated species associated with GO actually catalyse the ORR.

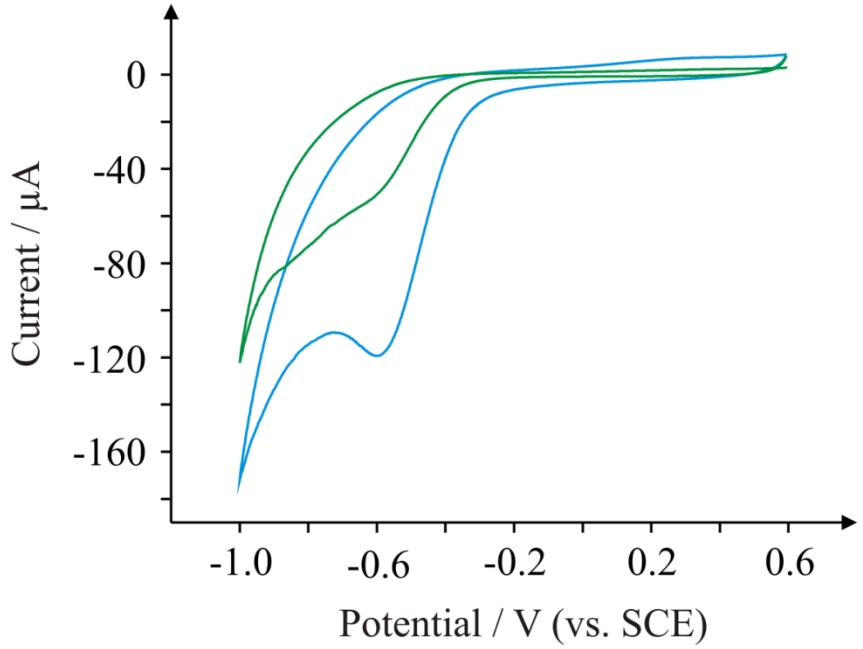

Figure 3.26: Cyclic voltammetric profiles of the electrochemical reduction of oxygen in 0.1 M H_2SO_4 using GO modified (blue line) EPPG and (green line) BPPG electrodes. Scan rate: 100 mV s^{-1}.

The scan rate study utilising GO in Figure 3.27 shows that the increase in scan rate yields a semi-linear increase in peak potential and hence a quasi-reversible system. Furthermore, analysis of $\log_{10} I_P$ *versus* $\log_{10} \upsilon$ showed that the electrochemical process does not exhibit any thin-layer effects, as has been observed in the case of carbon nanotubes.[326]

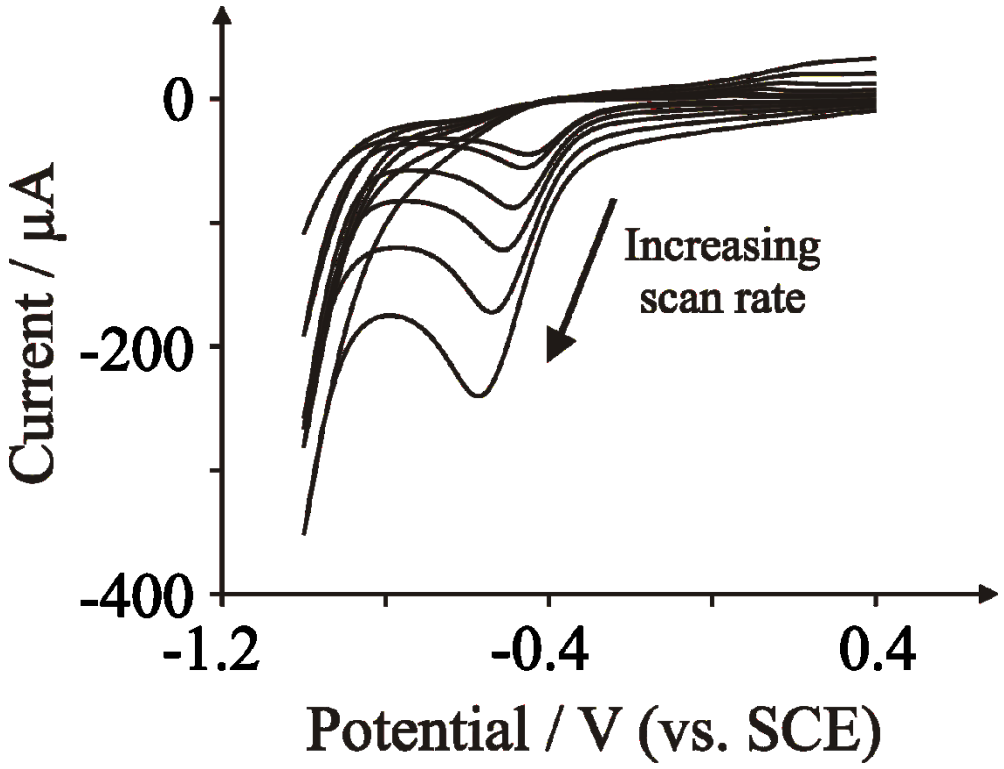

Figure 3.27: Scan rate study of a GO modified EPPG electrode. Scan rates: 10 mV s^{-1}; 20 mV s^{-1}; 50 mV s^{-1}; 100 mV s^{-1}; 200 mV s^{-1}; and 400 mV s^{-1}.

Further additions of GO immobilised upon the electrode surface were next explored due to the observed ability of graphene to reduce the peak potential. The peak potential was observed to become less electronegative upon the addition of small increments of GO; the peak potential decreases from -0.51 V with a 1.375 µg addition to -0.45 V (*vs*. SCE) with a 5.500 µg addition upon a BPPG electrode. The electrode is therefore initially exhibiting characteristics more akin to that of an EPPG electrode upon increasing additions of GO,

before decreasing to voltammetric potentials even lower than the bare EPPG electrode. Further additions did not improve the electrochemical response further.

In comparison with work by Sarapuu *et al.*,[324] this work infers that for oxygenated graphenes, in addition to the high amount of edge-plane-like sites and quinone species available, which produce H_2O_2 in the electrochemical reaction, there are 2 further factors which play an important role in the observed electrochemical responses: i) the graphene oxygen content (O/C) has to be high enough to catalyse the electrochemical reduction of O_2; and ii) the surface oxygen content has to be low enough so the oxygenated species do not reduce the observed peak currents as previously observed for anthraquinone species grafted upon glassy carbon electrodes.[323, 324] The GO displays a balance between oxygen and carbon content with an O/C ratio of 0.492,[284] exhibiting an E_P of -0.51 V (*vs*. SCE) and relatively large peak currents, whereas the Q-Graphene shows a far larger O/C ratio of 0.81,[325] exhibiting an E_P of -0.54 V but with small peak currents. In addition, it is noted that GO exhibits a higher percentage of C-O than carbonyl species, pertaining to an improved electrochemical response for such a terminating species (for example C-OH). Taking these factors into account, it is concluded that not only the amount of oxygenated species present, but the type of oxygenated species present has to be considered.

While one can observe that there are differences in the peak potentials corresponding from the electrochemical reduction of oxygen at the graphene modified electrodes, further insights can be derived from Tafel analysis which involves analysis of the voltammograms by plotting E_P *vs*. $\log_{10}I$. Such a plot was constructed for all modified electrodes and the bare EPPG electrode. Tafel analysis can subsequently be performed using equation 3.5:

$$b = \frac{2.303RT}{(\alpha n')F}, \tag{3.5}$$

where b (measured in V) is the slope of E_P against $\log_{10}I$, α is the electron transfer coefficient, F is the Faraday constant and n' is the number of electrodes transferred in the rate determining step. The Tafel gradient for the bare EPPG electrode was found to correspond to 0.15 V, which is in agreement with independent reports,[221] estimating a value for $\alpha n'$ of 0.39. This value suggests that it is the transfer of the first electron which is electrochemically irreversible, so that n' = 1 and α = 0.4. Using the literature value of an oxygen saturated solution (0.9 mM is assumed taking concentration and temperature into consideration according to Kaskiala[327]) and a literature diffusion coefficient value of 2.0 x 10^{-5} cm^2 s^{-1},[328] the number of electrons transferred overall, n, was deduced from the following Randles–Ševćik relationship for a diffusion controlled electrochemically irreversible reaction in which the first electron transfer is the rate determining step:

$$I_P = -0.496n\sqrt{n'\alpha}FA[O_2]\sqrt{\frac{F\upsilon D}{RT}} \quad . \tag{3.6}$$

Therefore, using equation 3.6, a value of n = 2 was deduced, indicating that the electrochemical reduction of oxygen at a bare EPPG electrode proceeds *via* equation 3.1, producing H_2O_2. In comparison, a bare BPPG electrode gives a Tafel value of 0.39 V, estimating a value of 0.5 for $\alpha n'$. Such analysis is in agreement with previous literature reports.[221] The Tafel gradients, and the corresponding values of $\alpha n'$ for the pristine, Q-Graphene, and GO modified electrodes, are as follows: 0.16 V, 0.37; 0.12 V, 0.51; 0.10 V, 0.57. It is interesting to note that in all cases, n' = 1, indicating that the transfer of the first electron is electrochemically irreversible and that a change in the symmetry of the transition state is evident following different modifications of graphene. It is also clear that GO gives rise to the more electrochemically "reversible" process with the smallest Tafel gradient being

observed; this is not surprising given that the material comprises a high density of edge plane sites, and the high oxygen content in the form of C-O groups will also contribute to the production of H_2O_2. Indeed, using equation 3.6 and the corresponding literature values and (baseline corrected) peak currents, the total number of electrons in the electrochemical process was found to correspond to 2 for the pristine, Q-Graphene and GO modified electrodes, which shows that the electrochemical reduction of oxygen corresponds to that described in equation 3.1, producing H_2O_2. It is clear that while slightly different potentials for the ORR reaction are observed, there is no substantial change in mechanism. These observations are highly important in applications where graphene (and its family, as studied here) is used *per se* in the ORR and also, for example, as a catalyst support.

The discussion is continued by estimating the peroxide yield through use of equations 3.7-3.9. Firstly, the capacitance of an electrochemical process can be estimated through equation 3.7 where C is the capacitance, I is the observed peak current at some potential and υ is the scan rate:

$$C = \frac{I}{\upsilon}. \tag{3.7}$$

The charge can then be calculated from equation 3.8 where Q is the charge and V is the potential:

$$Q = CV. \tag{3.8}$$

Finally the amount of oxygen electrolysed in the reaction can be calculated *via* equation 3.9 where n is the number of electrons transferred, F is the Faraday constant and N is the number of moles of oxygen electrolysed:

$$Q = nFN. \tag{3.9}$$

According to equation 3.2, the production of H_2O_2 is in a 1:1 stoichiometric ratio to oxygen and thus the concentration of oxygen electrolysed is theoretically the same as the concentration of H_2O_2 produced in the electrochemical reaction. A table of the estimated peroxide yields calculated from a cell without constant oxygen bubbling is presented in Table 3.4 at a fixed volume of 10 mL H_2SO_4 and at a scan rate of 100 mV s^{-1} for qualitative purposes.

Table 3.4: Estimated peroxide yields for each electrode in a fixed volume of H_2SO_4 recorded via cyclic voltammetry at 100 mV s^{-1}. Yields are determined via equations 3.7-3.9.

Electrode	Peroxide Yield / nM
EPPG	201
BPPG	116
Graphene oxide	190
Q-Graphene	43.9
Pristine graphene	30.8

Table 3.4 highlights that the magnitude of the peroxide yield of the different graphenes decreases as follows: EPPG > GO > BPPG > Q-graphene > pristine graphene. The magnitude of the peroxide yields do not follow the same pattern as the trend in peak potentials (GO > Q-Graphene > EPPG > BPPG > pristine graphene) however this is perhaps unsurprising considering the peroxide yield is related to the current, and not the potential. Future work with rotating disc and ring disc electrodes *via* Koutecký–Levich analysis[324] will allow deeper insights into the mechanism of the electrochemical reduction of oxygen. It is interesting that

if such analyses are correct and prisitne graphene creates the least amount of peroxide, then there should be further research into its usage in the ORR. The high activation potential of a graphene electrode for the ORR would be extremely beneficial to reduce the peroxide yield in a fuel cell, for instance. Furthermore, graphene electrodes could be useful for galvanic cells, provided low output currents are required.

Last considered is the impact of the above findings. Figure 3.28 shows a schematic representation of the scenario in which graphene is decorated with a catalyst for the ORR reaction. In this case, a heterogeneous surface results where the primary electrochemical reaction involving the catalyst, which converts oxygen to water, is also accompanied by a secondary unwanted electrochemical reaction on the graphene surface, converting oxygen to H_2O_2. Of course, the severity of this will depend upon the desired power density of the device, as the potentials to initiate the graphene ORR reaction and the catalyst ORR reaction differ immensely. For example if platinum is used as a catalyst upon a graphene-based support, the ORR would take place only at platinum the surface because the potential range for ORR at platinum in acid solution is from ~ 0.98 V to ~ 0.60 V *vs*. RHE, while at the mentioned potentials the same reaction at the carbon based materials, including graphene too, does not take place at all. In any case, the future for such work lies in galvanic cells where potentials are generated from two metals and not electrolytic cells where potentials are potentiostatically controlled.

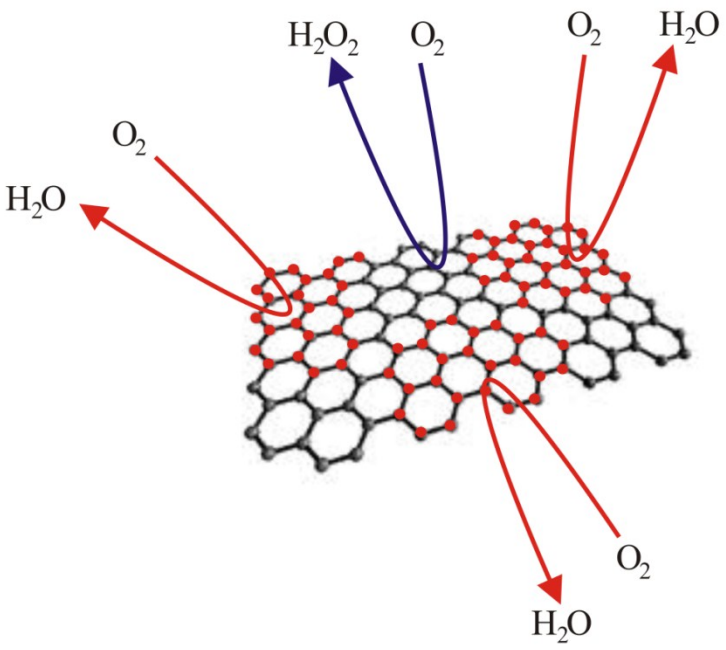

Figure 3.28: Schematic representation of the scenario in which graphene is decorated with a catalyst for the ORR reaction. A heterogeneous surface will result, where the primary electrochemical reaction converting oxygen to water is also accompanied by a secondary electrochemical reaction on the graphene, per se, which is converting oxygen to hydrogen peroxide. The exact electrochemical processes will depend upon the chosen catalyst and graphene (see text).

Clearly, for the case of ORR catalyst supported upon graphene, the major reason for choosing such a catalyst is to avoid the detrimental formation of hydrogen peroxide; as such researchers need to carefully consider the use of graphene as a catalyst support for use in the ORR reaction.

3.4.3 SUMMARY

This section has explored the electrochemical reduction of oxygen at pristine, Q-Graphene and GO modified electrodes due to the reported beneficial use of utilising graphene

within fuel cells. Analysis of the electrochemical reduction of oxygen at these graphenes has indicated that pristine, GO and Q-Graphene electrochemically reduce oxygen through a 2 electron pathway, which in acidic media as studied here, produced H_2O_2. Tafel analysis indicated that for each graphene modified electrode studied here, the transfer of the first electron is the rate determining step. Additionally it is found that it is not only the edge plane content of the graphene material that is important, but also the critical balance of oxygen groups residing on the graphene surface in terms of the density and the type of oxygen functional groups. As such, the use of graphene modified electrodes for the ORR is highly fascinating.

3.5 CONCLUSIONS

This Chapter has investigated the electrochemical responses of a variety of types of carbon materials, including pristine graphene, Q-Graphene, and graphene oxide, towards a range of different target analytes. The electrochemical response of each material is highly dependent on a number of parameters: the density and type of oxygenated functionality of the carbonaceous material; the surface sensitivity of the target analyte; and the ability of the analyte to adsorb upon the basal plane of a graphene sheet.

The electrochemistry of DNA bases was proven to be a complex scenario, particularly in the case of guanine, where a decrease in observed oxidation potential was observed. This observation is the first of its kind in terms of apparent electrocatalytic properties of a graphene structure. Many previous literature reports attribute graphenes to exhibit electrocatalytic effects, but such observations are typical of metal ions and surfactants catalysing the electrochemical processes. The adsorptive properties of guanine upon a basal plane of graphene is believed to be the major reason why the oxidation potential is reduced for guanine. However, the same is not observed for adenine. This was furthered towards SA, but the resulting voltammetry yielded no significant changes in peak potential, although a change in wave shape was evident, pertaining perhaps to a stripping mechanism.

The electrochemistry of oxygenated carbon materials was investigated by characterising Q-Graphene for the first time, and also exploring graphene oxide. Oxygenated species were shown to be highly analyte specific; in other words, specific interactions with oxygenated species can enhance or inhibit the electrochemical responses, depending upon the analyte in question. For instance, Q-Graphene was shown to not affect the electrochemistry of hexamine-ruthenium (III) chloride significantly, while for potassium ferrocyanide, the ΔE_P

was observed to decrease quite dramatically. Therefore, inner-sphere redox probes such as potassium ferrocyanide must exhibit a specific oxygenated species interaction to catalyse this process. However, such a process was shown to be species-dependent when the oxygen reduction reaction was investigated. The application of pristine graphene to an electrode surface inspired a large overpotential to catalyse oxygen reduction, compared to both Q-Graphene and graphene oxide. In fact, the graphene oxide exhibited a reduction in the reduction potential of oxygen compared to EPPG. Q-Graphene was shown to exhibit a similar response, though the voltammetry did allude to a number of processes taking place, suggesting that the range of oxygenated species on the Q-Graphene surfaces contributed differently to the observed voltammetry within the potential window.

The next section will consolidate work from this Chapter, particularly in relation to oxygenated species, and explore the application of SPEs to some model systems.

CHAPTER 4
SCREEN-PRINTED ELECTRODES: RELEVANT VOLTAMMETRIC APPLICATIONS

The previous section focussed upon carbon materials for use as working electrodes, and found that the surface functionalities were key to explaining observed voltammetric trends between electrochemical systems. Screen-Printed Electrodes (SPEs) also need to be considered prior to the impedimetric investigations which are explored later in this thesis. SPEs are normally thought of as an electroanalytical tool because of their portability, scale of economics, and disposability; thus investigation towards some novel systems is paramount to drive forward the use of SPEs. This Chapter will focus upon some novel systems and discuss them in terms of clinical applications. This section will build upon current knowledge of SPEs and contributes two papers to the literature: the first being the detection of bronchiodilatory medicine;[329] and the second being a novel detection strategy for kidney filtration problems.[330]

All chemicals were of the highest grade available, used without further purification, and obtained from Sigma Aldrich (UK). All aqueous solutions were made using deionised water of resistivity no less than 18.2 MΩ cm. Several buffer solutions were appropriately selected: 0.1 M acetate buffer (pH 4.0); 0.1 M Phosphate Buffer Solution (PBS) (pH 7.4); and 0.1 M borate buffer (pH 11.5). For pH 1.0, 0.1 M sulphuric acid was utilised as the aqueous medium. Theophylline (TP) stock solutions were prepared in each appropriate pH prior to testing. The creatinine source utilised within this work was creatinine hydrochloride, obtained from Sigma Aldrich, and was dissolved in pH 13 NaOH buffer solution for the alkaline picrate complex experiments. Picric acid solution (1.3% in water) was made into a 10 mM stock solution in pH 13 NaOH buffer solution. pH 13 was selected as interferents are more likely to react at a more neutral pH.[331] For the direct electrochemical measurements, creatinine hydrochloride was dissolved in a pH 9.4 Borate Buffer Solution (BBS).

Voltammetric data was obtained utilising an Ivium CompactStat^{TM} (Netherlands) potentiostat. SPEs (edge-plane-like, termed ESPE and basal-plane-like, termed BSPE) were fabricated in-house as described previously.[332] Briefly, a relevant carbon ink formulation for efficient connection of the three electrodes was printed onto a flexible polyester film and cured in an oven at 60 ^{o}C for 30 minutes. Next a silver/silver chloride reference electrode was included by screen-printing Ag/AgCl paste and subsequently curing at 60 ^{o}C for 30 minutes. Finally, a dielectric paste was printed on top to define the electrodes (3 mm working electrode) and protect the connections. Further information regarding the inks can be found in Reference 333. The single-walled carbon nanotube SPEs were made (termed SW-SPE) as above, except commercially available single-walled carbon nanotube ink was printed over the working electrode only following the third curing procedure[334]. The reproducibility of the batch of screen-printed sensors were found to correspond to 0.76 % RSD using the

$Ru(NH_3)^{2+/3+}$ redox probe in 1 M KCl. A *new* SPE was utilised for each experiment performed, including during concentration studies. The following macroelectrodes were also used: 3mm GC; 3 mm gold; and 4.9 mm EPPG/BPPG. All electrodes were polished prior to experimentation using diamond/alumina spray of decreasing particle sizes. UV/Vis measurements were recorded with a PerkinElmer Lambda 40 UV/Vis double beam Spectrometer. The software package was UV Winlab, which was set to measure in the range of 700-400 nm through a 1 nm slit, a cuvette path length of 1 cm and at a scan speed of 480 nm min^{-1}. All UV measurements were measured against a sample of 0.5 mM picric acid in pH 13 NaOH buffer solution.

For the direct oxidation of creatinine, CV was used with a potential window of +0.2 to +1.4 V. Creatinine additions were made from a 1 M stock solution. For the picric acid experiments, the picrate/creatinine reaction was left to proceed for five minutes before UV/Vis and voltammetric measurements. LSV in the potential window -0.1 to -1.5 V was used for electrochemical monitoring of the picrate reaction. Solutions were bubbled rigorously with oxygen-free nitrogen prior to electrochemical measurements. For the urine sample preparation, 10 mL of 1 M HCl was added to 100 mL urine, before adding 20 mL 1 M NaOH to bring it up to buffer pH. The basic urine mixture is then mixed 50:50 with pH 13 NaOH buffer solution. Overall this leaves the creatinine concentration diluted by a factor of 2.6.

4.1 DETECTION OF THEOPHYLLINE

4.1.1 INTRODUCTION

Theophylline (TP) is a commonly utilised clinical drug for treatment of respiratory diseases such as asthma, due to its bronchiodilatory effects.[335] However TP exhibits a narrow safety range,[336] which means that technologies need to exist which have the ability to monitor the levels of TP within the body. Currently, clinical practise requires regular monitoring of plasma by taking blood samples from patients, less chronic conditions may develop.[337] Such blood samples are fairly large (in excess of 25 mL and normally more than one sample is taken at once) and thus patients may consider providing these regular blood samples as problematic. Nevertheless TP still has to be monitored due to its toxicological effects; thus scaling down the detection technology for use on-site, with small sample sizes (< 100 μL), is an area worthy of serious consideration.

Current laboratory procedures for TP detection include radioimmunoassay,[338] HPLC,[339] and fluorescence polization immunoassay.[340] However such methods require skilled personnel, sample pre-treatment, and long analysis times. Consequently electrochemists have taken the opportunity to study the electrochemical oxidation of TP utilising a variety of electrode substrates.[341-345] These praiseworthy efforts of researchers have rarely been mimicked with SPEs, however; and those screen-printed sensors which have been reported require the design of complicated electrode composites.[346, 347] Such composites either contain enzymes or recognition proteins which make the electrochemistry complex. Surprisingly however, the *direct* oxidation of TP utilising SPEs appears to be overlooked in the literature. Hence, for the purposes of completeness, this section investigates the electrochemical activities of three screen-printed sensors (edge-plane-like, basal-plane-like,

and single-walled carbon nanotube SPEs) and compare to standard laboratory electrodes including gold, HOPG, GC, and BDD.

4.1.2 RESULTS AND DISCUSSION

ELECTRODE INVESTIGATION

Attention is first turned towards the electrochemical response of 1 mM TP, using several electrode substrates at physiological pH. Figure 4.1 compares all electrode substrates investigated. Inspection of Figure 4.1 reveals a general trend where the peak potential decreases as the peak current density increases; this is particularly evident for the case of electrodes such as EPPG, which exhibits a peak potential of +1.00 V and an average peak current density of 191 μA cm^{-2} (% RSD = 5%; *N* = 3). Conversely, by taking the gold electrode as an example, a large overpotential (+1.17 V) is required to drive the electrochemical oxidation of TP which compromises on both the average observed current density of 57 μA cm^{-2} and the reproducibility (% RSD = 46%; *N* = 3). Turning attention to the SPEs, a trio of SPEs are investigated, which are electrochemically divergent. Figure 4.1 shows the ESPE and the SW-SPE exhibiting similar behaviour, with peak potentials corresponding to +1.04 V and +1.03 V, respectively. The similar reactivities are likely due to the edge plane content of the respective electrodes. Remarkably, the ESPE exhibits the highest peak current density of all electrodes studied here, corresponding to an average value of 262 μA cm^{-2} and furthermore exhibiting a % RSD of 5% (*N* = 3); such an electrode could prove to be useful for electroanalytical sensing of TP. Conversely, the BSPE exhibits a high peak potential (+1.17 V) and a low peak current density of 129 μA cm^{-2}, similar to the case of the gold and BPPG electrodes. Though the observed current densities are not as high for BSPE and SW-SPE as that observed for EPPG, they still exhibit a magnitude and

reproducibility (< 5%) which are useful for electroanalytical sensing. GC and BDD both exhibit high peak potentials and low currents.

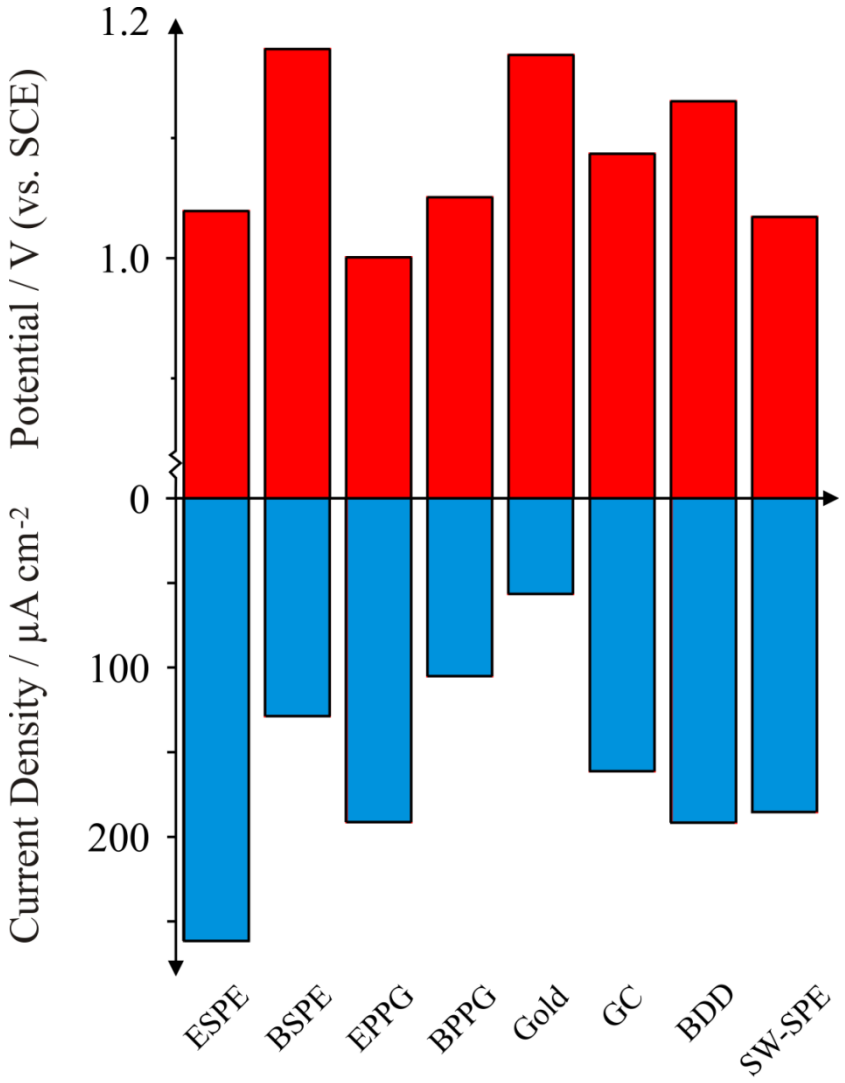

Figure 4.1: Graphical representation of peak current densities (blue) and peak potentials (red) for the series of electrodes utilised within this section. All experiments were conducted using 1 mM TP in 0.1 M PBS (pH 7.4). Scan rate: 100 mV s^{-1}.

From the above data, ESPE was chosen to continue the investigation in terms of pH and electroanalytical capabilities; the SW-SPE could potentially be also used but there is no further benefit of the carbon nanotubes in this instance, and the cost of the electrodes is much higher, rendering any further testing as frivolous.

To optimise the conditions for electroanalysis, it is necessary to investigate the effect of pH upon the observed peak potentials and currents for TP. Figure 4.2 depicts voltammetric profiles of 1 mM TP, corresponding to changes in pH. One can immediately observe that the peak potentials increase as the pH decreases (inset), yet the relative magnitude of the peak current fluctuates, indicating that the efficiency of electron transfer for TP is highly pH dependent. The plot of E_P *versus* pH, presented inset in Figure 4.2, illustrates the pH dependence of E_P for this system which is linear from pH 1 to 8.5, beyond which there is deviation; this is in agreement with its pK_a, reported to be ~8.6.[348]. The slope of the graph inset in Figure 4.2 corresponds to 61.7 mV pH^{-1} (R^2 = 0.994), corresponding to approximately an equal number of protons and electrons transferred. Above pH 8.5, a secondary wave appears (not reported), masking the analytical peak. The further peaks are believed to be a result of electrode fouling, which is apparent in strongly alkaline conditions. Given the lack of change of mechanism over the large pH range prior to the pK_a, physiological pH is selected for electroanalysis.

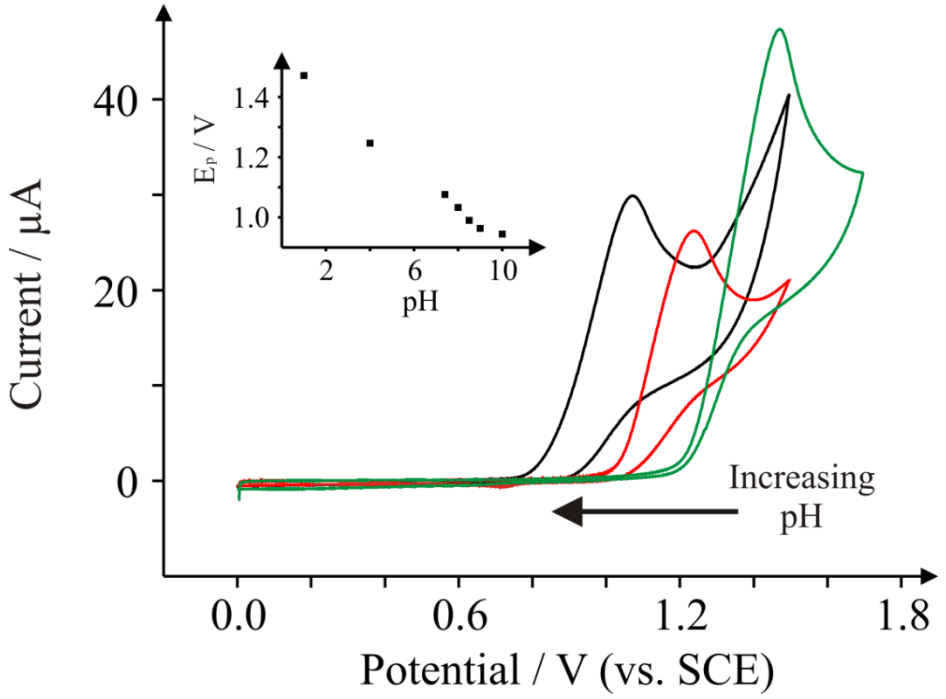

Figure 4.2: Cyclic voltammetric profiles obtained for 1 mM TP using an ESPE working electrode under various conditions: pH 1.0 (green); pH 4.2 (red); and pH 7.4 (black). Scan rate: 100 mV s^{-1}. Inset: E_P versus pH for the entire pH range utilised.

The mechanism of TP oxidation is next considered by taking into account the pH. The structure of TP is given in Figure 4.3, alongside two proposed reaction mechanisms. Given that TP has a structure which can be thought of as analogous to guanine, the proposed mechanism involves a two electron two proton oxidation of the aromatic carbon sandwiched between two electron-withdrawing nitrogen heteroatoms, as is in the case of the structurally similar guanine.[349] Of course, in highly basic conditions the oxidation of the nitrogen heteroatom to a hydroxylamine is possible in small quantities, yet the formation of the carbonyl is more likely. The fact that the E_P does not change dramatically above the pK_a acts as support for this mechanism.

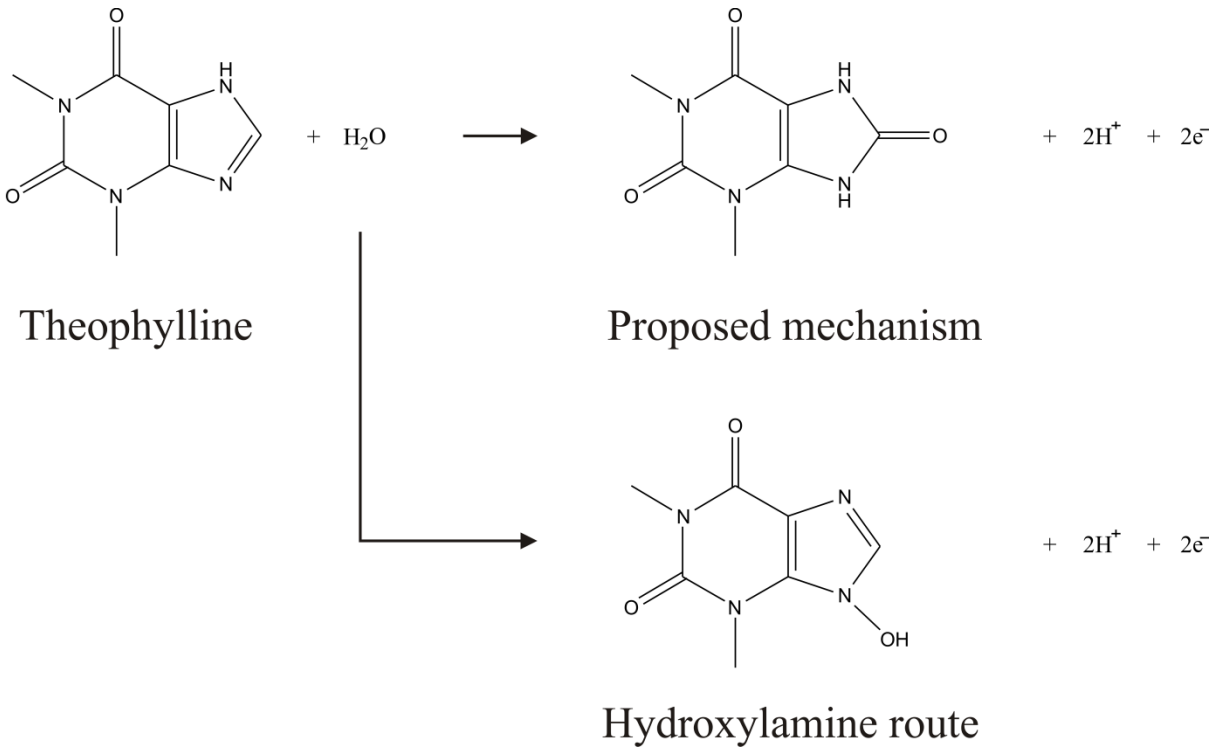

Figure 4.3: Structure of TP and two possible reaction mechanisms.

ELECTROANALYTICAL DETECTION OF THEOPHYLLINE

To demonstrate the applicability of SPEs to TP, the effect of peak currents with respect to the concentration of TP present within a buffer solution at physiological pH is investigated. Figure 4.4 depicts the effect of peak current as the concentration of TP in pH 7.4 PBS increases. The electroanalytical peak observed at +1.00 V increases linearly as a function of TP concentration, as depicted inset in Figure 4.4: I_P / μA = 12.28 μA mM^{-1} + 0.91 μA; N = 18; R^2 = 0.994, with a Limit of Detection (LoD) of 10 μM. The concentrations studied here range from 50 – 290 μM, which falls within the safe concentrations found in the plasma of medicinal TP users (55 – 110 μM – anything higher is considered dangerous),[350] indicating that this protocol is potentially acceptable for TP detection in plasma for clinical

screening applications. Furthermore, the sensors exhibit % RSD values of no more than 5% ($N = 3$) which is within the constraints of acceptable analytical chemistry.

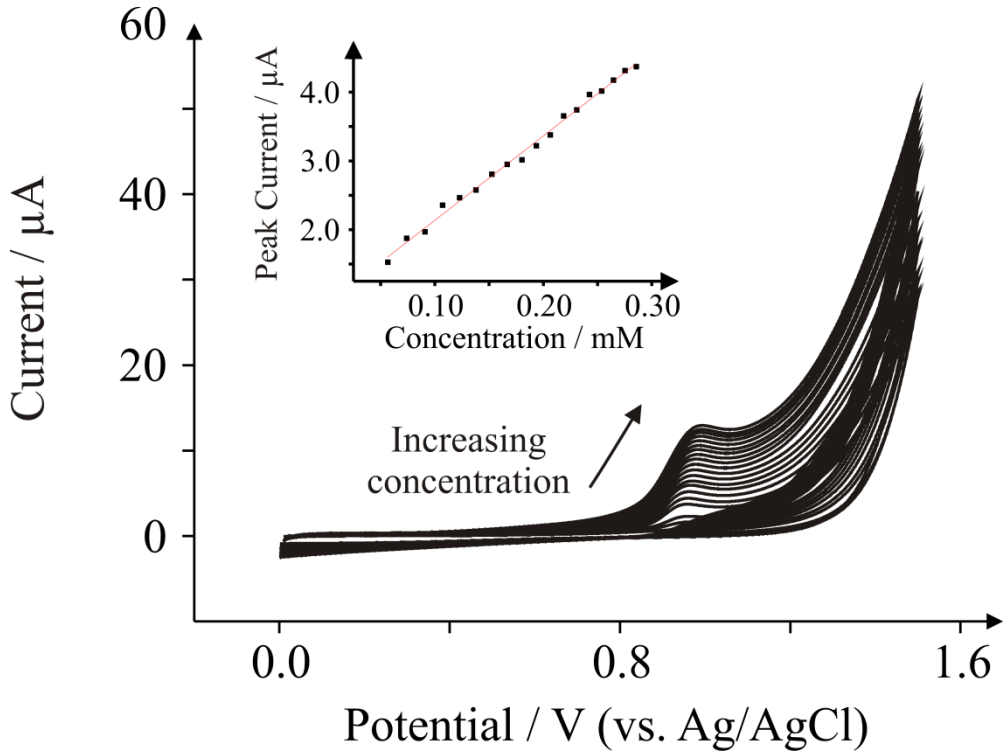

Figure 4.4: Electroanalytical cyclic voltammetric profiles of TP utilising an ESPE working electrode. The on-board carbon auxiliary and Ag/AgCl reference electrode is utilised in this instance. Scan rate: 100 mV s^{-1}.

4.1.3 SUMMARY

The detection of TP utilising SPEs has been described in this section. Screen-printed sensors such as SW-SPE and BSPE replicate standard macroelectrodes such as EPPG with a relatively small loss of peak current density and increase in peak potential. Compared to other working electrodes such as gold, BPPG, and GC, all the SPEs are superior in terms of peak current density and peak potential. ESPE however outperforms EPPG in terms of peak current density and thus is more suitable than EPPG for electroanalytical sensing of TP. SPEs also carry the added benefit of application to point-of-care systems. The SPEs are shown to

be applicable to the detection of TP under both acidic and physiological pH, yet display unstable voltammetric waves under highly alkaline conditions. A two proton two electron mechanism is proposed for the electrochemical oxidation of TP as a result of the pH investigations. The electrodes also display a remarkably high level of electroanalytical linearity at physiological pH. Such electrodes need to be investigated further towards medicinal formulations containing TP, as well as plasma samples for screening purposes; this is the focus of future work and the opportunities for such technologies are seemingly limitless in terms of electrochemically screening molecules for point-of-care applications. The next section will focus upon another medicinal application for SPEs, which is that of the detection of creatinine in urine.

4.2 DETECTION OF CREATININE FOR THE DIAGNOSIS OF KIDNEY FILTRATION PROBLEMS

4.2.1 INTRODUCTION

The monitoring of creatinine, a molecule which is produced as a waste product from the liberation of Adenosine TriPhosphate (ATP) from phosphocreatine in skeletal muscles, is regarded as the most useful way to deduce the efficiency of the kidneys and to diagnose renal failure;[351] a result of creatinine production within humans being reasonably constant.[352] Consequently, scientists have endeavoured for decades to report highly accurate and specific methods to deduce the concentration of creatinine within blood and urine.[353] Some methods to quantify creatinine are based upon the Jaffe procedure (Figure 4.5), developed by the German scientist Max Jaffe in 1886,[354-357] Capillary Zone Electrophoresis (CZE),[358-360] Liquid Chromatography-Isotope Dilution Mass Spectrometry (LC-IDMS),[361] amperometry,[362] and High Performance Liquid Chromatography (HPLC). [353, 363, 364] Most of the techniques offered are either expensive, immobile, or require rigorous sample pre-treatment, all of which are potential hurdles to overcome to provide a cheap, facile and portable detection method for creatinine for point-of-care diagnostics. Additionally, current point-of-care devices have drawbacks such as an experimental error of 11.4 %, and devices not being handheld/readily portable.[365]

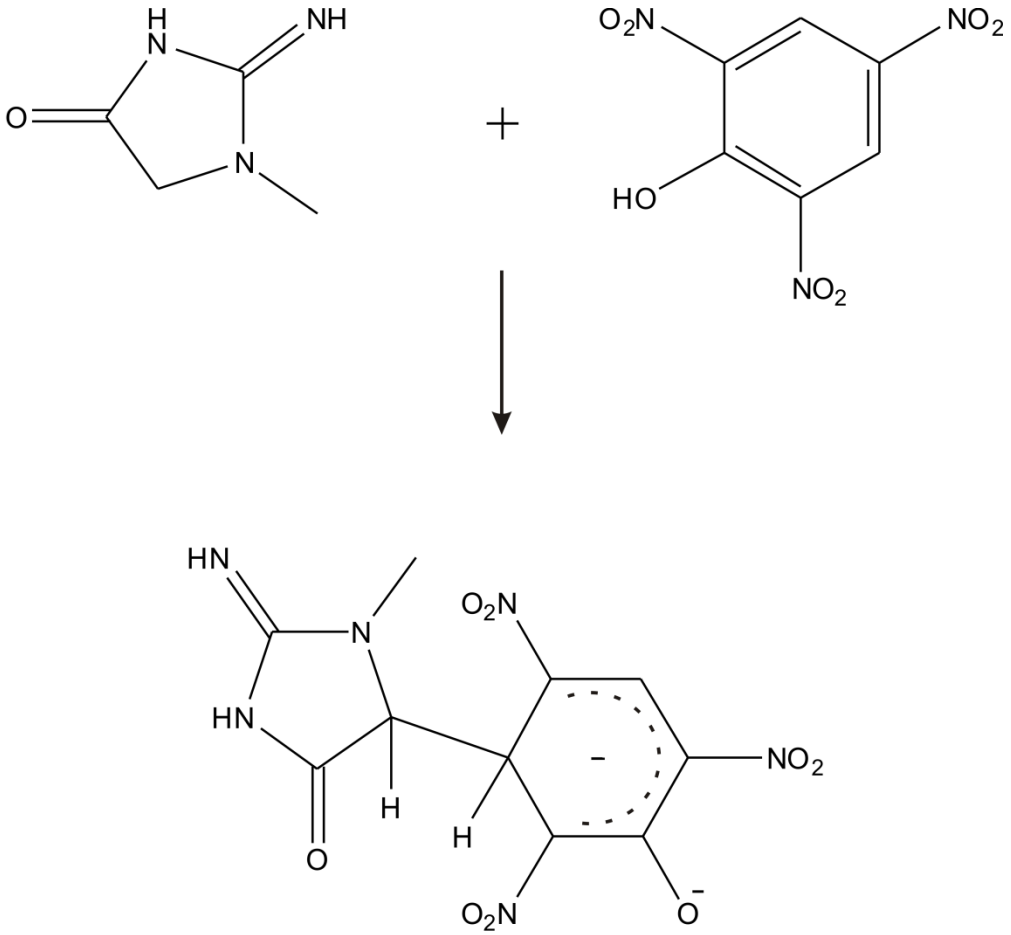

Figure 4.5: The formation of the Janovsky complex in the Jaffe reaction.[366] *Picric acid and creatinine react together to form the deep orange coloured Janovsky complex.*

Electrochemical methods to determine creatinine concentrations in blood and urine as an alternative to traditional methods such as the colourimetric Jaffe procedure have become a significant area of research in recent years, owing to the fast measurement time, the possibility of portability, inexpensiveness, and generally simple procedures.[353, 367-374] However basic the data collection may be, a problem with many of the sensor designs is the use of enzymes to produce the electrochemically detectable end product, H_2O_2.[362, 370, 375-378] Such systems carry obvious flaws of short life time, competitive inhibition and strict temperature control in addition to highly specific tailoring of the electrode surface.

Consequently, the field has taken the opportunity to focus upon enzymeless technologies for the same purpose.[367, 371, 373, 379]

The apparent sparseness of literature regarding the direct electrochemical oxidation of creatinine is a good indication of the relative difficulty in achieving such a goal, yet despite this there are several independent literature reports claiming that an enzymeless system for creatinine determination has been designed.[367, 371, 373, 379, 380] Such protocols include covalently bonding creatinine to a carbon substrate,[379] electrochemical monitoring of the picrate anion in the Jaffe procedure,[367] and through creation of polymeric films which specifically interact with creatinine.[380] These reports have had some success, particularly for the case of urinary creatinine detection; Chen *et al.* for example claim to detect creatinine concentrations within a linear range from 0.37 – 3.60 mM, with a % RSD of 3.4 %.[379] Such a detection range is perhaps satisfactory for urinary creatinine detection, as expected levels fall within a range of 500 – 2000 mg per day, equating to a mean concentration of 9 mM.[381] Hence one would expect a patient with kidney deficiency to exhibit a smaller creatinine concentration than 9 mM as creatinine is being retained by the body due to deficient glomerular filtration. Such detection ranges are unsuitable for detection of creatinine concentrations within blood and Interstitial Fluid (IF) however, both of which contain approximately 10 mg L^{-1} (88 μM) creatinine.[382]

This section endeavours to carry on the theme of enzymeless creatinine detection by investigating a previously mentioned system which electrochemically monitors the picrate anion as a function of creatinine concentration. This work by de Araújo and co-workers was the first of its kind and opens an exciting path towards the end goal of point-of-care creatinine detection.[367] The cheap, portable and facile nature of electrochemical methods could quite easily be applied to such a system. However there are some major discrepancies within their proof-of-concept work, such as the reaction times were excessively long (100 mins) and only

one electrode (GC) was tested in addition to strikingly low detection limits (the order of 10^{-7} M). These highlighted issues are addressed within this section, and in addition this section contributes further insights into different electrode substrates which can be used as electrochemical sensing platforms for this system. Some characteristic voltammetric profiles attributed to the direct oxidation of creatinine are also presented which has never been reported. The results are discussed in terms of the possibility of engineering a scaled down electrochemical platform for point-of-care creatinine detection through the use of SPEs. UV/Vis spectrophotometry is used as a benchmark reference technique.

4.2.2 RESULTS AND DISCUSSION

As discussed in the introduction, the notion that the *direct* oxidation of creatinine has rarely, if ever, been reported within the scientific literature. The opportunity has thus been taken in this section to present a method for the direct oxidation of creatinine and it will be seen that analytically detectable concentrations using a direct voltammetric approach are far in excess of bodily fluid concentrations. Resultantly this section proceeds to study a highly novel proof-of-concept approach reported by de Araújo *et al.,*[367] which monitors picrate anion concentrations in the Jaffe reaction using a GC electrode. Their work is extended to gain further insights into enzymeless electrochemical creatinine detection for point-of-care applications.

DIRECT ELECTROCHEMICAL OXIDATION OF CREATININE

Presented in Figure 4.6 are voltammetric profiles typically arising from the direct oxidation of creatinine at concentrations ranging between 0 mM and 200 mM in pH 9.4 BBS

with 150 mM NaCl electrolyte, using a gold working macroelectrode. First it is observed that initially there is no electrochemical oxidation of creatinine present at low concentrations, yet as the concentration increases, a large oxidation wave ascribed to the oxidation of creatinine is evident at +1.00 V. It is observed from Figure 4.6 that a linear range emerges at 80 – 160 mM with a correlation coefficient of 0.996. Investigations of lower concentrations yielded no analytical correlation and thus are not presented within this work. It should be noted that gold oxide is known to form at high potentials,[383] usually mediated by acidity. Though these experiments are in highly alkaline conditions, there is a possibility of creatinine mediating a gold oxide forming reaction. This is purely conjecture, however.

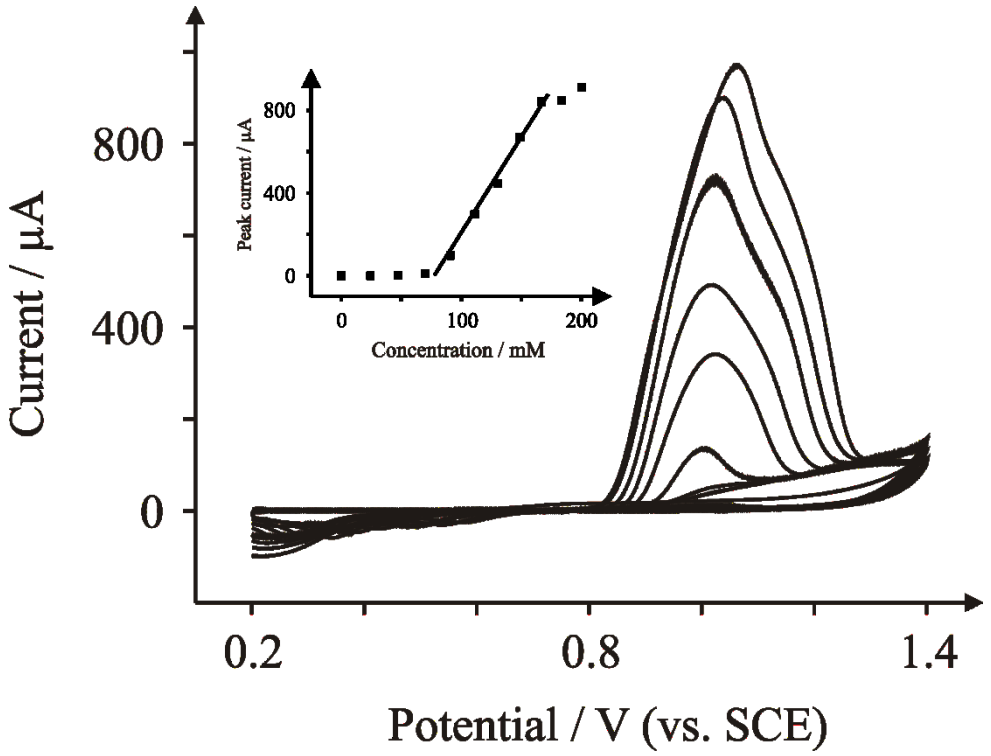

Figure 4.6: Voltammetric profiles typical of the electrochemical oxidation of creatinine in pH 9.4 BBS with 150 mM NaCl background electrolyte, utilising a gold electrode. Scan rate: 50 mV s^{-1}. Inset: concentration versus I_P^{ox} for the same experiment.

The more likely case is the hydroxylamine route. Previous literature reports have shown creatinine to tautomerise in solution (see Figure 4.7),[366] exposing an exocyclic amine

group for oxidation *via* a pathway proposed in Figure 4.8. The proposition here is that the hydroxylamine is formed. Indeed, hydroxylamines are known to undergo a further reversible oxidation step, yet the lack of an observed back peak suggests that (if the hydroxylamine is formed) in this system the hydroxylamine is indeed stable within the potential window. Furthermore, it is likely that the formation of gold oxide upon the surface of the electrode is key to the oxidation of the exocyclic amine; a previous study has reported that amine oxidation is catalysed by gold oxide.[384] Carbon based electrodes such as EPPG, BPPG, and GC were similarly tested, yet none revealed any evidence of the electrochemical oxidation over a 4.00 V potential range, which adds some weight to the gold oxide mediated reaction pathway.

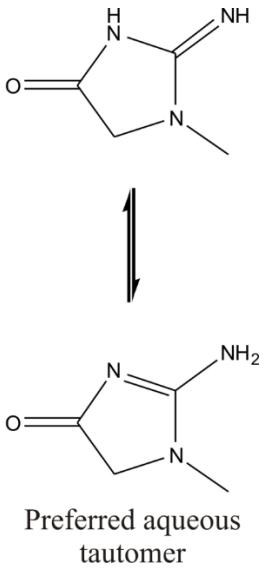

Figure 4.7: Tautomer of creatinine existing in aqueous conditions.

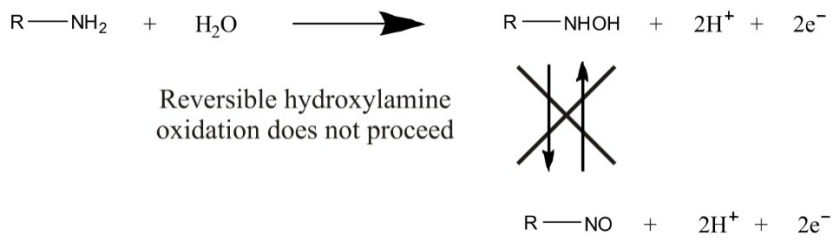

Figure 4.8: Proposed electrochemical mechanism for the direct oxidation of creatinine in pH 9.4 BBS at a gold electrode.

It is clear that the direct electrochemical sensing of creatinine is not a feasible strategy to analyse plasma, IF, or urine, as the concentration ranges of creatinine exhibited naturally within these media are all well below the lower end of the linear range (ideally detection within the range of 0 – 9 mM would be useful in the case of urine; for plasma and IF, even less). As a result of the required high concentrations required for detection *via* this strategy, it is clear why other analytical methods for creatinine detection are used by hospitals and scientists alike. Hence the next section turns to the electrochemical monitoring of the picrate anion in the Jaffe reaction, as previously reported by de Araújo *et al.*[367]

ELECTROCHEMICAL MONITORING OF THE PICRATE ANION IN THE JAFFE REACTION

It was briefly suggested in the introduction that there were some discrepancies with the picrate monitoring work conducted by de Araújo *et al.*[367] This section aims to, in a *bona fide* manner, critically examine the protocols utilised and hopefully correct some errors in their work. First, in the abstract the authors claim to electrochemically observe a linear range for creatinine detection of *1 – 80 μM* and a detection limit of *380 nM*. This is a strikingly low linear range for such a system and hence is investigated independently. Secondly, the statement: "For higher values of creatinine concentration, no Faradaic process was

observed….", is not entirely correct; this is investigated further. Indeed, if these two points are taken into consideration, they contradict the author's methods when they use their procedure to analyse urine in the same work; urine contains far larger creatinine concentrations than the 80 μM reported as the top end of their linear range and hence their methods, according to their words, would be far from useful for the purposes of urinary creatinine detection. Also investigated are the electrochemical activities of a range of commercially available electrodes, namely EPPG, BPPG, gold, and SPEs, towards this system. These results are compared to UV/Vis measurements as was conducted in the work by de Araújo and co-workers.[367]

With this in mind, focus is turned to the creatinine/picrate system. It is known that creatinine complexes with picric acid, turning from a yellow to a deep orange colour, the colour of which provides a UV-Vis method to quantify creatinine. In the electroanalytical approach, the electrochemical signal results from the electrochemical reduction of picric acid. Addition of creatinine to the picric acid sample reduces the analytical signal, thus the concentration of creatinine can be plotted against the peak current for picric acid to provide an indirect detection strategy. Figure 4.9A depicts typical voltammograms arising from the electrochemical reduction 0.5 mM picric acid, the creatinine/picrate complex, 0.5 mM creatinine, and a blank buffer solution, all at a fixed pH of 13 using SPEs. A large reduction wave typical of the electrochemical reduction of the picrate anion is evident at -0.80 V; this serves as the analytical peak for the remainder of the investigation. The observed peak reduction value is slightly higher than the -0.75 V reported previously for a GC electrode.[367] Figure 4.9B displays a clear graphical representation of the reduction waves observed in all four cases, and clearly demonstrates a significant difference in the peak currents between the picrate-containing solutions and the non-picrate-containing solutions. Additionally there is a

clear representation that the introduction of creatinine slightly reduces the magnitude of the peak current, thus consuming the picrate anion.

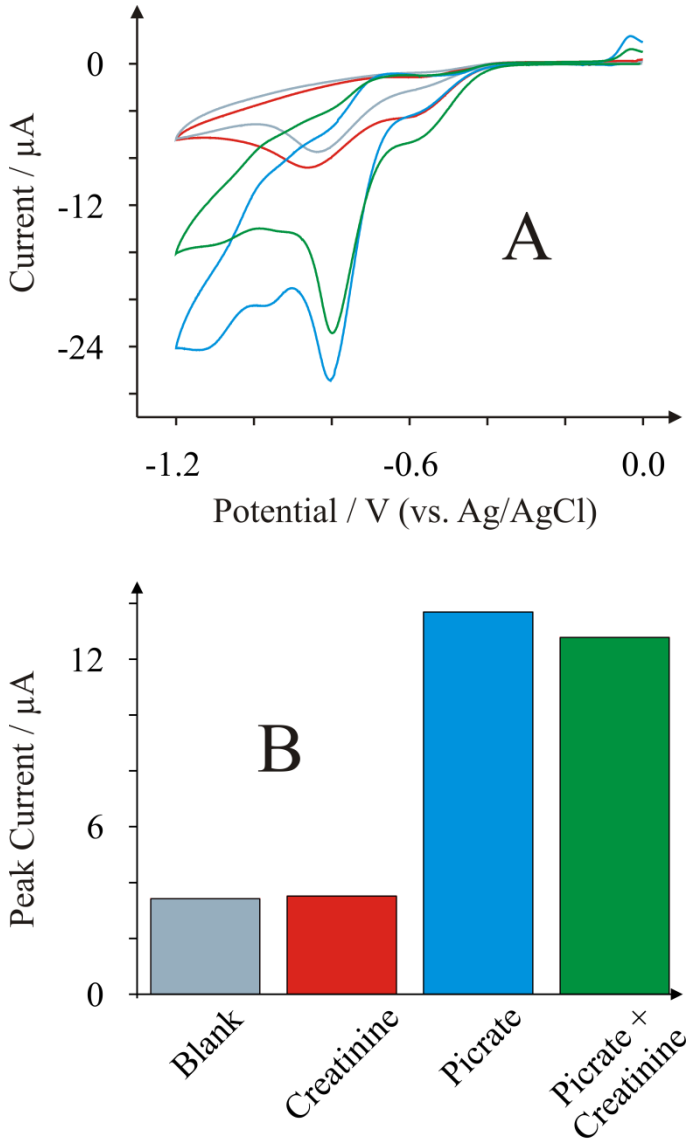

*Figure 4.9: **A**: Voltammetric profiles obtained at SPEs for the electrochemical reduction of: (grey line) blank NaOH buffer solution; (red line) 0.5 mM creatinine in pH 13 NaOH buffer solution; (blue line) 0.5 mM picrate in pH 13 NaOH buffer solution; and (green line) 0.5 mM creatinine reacted with 0.5 mM picrate for 5 minutes. Scan rate: 50 mV s^{-1}.*

***B**: Graphical summary of the peak heights presented in Figure 4.9A.*

A problem emerges with the concentrations, however, if one was to study urinary creatinine at these levels. One would assume that an excess of picrate would be required for analysis, assuming that the picrate/creatinine reaction is indeed a 1:1 stoichiometric reaction. Literature reports indeed largely suggest a 1:1 stoichiometry,[385-387] and hence an increased amount of picric acid would be desirable to calculate urinary creatinine concentrations using any Jaffe-based procedure. Another potential problem in the detection of creatinine in this manner is the presence of oxygen within the solution; the electrochemical reduction of oxygen at graphitic electrodes is known to occur at potential values around where the analytical signal is observed.[388] This was duly investigated and a graphical representation of the effect of degassing a solution is presented in Figure 4.10 where it is shown that degassing the solution for long periods of time has little effect upon the observed electrochemical response of the picrate anion; hence oxygen appears to not interfere with the analytical protocol and degassing the solution prior to analysis is not required.

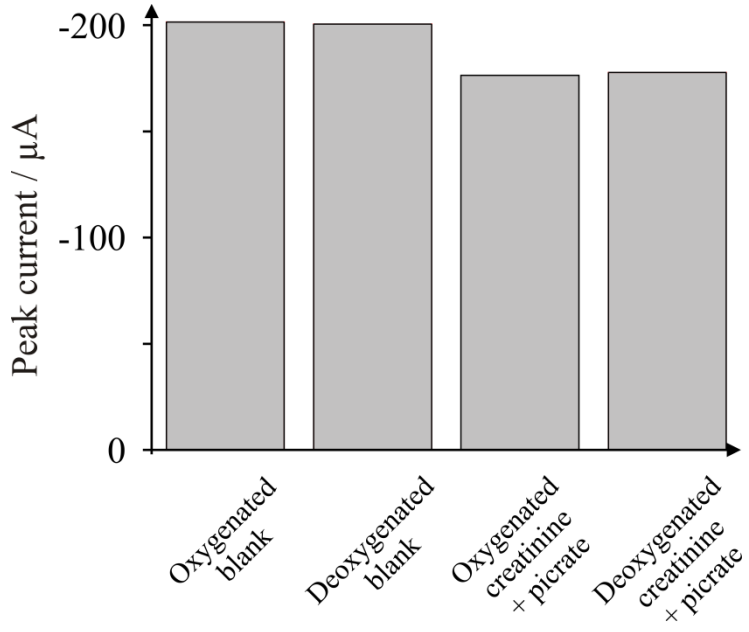

Figure 4.10: Graphical representation of the effect of degassing solutions upon the observed peak reduction current of the picrate anion in both blank picrate solutions (5.00 mM) and creatinine-containing (5.66 mM) solutions.

The investigation now turns to the electrochemical reduction of the picrate ion utilising different electrode substrates. In the work by de Araújo *et al.* only a GC electrode was used, which is limiting the opportunities for such an electrochemical system. Consequently, presented in Figure 4.11A are the typically observed voltammetric profiles which compare five different electrodes in terms of current density. Observed in Figure 4.11A are the variation in current densities for the reduction of the picrate anion in the order (starting with the highest current density) gold > EPPG > SPE > GC > BPPG. This is presented graphically in Figure 4.11B.

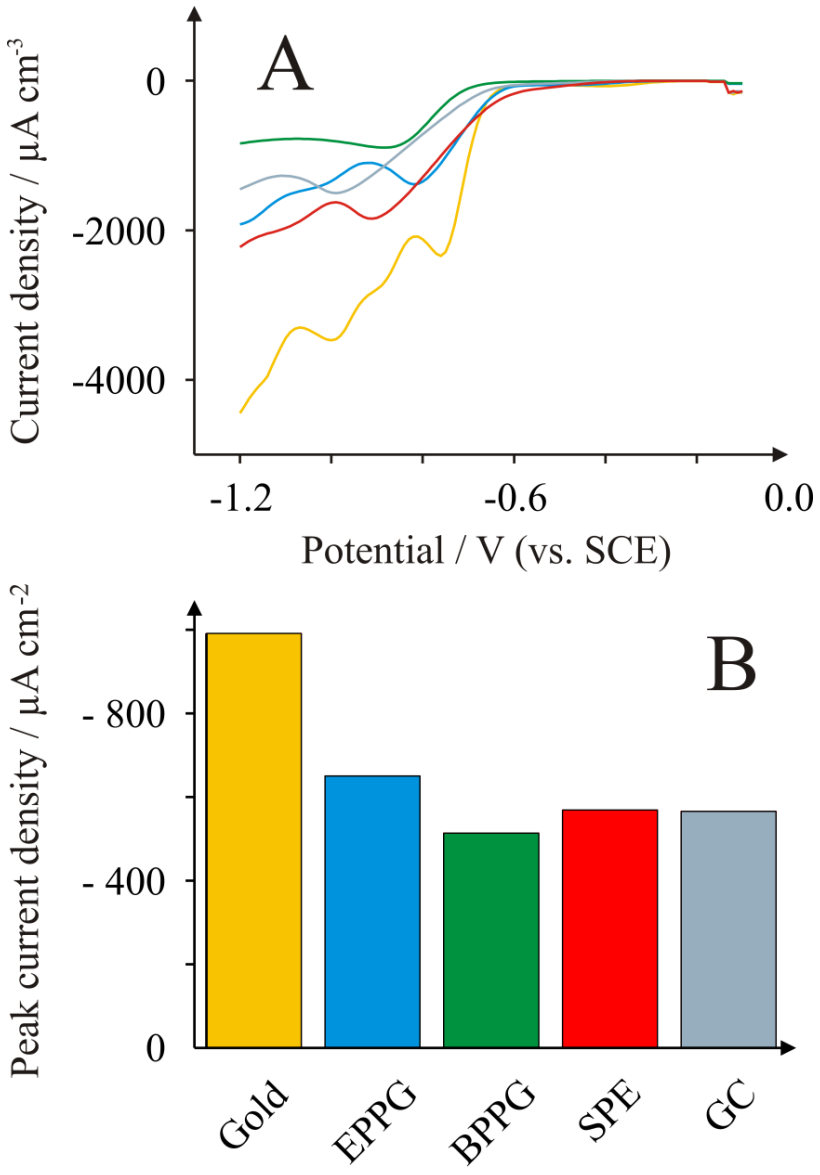

*Figure 4.11: **A**: Comparison of electrode responses towards 5 mM picrate in pH 13 NaOH buffer solution. Scan rate: 50 mV s^{-1}. **B**: Graphical representation of the peak current densities.*

The gold electrode exhibits the lowest peak reduction potential of -0.76 V along with the highest peak reduction current density of -992 µA cm^{-2}. Gold is subsequently used as a metal-based macroelectrode for data comparison, though picric acid is known to make explosive metal salts with a range of metals (see MSDS, Sigma Aldrich[389]). Gold is not reported to form such salts, but that should not discount the possibility of dangerous complexes. The gold electrode exhibits a secondary reduction wave, whereas the non-metallic electrodes utilised in

Figure 4.11 do not; the origin of which is unknown. EPPG exhibited the next highest peak reduction current density of -650 μA cm^{-2} after gold. The SPE exhibited a peak reduction current density of -514 μA cm^{-2}, which is similar to the GC electrode, yet over 100 μA cm^{-2} less than EPPG. Such a comparison to GC is encouraging, and shall be further investigated later for the purposes of point-of-care testing. The increase in peak potential from -0.80 V to -0.90 V at the SPE (comparing Figures 4.9 and 4.11) attributed to the concentration increase is unfavourable. This is not an effect of pH because the pH has remained constant between Figures 4.9 and 4.11. Therefore there is a concentration overpotential in this case, because the only change is a tenfold increase in picric acid concentration. Thus, concentration overpotentials must be carefully considered. Gold SPEs[390] were also tested for these purposes, yet yielded no electrochemical reduction peaks within this potential window.

Next considered is the effect of creatinine concentration upon the observed electrochemical response of picric acid using gold and EPPG electrodes *via* LSV. In these tests, the creatinine was left to react with the picric acid for five minutes prior to the electrochemical measurements. The reaction proceeds at a rate corresponding to an order of two when picric is in excess with respect to the concentration of creatinine and OH^-; thus five minutes is ample time for the reaction to proceed.[385] Previous literature left the creatinine to react for 100 minutes prior to testing,[367] which is too long for an application within clinical analysis. Current *versus* time experiments were conducted which show the reaction to have almost completely finished after five minutes.

Figure 4.12A depicts a typical calibration curve with respect to the concentration of creatinine, utilising a gold electrode. Two linear ranges are observed in Figure 4.12A: i) 0.0 – 7.5 mM (I / μA = 6.80 μA mM^{-1} – 75.33 μA; N = 5; R^2 = 0.989); and ii) 9.0 – 14.0 mM (I / μA = 7.71 μA mM^{-1} – 107.4 μA; N = 6; R^2 = 0.989) with a LoD (3σ) corresponding to 0.805 mM. Figure 4.12B depicts a calibration curve for the observed peak current at -0.82 V with

respect to the concentration of creatinine utilising an EPPG electrode. Two linear ranges are observed in Figure 4B: i) 0.0 – 6.0 mM (I / μA = 19.41 μA mM^{-1} – 180.4 μA; N = 7; R^2 = 0.997); and ii) 7.5 – 11.5 mM (I / μA = 7.705 μA mM^{-1} – 107.4 μA; N = 6; R^2 = 0.989) with a LoD (3σ) corresponding to 0.267 mM; these reported LoDs here a more realistic than the 380 nM reported by de Araújo *et al*. It should be noted that these linear ranges are likely a consequence of the picric acid being completely consumed because the creatinine concentration is increasing above the 5 mM concentration of picric acid, and the second linear range appears due to a second equivalent of creatinine reacting in another position on the already hybridised Janovsky complex. These Figures fall within two useful ranges for urinary creatinine detection: i) a low linear range for urinary detection which is required to detect glomerular filtration problems; and ii) a higher linear range which falls within the expected average urinary creatinine levels for healthy adults (9 mM). Comparing these results to that of de Araújo *et al.*, who report a detection limit of 380 nM and a linear range of 1 – 80 μM, their apparent results are at least *three* orders of magnitude less than observed in this work; albeit they use a lower picrate concentration (100 μM) and DPV which is a technique designed for measuring smaller quantities.[367] That said, three orders of magnitude difference is an unusually large difference. Indeed, such low concentrations were tested in-house whilst utilising DPV and revealed no Faradaic processes.

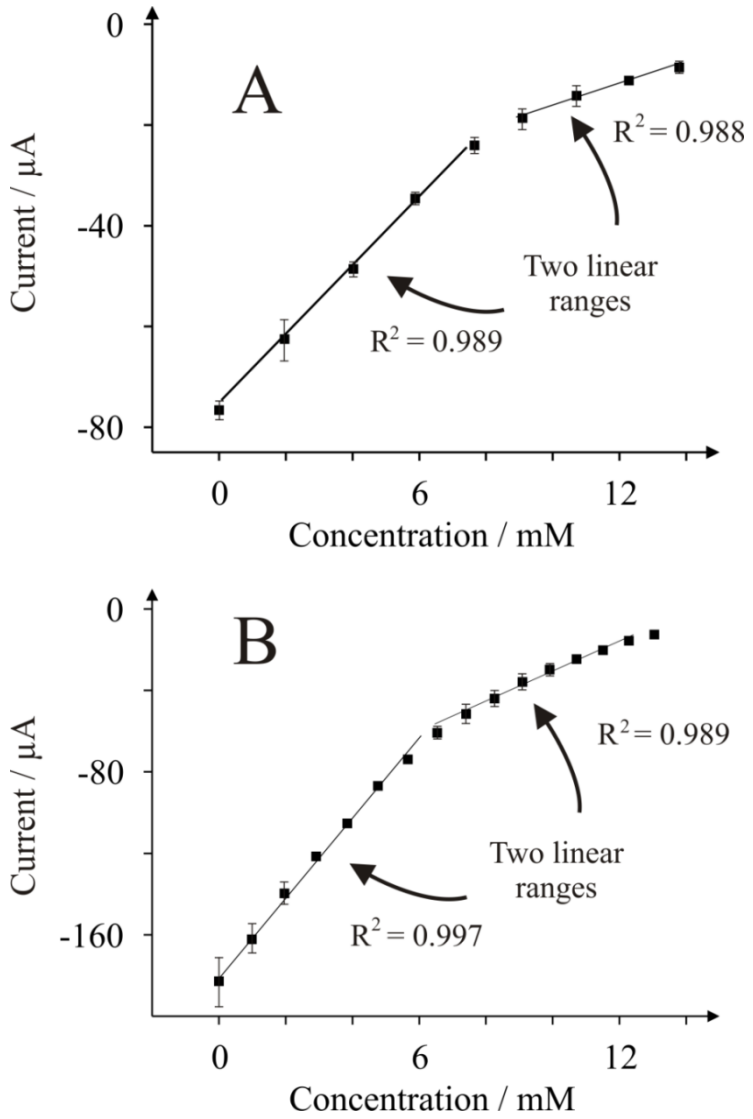

*Figure 4.12: The effect of creatinine concentration upon the observed peak reduction current of picric acid at: (**A**) a gold electrode; and (**B**) an EPPG electrode. Each point is an average of three separate experiments, all with a standard deviation of no more than 4 µA for gold and 12 µA EPPG. Scan rate: 50 mV s^{-1}.*

***A**: 0.0 – 7.5 mM; N = 6; R^2 = 0.989 and 9.0 – 14.0 mM; N = 4; R^2 = 0.988.*

***B**: 0.0 – 6.0 mM; N = 7; R^2 = 0.997 and 7.5 – 11.5 mM; N = 7; R^2 = 0.989.*

As with previous electrochemical reports, a benchmark is necessary to compare electrochemical data to. Given the extreme colour change of the reaction, UV/Vis spectrometry is an obvious choice. There are concentration limitations associated with UV/Vis spectrometry, so it was necessary to dilute samples ten times in order for some reasonable absorbance data which was at or around the optimum true absorbance value of 0.434 au. The method involved the reaction of the picric acid with creatinine at fixed concentrations for five minutes, then diluting the reacted solution ten times for measurement. Figure 4.13 depicts a calibration curve for a series of UV/Vis measurements taken from known concentrations of creatinine in 0.5 mM picric acid, where a linear calibration curve over the range of 0.025 – 0.5 mM (A / au = 0.625 au mM^{-1} + 0.017 au; N = 5; R^2 = 0.998) is observed with a LoD (3σ) of 0.0184 mM. The concentrations obtained are multiplied by ten after measurement to take into account the dilution.

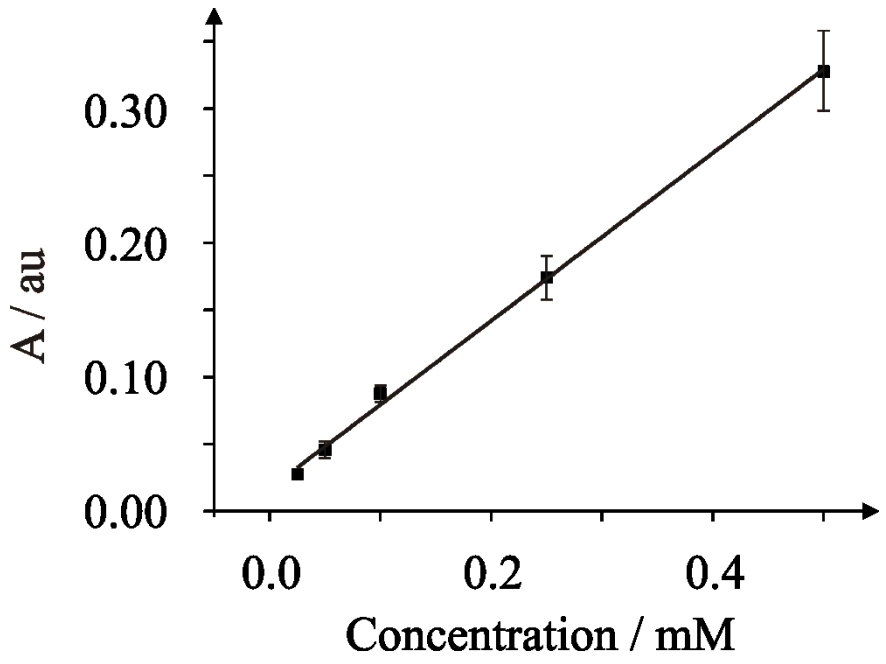

Figure 4.13: Calibration curve for the UV/Vis absorbance versus creatinine concentration (λ_{max} = 500 nm). Each point is an average of three separate experiments, all with a standard deviation of no more than 0.032 au.

A move away from conventional electrodes is desirable if electrochemical systems such as this are to be applied to in-field applications. SPEs are mass-produced, small scale electrodes which require no pre-treatment, require very small sample sizes (<100 μL), cheap, and most of all are generally analytically reproducible. Hence, this section discusses data collected for this electrochemical system in conjunction with SPEs; particularly in terms of reproducibility to assess whether such printed electrodes are a viable strategy for point-of-care creatinine testing.

Figure 4.14 depicts the effect of creatinine concentration upon the observed peak currents exhibited by 5 mM picric acid at SPEs; an SCE is utilised as a reference and a Pt wire as an auxiliary in these experiments for consistency with the above data but in the near-final product have their own on-board auxiliary and reference electrode (Ag/AgCl). Similar to the observed trends presented in Figure 4.12, there are two linear ranges exhibiting a linear increase in peak current with respect to the concentration: 0.0 – 6.0 mM (I / μA = 12.32 μA mM^{-1} -30.71 μA; N = 4; R^2 = 0.991); and 6.0 – 11.0 mM (I / μA = 1.18 μA mM^{-1} – 24.74; N = 4; R^2 = 0.997), with a LoD (3σ) of 0.72 mM additionally evident.

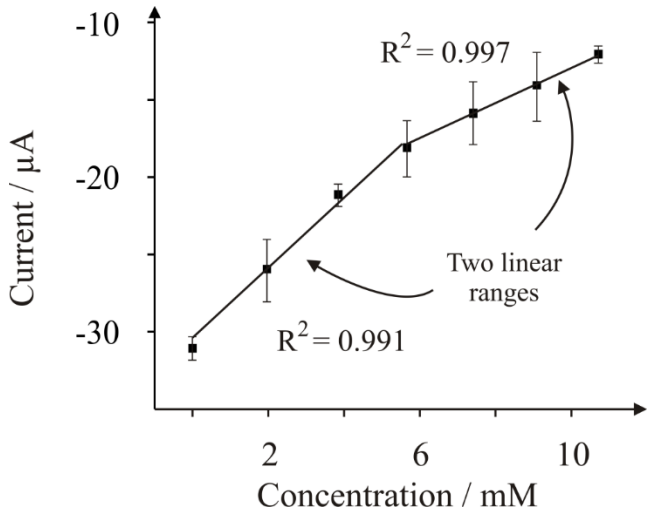

Figure 4.14: The effect of creatinine concentration upon the observed peak currents exhibited by 5 mM picric acid in pH 13 NaOH buffer solution at a graphite SPE. Data points are averaged over three separate scans. Scan rate: 50 mV s^{-1}.

Upon comparison to the results observed for the EPPG electrode previously, the linear ranges observed are near identical, which is an encouraging sign for SPEs to be used as a potential commercial solution for point-of-care creatinine testing. Less encouraging is the broad standard deviation associated with the SPEs towards this particular analyte. Error bars are supplied in Figure 4.14, some of which equate to a % RSD as high as 17%. This is clearly a stumbling block which needs removing before such electroanalytical sensing platforms can be considered for measuring creatinine clearance using a portable point-of-care device. Investigations such as utilising a variety of carbon inks and optimising the working electrodes and solution conditions are obvious avenues to explore for such a purpose. Table 4.1 compares gold, EPPG and SPEs in terms of creatinine content detected in urine, LoD, and % RSD.

Table 4.1: A summary of detected urinary creatinine content in three samples utilising several different electrode substrates.

Electrode substrate	Sample 1		Sample 2		Sample 3		LoD / mM
	Conc. / mM	% RSD	Conc. / mM	% RSD	Conc. / mM	% RSD	
Gold	14.8	4.5	16.4	6.3	15.1	5.8	0.805
EPPG	9.9	3.8	10.2	3.9	11.2	4.3	0.267
SPE	6.1	2.3	7.9	3.0	10.2	3.9	0.720

Observed in Table 4.1 is a general trend in the case of the carbon based electrodes, where sample 1 contains the least creatinine, sample 2 the second least, and sample 3 the most. The gold electrode does not agree with the carbon electrodes, as it predicts the creatinine content of sample 2 to be the highest, followed by sample 3, then sample 1. The reasons for this are unknown, but it is reasonable to suggest perhaps gold oxide is constantly forming over the lifetime of the analytical protocol and changing the electrochemical process. A simple experiment with a gold SPE (effectively gold oxide) showed that the oxide groups hindered the electrochemistry in this system.

A secondary approach was investigated, where a fixed amount of picric acid was drop-coated upon the working electrode surface of an SPE. This was left to dry in air until a crystalline solid was left, depicted in Figure 4.15. A fixed volume (50 μL) of creatinine in pH 13 NaOH buffer was syringed upon the electrode surface, covering the three electrodes (carbon working electrode, carbon auxiliary electrode and Ag/AgCl reference electrode) and in the process dissolving the residual picric acid on the electrode. After varying amounts of picric acid were tested, it was found that this method was not usable. A graphical representation of the effect of creatinine concentration upon the peak current using an effective picric acid concentration of 1.1 mM is presented in Figure 4.16. It is observed that the peak currents exhibited by the SPE fluctuate randomly. The same was observed for

several other picric acid concentrations; and given that no linearity was observed, the indication is that the electrode is being passivated by the picric acid when it is applied to a surface for a long period of time. This work needs extensive development but can potentially provide a simplified avenue for sensing creatinine using this protocol. The major drawback of this method is of course the explosive nature of dry picric acid.

Figure 4.15: SPE with dry picric acid on the working electrode. The picric acid crystallizes when dry.

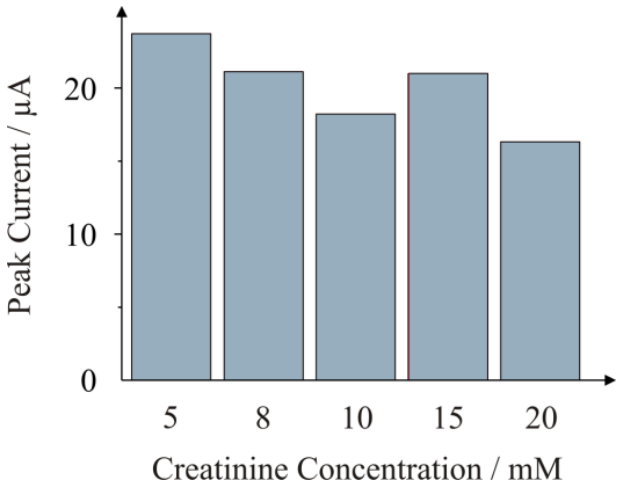

Figure 4.16: Graphical representation of the peak currents exhibited by a drop-coated picric acid SPE at varying creatinine concentrations; the picric acid concentration is calculated as an effective concentration from the mass of picric acid applied to the electrode surface, assuming 100% dissolution of the picric acid crystals into the 50 µL creatinine sample covering the SPE, and was calculated to be 1.1 mM.

Electrochemical and UV/Vis measurements are presented in Table 4.2, where it is seen that the electrochemical methods predict the concentrations to be less than the spectrometrically detected concentrations, even if the error is taken into account. It is

uncertain which technique predicts the concentrations wrongly, assuming one of them is better than the other. In the UV/Vis experiments, which are assumed to be the 'gold standard' for spectrophotometric techniques for creatinine/picrate detection (given that it has been used previously), there may well be other compounds within the urine which are responsible for the changes in absorbance, whereas with the electrochemical techniques, the method is specifically monitoring the picrate anion and thus one can assume in this case that the electrochemical methods are reliably looking at just the picrate anion. The origin of the discrepancies between the electrochemical determination and the UV/Vis determination need to be deconvoluted if a screen-printed sensor is to be utilised in a clinical application. Previous literature reported the electrochemical and UV/Vis experiments yielding similar concentrations;[367] this work disagrees with their observations. The % RSD of all the experiments are under the analytically acceptable level of 5 %, paving the way for an exciting approach for electrochemical monitoring of the Jaffe reaction *without* interferents upsetting the results.

Table 4.2: Comparison of electrochemically detected (via LSV at an EPPG electrode) and spectrometrically detected (via UV/Vis) creatinine concentrations in three urine samples.

Sample	UV/Vis / mM (% RSD)	EPPG / mM (% RSD)
1	11.58 (1.2)	9.91 (1.5)
2	13.91 (2.3)	10.21 (4.1)
3	17.84 (3.2)	11.22 (2.2)

4.2.3 SUMMARY

This Chapter has analysed a previously described method for electrochemical monitoring of the picrate anion in the Jaffe reaction and has seen some profound differences in results compared to previous literature reports. The novelty of this section is that it has greatly extended its understanding and provided a potential point-of-care approach utilising screen-printed sensors. This section has demonstrated that creatinine can be detected indirectly through the use of an enzymeless system, however the results disagree with a previously reported detection range of 1 – 80 μM;[367] two linear ranges are instead found (EPPG) at much higher concentrations (0.0 – 6.0 mM; 7.5 – 11.5 mM). Furthermore the detection limit reported previously as 380 nM is tenuous at best;[367] the value of 0.267 mM reported in this work for EPPG is a more realistic value for such techniques.

This work has also demonstrated the detection of creatinine using this enzymeless system, and its utility for urinary creatinine detection, taking into consideration two linear ranges which can be applied to low urinary creatinine (0.0 – 6.0 mM) and normal urinary creatinine (6.0 – 11.0 mM). Comparison to UV/Vis spectrometry shows some disparity in the results, where UV/Vis predicts the creatinine levels to be higher. However this may be as a result of reduced transmission due to other constituents within urine.

The ideas presented could potentially provide a more stable foundation for electrochemical detection of creatinine for point-of-care applications than seen in the literature already for such a system. In particular, the application to SPEs is an area which has been exploited here, exhibiting approximately the same linear ranges as seen for conventional electrodes, yet with less analytical reproducibility; this is an issue which must be overcome in order for SPEs to be applied to such a clinical application. The specific tailoring and optimisation of a reproducible SPE towards this system could open up an exciting opportunity to monitor creatinine clearance for point-of-care devices, while reducing the cost

of such a device *and* providing a facile approach which could be performed by patients and staff alike. Critically, such a procedure could eventually replace the many standard Jaffe procedures which are reported to be inaccurate; and even though a similar procedure is used, the reaction times have been reduced dramatically and one can assume that the removal of the picrate anion is almost entirely through the second order creatinine reaction which proceeds considerably faster than any other urinary constituent.

4.3 CONCLUSIONS

The application of SPEs has been investigated in this Chapter, towards two novel systems which have not been reported before. SPEs have been shown to be a viable option for the determination of the bronchiodilatory drug theophylline; this is useful because levels of theophylline must be closely monitored *via* blood sampling because it can be toxic in high concentrations. Thus, further development of this method to look at theophylline in blood would be a good strategy for future work into a point-of-care detection device for theophylline. A second system was investigated which used an indirect creatinine detection method for the monitoring of kidney filtration problems. This method proved to be particularly robust using urine samples, as it could detect both healthy and unhealthy levels of creatinine within urine. This method would require more research into the effects of interferents such as glucose, sodium, and urea, before the method could be implemented elsewhere. Such work would be the first of its kind, in terms of an indirect creatinine sensor which would be electrochemically robust enough for clinical procedures.

This section has gathered further understanding of the electrode substrates which will be used in the latter part of the thesis, and the next Chapter follows on from this by investigating the electrochemical properties of the first graphene SPEs.

CHAPTER 5
THE CHARACTERISATION OF GRAPHENE SCREEN-PRINTED ELECTRODES

This chapter follows on from Chapter 4 and carries on the screen-printed sensors section, by focussing exclusively upon the fabrication and characterisation of Graphene Screen-Printed Electrodes (GSPEs). In the past decade, several graphenes have been fabricated and characterised: chemically exfoliated; mechanically exfoliated; CVD; and chemically/thermally reduced graphene, are all types of graphene which produce radically divergent electrochemical characteristics.[391] Yet there is not yet a true GSPE reported within the electrochemical community. Hence this section describes the fabrication and characterisation of the first *true* GSPEs, which in this case is defined as a graphene SPE which carries an electrochemical response akin to that of a graphene structure, and not a catalytic effect which is apparent as a consequence of impurities or a reorganisation of the graphene into graphite.

All chemicals were of the highest grade available and were used as-received from Sigma Aldrich (UK). All solutions were prepared using deionised water of resistivity no less than 18.2 MΩ cm and were vigorously degassed prior to electrochemical measurements with high purity, oxygen-free nitrogen. All test solutions were prepared in 0.1 M (pH 7.4) PBS containing 0.1 M KCl supporting electrolyte.

Electrochemical measurements were performed using an Ivium CompactStat^{TM} (Netherlands) potentiostat. All measurements were conducted using a screen-printed three electrode system as described below. For SEM, Raman, XPS and ATR spectroscopy the respective inks or SPEs were used as received/fabricated without any further modification. SEM images and surface elemental analysis were obtained with a JEOL JSM-5600LV model equipped with an energy-dispersive X-ray microanalysis package. Raman Spectroscopy was performed using a 'Renishaw InVia' spectrometer with a confocal microscope (x50 objective) spectrometer with an argon laser (514.3 nm excitation) at a very low laser power level (0.8 mW) to avoid any heating effects. Spectra were recorded using a 10 s exposure time for 3 accumulations. 5 spectra were recorded and an average representation is presented within this section. XPS measurements were performed independently by CERAM[392] with a Kratos Axis Ultra spectrometer using monochromatic Al Kα X-rays (1486.6 eV). Charge compensation was achieved using a beam of magnetically focussed electrons as a flood current. The standard photoelectron take-off angle used for analysis was 90° (giving a maximum analysis depth in the range 5 - 8 nm). For each sample, the aim was to analyse as large an area as possible within the circular region of interest in order to provide an averaged response over the entire graphene domain. Infrared measurements were acquired using a Thermo Scientific Nicolet iS5 Attenuated Total Reflectance (ATR) spectrometer set to measure 8 scans per spectrum; the measurements taken after depositing the as-received

graphene inks onto the ATR diamond. Finally, electrode resistivity measurements were obtained utilising a Precision Gold WG 020 Digital Volt Meter (DVM). In order to do this, the two probes on the DVM were in contact with the electrode; one touching the working electrode and the other touching the working connection. It should be noted that a four-point probe would be the best way to probe the resistivity, but such equipment was not available.

FABRICATION OF THE GRAPHENE SCREEN-PRINTED ELECTRODES

The carbon-based SPEs were fabricated in-house with appropriate stencil designs using a microDEK 1760RS screen-printing machine (DEK, Weymouth, UK). This SPE design has been previously reported.[393-395] For the case of each fabricated electrode, first a carbon ink formulation utilised for the efficient connection of all three electrodes and the electrode material for both the working and counter electrodes was screen-printed onto a polyester (Autostat, 250 micron thickness) flexible film (*vide infra* for further details of the various inks utilised). The carbon ink layer was cured in a fan oven at 60 ^{o}C for 30 minutes. Next a silver/silver chloride reference electrode was included by screen-printing Ag/AgCl paste (Product Code: C2040308D2; Gwent Electronic Materials Ltd, UK) onto the polyester substrates, which was subsequently cured once more in a fan oven at 60 degrees for 30 minutes. Finally, a dielectric paste (Product Code: D2070423D5; Gwent Electronic Materials Ltd, UK) was then printed onto the polyester substrate to cover the connections and define the active electrode areas including that of the working electrode (3 mm diameter). After curing at 60 degrees for 30 minutes the SPEs are ready to be used. The fabricated disposable electrodes were strictly limited to one electrochemical use as the graphene SPEs in particular exhibit reduced functionality after the first use.

Different carbon-based inks were utilised for each of the four electrodes fabricated and were as follows: Edge-plane-like SPE (ESPE) (Product Code: C2000802P2; Gwent Electronic Materials Ltd, UK);[393] Basal-plane-like SPE (BSPE) (Product Code: ED5020; Electra Polymers Ltd, UK);[393] Graphene SPE1 (GSPE1) (Product Code: HDPlasTM Graphene Ink SC213; Haydale Ltd, UK); and Graphene SPE2 (GSPE2) (Product Code: Vor-ink S103; Vorbeck Materials Ltd, USA). GSPE1 is described as graphene in a carbon-based carrier ink (43.0 – 45.0 % solid content, similar to the ESPE, which exhibits 39.0 – 41.0 % solid content) which is suspended in diacetone alcohol (the solvent making up approximately 35% of the ink) according to the materials safety data sheet on the company's website.[396] Haydale also report a viscosity of 8.0 – 11.0 Pa for the GSPE1 ink which is much higher than the ESPE ink (2.0 – 3.5 Pa) and an ink screen life in excess of three hours. This ink is loaded with small amounts of carbon black (to improve conductivity as without it the ink was found to be highly resistive) and the graphene nanoplatelets are produced *via* a split plasma process, resulting in graphene which does not exhibit a basal surface containing structural damage (as is the case for wet chemical fabrication approaches). GSPE2 is an ink reportedly loaded with sheets of single-layer graphene produced *via* chemical exfoliation (information kindly provided by Vorbeck).[397] The major solvent utilised in this ink is hexanol according to correspondence from the manufacturer. The company also report *"various polymeric binders to improve adhesion, film cohesion, and printability"*. Viscosity and ink screen lifetime data is not reported by Vorbeck. The solid content of GSPE2 is reportedly 15 – 17 % wt (exhibiting a lower solid content than the other inks).

5.1.1 INTRODUCTION

One area that has completely embraced the graphene revolution is the electrochemical utilisation of graphene-based electrode substrates.[398] Graphene is potentially the world's thinnest electrode material, with numerous reports detailing the beneficial implementation of graphene in electrochemistry, for example in the fabrication of enhanced electroanalytical sensors and in a multitude of energy generation and storage devices.[399-402] Such reports demonstrate that, in certain cases, graphene can provide electrocatalysis for an improved analytical performance or improved *direct* electron transfer at the graphene|electrolyte interface when used as components for improved energy based devices.[399-402] However, although there are many optimistic reports concerning the electrochemical benefits of graphene, contrasting reports exist which demonstrate that this is not always the case.[320, 403]

The slow heterogeneous electron transfer kinetics ascribed to the fundamental electrochemical properties of *pristine* graphene have not stopped the electrochemical community from attempting to use graphene as an advantageous electrode material. Manipulation of the graphene utilised in electrochemical devices can give rise to beneficial properties and, as such, the electrochemical literature contains a vast array of reports utilising differing forms of graphene.[398] Such graphenes include chemically or thermally reduced graphene,[404, 405] CVD graphene,[406, 407] 3D graphene foam structures,[408, 409] graphene oxides,[410] chemically doped graphenes,[411] and of course pristine graphene.[320] The variation in graphene production methods results in a range of different graphene structures which exhibit distinct electrochemical properties, enabling the production of tailored graphene electrodes for specific applications.[398]

In terms of employing graphene as an electrode material, a major problem that researchers face is electrically 'wiring' the graphene in order for electrons to flow efficiently,

thus allowing one to observe the electrochemical benefits from the graphene structure.[398] The most widely used approach to study graphene is drop-casting aliquots of a graphene suspension onto an underlying supporting electrode surface, such that one immobilises graphene and effectively averages the total response over that of the graphene domains.[398, 325] However, modifying such surfaces has potential to leave underlying 'reactive' surfaces exposed, which can influence and *dominate* the observed electrochemistry.[320, 398] Furthermore, capillary forces present as a result of solvent evaporation can push graphene platelets to the edges of the underlying electrode, which can potentially leave concentrated zones of graphene at the edges of the electrode surface in addition to areas where there is little or no graphene coverage, which is akin to the so-called coffee ring effect; Figure 5.1 shows a schematic overview of this process. The resultant uneven graphene distribution effectively leaves areas of both fast (multi-layer graphene) and slow (single-layer graphene) electron transfer and thus an electrochemically inhomogeneous surface.

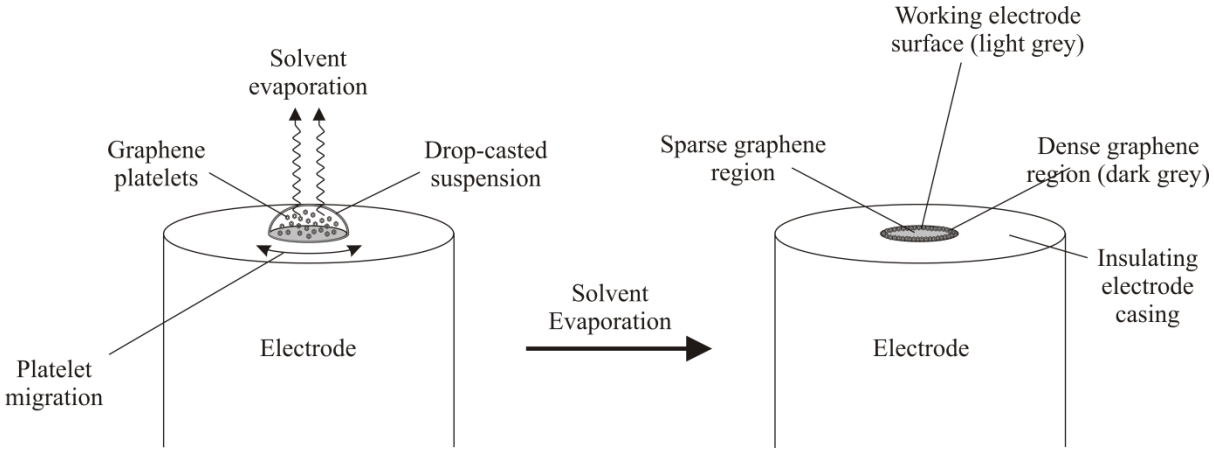

Figure 5.1: Typical coverage of graphene resulting from drop-casting a suspension of the graphene of interest onto a supporting electrode surface. Such an approach is extensively utilised within the academic literature in order to electrically wire graphene.

To try and overcome the aforementioned issues, researchers have turned to exploring the electrochemistry of graphene through the utilisation of CVD grown graphene.[407] Due to

the nature of the CVD process, pristine monolayer graphene domains can be grown and transferred onto electrochemically inert substrates such that one can study the fundamental electrochemical properties whilst controlling the thickness of graphene and perform *in-situ* characterisation of their electrode material. Such a process overcomes the earlier noted issues once one connects to the graphene.[398, 407, 412] It is important to note however, that in cases where CVD grown graphene is utilised, the more commonly encountered CVD substrates are nickel and copper,[407, 413] which can interfere with the observed electrochemistry either beneficially or detrimentally, if the graphene is not sufficiently transferred post-synthesis onto an electrochemically inert alternative substrate.[407, 414, 415] Notably, graphene of similar quality and controllability to that obtained *via* the CVD process can be produced to study its electrochemical properties utilising the original graphene isolation method of mechanically exfoliating layers from HOPG and subsequently applying the residue onto a silicon dioxide slide.[17, 416] This method has been investigated by Valota *et al.*,[416] who were successful in electrochemically characterising a graphene working electrode. Although the above noted methods are able to overcome the limitations of connecting to and studying the fundamental electrochemistry of graphene, they prove cumbersome if one wishes to mass produce graphene electrode substrates and indeed fabricate reproducible graphene electrodes, *i.e.* such as that required for the potential commercialisation of graphene-based devices.

SPEs have attracted a considerable degree of attention in recent years, particularly in terms of their application in electroanalysis.[417-419] Disposable SPEs generally offer beneficial attributes over the more traditional electrodes, given that they are portable and cost effective with their manufacturing process ultimately facilitating the rapid and facile mass production of reproducible sensors, which offer true potential for application in the field.[417] Resultantly there is wide potential scope for the implementation of mass producible graphene-based screen-printed electrochemical sensors in areas such as medicine, food and environmental

science.[398, 417] However, given the known benefits and widespread electrochemical exploration of both graphene and SPEs alike, reports concerning the fabrication and use of disposable graphene-based SPEs are surprisingly limited. The most commonly encountered method of utilising SPEs for graphene exploration in electrochemistry involves drop-casting aliquots of existing carbon black-based or graphite-based SPEs with graphenes, of which there are numerous examples.[243, 420-425] However, such examples fall foul of the earlier noted issues that arise when employing this modification method, and furthermore, the sensitivity and reproducibility of these electrodes is extremely poor.

To overcome such issues, the fabrication of graphene SPEs through the incorporation of graphene into the printable inks is the most plausible approach. Currently there is only one such example that has utilised a graphene-based screen-printing ink to fabricate an SPE.[426] In said work, Ping *et al.* demonstrate the fabrication and characterisation of a graphene SPE utilising an in-house synthesised graphene ink towards the beneficial 'electrocatalytic' detection of Ascorbic Acid (AA), Dopamine (DA) and Uric Acid (UA) in real samples.[426] However, the graphene utilised in their study was fabricated through the reduction of graphitic oxide created *via* the modified Hummers method and thus the reported electrocatalytic effects most likely result from the presence of a large number of edge-plane-like sites and defects present on the basal plane of the graphene surface,[398, 403] and likely has a contribution from metal ions impregnated into the graphene structures. As such, one can infer that the fabricated SPE is electrochemically more graphite-like than graphene-like in nature with respect to the reported edge plane content.[398, 427] Additionally, the developed ink was not a true screen-printable ink, defined as an ink that can be used on a screen for many hours (typically a screen life of >3 hours). Furthermore, although control experiments were performed with graphite-based alternative SPEs, the presence of oxygenated species have been shown to significantly contribute to the observed electrochemistry and, as such, a key

control experiment utilising a graphene oxide-based SPE is missing from this work in order to determine the origin of the reported electrocatalytic response.[398, 403] Through further critical analysis of this work, it must be noted that Raman spectra of the graphene ink utilised and the resultant graphene SPEs were not provided, thus there was no evidence to indicate the presence of single-layer graphene.[426] Rather, the surface topography of their graphene-SPE was examined *via* Atomic Force Microscopy (AFM) and SEM imaging and indicated an abundance of graphitic islands present instead of a uniform graphene coverage;[426] it is thus no surprise that the fabricated electrode exhibits edge-plane-like voltammetry given its composition deviates from that expected for true graphene.[414, 415]

This chapter reports the fabrication, characterisation and electrochemical utilisation of what is the first *real* GSPEs, which are fully characterised (*via* SEM, Raman, XPS and ATR spectroscopy) prior to experimental use. This work utilises newly commercially available printable graphene inks from reputable screen-printing companies rather than lab-synthesised graphene inks. Comparisons of the electrochemical properties are made between the two different graphene inks utilised to fabricate the screen-printed graphene electrodes, with further control experiments employed with respect to comparing the graphene-SPEs to alternative graphite-based SPEs;[403] thus the graphene electrodes are critically explored relative to the benefits of graphene implementation for the fabrication of commercially viable and disposable screen-printable electrodes. This work provides insight into the electrochemical properties of both graphene- and graphite-based SPEs, detailing a new perspective into the future design and fabrication of such SPEs with distinct electrode properties realised which results in possible enhancements for future graphene based bespoke screen-printing technology.

EFFECT OF CURING TEMPERATURE

First considered is the effect of curing temperature upon the graphene inks through comparison of its electrochemical performance using the $Ru(NH_3)_6^{3+/2+}$ redox probe. In addition to the electrodes fabricated using a curing temperature of 60 °C, as per the previous section, both GSPE1 and GSPE2 were also fabricated using a range of curing temperatures (60 – 250 °C) for a curing time period of 30 minutes. The effect of the varying the curing temperature was established not only through the physical effects upon the materials but also the effects on their electrochemical properties, which is elucidated through determination of the electron transfer rate kinetics (k^0) of the sensors. The k^0 is calculated using the Nicholson equation for an electrochemically quasi-reversible process as described by equation 5.1:[398]

$$\psi = k^0 \left[\pi D n \upsilon F / RT \right]^{-\frac{1}{2}}, \tag{8.1}$$

the parameters of which have been defined in Chapter 1. The kinetic parameter, ψ, is tabulated as a function of ΔE_P at a set temperature (298 K) for a one step, one electron process (where α = 0.5). The function of $\psi(\Delta E_P)$, which fits Nicholson's data, for practical usage (rather than producing a working curve) is given by:[428]

$$\psi = (-0.6288 + 0.021X) / (1 - 0.017X), \tag{8.2}$$

where $X = \Delta E_P$, in mV for a one electron process, is used to determine ψ as a function of ΔE_P from the experimentally recorded voltammetry. From this, a plot of ψ against $[\pi D n \upsilon F / (RT)]^{-1/2}$ is produced graphically, allowing k^0 to be readily determined, according to equation 5.1. It was evident that the maximum viable curing temperature for the fabrication of sensors utilising the desired substrate is 200 °C, with temperatures in excess of this resulting in degradation of the substrate. Utilising the remaining GPSE1s, fabricated over the

curing temperature range, scan rate studies were carried out with the resultant electron transfer rate of $Ru(NH_3)_6^{3+/2+}$ redox probe determined. A negligible increase in k^0 is apparent up to 150 °C (rising from 3.68 x 10^{-3} to 9.67 x 10^{-3} cm s^{-1} over a curing temperature range of 60 to 150 °C) utilising a literature D value of 9.1 x 10^{-6} cm^2 s^{-1} for $Ru(NH_3)_6^{3+/2+}$.[320] Notably, upon the utilisation of a curing temperature of 200 °C, a greater increase in the determined k^0 value was evident (4.98 x 10^{-2} cm s^{-1}), though this still represents only a minor deviation when comparisons are drawn with other electrode materials which possess much superior electron transfer kinetics, such as noble metals. Similarly, only minor changes in the determined k^0 were noted upon interrogation of the GPSE2s over the same temperature range, with the k^0 rising from 1.94 x 10^{-3} to 4.39 x 10^{-3} cm s^{-1} up to a curing temperature of 150 °C. However, in contrast with the observations made at the GSPE1, for the case of the GSPE2 the utilisation of a curing temperature of 200 °C was determined to result in a slight reduction in the calculated k^0 value to 1.96 x 10^{-3} cm s^{-1}. It is important to note that although deviations were apparent in the k^0 values calculated at each of the two sensors, no significant effects arise as a result of the curing temperature employed during the fabrication process and as such subsequent studies were carried out utilising sensors fabricated using curing parameters of 60 ºC for 30 minutes.

PHYSICOCHEMICAL CHARACTERISATION

In this section the two newly fabricated and novel GSPEs are characterised in addition to the previously fabricated/characterised edge- and basal-plane-like SPEs in order to provide accurate comparisons using SEM and a series of spectroscopic methods, including Raman spectroscopy, XPS and ATR spectroscopy.

SEM imaging is essential to reveal the surface morphology of the graphene-based electrodes. Figure 5.2 depicts typical SEM images of the four electrodes utilised throughout this work. There are striking similarities between the ESPE (Figure 5.2A) and GSPE1 (Figure 5.2C) electrode, where it can be seen that the surface is relatively rough and disordered, while the BSPE (Figure 5.2B) appears to have an overall smoother surface than ESPE or GSPE1, which is likely due to the high percentage of polymeric binder utilised in the electrode ink of the latter to fabricate a more compacted surface. However the flake sizes appear smaller than the case for GSPE2 (Figure 5.2D) where it is noted that there are large 'dark regions/flakes' which are tentatively attributed to relatively large graphene structures/domains. Figure 5.2A and 5.2B appear the same as SEM images previously reported,[429] where graphite-like structures appear to have assembled upon the surface, as is the case with Figure 5.2C. However 5.2D appears more graphene-like than the others; thus attention is turned to Raman spectroscopy to determine whether graphene-like structures are present upon the surface of the given electrodes.

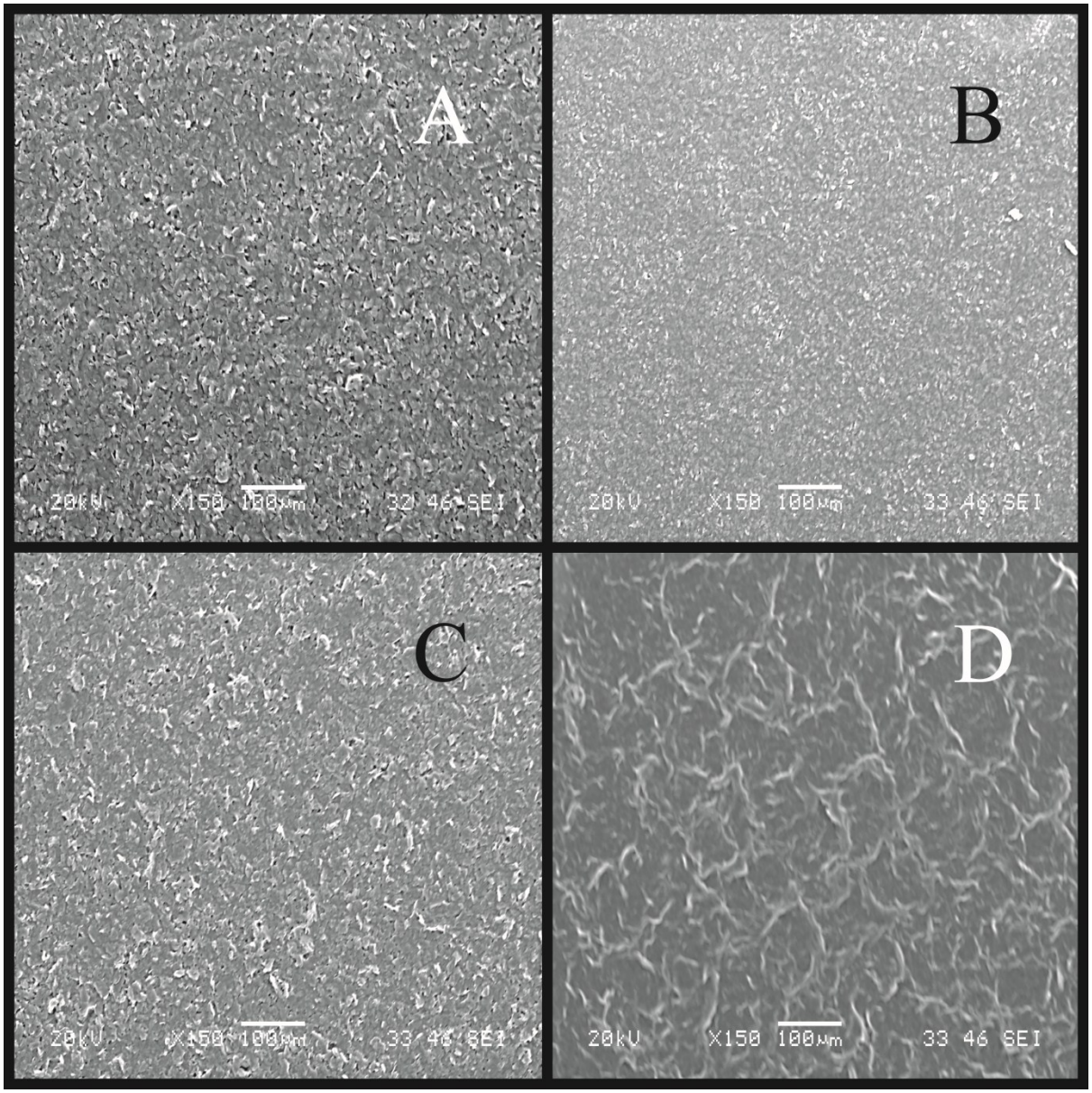

*Figure 5.2: SEM images of the various SPEs: ESPE (**A**); BSPE (**B**); GSPE1 (**C**); and GSPE2 (**D**).*

RAMAN SPECTROSCOPY

Raman analysis was performed to provide further information regarding the graphitic composition of the four SPEs utilised in this work. Figure 5.3 depicts the Raman spectra obtained for each electrode. Figure 5.3A is typical of the ESPE. The band observed at 1580 cm^{-1} is typical of graphite,[430] and is accompanied by a band at 1355 cm^{-1} which is characteristic of graphitic defects typically observed in commercially available graphite

samples.[431] The presence of a small peak at 2700 cm^{-1} (relative to the peak height of the 1580 cm^{-1} band) is also representative of graphite. Similarly, for the BSPE, these three characteristic bands are observed in Figure 3B. The graphitic structure is strikingly similar for these two electrodes; it is the difference in polymeric binder percentages between them which gives the electrodes the edge- or basal-like rate kinetics.[393] Attention is now turned towards characterising the two GSPEs. Through inspection of Figure 5.3C, it is clear that there are no apparent differences in the graphitic structure for GSPE1, in comparison to that of the previous two electrodes. Conversely GSPE2 (Figure 5.3D) exhibits a large characteristic graphene band at 2710 cm^{-1}, which has an intensity lower than the characteristic graphite peak at 1580 cm^{-1}, and does not exhibit the characteristics of that expected for graphite. Literature reports attribute this to few layer graphene, likely in the region of n = 6-8 where n is the number of graphene layers.[432, 433] This is despite the manufacturer claiming that single-layer graphene is utilised and thus, though this may be the case, it is likely that the graphene platelets flocculate and stack whilst in the ink, forming stacked graphite-like (few-layer graphene) structures as previously reported to be the case when utilising graphene paste electrodes.[403] Additionally this is complicated further through the incorporation of the polymeric binder. Hence from the two GSPEs fabricated, one might expect GSPE2 to exhibit more graphene-like electrochemistry. Indeed, the SEM images obtained for the GSPE2 (Figure 5.2D) show a surface that is akin to a graphene-like structure and thus the Raman spectrum and SEM combined confirms this observation.

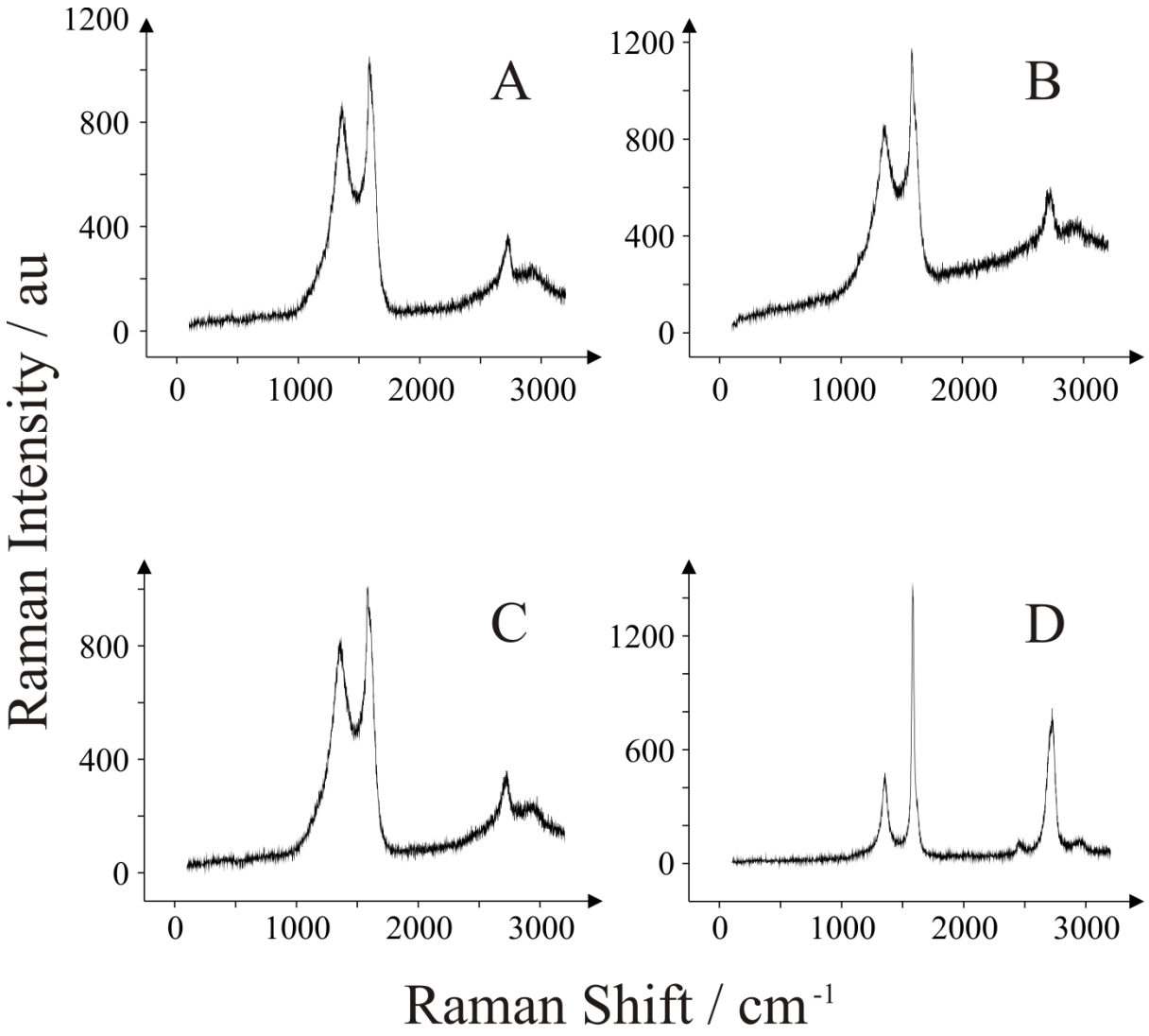

*Figure 5.3: Raman spectra obtained for each of the SPEs utilised: ESPE (**A**); BSPE (**B**); GSPE1 (**C**); and GSPE2 (**D**).*

X-RAY PHOTOELECTRON SPECTROSCOPY

XPS was performed to de-convolute the different types of graphitic species and surface terminations present upon the surface of the SPEs. The XPS spectra of the major components (C1s and O1s) are shown in Figures 5.4 and 5.5 for GSPE1 and GSPE2, respectively. Table 5.1 also lists the surface compositions of both electrodes in atomic percentage (At. %). The GSPE1 sample surface is dominated by graphitic material and a

chlorinated hydrocarbon, likely due to the use of a PVC binder (though the exact origin of this is unknown as ink compositions, especially binders, are proprietary information of the manufacturing company), along with traces of silicon and sulphur (probably as an organic sulphide). The C1s spectrum is complex due to the peak shape of the graphitic material which is very asymmetric; this includes a long tail to high binding energy which overlaps with the chlorinated hydrocarbon, where both obscure any oxygenated functionality. The O1s peak shows no evidence of structure and is difficult to define precisely but some form of alkoxy (C-O) species is likely.

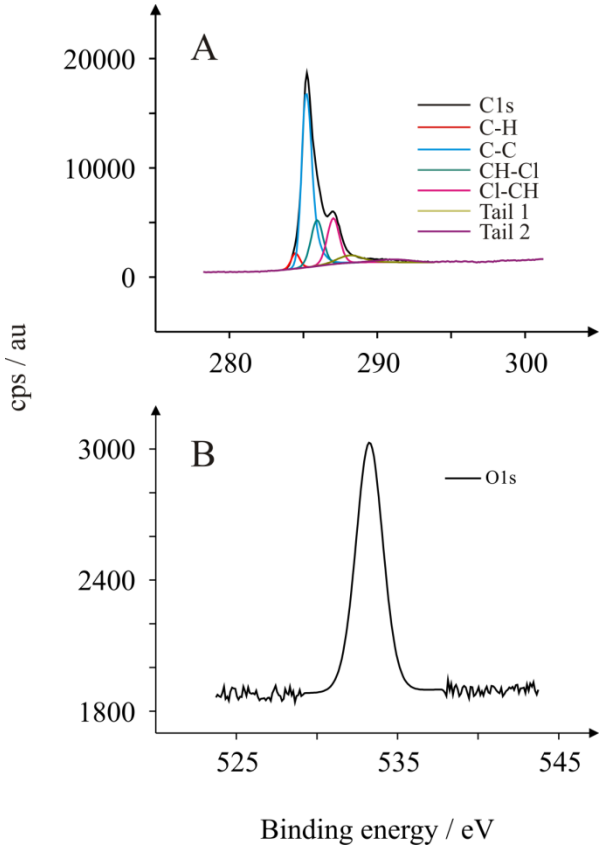

*Figure 5.4: De-convoluted XPS spectra obtained for the GSPE1 for surface carbon species (C1s – **A**) and surface oxygen species (O1s – **B**).*

The GSPE2 sample surface is different to GSPE1 in that there is no evidence of a chlorinated hydrocarbon. The indications are that the surface is mostly graphitic in nature,

with a substantial level of surface oxidation that is difficult to define precisely due to the asymmetric shape and tail of the graphitic C1s peak. There is, however, good evidence for some form of alkoxy (C-O) species in both the C1s and O1s spectra. There are traces of silicon, iron, manganese, sulphur (as sulphide and a sulphate/sulphonate) and bromine, as seen in table 5.1.

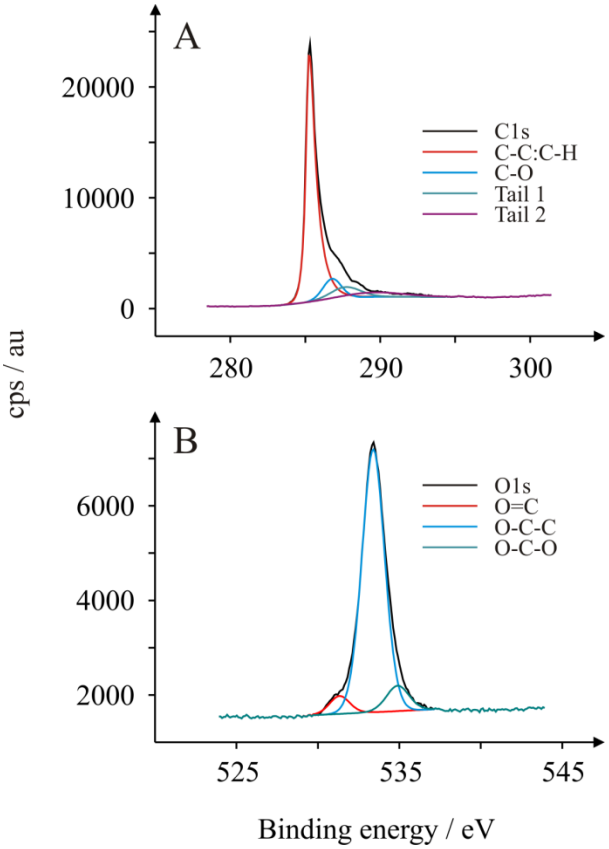

*Figure 5.5: De-convoluted XPS spectra obtained for the GSPE2 for surface carbon species (C1s – **A**) and surface oxygen species (O1s – **B**).*

Table 5.1: De-convolution of the functional group percentages via XPS for the fabricated graphene electrodes, presented as % totals.

Element	**GSPE1**	**Element**	**GSPE2**
Carbon	87.7	**Carbon**	86.8
C-H	3.4	C-C:C-H	64.8
C-C	48.6	C-O	8.7
CH_2-CHCl	14.3	Tail 1	7.4
CHCl	14.3	Tail 2	5.9
Tail 1	4.7	**TOTAL**	86.8
Tail 2	2.4		
TOTAL	87.7		
Chlorine	9.22	**Oxygen**	11.97
Oxygen (organic)	2.94	O=C	0.63
		O-C-C	10.34
		O-C-O	1.00
		TOTAL	11.97
Silicon	0.06	**Silicon**	0.16
Sulfur	0.08	**Iron**	0.30
		Manganese	0.08
		Sulfur, S-	0.21
		Sulfur, SO_x	0.39

	Bromine	0.09

XPS characterisation of the ESPE and BSPE have been performed and reported previously; a more detailed discussion can be found in original works by Gomis-Berenguer *et al*.[429] In their work, the ESPE was found to comprise of 85.9 % surface carbon, displaying graphitic, C-O, and carbonyl groups at 284.5 eV (65.3 %), 285.7 eV (10.5 %), and 286.6 eV (10.1 %), respectively. The BSPE exhibited similar levels of surface carbon (87.5 %), however only graphitic and C-O groups were observed at 284.2 eV (80.5 %) and 285.6 eV (7.0 %), respectively. It is noteworthy too that there is a higher percentage of oxygenated functionalities at the ESPE surfaces, making the electrode more hydrophilic and thus more electrochemically active in aqueous solutions.[429]

Finally the XPS spectra have been de-convoluted to show a range of O/C ratios: 0.315 (ESPE); 0.087 (BSPE); 0.034 (GSPE1); and 0.138 (GSPE2). Surface oxygen content in some cases has a major effect upon observed electrochemical responses and as such these ratios shall have to be considered in the electrochemical characterisation.

ATTENUATED TOTAL REFLECTANCE SPECTROSCOPY

Figure 5.6 illustrates the average ATR spectra for both graphene inks (analysed as-received and in their 'wet' form) being studied within this Chapter. For GSPE2, there is a broad peak at ~1049 cm^{-1}, and a similar band is observed for GSPE1 at ~1132 cm^{-1}. Such bands are typical of C-O bonds appearing in ethers, esters, alcohols or phenol compounds, though XPS conflicts with the report for GSPE1 as the XPS data suggests very little surface oxidation. Hence, the peak at 1132 cm^{-1} is attributed to the solvent utilised within the ink (diacetone alcohol). Next, a prominent band is observed in the GSPE1 sample at 1353 cm^{-1},

which is typical of sp^3 hybridised bending modes. Interestingly, this type of mode does not exist in the GSPE2 sample. There is a prominent sharp band at 1670 cm^{-1} in the GSPE1 sample which is typical of C=O groups; most probably carboxylic acid groups. The shoulder observed at the C=O band on the GSPE1 sample at 1714 cm^{-1} is indicative of –COOH species according to Chen *et al.,* whereas in the GSPE2 ink the C=O band appears at approximately 1659 cm^{-1}, which is more likely to be the deprotonated carboxylate species.[434] The carboxylic acid hypothesis is rationalised here by the appearance of the broad wave at 3400 cm^{-1}, which is typical of various types of –OH modes, however it is noted that the sample was introduced to the ATR spectrometer as a paste and hence there is solvent in the sample which will contribute to this. There is another high frequency triplet band noted in both cases at 2971 cm^{-1}. Reports suggest this is a stretching mode of sp^3 hybridised C-H groups.[435] While this makes little sense in terms of a graphene structure as graphene is sp^2 hybridised, it is reasonable to suggest that the ink is comprised of a variety of carbon structures including some sp^3 hybridised terminating species (such as carbon black which in dispersed in the GSPE1 ink) and the organic solvents (diacetone alcohol in the case of GSPE1 and hexanol in the case of GSPE2) suspending the carbon structures also exhibit sp^3 hybridised bonds and could be responsible for the C-H bonds observed in the ATR spectra.

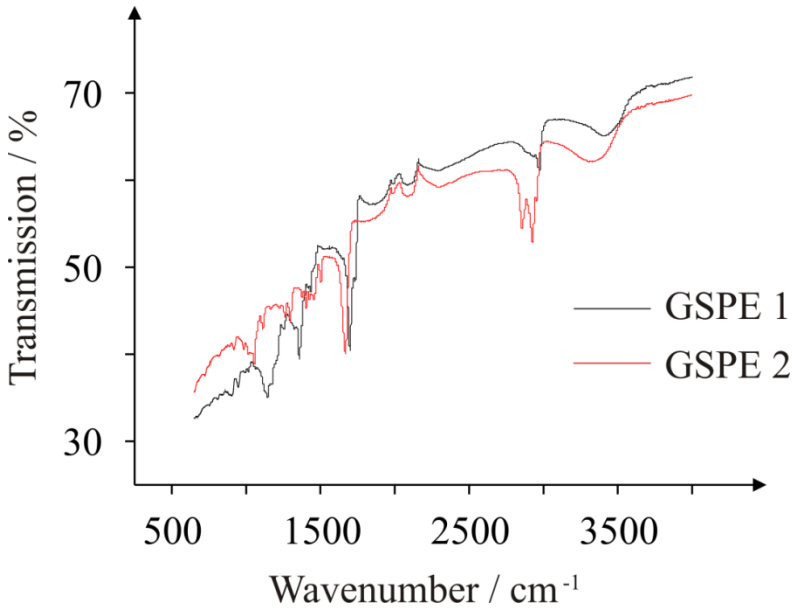

Figure 5.6: ATR spectra obtained for the as-received 'wet' graphene inks utilised in the screen-printing process: GSPE1 (black); and GSPE2 (red).

SUMMARY: PHYSICOCHEMICAL CHARACTERISATION

In summary, it can be concluded from SEM imaging that the surface morphologies of the ESPE and GSPE1 electrodes are strikingly similar and hence could potentially behave in a similar electrochemical manner, whereas the GSPE2 electrode appears to exhibit more basal-like character and will likely exhibit an electrochemical response more akin to that of the basal-plane-like BSPE electrode. Raman analysis of the electrodes confirms that GSPE2 is the most 'graphene-like' electrode fabricated, whereas the other SPEs show Raman spectra typical of graphite. The O/C ratios are 0.315, 0.087, 0.034, and 0.138 for ESPE, BSPE, GSPE1, and GSPE2, respectively. These O/C ratios arise not only from the graphene structures but from other constituents used in the ink fabrication process (solvents, polymeric binders, carbon black). Since the oxygenated groups can affect the voltammetric response, depending upon which probe is utilised, it is hard to de-convolute the electrochemical origin of the screen-printed graphene electrode response, *i.e.* electronic structure (DoS) or O/C

composition. Nevertheless, these screen-printed graphene inks are novel; hence attention is now turned to de-convoluting their electrochemical behaviour towards a selection of electrochemical probes.

ELECTROCHEMICAL CHARACTERISATION

This section focusses on the electrochemical characterisation of the GSPEs utilising the widely known and utilised electrochemical redox probes, hexamine-ruthenium (III) chloride, potassium ferrocyanide (II), and N,N,N′,N′-TetraMethyl-*p*-PhenyleneDiamine (TMPD). The electrochemical responses of biologically relevant analytes such as Ascorbic Acid (AA), β-Nicotinamide Adenine Dinucleotide (NADH), Uric Acid (UA) and DopAmine hydrochloride (DA) are then investigated.

However, first considered are appropriate background scans. Figure 5.7 depicts voltammetric curves for the four electrodes in pH 7.4 PBS (0.1 M) only. It is clear that in the case of ESPE, BSPE, and GSPE1, the electrodes have comparable wide potential windows, ranging from approximately –0.6 to +1.0 V (*vs.* Ag/AgCl), which are useful for voltammetry. Of interest is GSPE2, which exhibits unusual voltammetric behaviour. In the positive potential region there is a redox couple, likely originating from the polymeric binder or solvent used in its fabrication, and in the negative region there are also some other electrochemical processes taking place; the exact origin of these electrochemical responses are unknown since the exact information of the ink composition is proprietary information of the ink manufacturer. However, it has since been proved that there are metallic impurities, such as Fe^{III}, which are involved in electron transfer processes when studying hydrazine.[436] As a result of these observations, this electrode must be operated within a small potential

window (–0.5 to +0.5 V *vs.* Ag/AgCl) otherwise these voltammetric profiles observed in the blank will voltammetrically interfere. This may also affect the electrochemistry of the redox probes and is considered during the analysis.

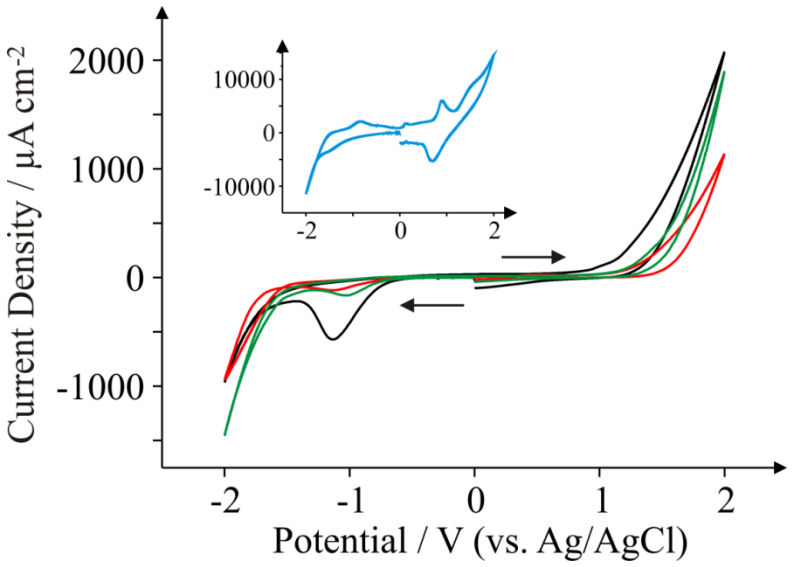

Figure 5.7: Background blank cyclic voltammograms obtained in pH 7.4 PBS (0.1 M). All recorded at a scan rate of 100 mV s^{-1}: ESPE (black); BSPE (red); GSPE1 (green); and GSPE2 (blue; inset).

HEXAAMINE-RUTHENIUM (III) CHLORIDE

Attention was next turned to exploring the voltammetric response of the SPEs with hexamine-ruthenium (III) chloride, a commonly used redox probe for the electrochemical characterisation of electrode surfaces.[437-439] Figure 5.8 depicts the observed redox behaviour of the four SPEs. Analysis of the voltammetric profiles in this section is undertaken in terms of the voltammetric ΔE_P of the oxidation and reduction reactions.

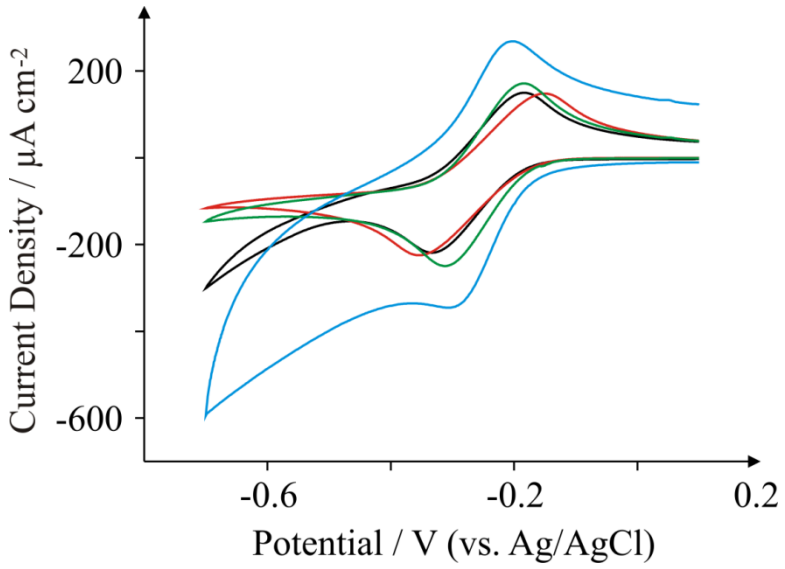

Figure 5.8: Cyclic voltammograms obtained for 1 mM hexamine-ruthenium chloride in pH 7.4 PBS. All recorded at a scan rate of 100 mV s^{-1}: ESPE (black); BSPE (red); GSPE1 (green); and GSPE2 (blue).

The voltammetric profiles presented in Figure 5.8 reveal that the GSPE2 exhibits a ΔE_P of 0.102 V whereas GSPE1 exhibits a slightly higher value of 0.127 V while the ESPE ΔE_P of 0.146 V and the BSPE an ΔE_P of 0.202 V (all *vs*. Ag/AgCl). The ΔE_P of the BSPE electrode is largely expected due to the electrode containing a high binder percentage, which effectively blocks fast electron transport at the carbon structure.[393] Therefore the basal-like voltammetry observed for the BSPE electrodes is not an effect of electronic anisotropy, rather the composition of the ink; hence the term ‘’basal-plane-like’’ rather than a “basal plane” SPE is preferred. To further characterise the SPEs, the heterogeneous electron transfer rate constant, k^0, was deduced as described by equations 5.1 and 5.2. The electron transfer rate constants of hexaammine-ruthenium (III) chloride for the four electrodes were found to correspond to: 3.36 x 10^{-3}, 2.09 x 10^{-3}, 3.68 x 10^{-3} and 4.07 x 10^{-3} cm s^{-1} for the ESPE, BSPE, GSPE1 and GSPE2 respectively. To ensure a diffusional process was indeed proceeding without thin-layer effects, the peak current was monitored as a function of the applied scan

rate. Analysis of a plot of $\log_{10} I_P$ *versus* $\log_{10} v$ revealed a linear gradient of around 0.5 for all the cases (range 0.45 – 0.51), which is indicative of a diffusional process without thin-layer effects, as noted in the case of carbon nanotubes.[440]

Previous reports regarding the observed electrochemical responses of this probe with electronically anisotropic carbon materials show the electron transfer process to be unhindered with an electrode surface comprising high basal plane density.[441] That is, a small proportion of edge-plane-like sites/defects are required in order to observe near reversible voltammetric profiles. However, going against this trend, recently Brownson *et al.* have explored mono-layer graphene, few layered (termed *quasi*-graphene) graphene and double layer graphene with edge plane and basal plane electrodes fabricated from HOPG, and found that the voltammetric response correlates with the proportion of edge plane sites.[442] This means that in this limit, the lower global percentage of edge plane sites results in voltammetric profiles with a large ΔE_P for a surface with a high basal plane content, and low proportion of edge plane sites or defects.[442] The surface oxygen content of the respective electrodes has no apparent effect upon the observed voltammetric profiles for hexamine-ruthenium (III) chloride. If one compares the experimentally observed electrochemical reactivities of the electrodes (ordered fastest to slowest) one can arrange them in the order GSPE2 > GSPE1 > ESPE > BSPE, which bears no correlation to the surface oxygen content of the electrodes which appear in the order ESPE > GSPE2 > BSPE > GSPE1. This is consistent with the literature reporting that the DoS, rather than the oxygenated species present at the electrode surface, dominate the electrochemical response towards this redox probe.[443] The observed electrochemical reactivity indicates that the ESPE and GSPE1 behave similarly, which is consistent with the physicochemical characterisation presented above. However, it must be pointed out that the origin of the electrochemical reactivity of the GSPE2 which gives the fastest in terms of electron transfer cannot be completely de-

convoluted. This is a result of the ink manufacturer withholding proprietary information concerning the ink formation which is necessary to ascribe the background voltammetry definitively. However, it can be stated that there are impurities found *via* XPS which contribute to the voltammetric responses as well as structural components (graphene) as identified by Raman spectroscopy. The relative contribution of these components to the voltammetry is however impossible to identify at this time.

POTASSIUM FERROCYANIDE (II)

The electrochemical properties of the GSPEs are further explored by observing the redox behaviour of potassium ferrocyanide (II), a frequently used redox probe[416, 444, 445] for characterising electrode surfaces. It is a probe which is known to be surface sensitive, requiring a specific surface interaction for electron transfer to proceed;[443, 446] essentially this means that the number and type of oxygenated species largely affects the observed voltammetry. Figure 5.9 depicts typical voltammetric profiles observed for the four in-house fabricated SPEs at 100 mV s^{-1}, where very different voltammetric behaviours between the two new graphene SPEs are noticed. The edge-plane-like ESPE electrode exhibits a ΔE_P of 0.234 V, while the basal-plane-like BSPE electrode exhibits a far larger ΔE_P of 0.510 V. GSPE1 exhibits characteristic redox behaviour more akin to edge-plane-like carbon electrodes with a ΔE_P of approximately 0.276 V, and GSPE2 exhibits a ΔE_P of 0.671 V (all *vs*. Ag/AgCl). The response observed at GSPE2 cannot be considered, since the response is due to its inherent impurities, as observed in the blank scan. The reactivity of ESPE > GSPE1 > BSPE can be taken into account in terms of GSPE1 being highly graphitic in nature according to the Raman analysis and thus exhibits more graphite-like electrochemical

characteristics than that of basal plane carbonaceous material. Furthermore, ESPE has greater oxygen content over that of GSPE1 giving rise to slightly faster electron transfer, and the BSPE response is expected given the lowest oxygen content and edge plane composition.

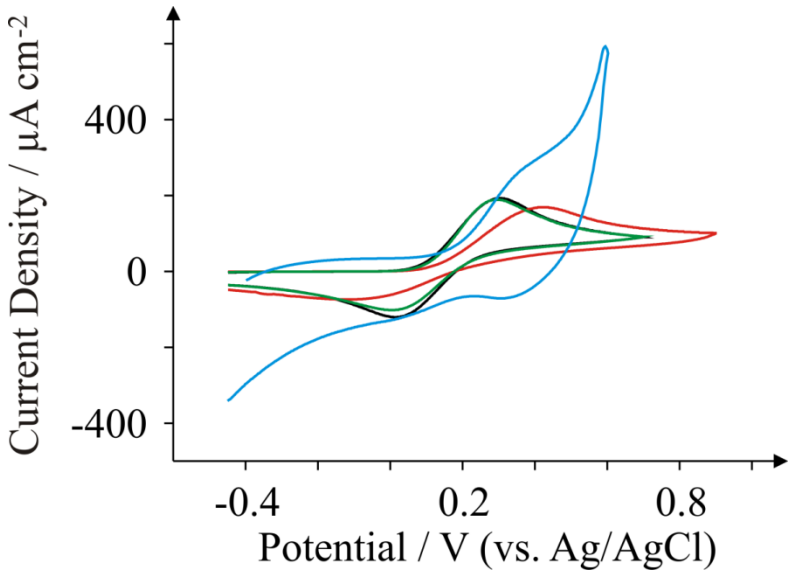

Figure 5.9: Cyclic voltammograms obtained for 1 mM potassium ferrocyanide in pH 7.4 PBS. All recorded at a scan rate of 100 mV s^{-1}: ESPE (black); BSPE (red); GSPE1 (green); and GSPE2 (blue).

N,N,N',N'-TETRAMETHYL-P-PHENYLENEDIAMINE

Another commonly used probe in electrochemistry is TMPD. TMPD is an outer-sphere redox probe utilised by many due to its versatile and unique voltammetric profile which exhibits two near-reversible peaks in organic and aqueous solvents as well as in ionic liquids.[447, 448] In this section, only the first reversible process is studied, which activates at around 0.0 V (*vs.* Ag/AgCl). Figure 5.10 presents voltammetric curves obtained for the four electrodes utilising 1 mM TMPD at 100 mV s^{-1}. The oxidation process occurs at low potentials for all four electrodes utilised here. For ESPE, the ΔE_P corresponds to 0.256 V, similar to that observed for BSPE which exhibits a ΔE_P of 0.249 V. However both graphene-based electrodes are shown to exhibit a reduced ΔE_P compared to graphite-based alternatives:

GSPE1 exhibits a ΔE_P of 0.149 V; whilst GSPE2 exhibits a ΔE_P of 0.093 V, which is the smallest ΔE_P of the four electrodes presented in this work. Since TMPD is known to be dependent on the content of edge plane sites, the response of the GSPE1 is not expected or predicted from prior work on graphitic electrodes; the response at the GSPE2 likely is a result of impurities in the ink, while the response of the GSPE1 is unknown.

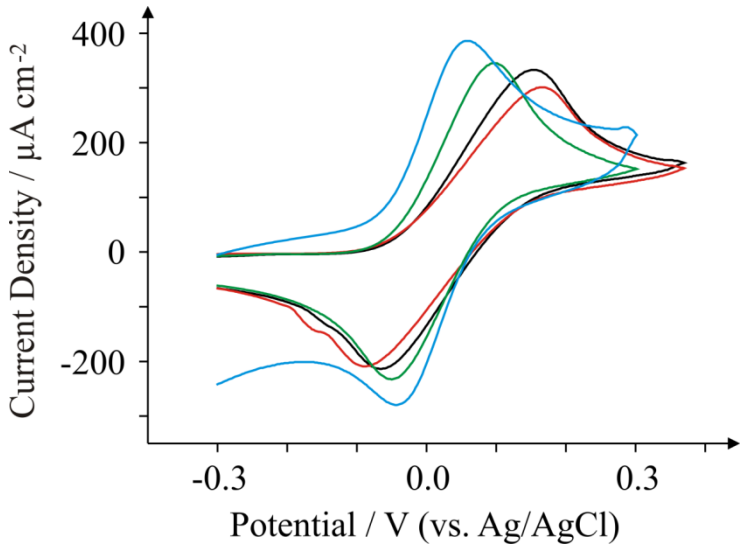

Figure 5.10: Cyclic voltammograms obtained for 1 mM TMPD in pH 7.4 PBS. All recorded at a scan rate of 100 mV s^{-1}: ESPE (black); BSPE (red); GSPE1 (green); and GSPE2 (blue).

B-NICOTINAMIDE ADENINE DINUCLEOTIDE

Attention now turned to NADH, a commonly used electroactive analyte used due to its involvement as a cofactor in enzymatic reactions.[449] The electrochemical performance of NADH is reported in the literature to be dependent upon the density of edge-plane-like sites residing on the electrode surface.[325] Figure 5.11 reveals the oxidation of NADH to occur at +0.61 V for the case of the GSPE1 which is similar to the response observed for the ESPE exhibiting a peak potential of +0.57 V. The peak heights for GSPE1 and ESPE at 100 mV s^{-1} were found to correspond to 261 and 283 µA cm^{-2}, respectively; the electroanalytical utility

of these electrodes is explored later. Referring to the similar surface morphologies which are strikingly similar, it comes as no surprise that these electrodes behave similarly towards NADH. Conversely the peak potentials for the BSPE and GSPE2, which correspond to +0.94 V and +0.99 V respectively, are much higher than observed for the case of ESPE and GSPE1. The peak heights for BSPE and GSPE2 correspond to 173 and 2394 μA cm^{-2}, respectively. The peak heights in all four cases will be investigated electroanalytically later in this investigation. Similar to previous literature, the voltammetric response observed for NADH is dependent upon the density of edge-plane-like sites available.[325] A tenfold increase in current density is observed for the GSPE2; this is rationalised if one observes the blank scans as depicted in Figure 5.7. The oxidation potentials for NADH at a GSPE2 electrode are higher than +0.60 V (*vs.* Ag/AgCl) which results in the voltammetric response for NADH combining with the background response.

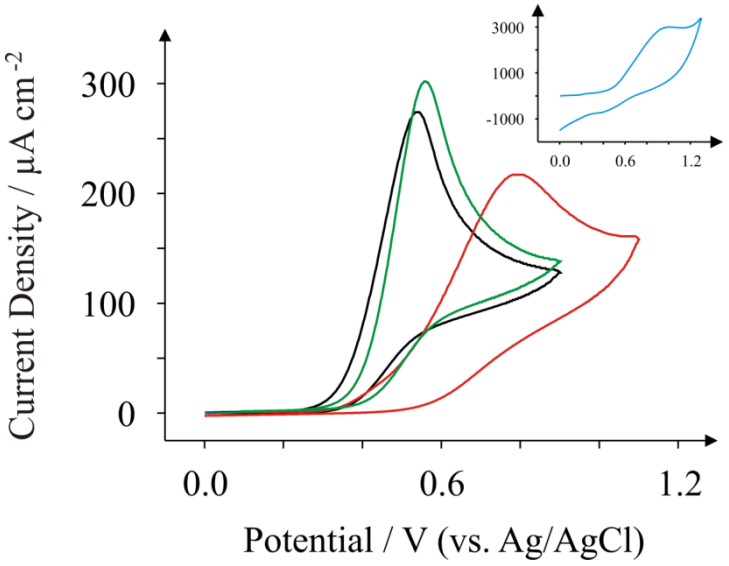

Figure 5.11: Cyclic voltammograms obtained for 1 mM NADH in pH 7.4 PBS. All recorded at a scan rate of 100 mV s^{-1}: ESPE (black); BSPE (red); GSPE1 (green); and GSPE2 (inset; blue).

AA is another commonly used electroactive analyte which is important not only as it is an antioxidant,[450] but also because urinary concentrations can be high and can interfere with desired urinary target analytes such as the neurotransmitter,[451] DA, or UA.[452] Consequently, a cornucopia of studies focus their attention on 'separating out' the signals observed for these analytes.[453-457] This section takes the opportunity to observe the electrochemical behaviour of the graphene SPEs towards these target analytes.

Figures 5.12 - 5.14 depict cyclic voltammograms obtained at 100 mV s^{-1} for 1 mM AA, DA, and UA respectively, at the four electrodes used within this work, where some interesting developments are observed in terms of peak potentials. In the case of AA, the expected E_P of +0.27 V is observed for the ESPE electrode as has been observed previously for edge plane electrodes.[320] It is also seen that the basal-plane-like BSPE electrode exhibits a E_P of +0.71 V as one may expect due to the slower electron transfer rate kinetics generally exhibited by such an electrode. In the case of the graphene electrodes, GSPE1 exhibits similar voltammetry to the ESPE electrode (E_P = +0.31 V) as has been the case on numerous instances throughout this section, yet GSPE2 exhibits a further increase in E_P corresponding to +0.98 V. In the case of DA, a different response is observed. The ESPE and BSPE electrodes exhibit E_Ps of +0.31 and +0.63 V respectively, whilst GSPE1 exhibits a E_P of +0.34 V and GSPE2 exhibits a E_P of +0.40 V. The observation at the GSPE2 is interesting as it does not fall within the same potential range as the E_P observed for AA; therefore said electrode could have a potential use for the simultaneous detection of AA and DA. However, the E_P of UA utilising GSPE2 is +0.82 V, which is similar to that observed towards AA and hence one envisages issues for simultaneous detection of these two target analytes at this electrode. It is also noted that the current densities for GSPE2, as seen in the case of NADH, AA, and UA, are far larger than the other SPEs utilised in this work. This is due to the

activation potentials of NADH, AA, and UA being over +0.60 V for the case of GSPE2, and thus there is background interference from the constituents of the electrode contributing to the overall voltammetric response, shown previously.

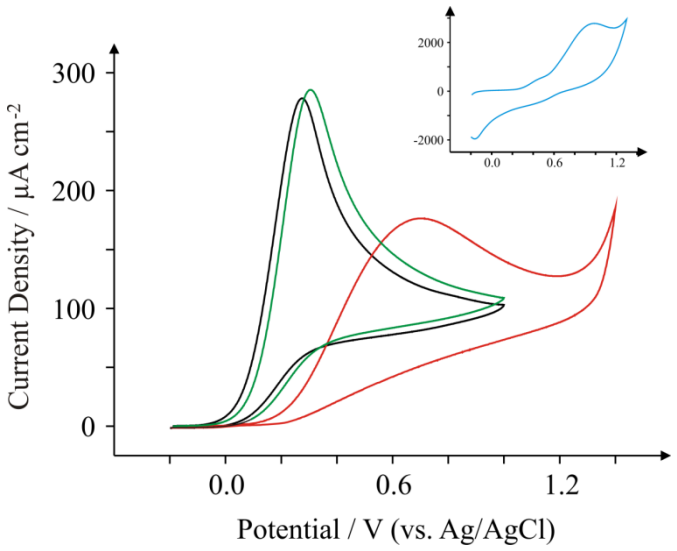

Figure 5.12: Cyclic voltammograms obtained for 1 mM AA in pH 7.4 PBS. All recorded at a scan rate of 100 mV s^{-1}: ESPE (black); BSPE (red); GSPE1 (green); and GSPE2 (inset; blue).

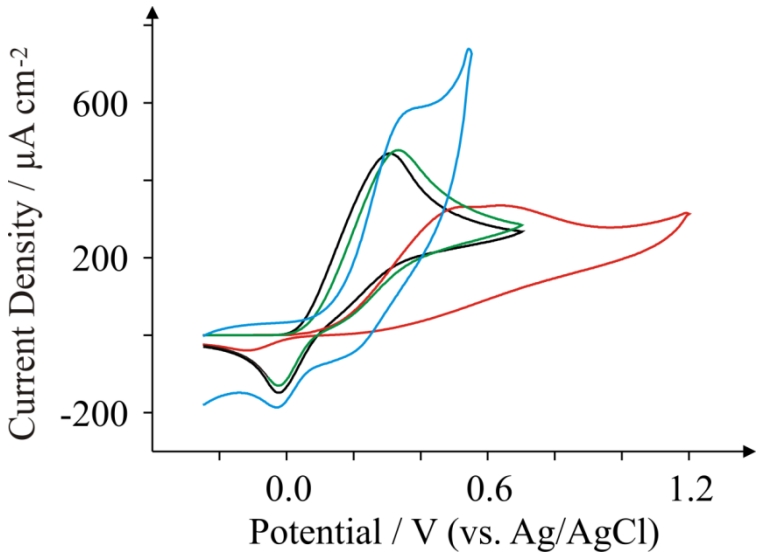

Figure 5.13: Cyclic voltammograms obtained for 1 mM DA in pH 7.4 PBS. All recorded at a scan rate of 100 mV s^{-1}: ESPE (black); BSPE (red); GSPE1 (green); and GSPE2 (blue).

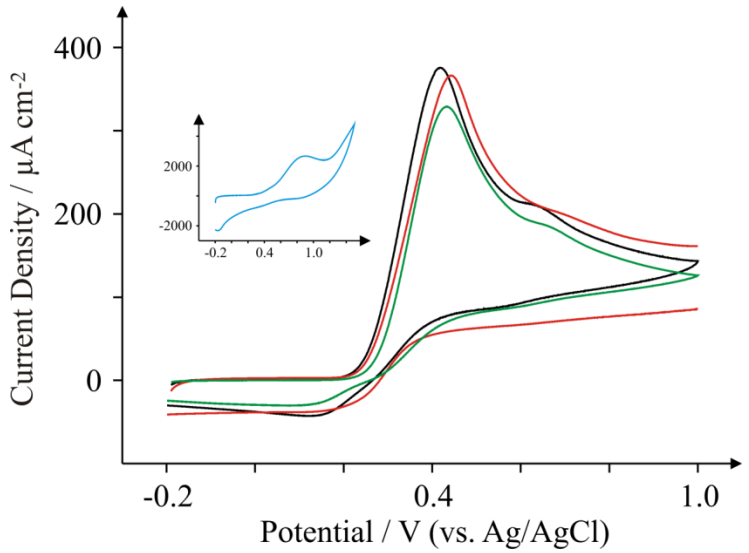

Figure 5.14: Cyclic voltammograms obtained for 1 mM UA in pH 7.4 PBS. All recorded at a scan rate of 100 mV s^{-1}: ESPE (black); BSPE (red); GSPE1 (green); and GSPE2 (inset; blue).

SUMMARY: ELECTROCHEMICAL CHARACTERISATION

Generally, it has been observed that the electrochemical reactivities of the ESPE and GSPE1 electrodes are similar and therefore it can be concluded that the DoS for the ESPE and GSPE1 are similar. That is, the ratio of edge and basal plane sites is similar. This is particularly apparent in the case of electrochemical redox probes studied and the biologically relevant analytes (NADH, AA, UA, DA) where it is observed that the DoS drastically affects the observed voltammetric profiles. Comparing to the physical characterisations presented, where high amounts of edge-plane-like sites are observed for ESPE and GSPE1, such observations are in agreement with the relative surface structures. It is likely that the graphene utilised in the ink for GSPE1 undergoes coalescence in the ink medium which results in multi-layer graphene structures within the ink (a phenomenon observed previously for graphene paste electrodes[458]). On the other hand the GSPE2 electrodes exhibit dramatically different voltammetric behaviour which likely due it the impurities within the ink. While the voltammetric responses are intriguing, fundamental insights from these

electrodes cannot be revealed since the exact composition on the ink is proprietary information.

The advantage of this range of carbon substrates of course lies within the tailoring of the heterogeneous electron transfer rate constant. For instance if one requires a slower electron transfer rate (such as in energy applications), GSPE2 or BSPE may be a wise choice given their slow electron transfer kinetics. Given that there are larger differences in electron transfer rate between the two electrodes, both inks could potentially be used depending upon the specific needs of the system. Furthermore the percentage of polymeric binders can easily be modified in the electrode ink to change the required electron transfer rate constant. Conversely, in the cases where fast heterogeneous electron transfer is required (such as in electroanalytical applications), the ESPE or GSPE1 electrodes are favourable.

CAPACITANCE AND RESISTIVITY INVESTIGATION

The capacitative properties of the newly printed electrodes are investigated. In order to do this *via* CV, the electrodes are scanned between a potential range of 0.0 to +0.8 V in 1.0 M Na_2SO_4. Figure 5.15 depicts cyclic voltammograms in 1M Na_2SO_4 for each electrode investigated within this work, where it is noted that there is little capacitative behaviour attributed to all four electrodes. The lack of capacitative effects associated with the electrodes is beneficial in terms of electroanalysis as the currents observed by the electrodes will not be "masked" by capacitative behaviour and hence limits of detection for such electrodes will effectively be lower.

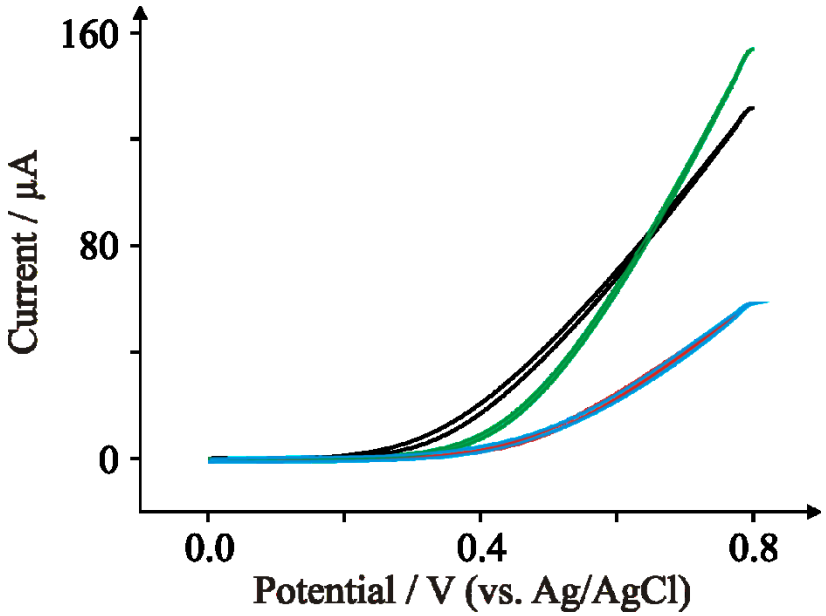

Figure 5.15: Cyclic voltammograms depicting the capacitive behaviour of ESPE (black), BSPE (red), GSPE1 (green), and GSPE2 (blue) in 1 M Na_2SO_4 at 100 mV s^{-1}.

The resistivity of all electrodes utilised is explored using a DVM. Table 5.2 lists the average resistivity obtained for each electrode (N = 5) and the corresponding % RSD. From the resultant resistivity tests, it is noted that the ESPE exhibits an average resistivity of 56.3 Ω cm, while the BSPE exhibits an average resistivity of 89.1 Ω cm. GSPE1 exhibits a relatively low resistivity of 41.8 Ω cm, whereas GSPE2 exhibits an extremely low average resistivity of 8.9 Ω cm. This is unsurprising as one would expect a *true* graphene structure to exhibit a very low resistivity. This also indicates a good patterning and overlap of the graphene platelets within the graphene ink.

Table 5.2: Average resistivity (N = 5) of the various SPEs (with % RSD).

Electrode	Resistivity / Ω cm	% RSD
ESPE	56.3	8.9
BSPE	89.1	4.8
GSPE1	41.8	14.4
GSPE2	8.9	1.6

ELECTROANALYTICAL PROPERTIES

This section focusses upon whether the electrodes are suitable to detect typical electroactive molecules in an analytical context. Figure 5.16 depicts a calibration graph typical of the peak current density observed as a function of concentration of AA in pH 7.4 PBS. Such a high analytical range (approximately 1 – 10 mM) is in contrast to the case of DA sensing, as the concentrations of AA observed within urine are generally higher than other molecules such as DA.[459] All of the electrodes studied exhibit a linear correlation in current density with respect to the concentration of AA. Paying particular attention to GSPE2, a linear range is noted (current density (j) = 130.40 μA cm^{-2} / mM -52.30 μA cm^{-2}; N = 11; R^2 = 0.98) with a LoD (3σ) of 0.68 mM. Such a linear regression over this range is satisfactory for the electroanalytical detection of AA, though it would be preferable to improve the error of the electrodes, and thus the regression coefficient, to facilitate a more accurate AA sensor. This lack of sensitivity is exemplified by studying the reproducibility of the GSPE2 electrode. The GSPE2 electrode exhibited % RSD values as high as 26% over ten additions during

electroanalysis. Comparably, the ESPE exhibited a maximum %RSD of 4%, the BSPE 10%, and finally the GSPE1 4%.

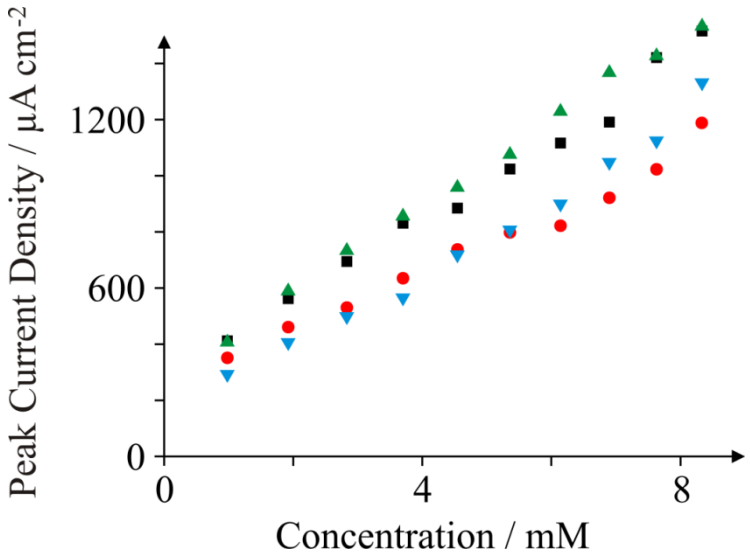

Figure 5.16: Calibration plots depicting I_P versus concentration towards the detection of AA in pH 7.4 PBS at 100 mV s^{-1} (vs. Ag/AgCl), utilising the various SPEs: ESPE (black squares); BSPE (red circles); GSPE1 (green triangles); and GSPE2 (blue inverted triangles).

Similarly, DA was tested electroanalytically utilising concentrations typically found in bodily fluid at normal (approximately 65 – 400 µg per day, equating to approximately 1 – 10 µM)[460] and abnormal levels as typically observed in substance abusers, thrill seekers, insomniacs, and regular exercisers. The results for all four electrodes for AA and DA are depicted in Table 5.3. Upon comparison of the relative sensitivities of each electrode towards both analytes, a different pattern is observed for both target analytes. In the case of AA, the relative sensitivities are (listing the highest current density per mM first): GSPE1 > ESPE > BSPE > GSPE2. Conversely for DA, the relative sensitivities (highest sensitivity per µM) are ESPE > GSPE2 > GSPE1 > BSPE. These trends can be explained in terms of the surface sensitivities of the relevant target analytes. DA is known to be highly sensitive to oxygenated species and as such will nucleate and at oxygenated moieties upon an electrode surface;[461]

hence, it would be expected that ESPE and GSPE2 exhibit a more profound reaction with DA as they are the two electrodes which exhibit the highest amount of oxygenated species according to the XPS results. Thus, such an interaction with oxygenated species will facilitate electron transfer and consequently an increased response observed with respect to increasing concentrations of DA. AA on the other hand is not sensitive to oxygenated species and hence it is the DoS which affects the electro-oxidation of AA. Therefore, one would typically expect to see either GSPE1 or ESPE being the most sensitive to AA due to a high density of edge plane sites, and GSPE2 being the least sensitive given its surface configuration being predominantly a graphene basal plane according to the Raman data.

Table 5.3: Comparison of the electroanalytical performance in terms of sensitivities and LoDs (3σ) obtained at the various SPEs towards the electroanalytical detection of AA and DA (N = 3).

Analyte	Electrode	LoD / AA: mM; DA: μM	Sensitivity / (AA: μA cm^{-2} mM^{-1}; DA: μA cm^{-2} μM^{-1})
Ascorbic acid (AA)	ESPE	0.53 ± 0.01	10.46
	BSPE	0.51 ± 0.03	7.16
	GSPE1	0.35 ± 0.01	11.07
	GSPE2	0.68 ± 0.08	1.024
Dopamine hydrochloride (DA)	ESPE	3.35 ± 0.04	0.66
	BSPE	4.41 ± 0.12	0.34
	GSPE1	1.60 ± 0.03	0.57
	GSPE2	8.08 ± 0.29	0.60

It is an exciting prospect that a mass producible graphene-based electrode exhibits such excellent electroanalytical properties for model target analytes; coupled with the fact that the electrochemical activation potentials are spread across a wider concentration range. The GSPE2 electrode has a potential application for urinary analysis of AA and DA. One major problem that needs addressing with the GSPE2 is that the analytical reproducibility is currently very poor, with some % RSD measurements as high as 25 %. Conversely the ESPE, BSPE, and GSPE1 exhibit % RSD values corresponding to no more than 5 %; this is what many would describe as analytically acceptable. It is clear that the graphene-based SPEs can be utilised electroanalytically if the reproducibility drawback is overcome, and further they could potentially be used for simultaneous detection of urinary analytes such as DA and AA as these reported analytical ranges are suitable for the detection of these analytes in urine samples, see for example;[459, 460] this will be the focus of future work. While such printed electrodes show no benefit over the likes of conventional electrode substrates such as EPPG, they do offer the benefit of tailoring the heterogeneous electrochemical response through the use of polymeric binders, and are easy to use, disposable, and more critically, reproducible. Furthermore in terms of producing graphene electrodes on a mass scale, screen-printed technologies are the front runner, ahead of paste electrodes as SPEs are more reproducible, and ahead of conventional electrodes as they are far cheaper and quicker to fabricate.

5.1.3 CONCLUSIONS

This work has demonstrated, for the first time, the fabrication of a *true* screen-printable graphene ink. The inks utilised in this work exhibit dramatically different electrochemical properties towards a range of analytes, with the responses shown to exhibit noticeable changes depending upon the DoS and binder content and also (although to a lesser

extent) exhibit distinct electrochemical responses with respect to the presence of surface oxygenated species. The experiments presented within this section offer a proof-of-concept approach for screen-printed graphene electrode designs. One of the fabricated graphene electrodes exhibited slow electron transfer properties (potentially beneficial for energy applications) and the other electrode was found to exhibit fast electron transfer kinetics (which can be beneficially employed where fast electron transfer is required, *i.e.* in electroanalysis), demonstrating that graphite control experiments are critical when investigating any type of graphene electrode. Unfortunately, until ink manufacturers declare the exact composition of their graphene (and graphitic) inks, fundamental graphene electrochemistry is precluded. That said, since this work was conducted, the electrodes have been further characterised to prove that Fe^{III} is present within the ink, which will contribute to electrochemical signals, particularly in the case of hydrazine.[436] Nevertheless, this work demonstrates that useful electrochemical responses can be obtained from such electrodes, but caution has to be paid to the excitation potential of the target analyte of interest.

The differing electrode characteristics were achieved due to the inks offering a range of electron transfer rates with one effectively able to tailor the electrode material to suit the application required; these may be implemented for specific purposes depending upon the desired electron transfer rate for a given system, whilst at the same time being mass producible and thus easily accessible for a relatively small cost. Furthermore, these inks can be printed into various shapes, diameters, bands, and arrays with little effort required to modify the electrode design. Consequently this Chapter has presented the fabrication and characterisation of what is believed to be the first real GSPEs which can be printed *via* screen-printing technology over numerous printing cycles and have an ink screen life of more than three hours. This approach utilises newly commercially available printable graphene inks from reputable screen-printing companies instead of lab-synthesized graphene.

The next chapter will focus upon electrochemical impedance spectroscopy for the first time in this thesis, using knowledge gained from the previous three Chapters. The impedance of the equipment utilised will be critically assessed, including the cell, the connections, the electrodes, and even electrode composite modifications. Chapter 6 will be critical for the understanding of the limitations of electrochemical impedance spectroscopy.

CHAPTER 6
ELECTROCHEMICAL IMPEDANCE SPECTROSCOPY OF CARBON ELECTRODES AND COMPOSITES

The aim of this Chapter is to bring together all the concepts discussed in the previous three chapters, and now use Electrochemical Impedance Spectroscopy (EIS) to critically analyse a vast array of carbon electrodes with a view to determining whether EIS is a suitable technique for the purposes of electroanalysis. For this endeavour, the frequency-dependent properties of the equipment are explored, in addition to carbon electrodes, SPEs, and carbon composite electrodes. There will also be a fundamental investigation towards the potential of zero charge for some of the in-house fabricated SPEs. Many fundamental concepts of EIS, discussed in Chapter 2, are applied within this Chapter.

All chemicals were used as-received, of the highest purity, and were obtained from Sigma-Aldrich (UK). Aqueous solutions were made up with deionised water of resistivity no less than 18.2 MΩ cm. HydroQuinone (HQ) and $K_3[IrCl_6]$ were chosen as the model analytes for this section. HQ and $K_3[IrCl_6]$ were made up to a concentration of 2 mM and 1 mM, respectively, in pH 7.4 PBS (0.1 M) with 0.1 M KCl background electrolyte.

All electrochemical experiments were performed in nitrogen degassed HQ solutions with an Ivium CompactStat^{TM} (Netherlands) potentiostat, housed within a home-built copper mesh Faraday cage. The Faraday cage was tested robustly and gave almost no background electromagnetic interference. The frequency range for the impedance tests depending upon the test; for the instrument tests a range of 10000000 – 0.2 Hz was used, whereas for other tests, a frequency range of 10000 – 0.2 Hz was selected. All Nyquist plots take into account the surface area of the electrode.

Ideal resistors (0.1, 1, and 10 kΩ) were obtained from RS electronics. The working and sense cables were twisted together, as were the reference and counter cables, as per online recommendation. Screen-printed connectors were obtained from Kanichi Research Services (Cheshire). The connection was modified using an RS connector card (stock no: 767-7067) with a 2.54 mm pitch. The connectors exhibit a total impedance of 1200 Ω over a frequency range of 100000 – 0-1 Hz.

A range of electrode substrates are investigated within this section: EPPG; BPPG; BDD; ESPE; BSPE; GSPE; and introducing two new printed electrodes, Single-Walled carbon nanotube SPE (SW-SPE) and Low-Resistance Ink SPE (LRI-SPE). Macroelectrodes are referenced against an SCE, while SPEs are referenced against the on-board Ag/AgCl pseudo-reference electrode. Carbon composite materials were suspended in equal measures of water and ethanol, to speed up the evaporation process. The exception is pristine graphene,

which was used as-received, and was suspended entirely in ethanol. All suspensions were sonicated prior to casting upon the surface. Sonication ensures agglomeration of graphene sheets is kept to a minimum.

The electrolytes selected for the potential of zero charge experiments were 0.1 M KCl/NaCl.

6.1 INTRODUCTION

In any scientific investigation, the user has to be wary of the limitations of the equipment and techniques being utilised. For instance, if one wishes to understand the effects of mass transport whilst using CV, the concept of natural convection must be considered when scan rates are slow. Likewise, when using EIS, many parameters have to be taken into account, and it is especially necessary to know the limitations of the equipment being used, so false positives are not confused with actual experimental data.

EIS is, at times, an unpredictable technique, and is certainly one in which is difficult to master. This is particularly the case when using Nyquist plots, because complex mathematical transforms are being used to present the data, and the user must understand any slight changes in impedance trace. In order to ascribe any changes to the electrochemical system only (that is, the interaction at the electrode|electrolyte interface), the impedance contributions from the equipment, electrodes, and electrolyte must be vigorously investigated. This is considered in this Chapter, as well as the comparison between impedance profiles of several carbon materials and composites.

IMPEDANCE CONTRIBUTIONS FROM THE EQUIPMENT

Though the impedance measurements conducted in the majority of this thesis look at *Faradaic* processes, it is still necessary to look at the total impedance contributions of the equipment, to predict and/or have an idea of the total "background" impedance due to the equipment. Several tests were conducted to determine the efficiency of the equipment being used for EIS experiments.

IDEAL RESISTORS

Ideal resistors (resistance should be the same across all frequencies) were tested using typical equipment check procedures detailed by Gamry.[462] Figure 6.1 depicts the change in total impedance, $|Z|$, and phase angle, as a function of the frequency of the AC signal. The resistance of three ideal resistors stays constant across a wide frequency range, however above 50 kHz the resistance fluctuates, particularly in the case of the 10 kΩ resistor. This is indicative of average quality impedance equipment. The manufacturer states that impedance measurements are obtainable up to 1 MHz; this is clearly not the case. Even with the copper Faraday cage, the maximum limit is 50 kHz. Fortunately the charge transfer frequency range normally lies within the region of 10000 – 1 Hz, so for the purposes of EIS, frequencies above 50 kHz are not required. The second thing to note is that the EIS spectra show the correct resistances for each resistor used, when the phase angle is zero. It is clear from Figure 6.1 that the uncertainty increases as the size of the resistor increases, in terms of the operational frequency range and the noise.

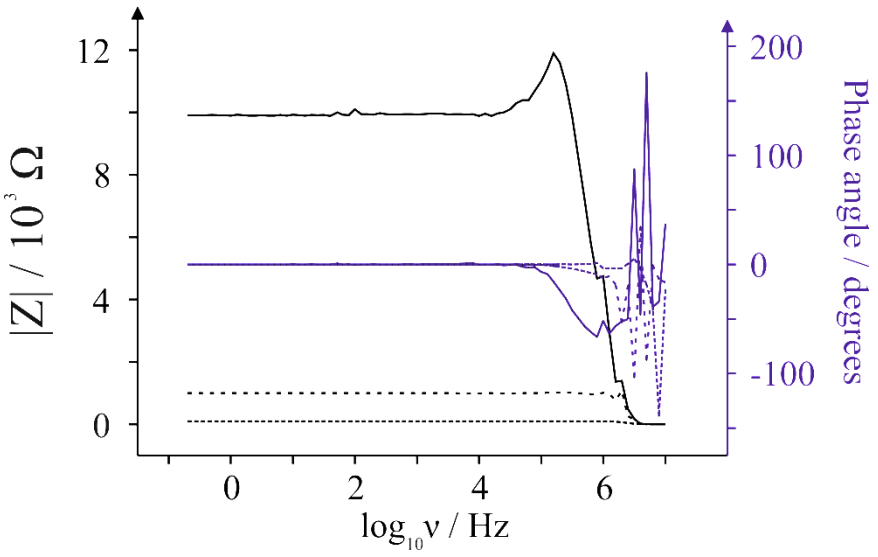

Figure 6.1: Bode plot, consisting of the (black) total impedance, and (purple) phase angle, for three ideal resistors: 10 kΩ (solid lines); 1 kΩ (dashed lines); and 0.1 kΩ (dotted lines). Parameters: +20 mV DC excitation potential; 10 mV AC amplitude; 10 frequencies recorded per decade.

MACROELECTRODES

Next considered is the total impedance and phase angle of edge- and basal-plane graphite electrodes, in addition to the common auxiliary electrode, platinum. Electrodes should be designed to have low impedances, and effectively not contribute significantly to an electrochemical response. Therefore, it is no surprise that the three electrodes tested exhibit small total impedances, as observed in Figure 6.2. For a platinum electrode, the impedance change is almost nil over an eight order of magnitude change in frequency. The macroelectrode EPPG and BPPG both exhibit far more stable phase angles across six orders of frequency change, but do become unstable above 100 kΩ. Perhaps the most surprising observation from Figure 6.2 is the fact that the impedance of a BPPG electrode (~5 Ω) is far smaller than that of an EPPG electrode (~130 Ω). This could suggest a faulty electrode, and needs to be kept in mind for the remainder of this section.

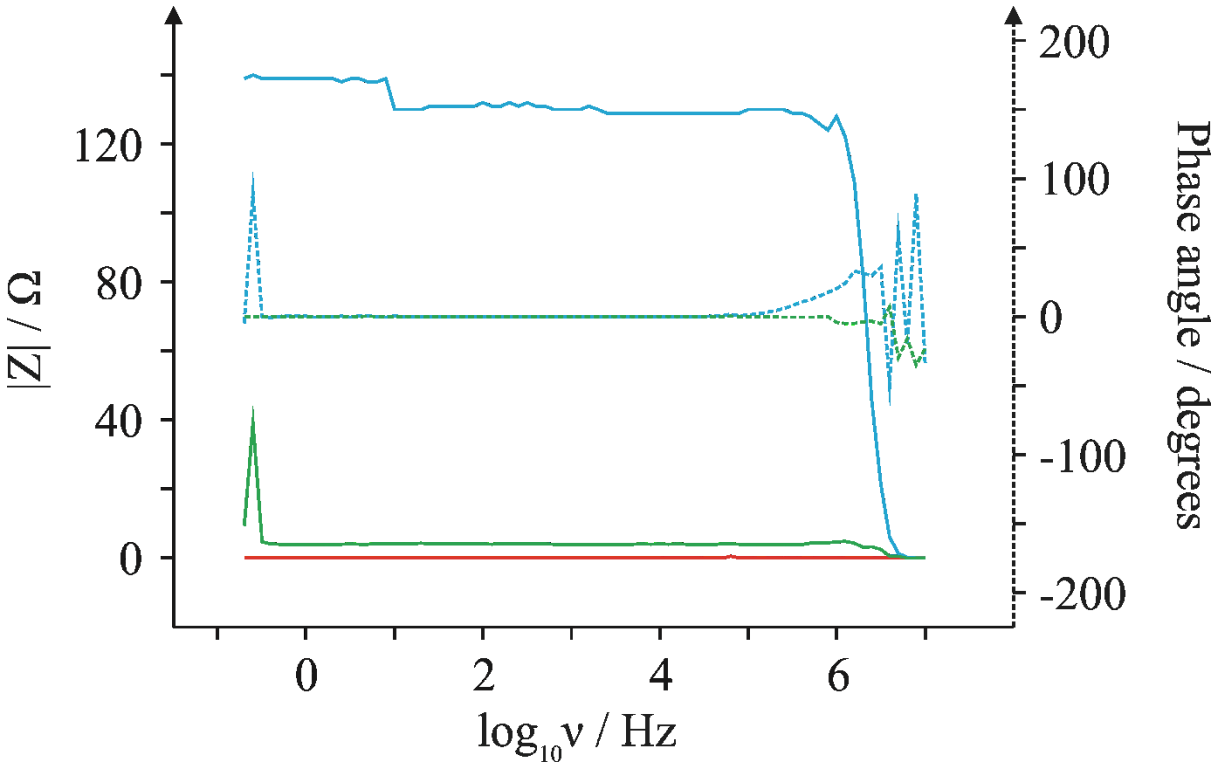

Figure 6.2: Bode plots for EPPG (blue), BPPG (green), and platinum (red) electrodes. Parameters: +20 mV DC excitation potential; 10 mV AC amplitude; 10 frequencies recorded per decade. A 20 mV DC excitation potential was used because a slight excitation is required for the experiment, but Faradaic exchanges needed to be avoided; such a small offset satisfies these needs.

PRINTED ELECTRODES

The next consideration is a key part of this section of work: the total impedance contribution of the SPEs. The printed carbon layers will likely contribute to the total impedance because the working surface of the electrode is not as homogeneous as a carbon macroelectrode, for instance. Figure 6.3 presents Bode plots for the five different types of SPE tested. From Figure 6.3 it is apparent that the ESPE and BSPE electrodes exhibit the highest total impedance for the five electrodes tested (~2750 Ω). Next, GSPE and SW-SPE both exhibit a total impedance of ~1500 Ω, within the analytical frequency range. The graphene SPE is more likely to be graphite-like, as discussed in Chapter 5, so will be akin to

the SW-SPE in terms of edge-plane-like sites. Therefore one may expect the SW-SPE and the GSPE to exhibit similar impedances. Finally, the Low Resistance Ink SPE (LRI-SPE), which is a new electrode tested for the first time in this thesis, exhibits the smallest total impedance of ~1100 Ω. This, though expected, is a significant result because it selects itself as the electrode of choice for standard EIS experiments. To put this into perspective, LRI-SPE exhibits a 33% decrease in impedance compared to carbon nanomaterial SPEs. This is a significant decrease, thus these electrodes will be used for future work where EIS is required.

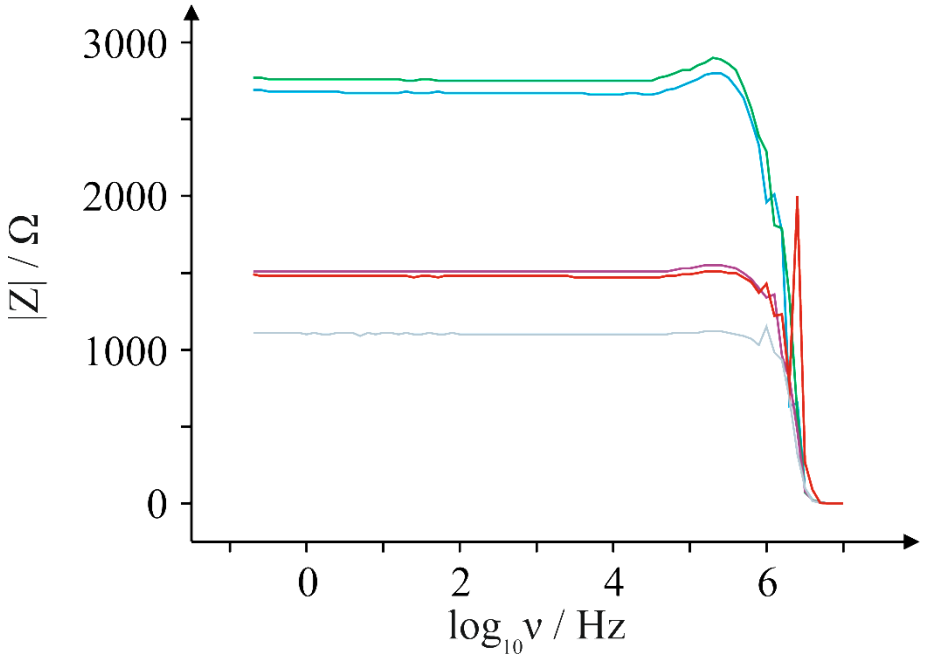

Figure 6.3: Bode plots for five SPEs: ESPE (blue); BSPE (green); SW-SPE (purple); GSPE (red); and LRI-SPE (grey). Parameters: +20 mV DC excitation potential; 10 mV AC amplitude; 10 frequencies recorded per decade.

In this section the resistance of the solution is considered. In a typical Randles circuit, the solution resistance in is series with the parallel contributions of R_{CT} and C_{DL}. The solution resistance is measured at high frequencies, and in the case of a Nyquist plot, it is equivalent the left-most point on the graph (see Chapter 2). To test the contribution of the electrolyte, an LRI-SPE is immersed in a solution of 1 mM $K_3[IrCl_6]$, with a 20 mV DC excitation potential. Figure 6.4 illustrates the total impedance contribution and the phase angle shifts over a frequency range of 0.1 – 10000000 Hz. At high frequencies, it can be observed that both the phase angle and the impedance contribution become unstable (above 1000000 Hz). In the mid-to-high frequency range, the phase angle tends to zero, thus in this region the system is purely resistive. In the solution-free tests previously, the equipment remains purely resistive over this range, in addition to frequency ranges down to 0.1 Hz. Therefore, this Figure shows quite succinctly that the total impedance of the solution is *highly* frequency dependent; and therefore the analytical range, when observing charge transfer resistances, should be limited to 100000 - 5000 Hz. Unlike in the case of the electrodes, the total impedance begins to rise significantly below 5000 Hz. This is due to capacitative charging. At high frequencies, charge dissipates from a capacitor more easily than the case of low frequencies, making lower frequencies more resistive to current flow. At lower frequencies, the electric field due to stored charge becomes more of an opposition to the current flow, thus the total impedance of the system increases. This phenomenon occurs at the working electrode surface.

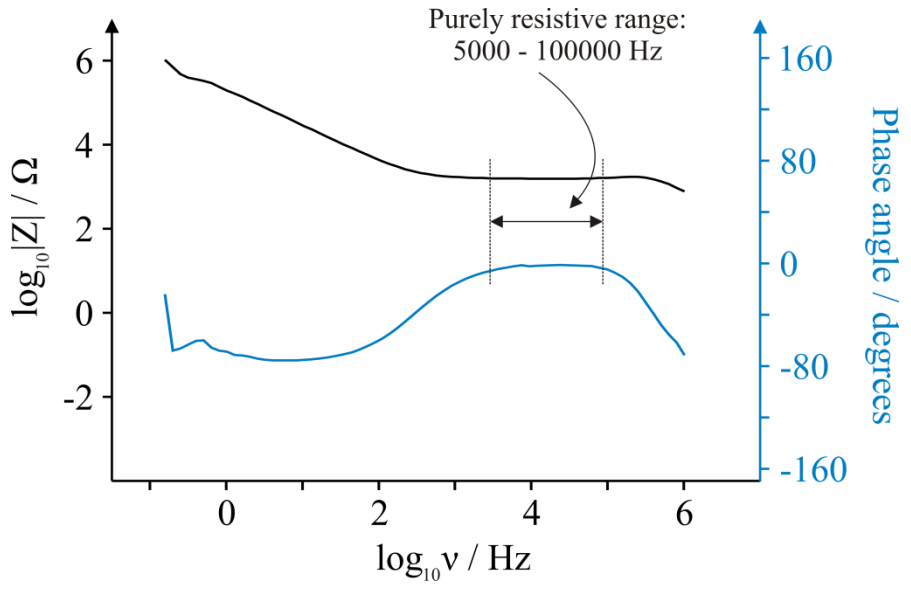

Figure 6.4: Bode plot for 1 mM $K_3[IrCl_6]$ in pH 7.4 PBS with 0.1 M KCl electrolyte. Parameters: +20 mV DC excitation potential; 10 mV AC amplitude; 10 frequencies recorded per decade; LRI-SPE utilised.

Next considered is the same system as presented in Figure 6.4, but with an excitation potential high enough to instigate a Faradaic process. In order to work out a suitable excitation potential, CV was performed, revealing an oxidation half-wave potential of 550 mV. This was chosen as the excitation potential for this system. Figure 6.5 depicts the Bode plot for the Faradaic case. In this case, the high- and medium- frequency zones behave exactly the same as the case in Figure 6.4. The total impedance in the medium-frequency range also remains similar in both cases. In the low-frequency range, the system changes. It is evident from Figure 6.5 that the phase angle tends to decrease, then increase again, whereas in Figure 6.4 the phase angle tends to decrease then remains at -80 degrees. Also, the total impedance increases as the frequency decreases, but in Figure 6.4, a continual decrease is evident up to 0.1 Hz, whereas in the Faradaic case in Figure 6.5, the impedances increases first, then remains relatively constant after 10 Hz. The point where the phase angle returns to zero in the low-frequency range is where the R_{CT} is measured in a Nyquist plot. From the

Bode plot, there is a change in impedance of approximately 17000 Ω between these two points, but a Bode plot cannot de-convolute this value into resistance and reactance contributions; thus a Nyquist plot must be inspected to assign the origin of these changes. It can be speculated, however, that the low-frequency contribution is not a diffusional contribution, because the phase angle change remains less than 45 degrees throughout the low-frequency domain. Between the two labelled regions on Figure 6.5, the change in phase angle is typical of capacitative charge; if the impedance is increasing as the frequency decreases, but the applied AC amplitude remains constant, then the current must be decreasing, which is a phenomenon typical of a capacitor.

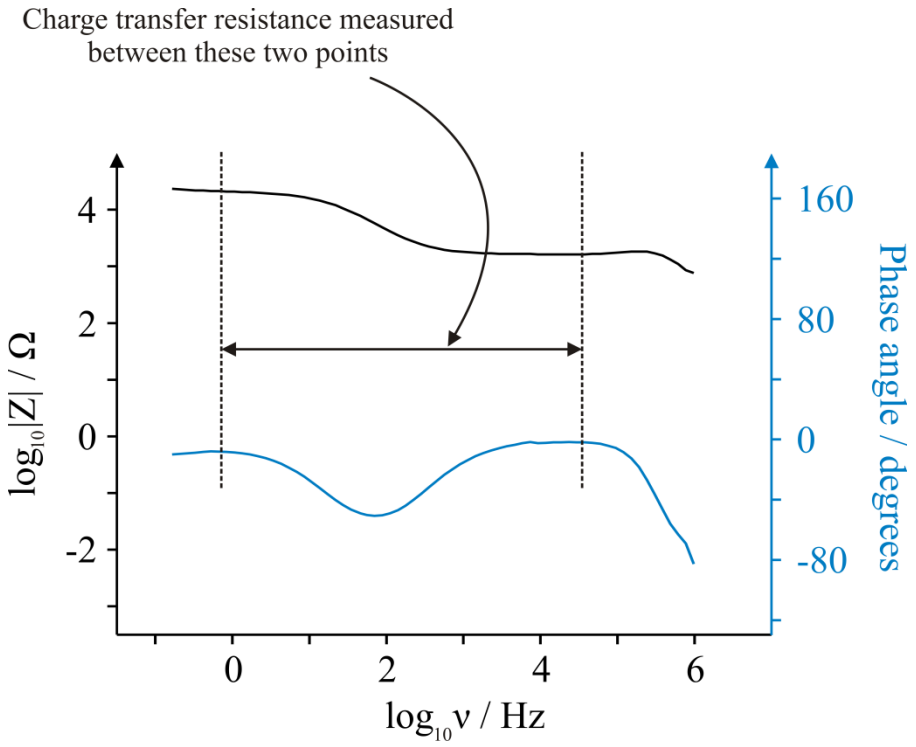

Figure 6.5: Bode plot for 1 mM $K_3[IrCl_6]$ in pH 7.4 PBS with 0.1 M KCl electrolyte. Parameters: +550 mV DC excitation potential; 10 mV AC amplitude; 10 frequencies recorded per decade; LRI-SPE utilised.

The above results are tabulated as a Nyquist plot in Figure 6.6 in order to de-convolute the relative contributions to the total impedance in the medium-frequency range. In the case of the non-Faradaic response, there is no charge transfer evident, as one would expect. In the lower frequency range, there is a large impedance contribution from both the real and imaginary components of the Nyquist plot. This is due to a high level of capacitative impedance as a result of the high electric field in the electric double layer. Conversely, in the case of the Faradaic experiment, the Nyquist plot displays two distinct regions. The first region in the high frequency range is the solution resistance, which equates to 1600 Ω, as per the Bode plots presented above. The second region is the charge transfer region, which exhibits a value of approximately 18000 Ω. This is similar to the total impedance observed in the low-frequency region in Figure 6.5. The Nyquist plot shows little diffusional behaviour within the frequency range; this is an indication that the rate of electron transfer is far quicker than the diffusion in the system, *ergo* an electrochemically reversible system. This would be expected for such a system.

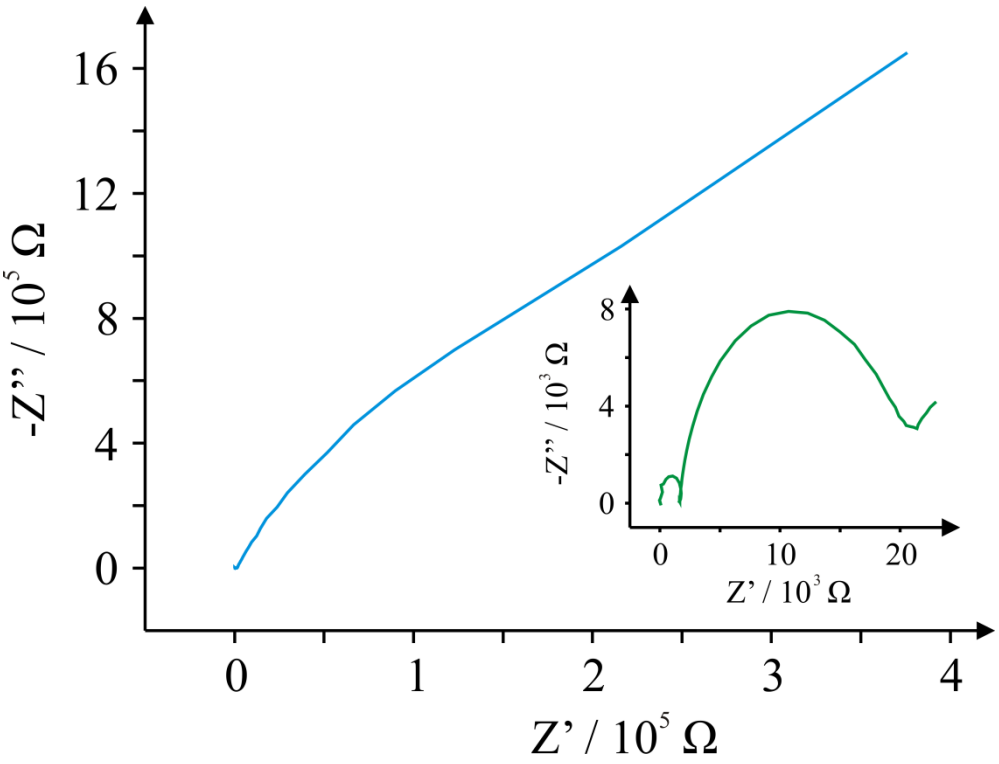

Figure 6.6: Nyquist plots for 1 mM $K_3[IrCl_6]$ in pH 7.4 PBS for the non-Fardaic (blue) and Faradaic (green) cases. Parameters: variable DC excitation potential; 10 mV AC amplitude; 10 frequencies recorded per decade; +20 mV DC potential (non-Faradaic case); +550 mV DC potential (Faradaic case); frequency range: 10000000 – 0.2 Hz.

POTENTIAL OF ZERO CHARGE

In physical chemistry, a fundamental concept exists, called the point of zero charge. The point of zero charge describes the point at which the electrical charge upon a surface equals zero. This concept is usually investigated in colloidal science, and is frequently described in terms of pH.[463] That is, the point of zero charge would be the pH at which the surface of a colloidal particle would exhibit zero charge. This would normally cover a pH range and is described as the isoelectronic point. Methods to deduce the point of zero charge include zeta potential measurements and potentiometric titrations.[464] This can also be applied to electrode surfaces. The Potential of Zero Charge (PZC) is the potential applied across an

electrode in which the net charge in the ion cloud surrounding the electrode is zero. This is dependent upon the type of electrode surface and the electrolyte (or more specifically, the mass/charge ratio of the anions and cations in the electrolyte). Mathematically, the PZC can be represented as[465]

$$\phi^E - \phi^S = 0, \tag{6.1}$$

where ϕ is the charge of the electrode (E) or solution (S). Intuitively, in the case of equation 6.1, the m/z ratio of the solution is enough to balance out the charge at the potential applied, ϕ^E.

This phenomenon can be observed at electrode surfaces through capacitance measurements, because

$$C = \frac{Q}{V}, \tag{6.2}$$

where C is the capacitance at the electrode surface, Q is the charge of the electrode surface, and V is the potential difference between the electrode and the solution. The capacitance can thus be measured utilising EIS, by scanning between a fixed frequency range and modelling with a simple RC circuit as depicted in Figure 6.7.

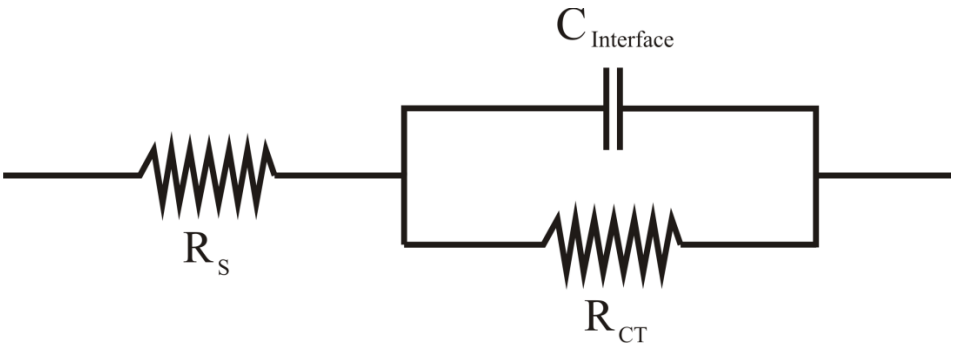

Figure 6.7: RC circuit used to model capacitance values from PZC experiments, utilising EIS.

In concentrated electrolytes, the interfacial capacitance, $C_{\text{Interface}}$, is equal to

$$\frac{1}{C_{Interface}} = \frac{1}{C_Q} + \frac{1}{C_H} + \frac{1}{C_{Diffusion}}, \tag{6.3}$$

where C_Q is the quantum capacitance, C_H is the capacitance due to the Helmholtz layer, and $C_{\text{Diffusion}}$ is the capacitance due to the diffuse double layer. These experiments assume that the capacitance due to the diffuse double layer can be neglected due to high concentrations of electrolyte,[466] and thus the last term is ignored. According to Stoller and co-workers, the liquid side of the interface dominates the interfacial capacitance at metal electrodes,[466] meaning that the capacitance due to the Helmholtz plane can be calculated by observing the capacitance at a metal electrode. As per the excellent work by Stoller, a capacitance value of 28 μF cm^{-2} is observed at gold and platinum electrodes.[466] An example of a quantum capacitance plot is depicted in Figure 6.8; it is this sort of relationship which is expected for SPEs, but in terms of $C_{\text{Interfacial}}$, not C_Q.

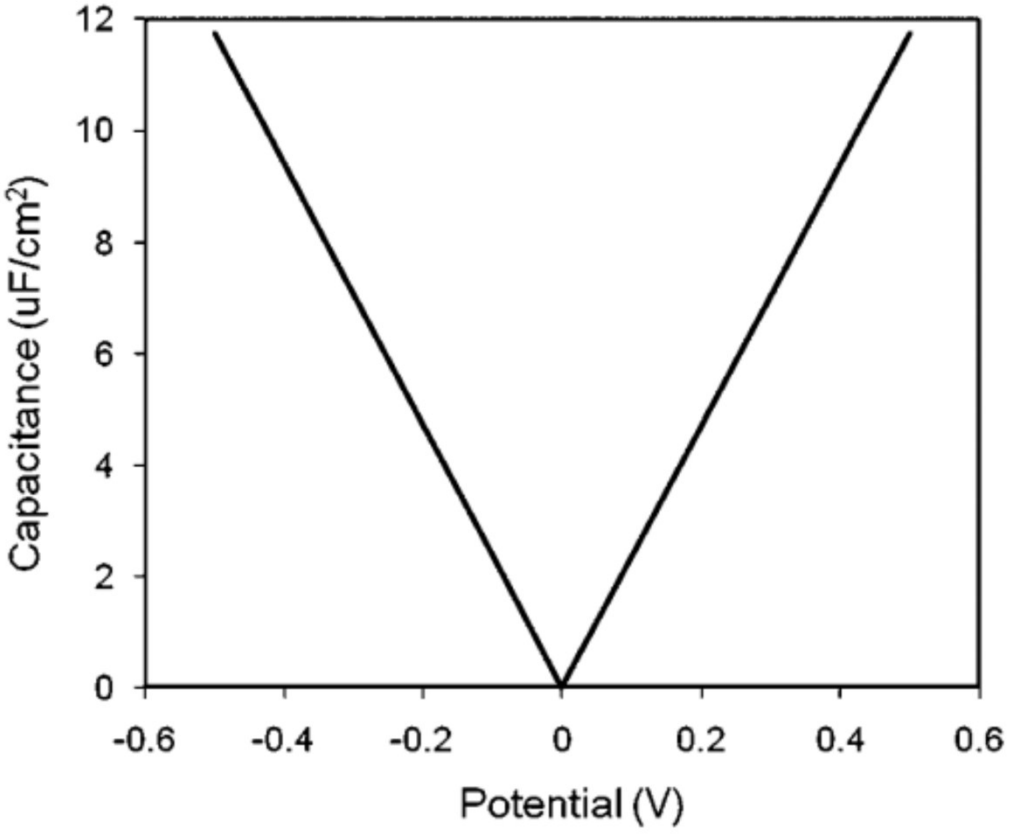

Figure 6.8: Quantum capacitance for single layer graphene. Reprinted from Reference 466.

Figure 6.9 depicts the experimentally obtained capacitance-potential plots for two electrodes: Edge-plane Screen-Printed Electrode (ESPE) in green, and Edge Plane Pyrolytic Graphite (EPPG) in blue. The electrolyte selected was KCl, as this has been used for similar experiments in previous studies.[467] The first noticeable difference between the two electrodes is that the potential closest to the PZC for the ESPE is approximately +0.2 V (*vs*. Ag/AgCl), while for EPPG the PZC is closer to 0.0 V (*vs*. SCE). Secondly, the observed *specific* capacitance obtained for EPPG is one order of magnitude higher than the ESPE electrode. Such a striking difference suggests that the EPPG electrode exhibits either a more porous structure than ESPE, or that the Helmholtz plane contributes much more at an EPPG electrode, which could be an effect of the high electron density at the edges of a pyrolytic graphite electrode, attracting more cations to the surface and thus creating a higher double-

layer capacitance. The plot shape assumes a similar pattern to the one found for graphene in Figure 6.8

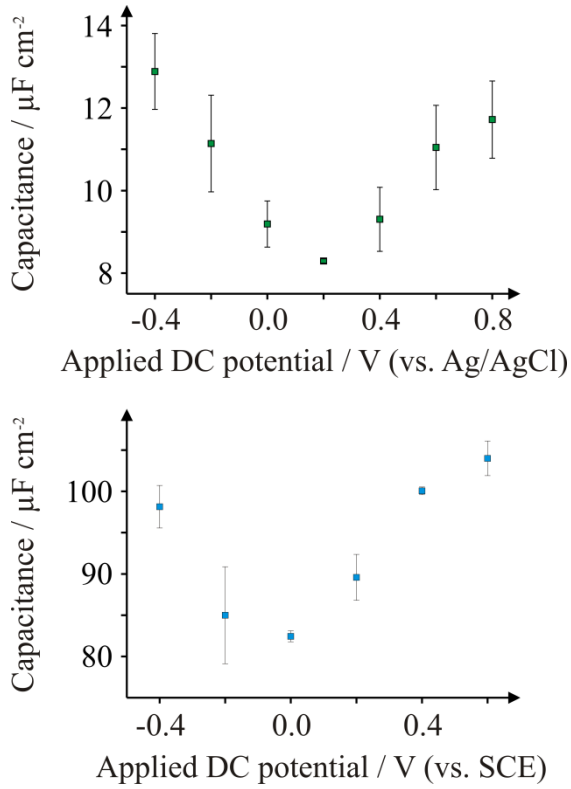

Figure 6.9: Capacitance versus applied potential plots for (top, green) ESPE and (bottom, blue) EPPG electrodes. Electrolyte: 0.1M KCl. Frequency range: 100000 - 1 Hz. Amplitude: 10 mV.

Assuming that the Helmholtz plane is the same as reported previously, the capacitance at the PZC can be calculated, through equation 6.3. Obviously, in an ideal environment, the PZC would exhibit no charge at all, but this is unlikely under normal circumstances. Thus, the total interfacial capacitance at the PZC in the case of the ESPE is estimated to be 8.29 μF cm^{-2}. Such a capacitance is small, and when compared to the ESPE, which is estimated to exhibit a total interfacial capacitance of 82.44 μF cm^{-2}, it is evident that the baseline capacitance for the ESPE will be more beneficial in terms of electroanalysis than that of the EPPG electrode, because the capacitance of the system will distort Faradaic currents less than in the case of the EPPG. Therefore, ESPE electrodes will require less ohmic compensation than its macroelectrode counterpart.

Next explored is the interfacial capacitance when the cation in the electrolyte is changed. Instead of KCl, NaCl was selected as an electrolyte, thus the higher *m/z* ratio of sodium is being investigated to see whether it has an effect upon the observed PZC of the electrodes. These experiments are depicted in Figure 6.10.

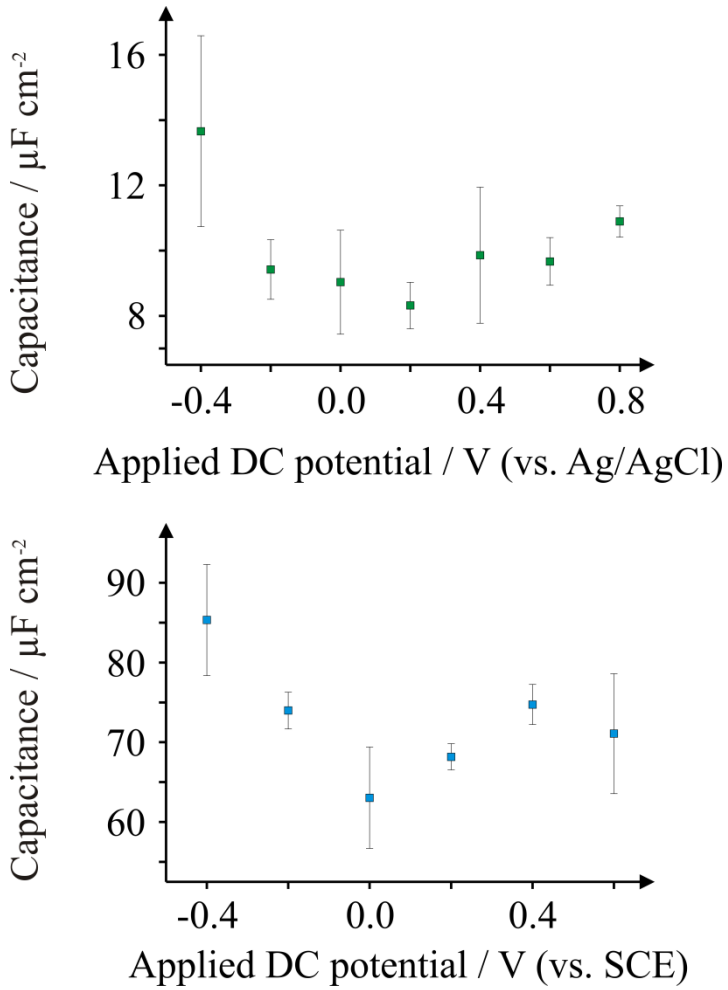

Figure 6.10: Capacitance versus applied potential plots for (top, green) ESPE, and (bottom, blue) EPPG electrodes. Electrolyte: 0.1M NaCl. Frequency: 100000 - 1 Hz. Amplitude: 10 mV.

It is clear from Figure 6.10 that the case of NaCl is more erroneous than that of KCl, with respect to the error bars presented between the two cases. However, the PZC remains the same for both electrodes: +0.2 and 0.0 V, respectively, for ESPE and EPPG. The total interfacial capacitance of the ESPE electrode at the PZC is calculated to be 8.32 µF cm^{-2}, which is similar to the case of KCl. However for the case of EPPG, the total interfacial

capacitance reduces to 63.03 µF cm^{-2} at the PZC, which is a reduction of nearly 20 µF cm^{-2} compared to the case of KCl. In any future PZC experiments, KCl is definitely the better choice of electrolyte to use.

ELECTROCHEMICAL IMPEDANCE SPECTROSCOPY OF CARBON ELECTRODES

This section investigates the Faradaic impedance observed for HQ at three carbon macroelectrodes: EPPG, BPPG, and BDD. Firstly, it is interesting to see the Faradaic and non-Faradaic impedance contributions at an electrode surface, and second it is especially interesting to observe whether the electronic anisotropy of the HOPG affects the impedance contributions observed. Therefore, EIS experiments were conducted at various frequencies in 2 mM HQ in pH 7.4 PBS with 0.1 M KCl supporting electrolyte. However, in order to determine an excitation potential for each electrode, a voltammetric experiment was conducted for each electrode, the results of which are plotted in Figure 6.11.

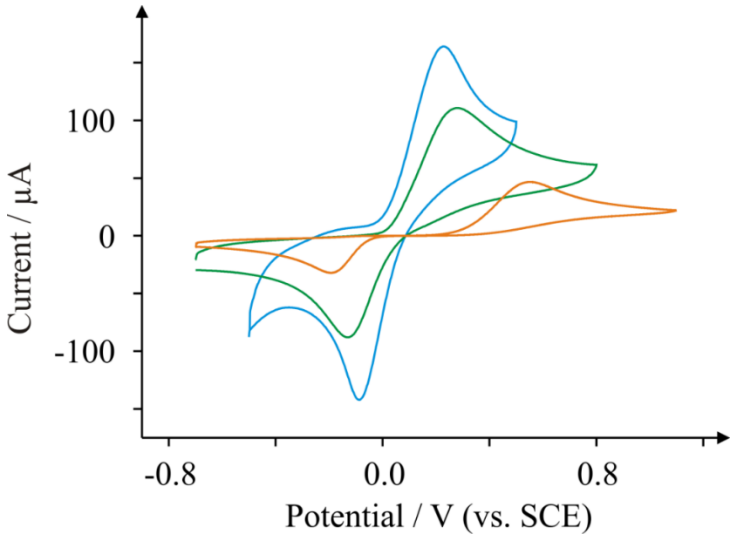

Figure 6.11: CV profiles of 2 mM HQ in pH 7.4 PBS using three working electrodes: EPPG (blue); BPPG (green); and BDD (orange).

Upon inspection of Figure 6.11, it is clear that the three carbon substrates exhibit similar voltammetry towards HQ. All three substrates exhibit a large redox couple, around a formal potential of approximately +0.07 V. EPPG displays the lowest ΔE_P of 0.295 V, and an oxidation wave potential of +0.216 V. The half wave potential of the oxidation wave is used as the excitation potential in subsequent Faradaic impedance measurements, because the half-wave potential is the point at which the products and reactants are approximately equal at the electrode surface; in the case of EPPG, this equates to +0.060 V. Also noticed in the case of EPPG is a much larger capacitative contribution when compared to the case of BPPG and BDD. BPPG exhibits a larger ΔE_P compared to the case of EPPG, which is to be expected considering the anisotropic differences between the two electrode substrates. The small overpotential compared to the EPPG electrode is indicative of the lesser proportion of edge planes available for passage of electrical current. BPPG displays a ΔE_P of 0.382 V, but less of a capacitative contribution than EPPG. The oxidation half-wave potential is +0.100 V. BDD on the other hand exhibits the lowest capacitative contribution by some distance, but a large overpotential is required to drive the redox behaviour of HQ, due to the unreactive BDD surface. A ΔE_P of 0.726 V is extremely large and is well into quasi-reversible territory. One would expect some diffusional behaviour in this case appearing on the EIS profile. Finally, the peak half-wave potential which is consolidated to EIS is +0.325 V. Table 6.1 summarises the peak half-wave potentials for this section, which are used in the EIS experiments, depicted in Figure 6.12.

Table 6.1: List of electrode substrates and the oxidation peak potentials observed for 2 mM HQ in pH 7.4 PBS. The half-wave potentials are listed in red, and are utilised for EIS experiments.

Electrode	Oxidation Potential / V	Oxidation half-wave potential / V
EPPG	+0.216	**+0.060**
BPPG	+0.265	**+0.100**
BDD	+0.538	**+0.325**

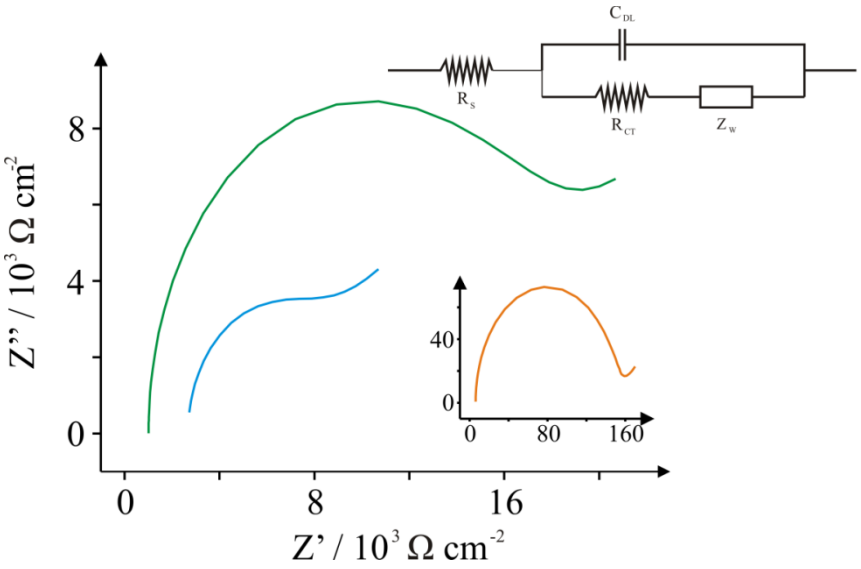

Figure 6.12: Nyquist plots of 2 mM HQ in pH 7.4 PBS using three working electrodes: EPPG (blue); BPPG (green); and BDD (orange; inset). Frequency range: 10000 – 0.2 Hz.

Depicted in Figure 6.12 are simulated EIS traces for 2 mM HQ in pH 7.4 PBS, modelled using the Randles circuit in the top right corner of Figure 6.12. Upon close inspection, there is a large disparity between the three profiles obtained. The case of the EPPG is intriguing for a number of reasons. A very typical Randles-type Nyquist plot was observed experimentally for EPPG, which exhibited two clear regions of charge transfer and diffusional behaviour in the high-to-mid and low frequency ranges, respectively.

Comparably, the case of BPPG reveals the R_{CT} value to be much higher than the case of EPPG, as one may expect because electron transfer at the electrode|solution interface is easier and more efficient at the edges of a graphite plane. The case of the BDD, where sp^3 hybridised carbon is present, reveals the R_{CT} to be about one order of magnitude higher than EPPG or BPPG. The R_{CT} values are summarised in table 6.2.

Table 6.2: Summary of charge transfer resistances and capacitance values obtained via equivalent circuit fitting.

Electrode	R_{CT} / Ω cm^{-2} (% RSD)	C_{DL} / μF cm^{-2} (% RSD)
EPPG	6641 (18.5)	365 (11.5)
BPPG	16440 (4.0)	97 (6.0)
BDD	139600 (2.5)	4 (2.5)

Of the three electrodes studied, the R_{CT} value increases in the order of EPPG < BPPG < BDD. This is unsurprising, considering the structure of the respective carbon electrodes. One would expect BBD to be the slowest as it is well known to be a relatively inert electrode substrate, compared to EPPG, for instance. Conversely, there is a decrease in the estimated capacitance values for the electrodes, in the order of EPPG > BPPG > BDD. This suggests that EPPG has a degree of porosity, at least in the case of HQ. The likelihood is that the HQ nucleates upon edge planes sites, which creates a pseudo-capacitance at the electrode surface. Indeed, the voltammetric profiles in Figure 6.11 indicate a large level of capacitance, and this is confirmed in a more quantitative manner by EIS.

This section investigates drop-casted carbon composites *via* EIS. The previous section investigated carbon macroelectrodes and found that the kinetically slower BPPG and BDD electrodes exhibited higher R_{CT} and lower C_{DL} values than the kinetically quicker EPPG. Thus, one may expect a carbon composite such as graphite powder to mimic that of an EPPG electrode. Similarly, pristine graphenes would be expected to exhibit larger R_{CT} and smaller C_{DL} values than graphite because graphene as an electrode material is kinetically slower than graphite.

Figure 6.13 depicts EIS traces for a range of carbon composites cast upon a bare EPPG electrode, in addition to the bare electrode. Upon closer inspection, there are some very striking differences between the different carbon materials. The EPPG electrode we already know exhibits a high C_{DL}, but a low R_{CT}. This is also the case for Q-Graphene, and GO. Surprisingly, however, the graphite composite exhibits a response akin to that of pristine graphene. Normally one would expect a graphite electrode modification to behave similarly to EPPG. Without further testing it is difficult to ascribe this observation, but there is some chance that the sonication procedure has affected the graphite in a way in which has broken apart the graphite into graphene. This would go some way to explaining this behaviour. On the other hand, the oxygenated graphenes perform in an EPPG-like manner, so it is clear that HQ is a surface-sensitive analyte as is the case with some redox probes and biologically relevant analytes discussed in Chapter 3.

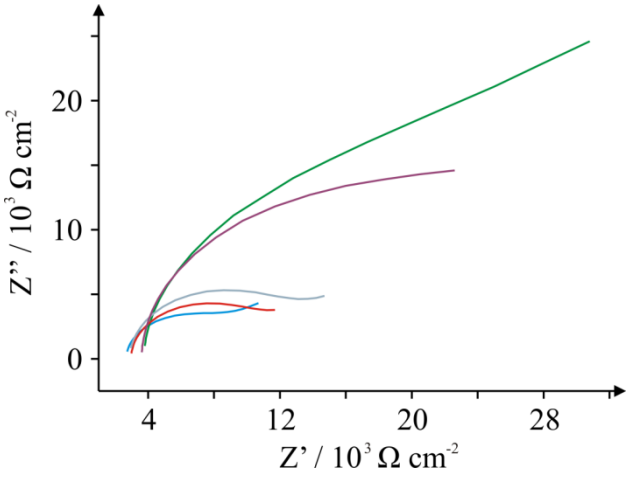

Figure 6.13: EIS spectra of 2 mM HQ in pH 7.4 PBS using several modified carbon electrodes: bare EPPG (blue); 20 ng pristine graphene (green); 20 ng GO (red); 20 ng Q-Graphene (grey); and 20 ng graphite (purple).

Finally, a quantitative summary of parameters is provided in table 6.3. The assumption is that the electrode surface area is equal to the surface area of the bare electrode after modification with each respective composite. Noted in table 6.3 is that the capacitance is inversely proportional to the charge transfer resistance observed in each case, with the exception of graphite.

Table 6.3: Electrode materials and their respective R_{CT} and C_{DL} values.

Electrode	R_{CT} / Ω cm^{-2}	C_{DL} / µF cm^{-2}	% RSD
EPPG	6640	363	15
Pristine graphene	27900	133	30
Graphene oxide	8500	280	27
Q-Graphene	12000	234	18
Graphite	19000	286	24

This section has rigorously tested the impedance of the equipment, revealing the instrument to be of sufficient standard for EIS tests below a frequency of 50 kHz. A series of electrode tests revealed the EPPG electrode to exhibit some erroneous behaviour, and similarly the phase angle of the platinum auxiliary electrode was observed to fluctuate throughout a very large frequency range. The latter case is likely due to the lack of surface homogeneity (lack of polishing). The SPEs all displayed higher total impedances than the macroelectrodes, but the total impedances are not large enough to preclude the testing of SPEs. The LRI-SPE exhibited the lowest total impedance as one may expect, and will be used in the rest of the thesis as the electrode of choice, unless otherwise stated. Finally, the resistance of the solution and the electroactive species was determined in a series of tests using $K_3[IrCl_6]$ as a model probe. The tests revealed the analytical window for 0.1 M PBS (with 0.1 M KCl), as well as a typical EIS trace for $K_3[IrCl_6]$ using SPEs. Such robust testing has demonstrated that EIS is applicable to SPEs, within very finite frequency constraints, with a high degree of care required for feasible results.

A number of carbon electrodes have been tested using the impedance equipment, revealing that they are suitable for EIS measurements. This section has demonstrated that the charge transfer resistances of EPPG and BPPG are less than that of a BBD electrode, whilst the capacitances are much higher. Furthermore, this section has tested numerous carbon-containing electrode composites and revealed that, particularly in the case of pristine graphene, the impedances were very high and, as such, not yet useable for EIS, at least not as an electrode material.

CHAPTER 7
CONCLUSIONS AND FUTURE WORK

7.1 OVERALL CONCLUSIONS

This thesis has reported many significant contributions to the field of electrochemistry. However, of the many things reported within, there are two main areas which have made good strides in electrochemistry and nanoelectrochemistry. This thesis reported the fabrication, characterisation, and electrochemical investigation of the first *true* graphene SPEs in Chapter 5. This work cross examined different types of carbon inks, including graphene-loaded inks, and it was shown that a *true* graphene ink, though hard to come by, was definitely possible, and offered some benefits as electrode materials if one was to require specific tailoring of an electrode surface in terms of electron transfer rate.

Another significant contribution this thesis has made is that in Chapter 6, which describes fundamental information regarding the impedimetric application of screen-printed electrodes. The work conducted in Chapter 6 on EIS spectra of carbon nanomaterials, demonstrates the applicability of screen-printed electrodes using EIS as the technique of choice, instead of traditional electroanalytical methods, such as CV, DPV, SWV, or chronoamperometry. The potential of zero charge experiments conducted in Chapter 6 were interesting because they physically characterised parameters of screen-printed electrodes which had not previously been considered, and have opened up a new dimension with respect to the useful potential ranges at which such carbon materials can operate, particularly in the case of EIS where strict control of parameters is essential for any meaningful data to be extrapolated from experiments.

Though many experiments have been conducted, many parameters been changed, and many conclusions have been drawn, there is still a wealth of unanswered questions spanning from this thesis. From Chapter 1, there are still questions as to whether graphene electrodes can be utilised in a medical context, for instance for assessing DNA damage. The valuable lesson from the DNA work was that a graphene electrode could, in theory, discriminate between an adenine and a guanine base. Therefore this could be consolidated towards a medicinal sensor, if required. The whole area of carbon nanomaterials electrochemistry is still an ongoing endeavour, thus work from Chapter 3 should be continued in the context of graphene-based electrodes for fuel cells, or catalyst supports in fuel cells, in terms of increasing efficiency and power density. The relative cost of graphitic materials will continue to be the reason why this field will continue to expand, until suitable technology is available.

Chapter 4 could quite easily be continued in terms of developing electroanalytical methods for a plethora of different target analytes, with a view to creating a multi-functional electrode for detection of a myriad of diseases. The major potential limitation to CV-based methods at the moment is that the target analytes must be electroactive, less an indirect method must be created, as with the case of creatinine. Nevertheless, the electrochemistry of theophylline must be tested in human serum, saliva, urine, blood, and other bodily fluids, in order to create a point-of-care theophylline sensor. Such work has never been conducted before, in terms of focussing entirely upon screen-printed electrodes for such a purpose. Similarly with the creatinine detection strategy, two things could be focussed upon. Firstly, the electrochemistry in the presence of interferents in urine must be investigated, and secondly, are there are other molecules which react with creatinine? Picric acid is a molecule which reacts with many compounds and surfaces, and will passivate electrodes quite quickly.

Therefore the investigation of another indirect method could be a suitable strategy for observing creatinine levels.

The graphene screen-printed electrodes reported in Chapter 5 need to be investigated in terms of more electroactive analytes (guanine could be a useful analyte). The fundamental behaviour of the electrodes was investigated, but the effect of the metal contaminants should be investigated in a lot of detail before such electrodes can be entirely trusted. In previous works, metal ions interloped within carbon nanotubes have been shown to be the source of some electrochemical responses,[494] while poorly made graphenes have also given incorrect electrochemical responses.[243, 495] Taking lessons from this, the electrodes must be characterised further.

The major piece of further work that spans from the efforts in this thesis is the possibility of the application of EIS to electroanalytical systems. Chapter 6 investigated the EIS spectra of screen-printed electrodes, and found that they are a good material for use with EIS. Therefore, EIS must be used more, and the possibility of detecting molecules, both Faradaically and non-Faradaically, must be investigated. Already in the literature are many reports of EIS utilised for biorecognition events, such as enzyme/substrate binding, with some reporting detection limits in the *femtomolar* range.[496-499] While such detection limits are great for analytical science in some contexts, such as metal detection, they are completely unnecessary for clinical approaches because higher levels, and specifically finite concentration ranges, need to be detected for a host of clinical applications (detection of medicines, for example). Thus, screen-printed electrodes and impedance spectroscopy need to be investigated further for point-of-care diagnosis of medicines in the body, as well as disease.

In terms of diagnosis of diseases, impedance has already seen some papers which observe DNA hybridisation events which are typical of specific ailments, such as HIV or

Alzheimer's disease, by monitoring the impedance of a working electrode as a function of the DNA concentration. Such procedures needs to be less complex; that is, EIS sensors could be produced for something other than DNA, because any work with DNA requires highly specific conditions and a lengthy sample pre-treatment step to isolate the required DNA. It would be more beneficial to observe substances in the blood or urine which act as biomarkers for a certain disease, as was the case in Chapter 4 for kidney disease. There is certainly a scope for an enzyme/substrate binding mechanism in the case of creatinine, if one could research a way into anchoring creatininase onto a working electrode. The enzyme/substrate interaction could easily be monitored impedimetrically and could prove to be a better method for creatinine detection, particularly because molecules like glucose, urea, and ammonia are less likely to interfere due to the highly specific nature of enzymes.

Finally, the specific interaction of molecules with ionophores is a logical route to proceed down, because it would enhance the selectivity of a system further, without the need for controlling the temperature of a surface, as is the case with enzymes. There are many commercially available ionophores for targets such as sodium, potassium, amines, and cyanide, all of which could be used for monitoring of substances levels within the human body and potentially act as a point-of-care technology for implementation in doctor's surgeries.

Further work can be summarised as follows:

1. The application of carbon nanomaterial electrochemistry to battery/fuel cell research, with a view to combating the nuisance of the oxygen reduction reaction.
2. Investigation of interferents for the oxidation of theophylline and the indirect reduction of creatinine.

3. Further fundamental study of graphene screen-printed electrodes, with a particular focus upon the influence of the metallic contaminants and how to remove them.
4. Application of EIS to clinical diagnosis, and the development of a point-of-care device capable of observing the frequency-dependent characteristics of a cell.

In reference to the electrodes discussion in Chapter 1, Figure A1 depicts the voltammetry of several electrode substrates in pH 7.4 PBS, with 0.1 M KCl as a background electrolyte. The potential window for each electrode is depicted schematically underneath the potential abscissa. It can be seen that the potential window for platinum is the smallest, while the potential window for BDD is the largest, due to its unreactive surface. The GC electrode would expect to have a larger potential window, but this is minor because GC is not used at great length within this thesis.

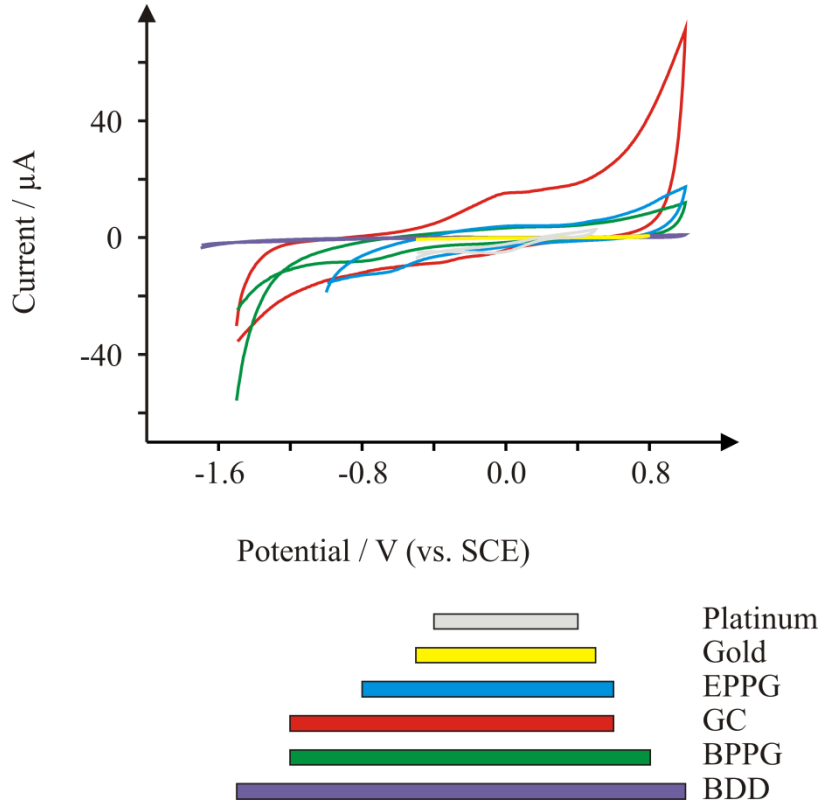

Figure A1: Cyclic voltammograms of several electrodes in pH 7.4 PBS with 0.1 M KCl electrolyte. The length of the bars underneath the abscissa represent the potential windows.

1. A. C. Fisher, *Electrode Dynamics*, Oxford University Press, 1996.
2. A. D. Robertson, A. R. West and A. G. Ritchie, *Solid State Ionics*, 1997, **104**, 1.
3. J.-P. Gattuso, D. Allemand and M. Frankignoulle, *American Zoologist*, 1999, **39**, 160.
4. M. R. Gunner, J. Madeo and Z. Zhu, *Journal of Bioenergy and Biomembranes*, 2008, **40**, 509.
5. A. J. Bard and L. R. Faulkner, *Electrochemical Methods: Fundamentals and Applications*, John Wileys & Sons, Inc., 2001.
6. C. C. Chan, *Proceedings of the IEEE*, 2007, **95**, 704.
7. M. Granovskii, I. Dincer and M. A. Rosen, *Journal of Power Sources*, 2006, **159**, 1186.
8. C. E. Thomas, *International Journal of Hydrogen Energy*, 2009, **34**, 6005.
9. P. Karabinas and D. Jannakoudakis, *Journal of Electroanalytical Chemistry and Interfacial Electrochemistry*, 1984, **160**, 159.
10. G. Instruments, http://www.gamry.com/application-notes/potentiostat-fundamentals/.
11. R. G. Compton and C. E. Banks, *Understanding Voltammetry*, Imperial College Press, 2011.
12. M. V. Williams, H. R. Kunz and J. M. Fenton, *Journal of The Electrochemical Society*, 2004, **151**, A1617.
13. W. H. Smyrl and J. Newman, *Journal of The Electrochemical Society*, 1971, **118**, 1079.
14. A. Fick, *Poggendorff's Annalen der Physik*, 1855, **94**, 59.
15. M. C. Buzzeo, R. G. Evans and R. G. Compton, *ChemPhysChem*, 2004, **5**, 1106.
16. X. Ji, C. E. Banks, A. Crossley and R. G. Compton, *ChemPhysChem*, 2006, **7**, 1337.
17. E. P. Randviir and C. E. Banks, *Electroanalysis*, 2014, **26**, 76.

18. E. P. Randviir, D. A. C. Brownson, M. Gomez-Mingot, D. K. Kampouris, J. Iniesta and C. E. Banks, *Nanoscale*, 2012, **4**, 6470.

19. R. S. Nicholson, *Analytical Chemistry*, 1965, **37**, 1351.

20. I. Lavagnini, R. Antiochia and F. Magno, *Electroanalysis*, 2004, **16**, 505.

21. R. S. Nicholson and I. Shain, *Analytical Chemistry*, 1964, **36**, 706.

22. G. Kear and F. C. Walsh, *Corrosion and Materials*, 2005, **30**, 51.

23. J. Tafel, *Zeitschrift für Physikalische Chemie,* 1905, **50**, 641.

24. F. Zhao, R. C. T. Slade and J. R. Varcoe, *Chemical Society Reviews*, 2009, **38**, 1926.

25. New Mexico State University, http://web.nmsu.edu/~snsm/classes/chem435/Lab14/double_layer.html.

26. V. K. Gupta, A. K. Jain, M. A. Khayat, S. K. Bhargava and J. R. Raisoni, *Electrochimica Acta*, 2008, **53**, 5409.

27. V. K. Gupta, R. Mangla and S. Agarwal, *Electroanalysis*, 2002, **14**, 1127.

28. S. B. Hocevar, J. Wang, R. P. Deo and B. Ogorevc, *Electroanalysis*, 2002, **14**, 112.

29. J.-W. Mo, B. Ogorevc, X. Zhang and B. Pihlar, *Electroanalysis*, 2000, **12**, 48.

30. J. P. Smith, J. P. Metters, D. K. Kampouris, C. Lledo-Fernandez, O. B. Sutcliffe and C. E. Banks, *Analyst*, 2013, **138**, 6185.

31. O. Ramdani, J. P. Metters, L. C. S. Figueiredo-Filho, O. Fatibello-Filho and C. E. Banks, *Analyst*, 2013, **138**, 1053.

32. C. E. Banks and E. P. Randviir, *Bioanalysis*, 2014, **6**, 109.

33. G. M. Jenkins and K. Kawamura, *Nature*, 1971, **231**, 175.

34. European Synchotron Research Facility, http://www.esrf.eu/news/spotlight/spotlight77.

35. A. K. Geim and K. S. Novoselov, *Nature Materials*, 2007, **6**, 183.

36. H. Pierson, *Handbook of Carbon, Graphite, Diamond and Fullerenes Properties: Processing and Applications*, Noyes Publications, New Jersey, 1995.

37. A. Yacoby, *Nature Physics*, 2011, **7**, 925.

38. J. Li, S. Guo, Y. Zhai and E. Wang, *Analytica Chimica Acta*, 2009, **649**, 196.

39. A. Salimi, R. G. Compton and R. Hallaj, *Analytical Biochemistry*, 2004, **333**, 49.

40. R. A. de Toledo and C. M. P. Vaz, *Microchemical Journal*, 2007, **86**, 161.

41. L. Hua, L. S. Chia, N. K. Goh and S. N. Tan, *Electroanalysis*, 2000, **12**, 287.

42. S. Liu, Z. Shi and S. Dong, *Electroanalysis*, 1998, **10**, 891.

43. H. Xu, L. Zeng, S. Xing, Y. Xian, G. Shi and L. Jin, *Electroanalysis*, 2008, **20**, 2655.

44. F. C. Moraes, D. L. C. Golinelli, L. H. Mascaro and S. A. S. Machado, *Sensors and Actuators B: Chemical*, 2010, **148**, 492.

45. J. P. Metters, R. O. Kadara and C. E. Banks, *Analyst*, 2011, **136**, 1067.

46. S. Kröger, A. P. F. Turner, K. Mosbach and K. Haupt, *Analytical Chemistry*, 1999, **71**, 3698.

47. J. Wang, J. Lu, S. B. Hocevar and B. Ogorevc, *Electroanalysis*, 2001, **13**, 13.

48. S. Carrara, V. V. Shumyantseva, A. I. Archakov and B. Samorì, *Biosensors and Bioelectronics*, 2008, **24**, 148.

49. I. L. de Mattos, L. Gorton and T. Ruzgas, *Biosensors and Bioelectronics*, 2003, **18**, 193.

50. E. Warburg, *Ann. Phys. Chem.*, 1899, **67**, 493.

51. W. Nernst, *Zeitschrift Elektrochemie*, 1894, **14**, 622.

52. A. Nishikata, Y. Ichihara, T. Tsuru, *Corrosion Science*, 1995, **37**, 897.

53. F. Mansfield, *Electrochimica Acta*, 1990, **35**, 1533.

54. Q. Mohsen, S. S. Fadl-allah, N. S. El-Shenawy, *Journal of Electrochemical Science*, 2012, **7**, 4510.

55. L. Strašák, J. Dvořák, S. Hasoň, V. Vetterl, *Bioelectrochemistry*, 2002, **56**, 37.

56. P. M. Gomadam, J. W. Weidner, *International Journal of Energy Research*, 2005, **29**, 1133.

57. Z. He, F. Mansfield, *Energy and Environmental Science*, 2009, **2**, 215.

58. A. G. Webster, *Proceedings of the National Academy of Sciences USA*, 1919, **5**, 275.

59. D. D. Macdonald, *Electrochimica Acta*, 2006, **51**, 1376.

60. E. Barsoukov, J. R. Macdonald, *Impedance Spectroscopy: Theory, Experiment, and Applications*, Wiley, 2005.

61. University of St. Andrews, http://www-groups.dcs.st-and.ac.uk/~history/Mathematicians/Heaviside.html.

62. P. Yang, Q. Zheng, H. Xu, J. Liu and L. Jin, *Chinese Journal of Chemistry*, 2012, **30**, 1155.

63. L. Wang, J. Zhao, X. He, J. Gao, J. Li, C. Wan and C. Jiang, *Journal of Electrochemical Science*, 2012, **7**, 345.

64. D. C. Graham, *Chemical Reviews*, 1947, **41**, 441.

65. K. Jüttner, *Electrochimica Acta*, 1990, **35**, 1501.

66. H. Fricke, *Cold Spring Harbor Symposia on Quantitative Biology*, 1933, **1**, 117.

67. F. Lisdat and D. Schäfer, *Analytical and Bioanalytical Chemistry*, 2008, **391**, 1555.

68. C. Alexander, M. Sadiku, *Fundamentals of Electric Circuits*, McGraw-Hill, 2006.

69. B. Hirschorn, I. Ibrahim, M. E. Orazem, H. Takenouti, B. Tribollet, *ECS Transactions*, 2008, **13**, 81.

70. D. A. C. Brownson, A. C. Lacombe, M. Gómez-Mingot and C. E. Banks, *RSC Advances*, 2012, **2**, 665.

71. E. P. Randviir, D. A. C. Brownson, M. Gómez-Mingot, D. K. Kampouris, J. Iniesta, C. E. Banks, *Nanoscale*, 2012, **4**, 6470.

72. http://www.solartronanalytical.com/Pages/SMaRTSoftware.htm.

73. http://www.thasar.com/cms/images/ivium/pdf/ivium_technologies_brochure.pdf.

74. J. R. Scully, D. C. Silverman, *Electrochemical Impedance: Analysis and Interpretation*, ASTM International, 1993.

75. J. R. MacDonald, *Journal of Electroanalytical Chemistry*, 1987, **223**, 25.

76. R. Kern, R. Sastrawan, J. Ferber, R. Stangl and J. Luther, *Electrochimica Acta*, 2002, **47**, 4213.

77. B. R. Hinderliter, S. G. Croll, D. E. Tallman, Q. Su and G. P. Bierwagen, *Electrochimica Acta*, 2006, **51**, 4505.

78. S. Buller, M. Thele, R. W. A. A. De Doncker and E. Karden, *IEEE Transactions on Industry Applications*, 2005, **41**, 742.

79. J.-T. Zhang, J.-M. Hu, J.-Q. Zhang and C.-N. Cao, *Progress in Organic Coatings*, 2004, **51**, 145.

80. J. R. Scully, D. C. Silverman and M. W. Kendig, *Electrochemical impedance: analysis and interpretation*, ASTM International, 1993.

81. J. H. Sluyters, *Recueil des Travaux Chimiques des Pays-Bas*, 1960, **79**, 1092.

82. J. E. B. Randles, *Discussions of the Faraday Society*, 1947, **1**, 11.

83. H. Wang, L. Pilon, *Electrochimica Acta*, 2012, **63**, 55.

84. F. Lufrano, P. Staiti, M. Minutoli, *Journal of Power Sources*, 2003, **124**, 314.

85. J. F. Rubinson, Y. P. Kayinamura, *Chemical Society Reviews*, 2009, **38**, 3339.

86. J. R. Macdonald, *Impedance Spectroscopy*, John Wiley, 1987.

87. X. Dominguez-Benetton, S. Sevda, K. Vanbroekhoven, D. Pant, *Chemical Society Reviews*, 2012, **41**, 7228.

88. J. H. Sluyters, J. J. C. Oomen, *Recueil des Travaux Chimiques des Pays-Bas*, 1960, **79**, 1101.

89. J. H. Sluyters, J. J. C. Oomen, *Recueil des Travaux Chimiques des Pays-Bas*, 1960, **79**, 1101-1110.

90. J. H. Sluyters, *Recueil des Travaux Chimiques des Pays-Bas*, 1960, **79**, 1092.

91. *USA Patent,* 1971.

92. A. S. Hamdy, E. El-Shenawy and T. El-Bitar, *International Journal of Electrochemical Science*, 2006, **1**, 171.

93. F. Mansfeld, *Electrochimica Acta*, 1990, **35**, 1533.

94. K. Jüttner, *Electrochimica Acta*, 1990, **35**, 1501.

95. D. A. López, S. N. Simison and S. R. de Sánchez, *Corrosion Science*, 2005, **47**, 735.

96. D. A. López, S. N. Simison and S. R. de Sánchez, *Electrochimica Acta*, 2003, **48**, 845.

97. Y. J. Tan, S. Bailey and B. Kinsella, *Corrosion Science*, 1996, **38**, 1545.

98. C. Liu, Q. Bi, A. Leyland and A. Matthews, *Corrosion Science*, 2003, **45**, 1257.

99. I. Epelboin, M. Keddam and H. Takenouti, *Journal of Applied Electrochemistry*, 1972, **2**, 71.

100. F. Mansfield, *Journal of Applied Electrochemistry*, 1995, **25**, 187.

101. J. Pan, D. Thierry, C. Leygraf, *Electrochimica Acta*, 1996, **41**, 1143.

102. D. Mareci, R. Chelariu, S. Iacoban, C. Munteanu, G. Bolat, D. Sutiman, *Journal of Materials Engineering and Performance*, 2012, **21**, 1431.

103. T. Fusayama, T. Katayori, S. Nomoto, *Journal of Dental Research*, 1963, **42**, 1183.

104. D. Xue, Z. Tan, M. J. Schulz, W. J. Vanooij, J. Sankar, Y. Yun, Z. Dong, *Materials Science and Engineering C*, 2012, **32**, 1230.

105. G. L. Song, S. Z. Song, *Advanced Engineering Materials*, 2007, **9**, 298.

106. http://batteryuniversity.com/learn/article/lithium_ion_safety_concerns.

107. J. Yan, W. Yuan, Z. Tang, H. Xie, W. Mao, L. Ma, *Journal of Power Sources*, 2012, **209**, 251.

108. S. Q. Liu, S. C. Li, K. L. Huang, B. L. Gong, G. Zhang, *Journal of Alloys and Compounds*, 2008, **450**, 499.

109. J. X. Ma, C. S. Wang, S. Wroblewski, *Journal of Power Sources*, 2007, **164**, 849.

110. R. Yazami, Y. Ozawa, *Journal of Power Sources*, 2006, **153**, 251.

111. K. Dokko, M. Mohamedi, M. Umeda, et al., *Journal of the Electrochemical Society*, 2003, **150**, A425.

112. S. Q. Liu, S. C. Li, K. L. Huang, *Chinese Journal of Inorganic Chemistry*, 2006, **22**, 645.

113. A. J. Bard and L. R. Faulkner, *Electrochemical methods: fundamentals and applications*, Wiley, 2000.

114. B. Jin, E. M. Jin, K.-H. Park and H.-B. Gu, *Electrochemistry Communications*, 2008, **10**, 1537-1540.

115. X. Yuan, H. Wang, J. C. Sun, J. Zhang, *International Journal of Hydrogen Energy*, 2007, **32**, 4365.

116. J. Wu, X. Z. Yuan, H. Wang, M. Blanco, J. J. Martin, J. Zhang, *International Journal of Hydrogen Energy*, 2008, **33**, 1735.

117. A. P. Borole, D. Aaron, C. Y. Hamilton, C. Tsouris, *Environmental Science and Technology*, 2010, **44**, 2740.

118. D. Samanta, A. Sarkar, *Chemical Society Reviews*, 2011, **40**, 2567.

119. L. Hlavata, K. Benikova, V. Vyskocil and J. Labuda, *Electrochimica Acta*, 2012, **71**, 134.

120. C. E. Banks, T. J. Davies, G. G. Wildgoose, R. G. Compton, *Chemical Communications*, 2005, 829.

121. S. Siddiqui, Z. Dai, C. J. Stavis, H. Zeng, N. Moldovan, R. J. Hamers, J. A. Carlisle and P. U. Arumugam, *Biosensors and Bioelectronics*, 2012, **35**, 284.

122. G. Zheng, F. Patolsky, Y. Cui, W. U. Wang, C. M. Lieber, *Nature Biotechnology*, 2005, **23**, 1294.

123. Y. Cui, Q. Wei, H. Park, C. M. Lieber, *Science*, 2001, **293**, 1289.

124. N. S. Mathebula, J. Pillay, G. Toschi, J. A. Verschoor, K. I. Ozoemena, *Chemical Communications*, 2009, 3345.

125. K. R. U. Devi, B. Ramalingam, A. Raja, *Diagnostic Microbiology and Infectious Disease*, 2003, **46**, 205.

126. G. Liu, S. G. Iyengar, J. J. Gooding, *Electroanalysis*, 2012, **24**, 1509.

127. M. Wang, Q. Sheng, D. Zhang, Y. He, J. Zheng, *Bioelectrochemistry*, 2012, **86**, 46.

128. A. Mokhtari, H. Karimi-Maleh, A. A. Ensafi, H. Beitollahi, *Sensors and Actuators B*, 2012, **169**, 96.

129. S. R. Santos, G. Maia, *Electrochimica Acta*, 2012, **71**, 116.

130. L. B. Venarusso, K. Tammeveski, G. Maia, *Electrochimica Acta*, 2011, **56**, 8926.

131. E. Prats-Alfonso, X. Sisquella, N. Zine, G. Gabriel, A. Guimerà, F. J. Del Campo, R. Villa, A. H. Mrksich, A. Errachid, J. Aquiló, F. Albericio, *Small*, 2012, **8**, 2106.

132. E. E. Ferapontova, K. V. Gothelf, *Current Organic Chemistry*, 2011, **15**, 498.

133. K. S. Novoselov, D. Jiang, F. Schedin, T. J. Booth, V. V. Khotkevich, S. V. Morozov, A. K. Geim, *Proceedings of the National Academy of Sciences USA*, 2005, **102**, 10451.

134. "The Nobel Prize in Physics 2010" http://www.nobelprize.org/nobel_prizes/physics/laureates/2010/.

135. D. A. C. Brownson, D. K. Kampouris and C. E. Banks, *Chemical Society Reviews*, 2012, **41**, 6944.

136. D. A. C. Brownson, L. J. Munro, D. K. Kampouris and C. E. Banks, *RSC Advances*, 2011, **1**, 978.

137. A. J. Bard, *Journal of Chemical Education*, 1983, **60**, 302.

138. C. D. Bain, J. Evall, G. M. Whitesides, *Journal of the American Chemical Society*, 1989, **111**, 7155.

139. R. G. Nuzzo, D. L. Allara, *Journal of the American Chemical Society*, 1983, **105**, 4481.

140. M. D. Porter, T. B. Bright, D. L. Allara, C. E. D. Chidsey, *Journal of the American Chemical Society*, 1987, **109**, 3559.

141. A. Bonanni, M. I. Pividori, M. del Valle, *Analyst*, 2010, **135**, 1765.

142. A. Bonanni, M. J. Esplandiu, M. del Valle, *Biosensors and Bioelectronics*, 2009, **24**, 2885.

143. H. L. Poh, A. Bonanni, M. Pumera, *RSC Advances*, 2012, **2**, 1021.

144. A. Bonanni, A. H. Loo, M. Pumera, *Trends in Analytical Chemistry*, 2012, **37**, 12.

145. A. Bonanni, M. Pumera, *ACS Nano*, 2011, **5**, 2356.

146. A. H. Loo, A. Bonanni, M. Pumera, *Nanoscale*, 2012, **4**, 143.

147. A. H. Loo, A. Bonanni, H. L. Poh, M. Pumera, *Nanoscale*, 2012, **4**, 921.

148. R. K. S. Raman, P. C. Banerjee, D. E. Lobo, H. Gullapalli, M. Sumandasa, A. Kumar, L. Choudhary, R. Tkacz, P. M. Ajayan, M. Majumder, *Carbon*, 2012, **50**, 4040.

149. D. Prasai, J. C. Tuberquia, R. R. Harl, G. K. Jennings, K. I. Bolotin, *ACS Nano*, 2012, **6**, 1102.

150. P. Liang, H. Wang, X. Xia, X. Huang, Y. Mo, X. Cao, M. Fan, *Biosensors and Bioelectronics*, 2011, **26**, 3000.

151. Y. Yuan, S. Zhou, B. Zhao, L. Zhuang, Y. Wang, *Bioresource Technology*, 2012, **116**, 453.

152. Y. Hu, F. Li, X. Bai, D. Li, S. Hua, K. Wang, L. Niu, *Chemical Communications*, 2011, **47**, 1743.

153. E. P. Randviir and C. E. Banks, *RSC Advances*, 2012, **2**, 5800.

154. R. Singh, Z. Matharu, A. K. Srivastava, S. Sood, R. K. Gupta, B. D. Malhotra, *Microchimica Acta*, 2012, **177**, 201.

155. Z. Wang, J. Zhang, P. Chen, X. Zhou, Y. Yang, S. Wu, L. Niu, Y. Han, L. Wang, P. Chen, F. Boey, Q. Zhang, B. Liedberg, H. Zhang, *Biosensors and Bioelectronics*, 2011, **26**, 3881.

156. Z. Wang, X. Zhou, J. Zhang, F. Boey, H. Zhang, *Journal of Physical Chemistry C*, 2009, **113**, 14071.

157. J. P. Metters, R. O. Kadara and C. E. Banks, *Analyst*, 2011, **136**, 1067-1076.

158. J. P. Metters, F. Tan, R. O. Kadara and C. E. Banks, *Analytical Methods*, 2012, **4**, 1272.

159. R. O Kadara, N. Jenkinson, C. E. Banks, *Electrochemical Communications*, 2009, **11**, 1377.

160. M. Khairy, R. O Kadara, C. E. Banks, *Analytical Methods*, 2010, **2**, 851.

161. B. Lu, W. Chen, *Journal of Magnetism and Magnetic Materials*, 2006, **304**, e400.

162. T. Balkenhohl, F. Lisdat, *Analytica Chimica Acta*, 2007, **597**, 50.

163. F. Rohrbach, H. Karadeniz, A. Erdem, M. Famulok, G. Mayer, *Analytical Biochemistry*, 2012, **421**, 454.

164. K. Yoshimura, A. Toibana, K. Nakahama, *Biochemical and Biophysical Research Communications*, 1988, **150**, 794.

165. J. C. Quintana, F. Arduini, A. Arnine, F. Punzo, G. Li Destri, C. Bianchini, D. Zane, A. Curulli, G. Palleschi, D. Moscone, *Analytica Chimica Acta*, 2011, **707**, 171.

166. L. Tran, B. Nguyen, N. Hieu, H. Tran, H. Nguyen, P. Nguyen, *Materials Science and Engineering C*, 2011, **31**, 477.

167. V. Gómez, S. Campuzano, M. Pedrero, J. M. Pingarrón, *Biosensors and Bioelectronics*, 2009, **24**, 3365.

168. T. Yang, N. Zhou, Q. Li, Q. Guan, W. Zhang, K. Jiao, *Colloid Surface B*, 2012, **97**, 150.

169. A. Erdem, M. Muti, H. Karadeniz, G. Congur, E. Canavar, *Colloid Surface B*, 2012, **95**, 222.

170. A. Gasnier, M. L. Pedano, F. Gutierrez, P. Labbé, G. A. Rivas, M. D. Rubianes, *Electrochimica Acta*, 2012, **71**, 73.

171. Y. Liu, Y. Liu, H. Feng, Y. Wu, L. Joshi, X. Zeng, J. Li, *Biosensors and Bioelectronics*, 2012, **35**, 63.

172. D. Zhang, F. Zhang, Y. Cui, Q. Deng, S. Krause, Y. Zhou, X. Zhang, *Talanta*, 2012, **92**, 65.

173. L. Shi, G. Liang, X. Li, X. Liu, *Analytical Methods*, 2012, **4**, 1036.

174. Y. Li, S. Chen, *International Journal of Electrochemical Science*, 2012, **7**, 2175.

175. X. Guo, A. Kulkarni, A. Doepke, H. B. Halsall, S. Iyer and W. R. Heineman, *Analytical Chemistry*, 2012, **84**, 241.

176. M. Venugopal, S. K. Arya, G. Chornokur, S. Bhansali, *Sensor Actuators A - Physical*, 2011, **172**, 154.

177. T. L. Adamson, F. A. Eusebio, C. B. Cook, J. T. Labelle, *Analyst*, 2012, **137**, 4179.

178. I. Ciani, H. Schulze, D. K. Corrigan, G. Henihan, G. Giraud, J. G. Terry, A. J. Walton, R. Pethig, P. Ghazal, J. Crain, C. J. Campbell, T. T. Bachmann, A. R. Mount, *Biosensors and Bioelectronics*, 2012, **31**, 413.

179. Q. Li, W. Cheng, D. Zhang, T. Yu, Y. Yin, H. Ju and S. Ding, *Journal of Electrochemical Science*, 2012, **7**, 844.

180. H. Xu, L. Wang, H. Ye, L. Yu, X. Zhu, Z. Lin, G. Wu, X. Li, X. Liu, G. Chen, *Chemical Communications*, 2012, **48**, 6390.

181. L. C. Z. Lin, G. Zhang, Q. Liu, B. Qiu, Z. Cai, G. Chen, *Analyst*, 2012, **137**, 819.

182. J. Liang, B. Chen, Y. Long, *Analyst*, 2011, **136**, 4053.

183. A. A. Ensafi, M Taei, H. R. Rahmani, T. Khayamian, *Electrochimica Acta*, 2011, **56**, 8176.

184. L. Yang, Y. Li, C. L. Griffis, M. G. Johnson, *Biosensors and Bioelectronics*, 2004, **19**, 1139.

185. L. Yang, C. Ruan, Y. Li, *Biosensors and Bioelectronics*, 2003, **19**, 495.

186. Y. Hou, S. Helali, A. Zhang, N. Jaffrezic-Renault, C. Martelet, J. Minic, T. Gorojankina, M. Persuy, E. Pajot-Augy, R. Salesse, F. Bessueille, J. Samatier, A. Errachid, V. Akimov, L. Reggiani, C. Pennetta and E. Alfinito, *Biosensors and Bioelectronics*, 2006, **21**, 1393.

187. F. Darain, D. Park, J. Park, Y. Shim, *Biosensors and Bioelectronics*, 2004, **19**, 609.

188. G. Liu, J. Liu, T. P. Davis, J. J. Gooding, *Biosensors and Bioelectronics*, 2011, **26**, 3660.

189. M. Grossi, M. Lanzoni, A. Pompei, R. Lazzarini, D. Matteuzzi, B. Riccò, *Biosensors and Bioelectronics*, 2008, **23**, 1616.

190. R. Pei, Z. Cheng, E. Wang, X. Yang, *Biosensors and Bioelectronics*, 2001, **16**, 355.

191. T. V. da Silva Santos, R. R. Teixeira, D. L. Franco, J. M. Madurro, A. C. Brito-Madurro, F. S. Espindola, *Materials Science and Engineering C*, 2012, **32**, 530.

192. Y. Chen, C. Wu, J. Tsai, G. Wang, *International Journal of Nanomedicine*, 2012, **7**, 133.

193. R. Devi, S. Yadav, C. S. Pundir, *Analyst*, 2012, **137**, 154.

194. A. Lund, T, Jacobsen, K. V. Hansen, M. Mogensen, *Sensors and Actuators B - Chemical*, 2011, **160**, 1159.

195. N. Meini, R. Kherrat, N. Jaffrezic-Renault, *Sensor Letters*, 2011, **9**, 2127.

196. B. Khadro, A. Betatache, C. Sanglar, A. Bonhomme, A. Errachid and A. Jaffrezic-Renault, *Sensor Letters*, 2011, **9**, 2261.

197. S. Zougar, O. Bechiri, S. Baali, R. Kherrat, M. Abbessi, N. Jaffrezic-Renault, N. Fertikh, *Sensor Letters*, 2011, **9**, 2287.

198. B. B. Narakathu, W. Guo, S. O. Obare, M. Z. Atashbar, *Sensor Letters*, 2011, **158**, 69.

199. V. Vermeeren, L. Grieten, N. V. Bon, N. Bijnens, S. Wenmackers, S. D. Janssens, K. Haenen, P. Wagner, L. Michiels, *Sensors and Actuators B - Chemical*, 2011, **157**, 130.

200. Z. Lin, X. Li, H, Kraatz, *Analytical Chemistry*, 2011, **83**, 6896.

201. S. Qiu, S. Gao, Q. Liu, Z. Lin, B. Qiu, G. Chen, *Biosensors and Bioelectronics*, 2011, **26**, 4326.

202. B. B. Narakathu, M. Z. Atashbar, B. Bejcek, *Sensors Letters*, 2011, **9**, 872.

203. B. B. Narakathu, M. Z. Atashbar, B. E. Bejcek, *Biosensors and Bioelectronics*, 2010, **26**, 923.

204. D. T. Tran, V. Vermeeren, L. Grieten, S. Wenmackers, P. Wagner, J. Pollet, K. P. F. Janssen, L. Michiels, J. Lammertyn, *Biosensors and Bioelectronics*, 2011, **26**, 2987.

205. S. Roy, N. Soin, R. Bajpai, D. S. Misra, J. A. McLaughlin, S. S. Roy, *Journal of Materials Chemistry*, 2011, **21**, 14725.

206. A. Bonanni, M. Pumera, Y. Miyahara, *Physical Chemistry Chemical Physics*, 2011, **13**, 4980.

207. S. Bourigua, M. Hnaien, F. Bessueille, F. Lagarde, S. Dzyadevych, A. Maaref, J. Bausells, A. Errachid, N. Jaffrezic-Renault, *Biosensors and Bioelectronics*, 2010, **26**, 1278.

208. P. R. Solanki, A. Kaushik, T. Manaka, M. K. Pandey, M. Iwamoto, V. V. Agrawal, B. D. Malhotra, *Nanoscale*, 2010, **2**, 2811.

209. J. Park, Y. Lee, B. Chang, B. H. Kim, S. Jeon, S. Park, *Analytical Chemistry*, 2010, **82**, 9342.

210. V. Pasceri, J. T. Willerson, E. T. Yeh, *Circulation*, 2000, **102**, 2165.

211. J. Lu, W. Wang, S. Wang, X. Shan, J. Li, N. Tao, *Analytical Chemistry*, 2012, **84**, 327.

212. E. P. Randviir and C. E. Banks, *RSC Advances*, 2012, **2**, 5800.

213. A. Dato, V. Radmilovic, Z. Lee, J. Phillips, M. Frenklach, *Nano Letters*, 2008, **8**, 2012.

214. A. Dato, Z. Lee, K. J. Jeon, R. Erni, V. Radmilovic, T. J. Richardson, M. Frenklach, *Chemical Communications*, 2009, 6095.

215. Z. Lee, K. J. Jeon, A. Dato, R. Erni, T. J. Richardson, M. Frenklach, V. Radmilovic, *Nano Letters*, 2009, **9**, 3365.

216. A. Dato, V. Radmilovic, Z. Lee, J. Phillips and M. Frenklach, *Nano Letters*, 2008, **8**, 2012.

217. http://www.graphene-supermarket.com.

218. L. M. Gonçalves, C. Batchelor-McAuley, A. A. Barros, R. G. Compton, *Journal of Physical Chemistry*, 2010, **114**, 14213.

219. Q. Li, C. Batchelor-McAuley, R. G. Compton, *Journal of Physical Chemistry*, 2010, **114**, 7423.

220. H. Perkampus, *UV-Vis Atlas of Organic Compounds: Part 2 Spectra D1/1 M-19*, Weinheim; New York: VCH, 1992.

221. M. Gara and R. G. Compton, *New Journal of Chemistry*, 2011, **35**, 2647.

222. K. S. Novoselov, A. M. Geim, S. V. Morozov, D. Jiang, Y. Zhang, S. V. Dubunos, I. V. Grigorieva, A. A. Firsov, *Science*, 2004, **306**, 666.

223. M. D. Stoller, S. J. Park, Y. W. Zhu, J. H. An, R. S. Ruoff, *Nano Letters*, 2008, **8**, 3498.

224. E. Yoo, J. Kim, E. Hosono, H. Zhou, T. Kudo, I. Honma, *Nano Letters*, 2008, **8**, 2277.

225. B. Seger, P. V. Kamat, *Journal of Physical Chemistry C*, 2009, **113**, 7990.

226. D. A. C. Brownson, M. Gomez-Mingót, C. E. Banks, *Physical Chemistry Chemical Physics*, 2011, **13**, 20284.

227. F. Li, J. Li, Y. Feng, L. Yang, Z. Du, *Sensors and Actuators B - Chemical*, 2011, **157**, 110.

228. Y. Xue, H. Zhao, Z. Wu, X. Li, Y. He, Z. Yuan, *Biosensors and Bioelectronics*, 2011, **29**, 102.

229. P. Si, H. Chen, P. Kannan, D. H. Kim, *Analyst*, 2011, **136**, 5134.

230. X. Kang, J. Wang, H. Wu, J. Liu, I. A. Aksay, Y. Lin, *Talanta*, 2010, **81**, 754.

231. M. Zhou, Y. Zhai, S. Dong, *Analytical Chemistry*, 2009, **81**, 5603.

232. V. C. Diculescu, A. C. Paquim, A. M. O. Brett, *Sensors*, 2005, **5**, 377.

233. M. S. Goh, M. Pumera, *Analytical Chemistry*, 2010, **82**, 8367.

234. D. A. C. Brownson, L. J. Munro, D. K. Kampouris, C. E. Banks, *RSC Advances*, 2011, **1**, 978.

235. M. Tomschik, F. Jelen, L. Havran, L. Trnková, P. E. Nielsen, E. Paleek, *J. Electroanalytical Chemistry*, 1999, **476**, 71.

236. E. E. Ferapontova, E. Dominguez, *Electroanalysis*, 2003, **15**, 629.

237. K. C. Honeychurch, M. R. O'Donovan, J. P. Hart, *Biosensors and Bioelectronics*, 2007, **22**, 2057.

238. J. Wang, A. Kawde, M. Musameh, *Analyst*, 2003, **128**, 912.

239. A. Erdem, P. Papakonstantinou, H. Murphy, *Analytical Chemistry*, 2006, **78**, 6656.

240. E. Dubuisson, Z. Yang, K. P. Loh, *Analytical Chemistry*, 2011, **83**, 2452.

241. A. Ambrosi, M. Pumera, *Physical Chemistry Chemical Physics*, 2010, **12**, 8943.

242. S. Husale, S. Sahoo, A. Radenovic, F. Traversi, P. Annibale, A. Kis, *Langmuir*, 2010, **26**, 18078.

243. D. A. C. Brownson, J. P. Metters, D. K. Kampouris and C. E. Banks, *Electroanalysis*, 2011, **23**, 894-899.

244. D. K. Kampouris, C. E. Banks, *Chemical Communications*, 2010, **46**, 8986.

245. G. e. Yuan, G. Zhang, J. Chen, L. Fu, L. Xu and F. Yang, *Journal of Solid State Electrochemistry*, 2013, **17**, 2711.

246. Y. Ferro, F. Marinelli and A. Allouche, *Journal of Chemical Physics*, 2002, **116**, 8124.

247. S. D. Chakarova-Käck, E. Schröder, B. I. Lundqvist and D. C. Langreth, *Physical Review Letters*, 2006, **96**, 146107.

248. K. Ito, K. Hashimoto, Y. Ishimori, *Kobunshi Ronbunshu*, 1994, **51**, 173S.

249. M. S. Goh, M. Pumera, *Analytical Chimica Acta*, 2012, **711**, 29.

250. D. A. C. Brownson, J. P. Metters, D. K. Kampouris, C. E. Banks, *Electroanalysis*, 2011, **23**, 894.

251. H. Cui, S. Li, F. Li, Y. Sun and X. Lin, *Analytical and Bioanalytical Chemistry*, 2002, **372**, 601.

252. E. J. Llorent-Martínez, P. Ortega-Barrales and A. Molina-Díaz, *Analytica Chimica Acta*, 2006, **580**, 149.

253. H. Doi, H. Iwasaki, Y. Masubuchi, R. Nishigaki and T. Horie, *Chemico-Biological Interactions*, 2002, **140**, 109.

254. D. P. Venema, P. C. H. Hollman, K. P. L. T. M. Janssen and M. B. Katan, *Journal of Agricultural and Food Chemistry*, 1996, **44**, 1762.

255. M. Shou, W. A. Galinada, Y.-C. Wei, Q. Tang, R. J. Markovich and A. M. Rustum, *Journal of Pharmaceutical and Biomedical Analysis*, 2009, **50**, 356.

256. R. M. Youssef, M. A. Korany and M. A. Afify, *Analytical Methods*, 2014, **6**, 3410.

257. M. Otero, C. A. Grande and A. E. Rodrigues, *Reactive and Functional Polymers*, 2004, **60**, 203.

258. G.-Q. Xiao, H. Li and M.-C. Xu, *Journal of Applied Polymer Science*, 2013, **127**, 3858.

259. X. Zhang, G. Li, H. Zhang, X. Wang, J. Qu, P. Liu and Y. Wang, *Soft Matter*, 2013, **9**, 6159.

260. A. A. J. Torriero, J. M. Luco, L. Sereno and J. Raba, *Talanta*, 2004, **62**, 247.

261. J. C. Suatoni, R. E. Snyder and R. O. Clark, *Analytical Chemistry*, 1961, **33**, 1894.

262. V. Supalkova, J. Petrek, L. Havel, S. Krizkova, J. Petrlova, V. Adam, D. Potesil, P. Babula, M. Beklova, A. Horna and R. Kizek, *Sensors*, 2006, **6**, 1483.

263. C. O. Ania, J. B. Parra and J. J. Pis, *Fuel Processing Technology*, 2002, **77–78**, 337.

264. D. A. C. Brownson, L. J. Munro, D. K. Kampouris and C. E. Banks, *RSC Advances*, 2011, **1**, 978.

265. D. A. C. Brownson, S. A. Varey, F. Hussain, S. J. Haigh and C. E. Banks, *Nanoscale*, 2014, **6**, 1607.

266. A. Ambrosi and M. Pumera, *The Journal of Physical Chemistry C*, 2013, **117**, 2053.

267. T. K. A. M. Yacynych, *Journal of the American Chemical Society*, 1978, **50**, 640.

268. R. L. McCreery, *Chemical Reviews*, 2008, **108**, 2646.

269. D. P. Upare, S. Yoon, C. W. Lee, *Korean Journal of Chemical Engineering*, 2011, **28**, 731.

270. L. L. Zhang, X. S. Zhao, *Chemical Society Reviews*, 2009, **38**, 2520.

271. E. G. Bushueva, P. S. Glakin, A. V. Okotrub, L. G. Bulusheva, N. N. Gavrilov, V. L. Kuznetsov, S. I. Moiseekov, *Physica Status Solidi*, 2008, **245**, 2296.

272. D. A. C. Brownson, D. K. Kampouris and C. E. Banks, *Chemical Society Reviews*, 2012, **41**, 6944.

273. C. Portet, G. Yushin, Y. Gogotsi, *Carbon*, 2007, **45**, 2511.

274. L. Wei, G. Yushin, *Carbon*, 2011, **49**, 4830.

275. D. A. C. Brownson, C. E. Banks, *Analyst*, 2010, **135**, 2768.

276. T. J. Davies, M. E. Hyde, R. G Compton, *Angewandte Chemie International Edition*, 2005, **44**, 5121.

277. T. J. Davies, R. R. Moore, C. E. Banks, R. G. Compton, *Journal of Electroanalytical Chemistry*, 2004, **574**, 123.

278. C. E. Banks, R. G. Compton, *Analyst*, 2006, **131**, 15.

279. J. J. Gooding, *Electrochimica Acta*, 2005, **50**, 3049.

280. C. P. Jones, K. Jurkschat, A. Crossley, C. E. Banks, *Journal of the Iranian Chemical Society*, 2008, **5**, 279.

281. B. Šljukić, C. E. Banks, R. G. Compton, *Nano Letters*, 2006, **6**, 1556.

282. C. E. Banks, A. Crossley, C. Salter, S. J. Wilkins, R. G. Compton, *Angewandte Chemie International Edition*, 2006, **45**, 2533.

283. K. A. Mkhoyan, A. W. Countryman, J. Silcox, D. A. Stewart, G. Eda, C. Mattevi, S. Miller, M. Chhowalla, *Nano Letters*, 2009, **9**, 1058.

284. D. A. C. Brownson, A. C. Lacombe, M. Gómez-Mingot, C. E. Banks, *RSC Advances*, 2012, **2**, 665.

285. M. S. Dresselhaus, A. Jorio, R. Saito, *Annual Review of Condensed Matter Physics*, 2010, **1**, 89.

286. L. M. Malard, M. H. D. Guimarães, D. L. Mafra, M. S. C. Mazzoni, A. Jorio, *Physical Reviews B*, 2009, **79**, 125426.

287. A. C. Ferrari, J. Robertson, *Physical Reviews B*, 2000, **61**, 14095.

288. A. Das, B. Chakraborty, A. K. Sood, *Bulletin of Materials Science*, 2008, **31**, 579.

289. X. Ji, C. E. Banks, A. Crossley, R. G. Compton, *ChemPhysChem*, 2006, **7**, 1337.

290. I. Streeter, G. G. Wildgoose, L. Shao, R. G. Compton, *Sensors and Actuators B - Chemical*, 2008, **133**, 462.

291. R. S. Nicholson, *Analytical Chemistry*, 1965, **37**, 1351.

292. C. E. Banks, R. G. Compton, A. C. Fisher, I. E. Healey, *Physical Chemistry Chemical Physics*, 2004, **6**, 3147.

293. R. R. Moore, C. E. Banks, R. G. Compton, *Analytical Chemistry*, 2004, **76**, 2677.

294. D. A. C. Brownson, C. W. Foster, C. E. Banks, *Analyst*, 2012, **137**, 1815.

295. M. C. Henstridge, L. Shao, G. G. Wildgoose, R. G. Compton, G. Tobias, M. L. H. Green, *Electroanalysis*, 2008, **20**, 498.

296. C. Batchelor-McAuley, L. M. Gonçalves, L. Xiong, A. A. Barros, R. G. Compton, *Chemical Communications*, 2010, **46**, 9037.

297. H. E. Webb, E. C. Fabianke-Kadue, R. R. Kraemer, G. H. Kamimori, V. D. Castracane, E. O. Acevedo, *Applied Psychophysiology and Biofeedback*, 2011, **36**, 243.

298. C. Zhu, S. Guo, Y. Fang, S. Dong, *ACS Nano*, 2010, **4**, 2429.

299. J. X. Qiaoa, H. Q. Luoa, N. B. Li, *Colloids and Surfaces B - Biointerfaces*, 2008, **62**, 31.

300. J. Chang, K. Chang, C. Hu, W. Cheng, J. Zen, *Electrochemical Communications*, 2010, **12**, 596.

301. H. Z. Li, H. Wen, S. C. Barton, *Electroanalysis*, 2012, **24**, 398.

302. J. You, S. Jeon, *Electrochimica Acta*, 2011, **56**, 10077.

303. H. R. Zare, N. Nasirizadeh, M. M. Ardakani, *Journal of Electroanalytical Chemistry*, 2005, **577**, 25.

304. M. C. Granger, M. Witek, J. Xu, J. Wang, M. Hupert, A. Hanks, M. D. Koppang, J. E. Butler, G. Lucazeau, M. Mermoux, J. W. Strojek, G. M. Swain, *Analytical Chemistry*, 2000, **72**, 3793.

305. C. E. Banks, G. G. Wildgoose, C. G. R. Heald and R. G. Compton, *Journal of the Iranian Chemical Society*, 2005, **2**, 60.

306. T. J. Schmidt, U. A. Paulus, H. A. Gasteiger, R. J. Behm, *Journal of Electroanalytical Chemistry*, 2001, **508**, 41.

307. I. Kruusenberg, J. Leis, M. Arulepp, *Journal of Solid State Electrochemistry*, 2010, **14**, 1269.

308. G. Gupta, V. Rajendran, P. Atanassov, *Electroanalysis*, 2004, **16**, 1182.

309. S. Guo, S. Dong, E. Wang, *Journal of Physical Chemistry C*, 2008, **112**, 2389.

310. L. Mao, D. Zhang, T. Sotomura, K. Nakatsu, N. Koshiba, T. Ohsaka, *Electrochimica Acta*, 2003, **48**, 1015.

311. J. Yang, J. J. Xu, *Electrochemistry Communications*, 2003, **5**, 306.

312. T. Kuboki, T. Okuyama, T. Ohsaki, N. Takami, *Journal of Power Sources*, 2005, **146**, 766.

313. A. A. Gewirth, M. S. Thorum, *Inorganic Chemistry*, 2010, **49**, 3557.

314. Q. Li, C. Batchelor-McAuley, N. S. Lawrence, R. S. Hartshorne, R. G. Compton, *New Journal of Chemistry*, 2011, **35**, 2462.

315. E. Yeager, *Electrochimica Acta*, 1984, **29**, 1527.

316. E. Yeager, *Journal of Molecular Catalysis*, 1986, **38**, 5.

317. D. E. Curtin, R. D. Lousenberg, T. J. Henry, P. C. Tangeman, M. E. Tisack, *Journal of Power Sources*, 2004, **131**, 41.

318. A. Bosnjakovic, S. Schlick, *Journal of Physical Chemistry B*, 2004, **108**, 4332.

319. A. Ambrosi, A. Bonanni, Z. Sofer, J. S. Cross, M. Pumera, *Chemistry - A European Journal*, 2011, **17**, 10763.

320. D. A. C. Brownson, L. J. Munro, D. K. Kampouris and C. E. Banks, *RSC Advances*, 2011, **1**, 978.

321. C. E. Banks and R. G. Compton, *Analyst*, 2005, **130**, 1232.

322. C. E. Banks and R. G. Compton, *Analyst*, 2006, **131**, 15.

323. K. Tammeveski, K. Kontturi, R. J. Nichols, R. J. Potter, D. J. Schiffrin, *Journal of Electroanalytical Chemistry*, 2001, **515**, 101.

324. A. Sarapuu, K. Vaik, D. J. Schiffrin and K. Tammeveski, *Journal of Electroanalytical Chemistry*, 2003, **541**, 23.

325. E. P. Randviir, D. A. C. Brownson, M. Gómez-Mingot, D. K. Kampouris, J. Iniesta and C. E. Banks, *Nanoscale*, 2012, **4**, 6470.

326. I. Streeter, G. G. Wildgoose, L. Shao and R. G. Compton, *Sensors and Actuators B - Chemical*, 2008, **133**, 462.

327. T. Kaskiala, *Minerals Engineering*, 2002, **15**, 853.

328. P. Han and D. M. Bartels, *Journal of Physical Chemistry*, 1996, **100**, 5597.

329. T. Wang, E. P. Randviir and C. E. Banks, *Analyst*, 2014, **139**, 2000.

330. E. P. Randviir, D. K. Kampouris and C. E. Banks, *Analyst*, 2013, **138**, 6565.

331. M. Peake and M. Whiting, *Clinical Biochemist Reviews*, 2006, **27**, 173.

332. N. A. Choudry, D. K. Kampouris, R. O. Kadara and C. E. Banks, *Electrochemical Communications*, 2010, **12**, 6.

333. E. P. Randviir, D. A. C. Brownson, J. P. Metters, R. O. Kadara and C. E. Banks, *Physical Chemistry Chemical Physics*, 2014, **16**, 4598.

334. E. P. Randviir, J. P. Metters, J. Stainton and C. E. Banks, *Analyst*, 2013, **138**, 2970.

335. P. J. Barnes and R. A. Pauwels, *European Respiratory Journal*, 1994, **7**, 579.

336. A. H. Dawson and I. M. Whyte, *British Journal of Clinical Pharmacology*, 1999, **48**, 278.

337. M. Shannon, *Annals of Internal Medicine*, 1993, **119**, 1161.

338. C. E. Cook, M. E. Twine, M. Myers, E. Amerson, J. A. Kepler and G. F. Taylor, *Research Communications in Chemical Pathology and Pharmacology*, 1976, **13**, 497.

339. B. Srdjenovic, V. Djordjevic-Milic, N. Grujic, R. Injac and Z. Lepojevic, *Journal of Chromatographic Science*, 2008, **46**, 144.

340. M. E. Jolley, *Journal of Analytical Toxicology*, 1981, **5**, 236.

341. E. E. Ferapontova, E. M. Olsen and K. V. Gothelf, *Journal of the American Chemical Society*, 2008, **130**, 4256.

342. Y.-H. Zhu, Z.-L. Zhang and D.-W. Pang, *Journal of Electroanalytical Chemistry*, 2005, **581**, 303.

343. N. Spătaru, B. V. Sarada, D. A. Tryk and A. Fujishima, *Electroanalysis*, 2002, **14**, 721.

344. Y. V. Ulyanova, A. E. Blackwell and S. D. Minteer, *Analyst*, 2006, **131**, 257.

345. B. H. Hansen and G. Dryhurst, *Journal of Electroanalytical Chemistry and Interfacial Electrochemistry*, 1971, **32**, 405.

346. N. C. Foulds, J. M. Wilshere and M. J. Green, *Analytica Chimica Acta*, 1990, **229**, 57.

347. K. S. Lee, T.-H. Kim, M.-C. Shin, W.-Y. Lee and J.-K. Park, *Analytica Chimica Acta*, 1999, **380**, 17.

348. A. V. Trask, W. D. S. Motherwell and W. Jones, *International Journal of Pharmaceutics*, 2006, **320**, 114.

349. R. N. Goyal, B. K. Puri and N. Jain, *Journal of the Chemical Society Perkin Transactions*, 2001, **2**, 832.

350. P. A. Mitenko and R. I. Ogilvie, The *New England Journal of Medicine*, 1973, **289**, 600.

351. H. Schiffl and S. M. Lang, *Molecular Diagnosis and Therapy*, 2012, **16**, 199.

352. M. del Carmen Hurtado-Sanchez, A. Espinosa-Mansilla, M. I. Rodriguez-Cacares, E. Martin-Tornero and I. Duran-Meras, *Journal of Separation Science*, 2012, **35**, 2575.

353. E. P. Randviir and C. E. Banks, *Sensors and Actuators B - Chemical*, 2013, **183**, 239.

354. M. Jaffe, *Zeitschrift für Physiologische Chemie*, 1886, **10**, 391.

355. P. Campins Falcó, L. A. Tortajada Genaro, S. Meseger Lloret, F. Blasco Gomez, A. Sevillano Cabeze and C. Molins Legua, *Talanta*, 2001, **55**, 1079.

356. C. M. Cobbaert, H. Baadenhuijsen and C. W. Weykamp, *Clinical Chemistry*, 2009, **55**, 549.

357. L. Ford and J. Berg, *Annals of Clinical Biochemistry*, 2008, **45**, 83.

358. H. Huang, Z. Chen and X. Yan, *Journal of Separation Science*, 2012, **35**, 436.

359. J. A. Muñoz, M. Lopez-Mesas and M. Valiente, *Talanta*, 2010, **81**, 392.

360. M. A. Muñoz, J. Eijkel, A. Floris, S. Staal, A. Ríos and A. van den Berg, presented in part at the 15th International Conference on Miniaturized Systems for Chemistry and Life Sciences, Seattle, Washington, USA, 2011.

361. R. Harlan, W. Clarke, J. M. Di Bussolo, M. Kozak, J. Straseski and D. L. Meany, *Clinica Chimica Acta*, 2010, **411**, 1728.

362. T. Tshuchida and K. Yoda, *Clinical Chemistry*, 1983, **29**, 51.

363. V. F. Samanidou, A. S. Metaxa and I. N. Papadoyannis, *Journal of Liquid Chromatography and Related Technologies*, 2002, **25**, 43.

364. J.-F. Jen, S.-L. Hsiao and K.-H. Liu, *Talanta*, 2002, **58**, 711.

365. Cross referenced from and M. D. S. Shepherd, *Clinical Biochemist Reviews*, 2011, **32**, 109.

366. A. R. Butler and C. Glidewell, *Journal of the Chemical Society Perkin Transactions II*, 1985, 1465.

367. W. R. de Araújo, M. O. Salles and T. R. L. C. Paixão, *Sensors and Actuators B - Chemical*, 2012, **173**, 847.

368. F. Wei, S. Cheng, Y. Korin, E. F. Reed, D. Gjerston, C. Ho, H. A. Gritsch and J. Veale, *Analytical Chemistry*, 2012, **84**, 7933.

369. S. Yadav, A. Kumar and C. S. Pundir, *Analytical Biochemistry*, 2011, **419**, 277.

370. S. Yadav, R. Devi, A. Kumar and C. S. Pundir, *Biosensors and Bioelectronics*, 2011, **28**, 67.

371. B. Khadro, C. Sanglar, A. Bonhomme, A. Errachid and N. Jaffrezic-Renault, *Procedia Engineering*, 2010, **5**, 371.

372. E. J. Kim, T. Haruyama, Y. Yanagida, E. Kobatake and M. Aizawa, *Analytica Chimica Acta*, 1999, **394**, 225.

373. M. Guo, H. Liu and Y. Li, *Chinese Journal of Analytical Chemistry*, 1999, **27**, 475.

374. M. B. Mădăraş and R. P. Buck, *Analytical Chemistry*, 1996, **68**, 3832.

375. J. A. Berberich, L. W. Yang, J. Madura, I. Bahar and A. J. Russell, *Acta Biomaterialia*, 2005, **1**, 173.

376. J. A. Berberich, L. W. Yang, I. Bahar and A. J. Russell, *Acta Biomaterialia*, 2005, **1**, 183.

377. J. A. Berberich, A. Chan, M. Boden and A. J. Russell, *Acta Biomaterialia*, 2005, **1**, 193.

378. H. Yamato, M. Ohwa and W. Wernet, *Analytical Chemistry*, 1995, **67**, 2776.

379. J. Chen, A. S. Kumar, H. Chung, C. S., M. Kuo and J. Zen, *Sensors and Actuators B - Chemical*, 2006, **115**, 473.

380. T. Nareshkumar, A. Ananthi, J. Mathiyarasu, J. Joseph, K. L. N. Phani and V. Yegnaraman, *Journal of Electroanalytical Chemistry*, 2011, **661**, 303.

381. M. J. Ruedas-Rama and E. A. H. Hall, *Analytical Chemistry*, 2010, **82**, 9043.

382. R. A. Rhoades and D. R. Bell, *Medical Physiology: Principles for Clinical Medicine*, Lippincott Williams & Wilkins, US, 2008.

383. L. D. Burke and P. F. Nugent, *Gold Bulletin*, 1997, **30**, 43.

384. T. Łuczak, *Journal of Applied Electrochemistry*, 2007, 269.

385. E. P. Diamandis and T. P. Hadjiioannou, *Microchemical Journal*, 1983, **28**, 399.

386. K. G. Blass and R. J. Thilbert, *Microchemical Journal*, 1974, **19**, 1.

387. D. L. Fabini and G. Ertinghausen, *Clinical Chemistry*, 1971, **17**, 696.

388. E. P. Randviir and C. E. Banks, *RSC Adv.*, 2013, **26**, 76.

389. Sigma Aldrich, http://www.sigmaaldrich.com.

390. J. P. Metters, R. O. Kadara and C. E. Banks, *Analyst*, 2012, **137**, 896.

391. D. A. C. Brownson, D. K. Kampouris and C. E. Banks, *Chemical Society Reviews*, 2012, **41**, 6944.

392. Ceram, http://www.ceram.com.

393. N. A. Choudry, D. K. Kampouris, R. O. Kadara and C. E. Banks, *Electrochemical Communications*, 2010, **12**, 6.

394. M. Khairy, D. K. Kampouris, R. O. Kadara and C. E. Banks, *Electroanalysis*, 2010, **22**, 2496.

395. P. M. Hallam, D. K. Kampouris, R. O. Kadara and C. E. Banks, *Analyst*, 2010, **135**, 1947.

396. Haydale, http://www.haydale.com.

397. Vorbeck, http://vorbeck.com.

398. D. A. C. Brownson, D. K. Kampouris and C. E. Banks, *Chemical Society Reviews*, 2012, **41**, 6944.

399. D. A. C. Brownson and C. E. Banks, *Analyst*, 2010, **135**, 2768.

400. T. Gan and S. Hu, *Microchimica Acta*, 2011, **175**, 1.

401. D. A. C. Brownson, D. K. Kampouris and C. E. Banks, *Journal of Power Sources*, 2011, **196**, 4837.

402. L. Dai, D. W. Chang, J. B. Baek and W. Lu, *Small.*, 2012, **8**, 1130.

403. L. C. S. Figueiredo-Filho, D. A. C. Brownson, O. Fatibello-Filho and C. E. Banks, *Analyst*, 2013, **138**, 4436.

404. M. Zhou, Y. Zhai and S. Dong, *Analytical Chemistry*, 2009, **81**, 5603.

405. S. Mao, G. Lu, K. Yu, Z. Bo and J. Chen, *Advanced Materials*, 2010, **22**, 3521.

406. W. Wu, Z. Liu, L. A. Jauregui, Q. Yu, R. Pillai, H. Cao, J. Bao, Y. P. Chen and S.-S. Pei, *Sensors and Actuators B - Chemical*, 2010, **150**, 296.

407. D. A. C. Brownson and C. E. Banks, *Physical Chemistry Chemical Physics*, 2012, **14**, 8264.

408. F. Yavari, Z. Chen, A. V. Thomas, W. Ren, H.-M. Cheng and N. Koratkar, *Scientific Reports*, 2011, **1**, Article no. 166.

409. D. A. C. Brownson, L. C. S. Figueiredo-Filho, X. Ji, M. Gómez-Mingot, J. Iniesta, O. Fatibello-Filho, D. K. Kampouris and C. E. Banks, *Journal of Materials Chemistry A*, 2013, **1**, 5962.

410. D. A. C. Brownson, A. C. Lacombe, M. Gómez-Mingot and C. E. Banks, *RSC Advances*, 2012, **2**, 665.

411. D.-W. Wang, I. R. Gentle and G. Q. Lu, *Electrochemistry Communications*, 2010, **12**, 1423.

412. D. A. C. Brownson, S. A. Varey, F. Hussain, S. J. Haigh and C. E. Banks, *Nanoscale*, 2012, **6**, 1607.

413. A. Ambrosi, A. Bonanni, Z. Sofer and M. Pumera, *Nanoscale*, 2013, **5**, 2379.

414. D. A. C. Brownson and C. E. Banks, *Physical Chemistry Chemical Physics*, 2011, **13**, 15825.

415. D. A. C. Brownson, R. V. Gorbachev, S. J. Haigh and C. E. Banks, *Analyst*, 2012, **137**, 833.

416. A. T. Valota, I. A. Kinloch, K. S. Novoselov, C. Casiraghi, A. Eckmann, E. W. Hill and R. A. W. Dryfe, *ACS Nano*, 2011, **5**, 8809.

417. J. P. Metters, R. O. Kadara and C. E. Banks, *Analyst*, 2011, **136**, 1067.

418. J. P. Smith, J. P. Metters, D. K. Kampouris, C. Lledo-Fernandez, O. B. Sutcliffe and C. E. Banks, *Analyst*, 2013, **138**, 6185.

419. J. P. Smith, J. P. Metters, C. Irving, O. B. Sutcliffe and C. E. Banks, *Analyst*, 2014, **139**, 389.

420. L. Zhang, L. Yang, L. Zhang, D.-W. Li, D. Karpuzov and Y.-T. Long, *International Journal of Electrochemical Science*, 2011, **6**, 819.

421. D. A. C. Brownson and C. E. Banks, *Electrochemistry Communications*, 2011, **13**, 111.

422. S. Eissa, C. Tlili, L. L'Hocine and M. Zourob, *Biosensors and Bioelectronics*, 2012, **38**, 308.

423. F. Valentini, D. Romanazzo, M. Carbone and G. Palleschi, *Electroanalysis*, 2012, **24**, 872.

424. D. A. C. Brownson and C. E. Banks, *Analyst*, 2011, **136**, 2084.

425. W. Song, D.-W. Li, Y.-T. Li, Y. Li and Y.-T. Long, *Biosensors and Bioelectronics*, 2011, **26**, 3181.

426. J. Ping, J. Wu, Y. Wang and Y. Ying, *Biosensors and Bioelectronics*, 2012, **34**, 70.

427. P. M. Hallam and C. E. Banks, *Electrochemistry Communications*, 2011, **13**, 8.

428. I. Lavagnini, R. Antiochia and F. Magno, *Electroanalysis*, 2004, **16**, 505.

429. A. Gomis-Berenguer, M. Gómez-Mingot, V. Montiel, A. Canals, T. Thiemann, R. O. Kadara, C. E. Banks and J. Iniesta, *RSC Advances*, 2012, **2**, 7735.

430. A. C. Ferrari, J. C. Meyer, V. Scardaci, C. Casiraghi, M. Lazzeri, F. Mauri, S. Piscanec, D. Jiang, K. S. Novoseloc, S. Roth and A. K. Geim, *Applied Physics Letters*, 2006, **97**, 187401.

431. F. Tuinstra and J. L. Koenig, *Journal of Chemical Physics*, 1970, **53**, 1126.

432. A. Gupta, G. Chen, P. Joshi, S. Tadigadapa and P. C. Eklund, *Nano Letters*, 2006, **6**, 2667.

433. Y. Y. Wang, Z. H. Ni, Y. Yu, Z. X. Shen, H. M. Wang, Y. H. Wu, W. Chen and A. T. S. Wee, *Journal of Physical Chemistry C*, 2008, **112**, 10637.

434. J. Chen, M. A. Hamon, H. Hu, Y. P. Chen, A. M. Rao, P. C. Eklund and R. C. Haddon, *Science*, 1998, **282**, 95.

435. U. J. Kim, C. A. Furtado, X. Liu, G. Chen and P. C. Eklund, *Journal of the American Chemical Society*, 2005, **127**, 15437.

436. J. P. Smith, C. W. Foster, J. P. Metters, O. B. Sutcliffe and C. E. Banks, *Electroanalysis*, 2014, **26**, 2429.

437. S. Alwarappan, A. Erdem, C. Liu and C.-Z. Li, *Journal of Physical Chemistry C.*, 2009, **113**, 8853.

438. A. Andreu, J. W. Merkert, L. A. Lecaros, B. L. Broglin, J. T. Brazell and M. El-Kouedi, *Sensors and Actuators B - Chemical*, 2006, **114**, 1116.

439. M. Manesse, R. Sanjines, V. Stambouli, R. Boukherroub and S. Szunerits, *Electrochemistry Communications*, 2008, **10**, 1041.

440. I. Streeter, G. G. Wildgoose, L. Shao and R. G. Compton, *Sensors and Actuators B - Chemical*, 2008, **133**, 462.

441. M. C. Henstridge, L. Shao, G. G. Wildgoose, R. G. Compton, G. Tobias and M. L. H. Green, *Electroanalysis*, 2008, **20**, 498.

442. D. A. C. Brownson, S. A. Varey, F. Hussain, S. J. Haigh and C. E. Banks, *Nanoscale*, 2014, **6**, 1607.

443. P. Chen and R. L. McCreery, *Analytical Chemistry*, 1996, **68**, 3958.

444. K. C. Honeychurch and J. P. Hart, *Advances in Analytical Chemistry*, 2012, **2**, 46.

445. M. Pumera, *Nanoscale Research Letters*, 2007, **2**, 87.

446. M. C. Granger and G. M. Swain, *Journal of the Electrochemical Society*, 1999, **146**, 4551.

447. R. G. Evans, O. V. Klymenko, P. D. Price, S. G. Davies, C. Hardacre and R. G. Compton, *ChemPhysChem*, 2005, **6**, 526.

448. F. Marken, R. G. Compton, C. H. Goeting, J. S. Foord, S. D. Bull and S. G. Davies, *Journal of Solid State Electrochemistry*, 2001, **5**, 88.

449. N. S. Lawrence and J. Wang, *Electrochemistry Communications*, 2006, **8**, 71.

450. N. Smirnoff, *Current Opinion in Plant Biology*, 2000, **3**, 229.

451. N. Ben-Jonathan, *Endocrine Reviews*, 1985, **6**, 564.

452. V. Vitart, I. Rudan, C. Hayward, N. K. Gray, J. Floyd, C. N. A. Palmer, S. A. Knott, I. Kolcic, O. Polasek, J. Graessler, J. F. Wilson, A. Marinaki, P. L. Riches, X. Shu, B. Janicijevic, N. Smolej-Narancic, B. Gorgoni, J. Morgan, S. Campbell, Z. Biloglav, L. Barac-Lauc, M. Pericic, I. M. Klaric, L. Zgaga, T. Skaric-Juric, S. H. Wild, W. A. Richardson, P. Hohenstein, C. H. Kimber, A. Tenesa, L. A. Donnelly, L. D. Fairbanks, M. Aringer, P. M. McKeigue, S. H. Ralston, A. D. Morris, P. Rudan, N. D. Hastie, H. Campbell and A. F. Wright, *Nature Genetics*, 2008, **40**, 437.

453. J. Huang, Y. Liu, H. Hou and Y. T., *Biosensors and Bioelectronics*, 2008, **24**, 632.

454. K. Iriyama, M. Yoshiura, T. Iwamoto and Y. Ozaki, *Analytical Biochemistry*, 1984, **141**, 238.

455. C.-L. Sun, H.-H. Lee, J.-M. Yang and C.-C. Wu, *Biosensors and Bioelectronics*, 2011, **26**, 3450.

456. A. Safavi, N. Maleki, O. Moradlou and F. Tajabadi, *Analytical Biochemistry*, 2006, **359**, 224.

457. H. R. Zare, N. Nasirizadeh and M. M. Ardakani, *Journal of Electroanalytical Chemistry*, 2005, **577**, 25.

458. L. C. S. Figueiredo-Filho, D. A. C. Brownson, M. Gómez-Mingot, J. Iniesta, O. Fatibello-Filho and C. E. Banks, *Analyst*, 2013, **138**, 6354.

459. M. L. Brigden, D. Edgell, M. McPherson, A. Leadbeater and G. Hoag, *Clinical Chemistry*, 1992, **38**, 426.

460. Medline Plus, http://www.nlm.nih.gov/medlineplus/ency/article/003613.htm.

461. D. A. C. Brownson, C. W. Foster and C. E. Banks, *Analyst*, 2012, **137**, 1815.

462. Gamry, http://www.gamry.com/application-notes/quick-check-of-eis-system-performance/.

463. W. B. Russell, D. A. Saville and W. R. Schowalter, *Colloidal Dispersions*, Cambridge University Press, 1989.

464. A. Salis, M. Boström, L. Medda, F. Cugia, B. Barse, D. F. Parsons, B. W. Ninham and M. Monduzzi, *Langmuir*, 2011, **27**, 11597.

465. S. Trasatti and E. Lust, in *Modern Aspects of Electrochemistry*, eds. R. White, J. O. M. Bockris and B. E. Conway, Springer US, 1999, vol. 33, ch. 1, pp. 1.

466. M. D. Stoller, C. W. Magnuson, Y. Zhu, S. Murali, J. W. Suk, R. Piner and R. S. Ruoff, *Energy and Environmental Science*, 2011, **4**, 4685.

467. A. C. Hillier, S. Kim and A. J. Bard, *The Journal of Physical Chemistry*, 1996, **100**, 18808.

468. E. P. Randviir, D. A. C. Brownson, J. P. Metters, R. O. Kadara and C. E. Banks, *Physical Chemistry Chemical Physics*, 2014, **16**, 4598.

469. N. A. Choudry, D. K. Kampouris, R. O. Kadara and C. E. Banks, *Electrochemistry Communications*, 2010, **12**, 6.

470. E. P. Randviir, D. A. C. Brownson and C. E. Banks, *Materials Today*, 2014, **17**, 426.

471. R. A. Marcus, *The Journal of Chemical Physics*, 1956, **24**, 966.

472. R. A. Marcus, *The Journal of Chemical Physics*, 1957, **26**, 867.

473. R. A. Marcus, *Reviews of Modern Physics*, 1993, **65**, 599.

474. R. S. Nicholson, *Analytical Chemistry*, 1966, **38**, 1406.

475. N. Siraj, G. Grampp, S. Landgraf and K. Punyain, in *Zeitschrift für Physikalische Chemie International* Edition, 2013, **227**, 105.

476. R. Feeney and S. P. Kounaves, *Electrochemistry Communications*, 1999, **1**, 453.

477. M. E. Ortiz, L. J. Núñez-Vergara and J. A. Squella, *Journal of Electroanalytical Chemistry*, 2003, **549**, 157.

478. C. W. Foster, J. P. Metters, D. K. Kampouris and C. E. Banks, *Electroanalysis*, 2014, **26**, 26.

479. N. K. Bhatti, M. S. Subhani, A. Y. Khan, R. Qureshi and A. Rahman, *Turkish Journal of Chemistry*, 2005, **29**, 659.

480. E. P. Randviir and C. E. Banks, *Analytical Methods*, 2013, **5**, 1098.

481. V. Ganesh, S. K. Pal, S. Kumar and V. Lakshminarayanan, *Journal of Colloid and Interface Science*, 2006, **296**, 195.

482. F. Sundfors, J. Bobacka, A. Ivaska and A. Lewenstam, *Electrochimica Acta*, 2002, **47**, 2245.

483. C. Saby, B. Ortiz, G. Y. Champagne and D. Bélanger, *Langmuir*, 1997, **13**, 6805.

484. A. M. Oliveira-Brett, L. A. d. Silva and C. M. A. Brett, *Langmuir*, 2002, **18**, 2326.

485. F. Cruz Moraes, M. F. Cabral, S. A. S. Machado and L. H. Mascaro, *Electroanalysis*, 2008, **20**, 851.

486. A. Curulli, F. Valentini, S. Orlanducci and M. L. Terranova, *Indian Journal of Chemsitry*, 2005, **44A**, 956.

487. S. Shahrokhian and S. Bozorgzadeh, *Electrochimica Acta*, 2006, **51**, 4271.

488. S. Corona-Avendaño, G. Alarcón-Angeles, M. T. Ramírez-Silva, G. Rosquete-Pina, M. Romero-Romo and M. Palomar-Pardavé, *Journal of Electroanalytical Chemistry*, 2007, **609**, 17.

489. A. Hermans, *Fabrication and applications of dopamine-sensitive electrodes*, ProQuest, http://gradworks.umi.com/32/88/3288989.html.

490. E. Ekinci, G. Erdogdu and A. E. Karagözler, *Polymer Bulletin*, 2000, **44**, 547.

491. T. A. Enache and A. M. Oliveira-Brett, *Journal of Electroanalytical Chemistry*, 2011, **655**, 9.

492. C. Bian, Q. Zeng, H. Xiong, X. Zhang and S. Wang, *Bioelectrochemistry*, 2010, **79**, 1.

493. M. R. Deakin, P. M. Kovach, K. J. Stutts and R. M. Wightman, *Analytical Chemistry*, 1986, **58**, 1474.

494. G. Che, B. B. Lakshmi, C. R. Martin and E. R. Fisher, *Langmuir*, 1999, **15**, 750.

495. D. A. C. Brownson and C. E. Banks, *Electrochemistry Communications*, 2011, **13**, 111.

496. C. Jiang, T. Yang, K. Jiao and H. Gao, *Electrochimica Acta*, 2008, **53**, 2917.

497. A. Poghossian, T. Yoshinobu, A. Simonis, H. Ecken, H. Lüth and M. J. Schöning, *Sensors and Actuators B - Chemical*, 2001, **78**, 237.

498. N. F. Atta and M. F. El-Kady, *Talanta*, 2009, **79**, 639.

499. D. Xu, D. Xu, X. Yu, Z. Liu, W. He and Z. Ma, *Analytical Chemistry*, 2005, **77**, 5107.

1. E. P. Randviir, C. E. Banks, *"Electrochemical Impedance Spectroscopy: an Overview of Bioanalytical Applications"*, *Anal. Methods*, 2013, **5**, 1098-1115.
   Contribution: Literature review and writing of a peer-reviewed article.

2. E. P. Randviir, C. E. Banks, "*Electrochemical Measurement of the DNA Bases Adenine and Guanine at Surfactant-Free Graphene Modified Electrodes"*, *RSC Adv.*, 2012, **2**, 5800-5805.
   Contribution: Experimental contribution to carbon nanoelectrochemistry through a peer-reviewed article.

3. E. P. Randviir, D. A. C. Brownson, M. Gómez-Mingot, D. K. Kampouris, J. Iniesta, C. E. Banks, *"Electrochemistry of Q-Graphene"*, *Nanoscale*, 2012, **4**, 6470-6480.
   Contribution: Experimental contribution to carbon nanoelectrochemistry through a peer-reviewed article.

4. E. P. Randviir, C. E. Banks, *"The Oxygen Reduction Reaction at Graphene Modified Electrodes"*, *Electroanalysis*, 2014, **26**, 76-83.
   Contribution: Experimental contribution to carbon nanoelectrochemistry and new insights into the oxygen reduction reaction, through a peer-reviewed article.

5. T. Wang, E. P. Randviir, C. E. Banks, *"Detection of Theophylline Using Portable Electrochemical Sensors"*, *Analyst*, **139**, 2000-2003.
   Contribution: Experimental contribution to medicinal electrochemistry, through a peer-reviewed article.

6. E. P. Randviir, D. K. Kampouris, C. E. Banks, *"An Improved Electrochemical Creatinine Detection Method Via a Jaffe-Based Procedure"*, *Analyst*, **138**, 6565-6572.
   Contribution: Experimental contribution to medicinal electrochemistry, through a peer-reviewed article.

7. E. P. Randviir, D. A. C. Brownson, J. P. Metters, R. O. Kadara, C. E. Banks, *"The Fabrication, Characterisation, and Electrochemical Investigation of Screen-Printed Graphene Electrodes"*, *Phys. Chem. Chem. Phys.*, 2014, **16**, 4598-4611.
   Contribution: Fundamental contribution to graphene electrochemistry through a peer-reviewed article.